CONCRETE PAVEMENTS: DETERIORATION DUE TO DE-ICING SALTS AND REPAIR

by

Ahmed Ali Mohamed Ghazy

A Thesis Submitted to the Faculty of Graduate Studies of

The University of Manitoba

in partial fulfillment of the requirements for the degree of

Doctor of Philosophy

Department of Civil Engineering

University of Manitoba

Winnipeg

October 2017

ABSTRACT

With intensive use of chloride-based ice control chemicals for winter maintenance operations (de-icing, anti-icing and pre-wetting), concrete pavements may undergo significant alterations resulting in adverse consequences on their engineering properties. Formation of complex salts (oxychlorides) has been suspected for causing chemical degradation of concrete pavements, but without direct microstructural evidence due to their instability. Thus, an effort was made to elucidate the damage mechanisms of field and laboratory concrete exposed to the most widely used chloride-based de-icing salts (individual and combined) under different exposure conditions. This thesis aimed at capturing/linking the formation of these complex phases, if any, with the physico-mechanical properties of real cementitious systems/concretes and proposing their roles in the damage process. Also, this thesis explored the potential benefits of supplementary cementitious materials (SCMs: fly ash and nanosilica) and portland limestone cement (PLC) to mitigate this type of damage.

In the field investigation (Phase I), forensic evaluation was used to classify the source of damage and identify aspects contributing to the deterioration of regional (chloride-based salts are directly applied) and residential (salts are borne by vehicles tires) roads in Winnipeg, Canada. The results revealed that the regional roads had a high intensity of micro-cracks and most air voids were infilled with various levels of secondary depositions compared to residential roads. The deterioration of concrete is explained by a combination of physical and chemical aspects, due to the interaction of salts, freezing/thawing (F/T) and wetting/drying (W/D) cycles with the hydrated paste.

In the laboratory component involving simulation experiments (Phase II), conditioned mode environmental scanning electron microscopy (ESEM) was used to minimize changes in the crystal structures of the reaction products to explicitly capture their unaltered morphology and effects on concrete specimens. Formation of acicular flattened blades of 3- and 5-form

magnesium oxychloride (MOX) and tiny fibrous crystals, as well as subhedral pseudo-hexagonal calcium oxychloride plates (COX), were found in the deteriorated concrete specimens, depending on the type of solution. The combined salt, which simulates a maintenance and protective strategy for pavements, was the most aggressive solution. Also, the combined exposure involving cyclic environments had additive and synergistic effects on specimens, causing the coexistence of multiple degradation mechanisms and complex assemblages depositing in the matrix. The overall results indicated that the restrictive limits on fly ash in concrete serving in chloride-rich environments may produce less durable concrete than noncompliant mixtures with higher fly ash dosages. Indeed, the performance of concrete exposed to de-icing salts was much enhanced by an innovative SCM such as nanosilica. Also, PLC mixtures exhibited better resistance to de-icing salts due to dual physical and chemical actions of limestone in the matrix. An adaptive neuro-fuzzy inference system (ANFIS) was also developed in Phase II to model the time of failure (*TF*) of concrete mixtures under various exposure regimes combined with de-icing salts. The results showed that predictions of the ANFIS model were rational and accurate, with marginal errors not exceeding 3%.

Phase III of the thesis aimed at developing durable repair materials (nano-modified fly ash concrete, NMFC) and enhancing the overall process of rehabilitating concrete pavements to achieve optimum performance, longevity and life-cycle cost effectiveness. The results showed that the NMFC mixtures produced in the laboratory achieved a reasonable balance of early-age and long-term behavior, as demonstrated by setting time, strength development, compatibility/bonding, and resistance to infiltration of fluids and salt-frost scaling. In addition, the field trial demonstrated the mixing, placement, and testing procedures of NMFC as a novel repair material for concrete pavements with promising long-term performance.

CO-AUTHORSHIP

This thesis has been prepared in accordance with the regulation of integrated-article format stipulated by the Faculty of Graduate Studies at the University of Manitoba. Substantial parts of this thesis were either published in or submitted for publication to peer-reviewed technical journals and international conferences as well as technical reports and guidelines as shown below:

<u>Journal Papers</u>

1. **Ghazy, A.**, Bassuoni, M.T. "Neuro-fuzzy Based Prediction of the Durability of Concrete to Various Exposures Combined with De-icing Salts", *Computers and Concrete*. (Submitted in Oct. 2017, Under Review) **[Chapter 7]**

2. **Ghazy, A.**, Bassuoni, M.T. "Response of Concrete with Blended Binders and Nanosilica to Cyclic Environments and Chloride-Based Salts", *Magazine of Concrete Research.* (Submitted in Sep. 2017, Under Review) **[Chapter 6]**

3. **Ghazy, A.**, Bassuoni, M.T. "Response of Concrete with Blended Binders and Nanosilica to Freezing-Thawing Cycles and Different Concentrations of De-Icing Salts", *ASCE Journal of Materials in Civil Engineering*. (Accepted in Oct. 2017) **[Chapter 5]**

4. **Ghazy, A.**, Bassuoni, M.T. "Resistance of Concrete to Different Exposures with Chloride-Based Salts", *Cement and Concrete Research*, Vol. 101, 2017, pp. 144-158. **[Chapter 4]**

5. **Ghazy, A.**, Bassuoni, M.T. A.K.M. R. Islam. "Assessment of Joints in Concrete Pavements Exposed to Different Winter Conditions", *ASCE Journal of Performance of Constructed Facilities*, Vol. 32, No. 2, 20187, doi: 04017135. **[Chapter 3]**

6. **Ghazy, A.**, Bassuoni, M.T. "Shrinkage of Nano-Modified Fly Ash Concrete as A Repair Material for Concrete Pavements", *ACI Materials Journal*, Vol. 114, No. 6, 2017, doi: 10.14359/51700891. **[Chapter 9]**

7. **Ghazy, A.**, Bassuoni, M.T. And Shalaby, A. "Field Trial of Nano-modified Concrete as A Repair Material for Concrete Pavements", *Concrete International*, Vol. 39, Issue. 2, 2017, pp. 38-44. **[Chapter 10]**

8. **Ghazy, A.**, Bassuoni, M.T. And Shalaby, A. "Nano-Modified Fly Ash Concrete: A Repair Option for Concrete Pavements", *ACI Materials Journal*, Vol. 113, No. 2, 2016, pp. 231-242. **[Chapter 8]**

Conference Proceedings

1. A.K.M. R. Islam, **Ghazy, A.**, Bassuoni, M.T. "Deterioration of Joints in Concrete Pavements: Investigation of Field Cores", *Canadian Society for Civil Engineering Conference*, Vancouver, Bk, Canada, May 27-30, 2017.

2. **Ghazy, A.**, Bassuoni, M.T. "Repair of Concrete Pavements with Nano-Modified Concrete", *14th International Conference on Structural and Geotechnical Engineering* (ICSGE), Cairo, Egypt, Dec. 26-29, 2015.

3. **Ghazy, A.**, Bassuoni, M.T. "A New Repair Material for Concrete Pavements", *Canadian Society for Civil Engineering Conference*, Regina, Sk, Canada, May 27-30, 2015.

Technical Reports and Guidelines

1. **Ghazy, A.,** Bassuoni, M.T., Shalaby, A., "Guide for Partial Depth Repair of Concrete Pavements", *Public Works Department, City of Winnipeg*, (Apr. 2015), 20 P.

2. **Ghazy, A.,** Bassuoni, M.T., Shalaby, A. "Partial Depth Repair of Concrete Pavements –Phase II: Final Report", *Public Works Department, City of Winnipeg*, (Mar. 2015), 46 P.

3. **Ghazy, A.**, Ezisi, U., Bassuoni, M.T., Shalaby, A. "Partial Depth Repair of Concrete Pavements - Phase I: Progress Report", *Public Works Department*, City of Winnipeg, (June 2014), 13 P.

Dedication

The work is dedicated to:

My Parents, Ali and Nagwa,

My Siblings, Mohamed and Zeinab,

My lovely Wife Hala,

My son Fares, and

My late friend Mahmud Rahmaa

Acknowledgements

All praise and thanks be to Almighty Allah who bestowed upon me guidance and benevolence to complete this work.

First and foremost, I would like to express my sincere gratitude to my advisor Dr. Mohamed T. Bassuoni, for his continuous support throughout this research. I attribute the level of this work to his patience, encouragement, enthusiasm, and immense knowledge without which this thesis would not have been possible. I could not wish for a better or friendlier advisor and mentor.

Special thanks go to Prof. Ahmed Shalaby for his encouragement and insightful comments and suggestions.

In addition, the author would like to thank his colleagues for their support during all work stages, especially Dr. Karam Mahmoud, Mohamed Sakr, and Mohamed Tiznobaik. Also, the assistance of the McQuade Heavy Structures Laboratory staff, Dr. Chad Klowak, Mr. Brendan Pachal and Mr. Grant Whiteside and the valuable technical support during the construction and testing of the specimens are greatly acknowledged.

I highly appreciate the financial support from Natural Sciences and Engineering Research Council of Canada, University of Manitoba Graduate Fellowship, and City of Winnipeg. The IKO Construction Materials Testing Facility and Manitoba Institute for Materials at the University of Manitoba in which these experiments were conducted have been instrumental to this research.

I would like to express my gratitude to my mother, father, brother, and sister for helping me to realize my own potential and supporting me throughout my entire life. I also thank my family and friends for their love and encouragement.

Last but not least, I must acknowledge my lovely wife and best friend, Hala. Without her love and encouragement, I would not have finished this thesis. I also express my gratitude to my son, Fares, who added a great value for everything in my life.

TABLE OF CONTENTS

LIST OF TABLES

LIST OF FIGURES

Abbreviations

ACR	Alkali-carbonate reactivity
ANFIS	Adaptive neuro-fuzzy inference system
ANOVA	Analysis of Variance
ASR	Alkali-silica reactivity
BSEM	Backscattered scanning electron microscopy
C_3A	Tricalcium aluminate, $3Cao.Al_2O_3$
Ca^{2+}	Calcium ions
$CaCl_2$	Calcium chloride
$CaSO_4$	Calcium sulfate
CC	Curing compound
CH	Calcium hydroxide (portlandite)
Cl^-	Chloride ions
COV	Coefficient of variation
COW	City of Winnipeg
COX	Calcium oxychloride
C-S-H	Calcium-silicate-hydrate
DSC	Differential scanning calorimetry
EDX	Energy dispersive x-ray analysis
EDX	Energy-dispersive X-ray
ESEM	Environmental scanning electron microscopy
F	Fly ash
F/T	Freezing-thawing

FDR	Full depth repair
FL	Fuzzy logic
GU	General use portland cement
HRWRA	High-range water reducing admixture
ITZ	Interfacial transition zone
MAE	Mean absolute error
$Mg(OH)_2$	brucite
Mg^{2+}	Magnesium ions
$MgCl_2$	Magnesium chloride
MIP	Mercury intrusion porosimetry
MOX	Magnesium oxychloride
M-S-H	magnesium-silicate-hydrate
N	Normal nano-modified fly ash concrete
Na^+	Sodium ions
NaCl	Sodium chloride
NMFC	Nano-modified fly ash concrete
NNs	Neural networks
PDR	Partial depth repair
pH	Potential of hydrogen
PLC	Portland limestone cement
R	Rapid nano-modified fly ash concrete (with accelerator)
r_a	Radius of cluster
RCPT	Rapid chloride penetrability test
RE_d	Relative dynamic modulus of elasticity

RH	Relative humidity
RMSE	Root mean square error
S	nanosilica
SCMs	Supplementary cementitious materials
SEM	Scanning electron microscopy
TF	Time of failure
TG	Thermogravimetry
VAF	Variance account
w/b	water-to-binder ratio
w/cm	water-to-cementitious materials ratio
W/D	Wetting/drying
x, y, z	Input and output parameters for ANFIS
XRD	X-ray Diffraction
A_i, B_i	Fuzzy sets
N	Number of rules
p_i, q_i, r_i	Design parameters for ANFIS during the training process
Q_i	The firing strength of a rule
$M_{air(t_0)}$	Initial mass of sample measured in air
$M_{sub(t_0)}$	Initial mass of sample measured in the buoyancy liquid (paraffin oil)
$M_{sub(t)}$	Mass of the sample in the buoyancy liquid at time (*t*)
r_a	Radius of cluster
r_b	Positive constant that is relatively greater than the r_a

R^2	Correlation coefficient
$\overline{W}_i$	Weight of a performance criterion
w_i	Weight (consequent) of the ith rule
$V_{paste(t_0)}$	Initial volume of the paste
$V_{paste(t)}$	Volume of the paste at time (*t*)
x_i and x_j	Data vectors
z_i	Output of the ith rule
ρ_L	Density of the buoyancy liquid at 23°C
v_i, σ_i	Parameters set that changes the shape of the membership function
ε	Acceptance threshold (error value)
$\acute{\varepsilon}$	Rejection threshold
η	Squash factor

CHAPTER 1: INTRODUCTION

1.1 Overview

Many government agencies in North America and Europe require the service life of concrete pavements to be in the range of 30 to 50 years (Holt et al. 2011; Hall et al. 2007; American Concrete Pavement Association 2002). However, there have been frequent cases of concrete pavements constructed within the last 10 to 20 years showing premature deterioration, especially in the areas adjacent to longitudinal and transverse joints (Jain et al. 2012; Arribas-Colón et al. 2012). This deterioration is considered problematic because it compromises the performance and functionality of an otherwise sound pavement, thus impairing the ride quality. Previous field investigations (Jain et al. 2012; Kang et al. 2012; Arribas-Colón et al. 2012; Ranjaraju 2002) aimed at finding the root causes of this deterioration reported several causes such as freezing-thawing (F/T) cycles, wetting-drying (W/D) cycles, de-icing salts, D-cracking, alkali-aggregate reactions, degree of saturation, corrosion of dowel bars at joints, drainage conditions and maintenance. In most of these cases, water/solution (due to application of de-icing salts) is involved in the deterioration by physical actions, i.e. generation of micro- and macro-cracks by increasing the degree of saturation (Arribas-Colón et al. 2012; Kang et al. 2012; Valenza et al. 2006; Litvan 1976; Powers 1975), or chemical reactions, i.e. leaching/decomposition of hydration products and formation of expansive phases (Álava et al. 2016; Galan et al. 2015; Peterson et al. 2013).

Chloride-based de-icing salts such as sodium chloride (NaCl), magnesium chloride ($MgCl_2$) and calcium chloride ($CaCl_2$) are the most readily available and widely used in either solid or liquid form in winter maintenance operations (Shi et al. 2013; Yehia et al.

1998). Despite their functionality, the extensive use of de-icing chemicals has raised concerns about their role in triggering and accelerating concrete distresses (Peterson et al. 2013; Monosi et al. 1990). The transition from implementing a maintenance strategy 'de-icing' to melt and break down the bond between the ice layer and road surface to proactive strategy 'anti-icing' to prevent bonding of ice to the road surface before icy storms) may impart deleterious effects on concrete as anti-icers are mostly liquid chemicals with high concentrations of chlorides (Shi et al. 2013).

Since the 1980s, fly ash, a by-product of burning coal in power plants, has been used as an inexpensive replacement of ordinary portland cement in concrete to improve sustainability practices. Previous research on the use of fly ash showed that incorporation of Class F (low calcium oxide) fly ash can generally improve the durability characteristics of concrete (Mehta et al. 2014). Despite the ecological and engineering benefits of fly ash concrete, the use of fly ash as a cement replacement in concrete pavements in North America is optional and typically limited by departments of transportation to dosages less than 15 or 20% (Standard Construction Specifications - Manitoba 2014; Ontario Provincial Standard Specification 2014; Standard Specifications for Construction of Roads and Bridges on Federal Highway Projects 2014). The slow rate of strength gain and microstructural development at early-age, as well as vulnerability to surface scaling of fly ash concrete are considered to be the major issues which deter its wider use and acceptance (Malhotra et al. 2000). However, these performance limitations associated with the use of slowly reactive pozzolans (e.g. fly ash) can be mitigated by incorporation of nanoparticles (size scale of 1-100 billionth of a meter) in concrete (Said et al. 2012). Nanoparticles (e.g. nanosilica) have been applied in concrete research and proven to enhance fresh and hardened properties by modifying the structure of the cementitious matrix at the nano and

micro levels (Kong et al. 2015; Said et al. 2012). Therefore, their application in concrete may have a greater potential to produce innovative types of fly ash concrete with superior performance for harsh environments.

In addition, a new type of portland cement has been introduced to the North American market which contains 6 to 15% of interground limestone powder (portland limestone cement: PLC) with clinker due to their technical, economic, and ecological benefits. Limestone substitution in cement may affect the physical and mechanical properties of concrete; thereby, enhancing its resistance to degradation. While there are a number of studies on the hydration and strength characterization of concrete made from PLC (Marzouki et al. 2013), and its response to durability issues such as sulfate attack (Ramezanianpour et al. 2013), alkali-aggregate reactions and chloride ions penetration (Thomas et al. 2010), the long-term performance of PLC concrete exposed to harsh environments combined with de-icing salts is still uncertain.

While significant efforts have been expended in laboratory and field studies of concrete pavements, only few computer-based tools have been introduced to assist engineers in the prediction of concrete pavement deterioration exposed to de-icing salts (Marchand et al. 2009). These approaches have focused on modeling the transport properties of concrete, to implicitly predict its durability and service-life (Tamimi et al. 2008; Samson et al. 2007; Johannesson 2003). Irrespective of the significant improvements in the sophistication of these service-life models, it is still challenging to predict the behaviour of concrete exposed to aggressive environments including chemical and physical attacks due to the simplified assumptions included in these approaches. Artificial intelligence techniques, such as neural networks (NNs), fuzzy logic (FL), adaptive neuro-fuzzy inference systems (ANFIS), have been recently applied in concrete research. Using

a well-defined experimental database (input-output), artificial intelligence can be an efficient tool in modeling complex durability issues such as chloride-induced corrosion, alkali-aggregate reaction and sulfate attack of concrete as shown by many investigators (Štemberk et al. 2013; Bassuoni et al. 2008; Ïnan et al. 2007; Hu et al. 2006). Thus, these modeling tools can be applied to concrete pavements exposed to harsh environments.

Concrete is a viable choice for building durable, energy efficient and eco-friendly pavements. However, the failure and subsequent repair of concrete pavements often cause traffic jams and disruption to road users. Recently, several high early-strength cement-based repair materials (both generic and proprietary) have been developed and used for concrete pavements (Soliman et al. 2014). While such materials can be placed and hardened within a relatively short period of time, many of these materials are vulnerable to cracking, poor bonding, and premature deterioration, for example, due to incompatibility with the existing concrete pavement (Soliman et al. 2014; Li et al. 2011). Hence, carefully balancing the early- and long-term performance of cement-based repair materials remains a challenging task, which warrants further investigation.

1.2 Need for Research

Numerous cases of premature deterioration and costly rehabilitation of concrete pavements have been reported in cold climatic regions. The information on the design of concrete mixtures that resist the physical and chemical degradations appears to be inadequately addressed in the scientific literature. Few research studies have focused on the physical and chemical roles of Supplementary Cementitious Materials (SCMs: e.g. fly ash) in concrete exposed to de-icing salts under various environmental conditions. Also, the potential benefits of nanoparticles (e.g. nano-silica) in mitigating this type of damage are still uncertain. Such data can improve the current specifications and guidelines for

concrete exposed to extensive use of de-icing salts. Hence, research is required to investigate the performance of nano-modified fly ash concrete as a proposed material for concrete pavements to demonstrate/document its performance under multiple exposures correlating to service conditions, in order to pave the way for its future use. Also, PLC has recently been introduced to the North American market due to its technical, economic, and ecological benefits. With the absence of long-term field performance and robust research data, the application of PLC in concrete pavements might be risky. Investigating the performance of PLC in concrete pavements should be based on an integrated/'holistic' approach that includes key in-service parameters such as extreme environmental conditions combined with de-icing salts.

While there are many studies involving the physical degradation of concrete under de-icing salts and F/T cycles, the chemical degradation of concrete by de-icers, due to W/D cycles, have been studied less frequently. In addition, most of the studies investigating the effect of W/D cycles on concrete degradation typically applied insufficient periods/regimes for drying (Jain et al. 2012; Wang et al. 2006a; Collepardi et al. 1994). Drying may simulate conditions experienced by concrete pavements during hot and arid periods, which may lead to synergistic actions of salt crystallization, and reversible formation of high and low-density reaction products (e.g. hydrous and anhydrous oxychloride phases). Also, the impact of W/D on the formation/stability of oxychloride phases in cementitious matrices has not been adequately documented in literature, specifically regarding the damage process/mechanism. Actually, the formation of these oxychloride phases has mostly been studied in synthetic hydrated materials using implicit methods without direct evidence on their roles in the damaging process under different environmental conditions in real cementitious systems (Galan et al. 2015). Also, the exact nature and morphology of these

phases are not adequately established in literature, and their stability/coexistence with other cement phases (e.g. Friedel's salt and ettringite) are not known with certainty. Likewise, the ability of highly concentrated chloride solutions to stabilise reaction products such as ettringite remains questionable. Therefore, these aspects need to be reinvestigated in real cementitious systems to reliably understand their roles in the damage process of concrete.

Previous studies strongly referred the extent of damage due to oxychloride formation (chemical action) to the type of de-icing salt used; however, these studies have focused on single de-icing salt solutions, i.e. NaCl, $MgCl_2$, and $CaCl_2$ (Wu et al. 2015; Peterson et al. 2013; Wang et al. 2006a; Lee et al. 2000; Santagata et al. 2000; Cody et al. 1996). In practice, transportation agencies may maximize the safety of roadways during wintery weather by applying de-icing, anti-icing and pre-wetting strategies (combined salts) (City of Toronto 2016; Minnesota Snow and Ice Control 2012; Policy on Snow Clearing and Ice Control – City of Winnipeg 2011), which may impart deleterious effects on concrete pavements. Yet, no data has been published on the extent of damaged concrete when combined de-icing salts are used under different environmental conditions.

Furthermore, in the field, the damage of concrete often occurs due to a multitude of mechanisms (chemical and physical) acting in a combined and possibly synergistic manner rather than under individual schemes. Also, discrepancies in the data have been reported for the effects of de-icing salts on the performance of concrete, which were associated with the testing variables including de-icer concentration, temperature, and environmental conditions (Wu et al. 2015; Darwin et al. 2008; Wang et al. 2006a; Santagata et al. 2000). Thus, there is need to develop performance-based tests that mobilize multiple damage mechanisms to improve the understanding of their combined effects on normal and

emerging concretes, and hence allow for a better modeling of the life-cycle performance of concrete exposed to such environments.

Although there are significant improvements and sophistication of computer models for the transport processes of fluids, it is still challenging to predict the behaviour of concrete exposed to aggressive environments including chemical and physical action, based only on transport parameters. By using a well-defined experimental database (input-output), artificial intelligence techniques such as ANFIS can be efficient in modeling such complex durability issues of concrete and predict the performance of cementitious materials exposed to harsh environments. In the prequalification stage of a construction project, these models can effectively assist in selecting optimum mixtures proposed for a specified exposure to avoid potential durability risks and associated repair cycles.

Finally, due to the premature deterioration and costly rehabilitation of pavement repairs, there is a need to specify durable and more permanent high-performing patching products. Carefully balancing the early and long-term performance of the repair materials remains a challenging task, which warrants further investigation. Nano-modified fly ash concrete may present a sustainable and cost-effective option for repair of concrete pavements, with an anticipated measurable impact on reducing life-cycle costs due to its projected durability and longevity. However, this has still not been substantiated by experimental or field data.

1.3 Objectives of Research

To respond to the aforementioned research needs, the fundamental theme of this research is to improve the current level of knowledge on the synergistic effects of environmental conditions with different types/concentrations of de-icing salts on concrete

degradation to minimize the risk of premature deterioration. The specific objectives of this thesis are to:

- Apply forensic evaluation to classify the source of durability damage in concrete pavements, and identify aspects contributing to premature joint deterioration of concrete pavement in Winnipeg, Manitoba, Canada.

- Investigate the physico-mechanical properties and microstructural features, of concrete made with two types of cement (general use (GU) and PLC) without or with fly ash and nanosilica 'nano-modified fly ash concrete' to harsh environments, and thereby propose an efficient concrete mixture for concrete pavements.

- Improve the understanding of the synergistic effects of environmental conditions (F/T, W/D and their combination) with different types of de-icing salts on a wide range of concrete mixtures.

- Apply conditioned-mode environmental scanning electron microscopy (ESEM) to capture unstable oxychloride phases and identify their nature/morphology due to temperature changes, and link their formation to the physico-mechanical properties of real cementitious systems and propose their roles in the damage process of concrete under different exposure conditions and de-icing salts.

- Build a model using ANFIS that is capable of predicting the time of failure (*TF*) of concrete under various exposure regimes combined with chloride-based de-icing salts.

- Explore the potential of nano-modified fly ash concrete as a repair material for concrete pavements to achieve balanced performance in terms of early-age and long-term performance.

1.4 Scope of Research

To achieve the aforementioned objectives, the scope of work involves three phases as described below.

1.4.1   Phase I: assessment of joints in concrete pavements

For better understanding of the source of the damage and identifying aspects contributing to the premature joint deterioration of concrete pavements, this section involves analyzing concrete core samples collected from both distressed and sound joint locations in concrete pavements in Winnipeg, Manitoba, Canada. The pavement sections in regional roads and residential streets were exposed to different winter treatments (type, rate, and application [direct/indirect] of de-icing salts) and had been in service in wet and long-freezing conditions for a period between 15 to 20 years. The changes in bulk properties and microstructure features of concrete pavements were examined.

1.4.2   Phase II: laboratory exposures and modeling

1.4.2.1 Laboratory exposures

A wide range of concrete mixtures containing GU cement or PLC, Class F fly ash and nanoparticles (nano-silica) were designed to provide guidance to produce durable concrete pavements and enhance the overall process of constructing/rehabilitating concrete pavements to achieve optimum performance, longevity and life-cycle cost-effectiveness. In comparison to conventional concrete mixtures typically used for pavements, the newly developed nano-modified fly ash concrete mixtures were subjected to different exposure regimes to simulate environmental conditions experienced by concrete pavements, which involve F/T cycles, W/D cycles, and combined exposure (alternating W/D and F/T cycles) with the most widely used chloride-based de-icing salts (individual and combined).

1.4.2.2   Modeling

To predict the durability performance of the proposed mixtures for concrete pavements service under different environmental conditions, a computer model based on neural networks combined with fuzzy logic (ANFIS), an emerging computational intelligence-based tool in infrastructure research, was developed. The merit of a trained model lies in its ability to estimate the time of failure (*TF*) of concrete exposed to various exposure regimes combined with chloride-based de-icing salts.

1.4.3   Phase III: nano-modified fly ash concrete 'NMFC' as a repair material

Nano-modified fly ash concrete was developed as a repair material for concrete pavements to produce a durable repair material and enhance the overall process of rehabilitating concrete pavements to achieve optimum performance, longevity and life-cycle cost-effectiveness. The performance of the innovative mixtures was compared to two cementitious products customarily used by transportation agencies for partial depth repair (PDR) of concrete pavements. A series of laboratory tests were conducted to evaluate their early-age and long-term performance as well as their compatibility with the substrate concrete. Finally, the customized mixtures were applied in a field trial as a partial-depth repair material to repair transverse joints located on a major urban arterial road in Winnipeg to document its performance under real service conditions.

1.5 Structure of the Thesis

This thesis consists of eleven chapters as described below and shown in Fig. 1.1.

➢ CHAPTER 1 provides a brief description of the problem statement and the significance of the research program.

➢ CHAPTER 2 includes a comprehensive literature review on the effect of de-icers on the deterioration of the concrete pavements and the repair materials/strategies.

➢ CHAPTER 3 focuses on the inspection, testing, and analyzing concrete core samples collected from both distressed and sound joint locations in concrete pavements in Winnipeg, Manitoba, Canada. (**Phase I**)

➢ CHAPTERS 4, 5, and 6 include laboratory-simulated regimes to mimic environmental conditions experienced by concrete pavements in order to investigate their response, in terms of physico-mechanical properties and microstructural features, of a wide range of concrete mixtures containing GU cement or PLC, Class F fly ash and nanoparticles (nano-silica). (**Phase II**)

➢ CHAPTER 7 introduces the ANFIS model based on the comprehensive datasets obtained from the laboratory simulation work (Chapters 4, 5, and 6). (**Phase II**)

➢ CHAPTERS 8 and 9 aim at developing innovative repair mixtures for concrete pavements to achieve balanced early-age and long-term performance and improving the overall process of partial depth repair (PDR) of concrete pavements. (**Phase III**)

➢ CHAPTER 10 presents the field trial findings for the nano-modified fly ash concrete as a repair material for deteriorated joints located on a major urban arterial road in Winnipeg, Manitoba, Canada. (**Phase III**)

➢ CHAPTER 11 contains a summary of the major findings, significant conclusions of this thesis and recommendations for future research.
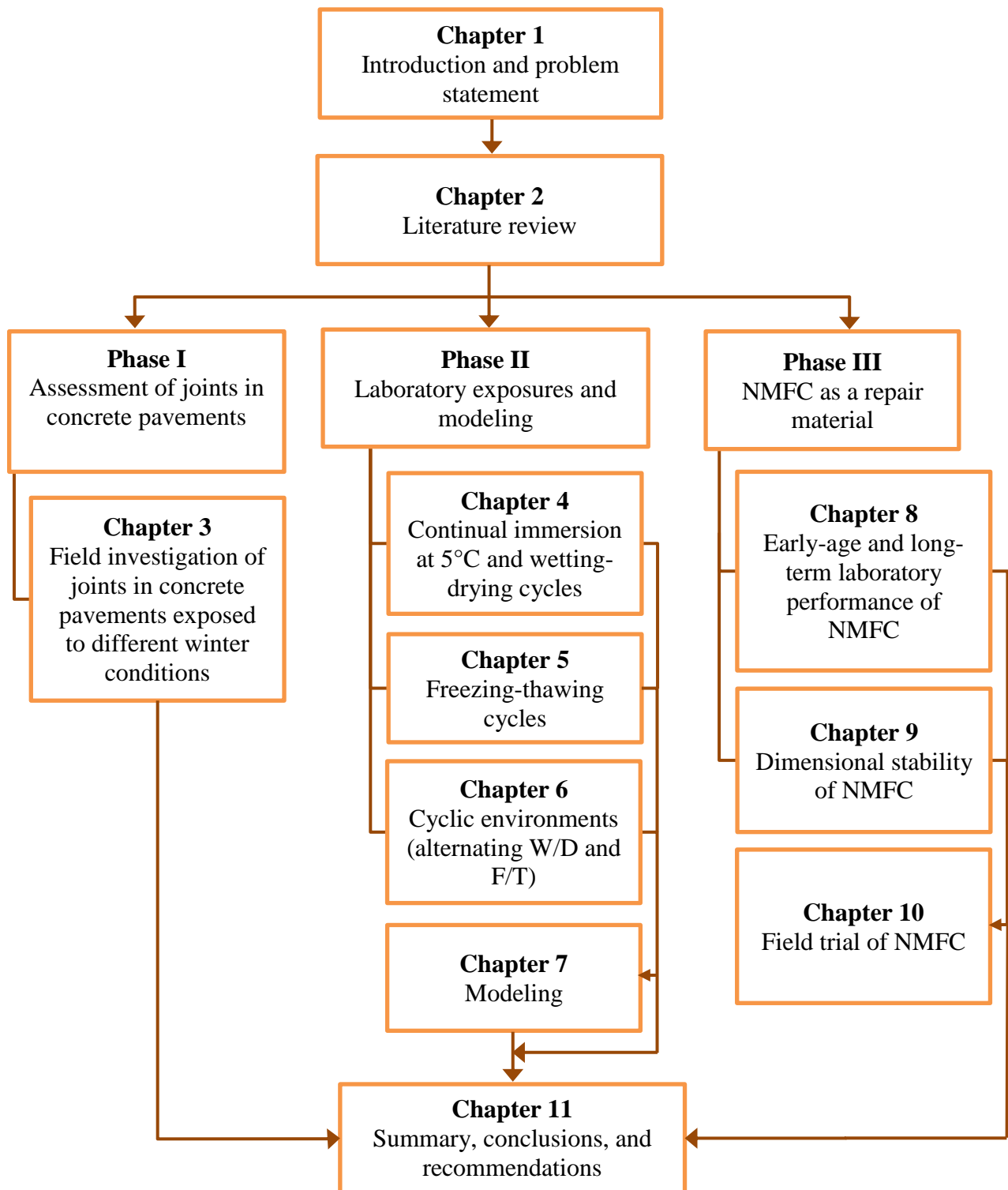
Figure 1.1: Flow chart of the thesis structure.

CHAPTER 2: LITERATURE REVIEW

Concrete pavements represent a large portion of the transportation infrastructure (highways, streets, parking lots, bridge decks and airfield pavement) in North America and Europe. The life-cycle differential for concrete pavements depends on the traffic level and climate conditions; however, concrete pavements are generally assumed to have an initial service life of 25 to 30 years to the first major rehabilitation (Hall et al. 2007; American Concrete Pavement Association 2002). Recently, there have been frequent cases of concrete pavements constructed within the last 10 to 15 years showing premature deterioration, especially in the areas adjacent to longitudinal and transverse joints (Jain et al. 2012; Arribas-Colón et al. 2012). Structural design (e.g. joint spacing, saw-cutting window and depth, drainage system), construction practices (e.g. addition of excessive amounts of water during placement, vibration rates, improper curing), harsh service conditions (e.g. de-icing salts, freezing/thawing (F/T) cycles, wetting/drying (W/D) cycles) and properties of concrete (e.g. penetrability, air-void quality) have been broadly linked to joint deterioration of concrete pavements. To date, no single mechanism has been found that accounts for all reported occurrences of joint deterioration. Investigations thus far have revealed various damage mechanisms which can lead to the deterioration of concrete pavements as shown in Fig. 2.1. These mechanisms have different manifestations as depicted in Fig. 2.2. As indicated in Chapter 1, the scope of the current thesis is limited to the durability issues of concrete due to the extensive use of de-icing salts in harsh environments. In this chapter, general literature pertinent to this degradation mechanism is presented. Throughout the chapter, critical analysis of the state-of-the-art in this area has identified research gaps and needs, which have been addressed in the present thesis.

13
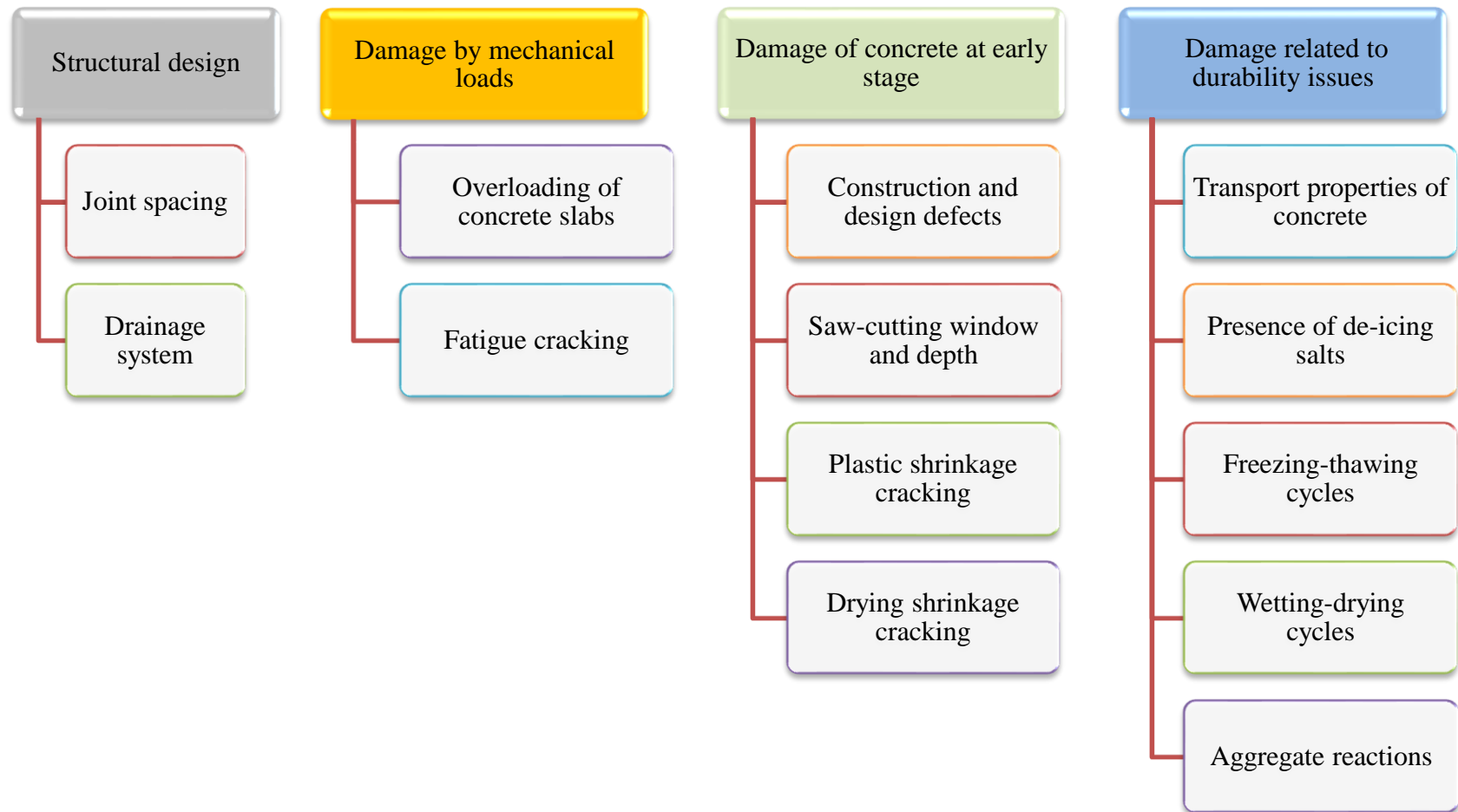
Figure 2.1: Potential damage mechanisms of concrete pavements.

D-cracking
- occurs as a result of freeze -thaw damage to coarse aggregate
- found initially at longitudinal and transverse joint intersections

Scaling
- progressive loss of paste with or without aggregates from the surface of concrete
- a typical damage manifestation of inadequately air-entrained concrete, or overly finished concrete

Pop-outs
- occur when water freezes in pores of coarse aggregate particles near the surface of a concrete slab

Map Cracking
- a pattern of interconnected random cracks in the top surface of a concrete slab
- usually caused by excessive bleeding, over-finishing or improperly cured concrete

Joint Spalling
- occurs when water and/or debris in the joint freezes and expands, inducing pressure on concrete along the joint

Blow-ups
- occure when concrete expands during hot weather, pressure can build up in the concrete along the joints until the panels rise at the joints and shatter

Faulting
- caused by slab settlement on one or both sides of the crack/joint, or by rocking of the slab at the crack/joint as traffic moves across it.

Pumping
- the seeping or ejection of water and sub-base material from beneath the pavement through pavement cracks under heavy loads

Polishing
- develops due to friction between vehicular tires and pavement

Figure 2.2:
Various damage manifestations in concrete pavements (definitions are extracted from Harrington et al. 2014; Shahin 2005; Rangaraju 2002; Fang 2001).

2.1 De-icers/Anti-icers for Concrete Pavement

In cold climate regions, winter maintenance operations for concrete roads and bridges are essential for safe driving conditions and hazard mitigation. Chemicals play a key role in such operations due to their ability to depress the freezing temperature of ice/snow. Chloride-based de-icing salts such as sodium chloride (NaCl), magnesium chloride ($MgCl_2$) and calcium chloride ($CaCl_2$), are the most readily available and widely used in either solid or liquid form; they are effective over a wide range of temperatures (Shi et al. 2013; Amsler et al. 2006; Yehia et al. 1998).

De-icing, anti-icing, and pre-wetting are one of the effective snow/ice control methods that have been used on roads during the winter to meet safety and functionality goals while being cost-effective and environmentally friendly (Shi et al. 2013; Kelting et al. 2010; Yehia et al. 1998). The key difference between de-icing and anti-icing agents is at the time when these chemicals are applied to the road surface. De-icing is defined as any effort to remove snow/ice from road surfaces after snow/ice deposition on such surfaces has occurred (Yehia et al. 1998). It is a technique of applying chemicals/salts directly on top of accumulated snow/ice to break the bond between the snow/ice layer and the road surface to facilitate easier removal of the former. This is in contrast to anti-icing, which is defined as a surface treatment applied prior to snow/ice deposition that eliminates snow/ice accumulation or facilitates ice removal by lessening the bond between the snow/ice and the pavement surface (Yehia et al. 1998). The pre-wetting strategy is adding liquid or solid salts to abrasives (sand) to make them easier to manage and distribute, and help them stay on roads (Amsler et al. 2006).

Despite their functionality, the extensive use of these chemicals has raised concerns about their effects at triggering or accelerating distress of concrete. Also, the transition

from implementing a maintenance strategy (de-icers) to protective strategy (anti-icers) may impart deleterious effects on concrete as anti-icers are mostly liquid chemicals with high concentrations of chlorides (Shi et al. 2013).

2.1.1   Types of Commonly Used De-icers/Anti-icers

Sodium chloride (NaCl) is the most common de-icing salt used on roadways mainly due to its low cost compared to other de-icers. It represents over 55% of the total amount of de-icing materials applied to roadways in USA and Canada each year (Kelting et al. 2010; Vol'nov et al. 1957). NaCl was used as either a rock salt form for de-icing or as salt brine for anti-icing. Despite the popularity of rock salt/salt brine, its effectiveness is limited below pavement temperatures of $-12°C$. Recently, magnesium chloride ($MgCl_2$) and calcium chloride ($CaCl_2$) are widely perceived by transportation agencies as being particularly effective in melting ice/snow due to their ability to depress the freezing temperature to a lower temperature (up to $-40°C$) when high concentrations ($\geq 20\%$ by weight) are used (Kelting et al. 2010; Amsler et al. 2006).

The theoretical melting capacities of the de-icing salts are characterized by their eutectic curves, as shown in Fig. 2.3. The eutectic temperatures are used as a guide in determining the target solution concentration for de-icers. The eutectic temperature corresponds to the point at which the liquid phase borders directly on the solid phase. For a binary de-icer-water phase diagram, this defines the lowest temperature at which a de-icer can melt ice/snow. The general pattern of the curved lines shows that as temperature declines, more solute is required to melt the ice until the eutectic temperature is reached (Kelting et al. 2010; Vol'nov et al. 1957). As the temperature of the ice goes down, the chemical potential of the ice also goes down, so a higher concentration of solute is needed at lower temperatures to maintain the chemical potential gradient to melt ice. Recently,

Farnam et al. (2015a and 2015b) stated that the chemistry of concrete can alter the appropriateness of using the conventional ($CaCl_2$–H_2O) phase diagram. These studies show that the $Ca(OH)_2$ present in hydrated cement paste can interact with $CaCl_2$ solution creating a behaviour that is similar to that observed in isoplethal sections of a ternary phase diagram for a $Ca(OH)_2$–$CaCl_2$–H_2O system. Thus, it is suggested that such isoplethal sections provide a reasonable model that can be used to describe the behaviour of concrete exposed to $MgCl_2$ or $CaCl_2$ solutions as the temperature changes.
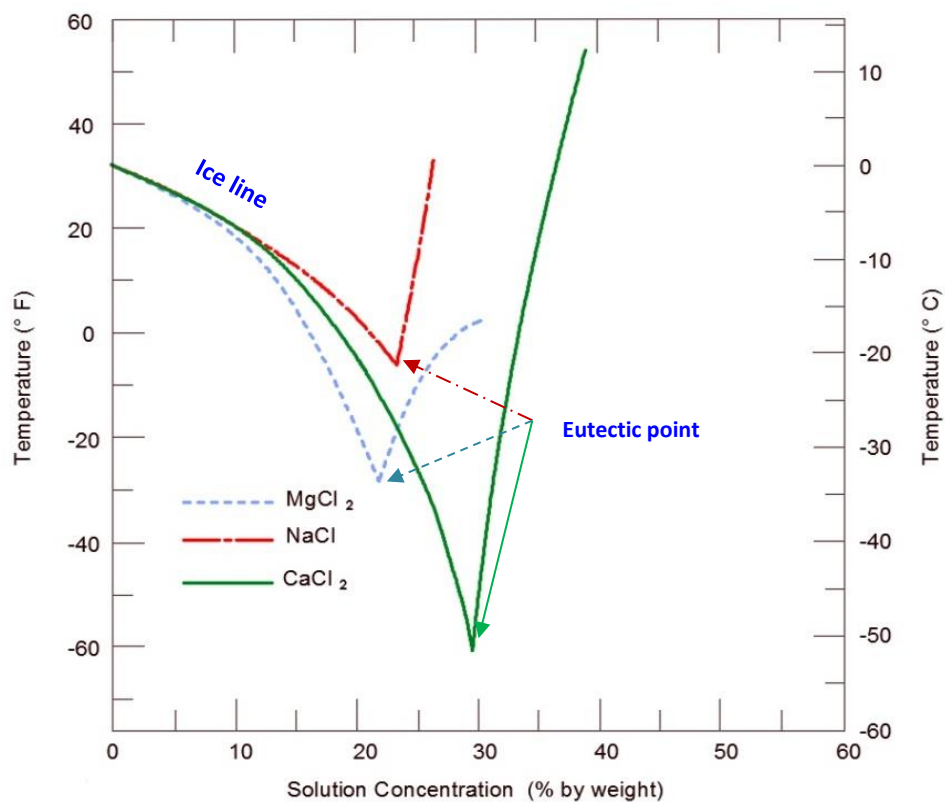
Figure 2.3: Phase diagrams of various de-icing salts (adapted from Kelting et al. 2010).

2.1.2   Effect of De-icers/Anti-icers on Concrete Deterioration

The adverse effects of de-icing salts on cement-based materials have been a key durability issue and a subject of extensive investigation for many decades. Historically, the damage of concrete due to the presence of de-icing salts was linked to physical mechanisms such as frost damage (bulk cracking) and salt scaling (superficial damage) (Sun et al. 2010; Valenza et al. 2006; Penttala 2006; Litvan 1976; Powers 1975; Powers et al. 1953; Powers 1945). Salts can also chemically interact with concrete, resulting in leaching and decomposition of the hydrated cement products (Álava et al. 2016; Peterson et al. 2013; Wang et al. 2006a; Sutter et al. 2006). Formation of oxychloride phases was suspected of causing chemical degradation when exposed to concentrated de-icing salts; however, these phases were mostly reported in synthetic hydrated materials and their morphology has not been unequivocally established in field or laboratory concrete (Álava et al. 2016; Galan et al. 2015; Peterson et al. 2013; Brown et al. 2004; Damidot et al. 1994).

2.1.2.1   Physical effects

Most reported cases of concrete deterioration induced by de-icers are principally a result of physical processes (Liu et al. 2015; Valenza et al. 2006; Marchand et al. 1999; Harnik et al. 1980; Litvan 1976; Powers et al. 1953). Previous studies have demonstrated that concentrations between 3 to 10% by mass of de-icing salts caused the most deleterious

effects with respect to salt frost scaling of concrete surface (Harnik et al. 1980). Scaling is defined as superficial damage caused by freezing a saline solution on the surface of a concrete specimen (Valenza et al. 2006). Scaling by itself may not significantly impair bulk concrete, but it leads to increasing the level of concrete saturation and ingress of aggressive chemicals that may be present in the environment, making the concrete more susceptible to frost action and chemical attack. Several theories have been proposed to explain the phenomenon of salt scaling, including osmotic pressure, thermal shock, precipitation and growth of salt crystals, and glue spalling.

The osmotic pressure theory (Powers 1975) is contrary to the hydraulic pressure theory introduced by Power (1945) in the sense that during freezing, most of water was found to diffuse toward, not away from, the sites of freezing, and the expansion decreased with the increase of cooling rate. Dissolved de-icing chemicals can become concentrated in pores within the concrete, which causes an initial super-cooling. When the temperature goes down to the freezing point of water, ice crystals will form in the larger capillaries, thus increasing the alkalinity of the unfrozen solution at the freezing sites, which raises the osmotic potential of the unfrozen solution. In order to maintain thermodynamic equilibrium, unfrozen water from the smaller pores migrates to the larger pores causing growth of crystals and increasing pressure within the pore structure. The osmotic pressure resulting from this water diffusion creates tensile stresses in concrete, especially near the surface where salt concentrations are high. This theory considers osmotic potential to be the primary cause of paste F/T damage and partially explains the amplifying deleterious effects of de-icing chemicals. Moreover, this theory explains why air-entrained paste/concrete contracts as it freezes, rather than expanding, even as ice continues to develop in the capillary pores as the temperature decreases below 0ºC (Powers 1975).

Rösli et al. (1980) introduced another theory termed 'thermal shock' describing freezing/thawing processes in the hydrated cement paste. Thermal shock occurs in concrete when de-icers are applied to the frozen concrete surface, which reduces the melting point of the ice and then the ice begins to melt. The requisite energy for melting is mostly drawn from the concrete surface, which causes rapid cooling of the concrete surface (usually only a few millimeters below the surface). A temperature gradient is quickly formed that results in differential strains within the concrete, causing a thermal shock that leads to scaling of the concrete surface. Pigeon et al. (1996) stated that stress induced in the surface layers by the thermal gradient can surpass the tensile strength of concrete and lead to micro-cracking. Pigeon et al. (1996) and Rösli et al. (1980) also suggested that a layer-by-layer freezing could lead to surface scaling as the outer layer of the concrete contains relatively little de-icing salt as it is washed out by the liquid water at the surface than the layer just beneath. This difference in salt concentration creates stresses due to different thermal expansion of the two layers, leading to scaling. Valenza et al. (2006) and (2007) stated that this drastic shock never occurs in the field. They also reported that this mechanism is not a significant contributor to salt scaling damage since it does not account for the level of de-icer concentration. Also, it does not apply to most laboratory experiments, which involve freezing a saline solution on the surface of concrete body, rather than applying a salt on top of existing ice.

Pigeon et al. (1996) reported that significant tensile stress in the concrete surface can be generated by the formation and growth of salt crystals in concrete pores surface. They hypothesized that the pore solution can become supersaturated as wetting and drying cycles concentrate salts in the pores. The concentration of salt ions at the surface of the concrete generally exceeds the concentration of salt ions within the pores of the concrete, causing a

downward diffusion of salt ions into concrete. As the concrete dries during periods of low precipitation and/or low humidity, the concentration of salt ions in the pore solution increases due to the evaporation of water from the pores. Salt then begins precipitating from the solution to form crystals within the pores. This crystal growth has been shown to be capable of producing enough tensile hoop stresses for damaging the concrete (Scherer et al. 2004; Winkler et al. 1972). Winkler et al. (1972) estimated that the magnitude of the crystallization pressure resulting from salt crystal (gypsum and halite crystal) may exceed 200 MPa.

It was reported that drying does not sufficiently occur in laboratory tests for salt-frost scaling; thus, growth of the salt crystals would not contribute to the surface scaling damage in the laboratory; however, this mechanism may contribute to the surface scaling damage in the field otherwise (Valenza et al. 2007; Mindess et al. 2003).

Valenza et al. (2006) suggested a mechanism similar to glue-spalling, a technique that is used to create shallow scallops in decorative glass, as a primary cause of salt scaling, due to the similarity between scaled concrete and scalloped glass. The fundamental procedures of glue-spalling are that an epoxy is spread on a sandblasted surface of glass at high temperature and then it is allowed to cool. Stress from the thermal expansion mismatch causes the epoxy to crack into small islands, which creates tensile stress in the glass at the islands' edges and then spreads on the glass surface. Valenza et al. (2006) applied this theory to scaled concrete, in the sense that ice forms on the surface while temperatures continue to drop, making the ice and concrete behave like an epoxy/glass composite. As the thawing cycle begins, tensile stresses develop in the ice, which has much higher coefficient of thermal expansion ($\sim 50 \times 10^{-6}$/°C) compared to concrete ($\sim 10^{-6}$/°C). These stresses eventually cause a crack in the ice to form, which can propagate below the

concrete surface, turn and chip off a thin flake of concrete. According to the glue-spall theory, which employs fracture mechanics to explain the process of salt-frost scaling, the tensile capacity of the cementitious matrix substantially controls its resistance to scaling.

Despite the fact that the glue-spall theory correlates well with many observations under laboratory conditions, it cannot convincingly explain the improvement in salt scaling in regards to air entrainment. Also, this theory did not count for the role of internal ice formation on salt scaling. Finally, the influence of supplementary cementitious materials (SCMs) on the scaling of concrete is not clearly explained by this theory.

It is likely that the combined increases in osmotic pressures, thermal stress, level of saturation, and salt crystallization contribute to scaling of concrete in the presence of de-icer chemicals. These combined mechanisms are especially damaging for concrete exposed to de-icers when subjected to F/T cycles.

2.1.2.2   Chemical effects

Although most previous studies suggest that the damage is primarily a physical action, some researchers, in the last decade, reported that chemical interactions may also be occurring and can be significant, but their effects are often overshadowed by the physical actions (Peterson et al. 2013; Sutter et al. 2006; Wang et al. 2006a; Collepardi et al. 1994). At high concentrations (≥ 3 mol), chloride (Cl^-) ions and cations (e.g. Na^+, Mg^{2+}, and Ca^{2+}) in de-icing salts can enter into chemical reactions with cement-based materials forming complex salts and cause pH shifts. Formation of calcium oxychloride ($x Ca(OH)_2 \cdot y CaCl_2 \cdot z H_2O$ (COX), where $x{:}y{:}z$ can be 3-4:1:8-15, depending on $Ca(OH)_2/CaCl_2$ molar ratio, surrounding temperature, relative humidity (RH), and pH of the pore solution (Galan et al. 2015; Peterson et al. 2013; Monosi et al. 1990)) and magnesium oxychloride ($m Mg(OH)_2 \cdot n MgCl_2 \cdot 8 H_2O$, where the ratio of $m{:}n$ is 3:1 or 5:1,

termed as 3- or 5-form MOX, respectively) were suspected for causing chemical degradation of hardened concrete exposed to deicer solutions (Peterson et al. 2013; Monosi et al. 1990). However, the formation of COX/MOX has mostly been studied in synthetic hydrated materials using indirect methods such as longitudinal guarded comparative calorimetry (Farnam et al. 2015a and 2015b), low-temperature differential scanning calorimetry (Monical et al. 2016), thermogravimetric analysis (Suraneni et al. 2016), volume change measurements (Qiao et al. 2017) and the nature and morphology of these phases were not unequivocally established in hardened concrete systems due to their instability when subjected to conditions (e.g., sawing, polishing, washing, filtering, coating) normally applied for sample preparation before microstructural and mineralogical tests (Galan et al. 2015; Peterson et al. 2013; Shi 2001; Monosi et al. 1990). Drying and elevated temperatures lead to losing some of or all their combined water resulting in changes in their crystal structure (Galan et al. 2015; Peterson et al. 2013; Shi 2001; Monosi et al. 1990). The sensitivity of these phases to vacuum drying in the scanning electron microscope makes it difficult to observe their unaltered morphology (Galan et al. 2015). Therefore, the instability of these phases might be the reason that fewer studies could successfully correlate the damage of concrete to the formation of these complex salts (Qiao et al. 2017; Galan et al. 2015; Peterson et al. 2013).

The use of de-icing chemicals has also been implicated in both alkali-silica reactivity (ASR), and alkali-carbonate reactivity (ACR), and aggregate freeze-thaw deterioration (D-cracking) due to dramatic pH shifts and degree of saturation of concrete (Heisig et al. 2016; Katayama et al. 2004; Delagrave et al. 1994; Nixon et al. 1987; Dubberke et al. 1985). Prior studies reported that NaCl can initiate and/or accelerate ASR by supplying additional alkalis to concrete if reactive aggregates are included in concrete (Heisig et al. 2016;

Katayama et al. 2004; Sibbick et al. 1998; Nixon et al. 1988). Nevertheless, this process was found to be quite slow and might be masked by other short-term effects. ACR has also been found to occur in concrete with dolomitic aggregate (Heisig et al. 2016; Dubberke et al. 1985). The dolomite present in the aggregate reacts with alkalis from the de-icers (e.g. NaCl and $CaCl_2$) and cement paste forming brucite and calcite, resulting in a volume increase and subsequent concrete deterioration. Some studies stated that the drop in pH of the concrete pore solution due to applying specific de-icing solution such as $MgCl_2$ can also indirectly provoke the aggregate deterioration, as the lower the pH, the higher the increase in total porosity and the leaching front penetration and, in turn, the degree of saturation (Delagrave et al. 1994 and 1996).

The following sections describe potential deleterious effects of NaCl, $MgCl_2$, and $CaCl_2$ on the cementitious system:

- *Sodium Chloride (NaCl)*

Unless reactive aggregates are included in concrete, NaCl was reported to be an environmentally friendly and non-corrosive de-icer, except for the surface distress caused by the physical mechanism of salt-frost scaling when pessimum concentrations (2 to 10%) was used (Yener et al. 2015; Liu et al. 2015; Valenza et al. 2007). Glasser et al. (2005) reported that the solubility of CH increases in the presence of NaCl compared with pure water. Also, they hypothesized that this effect increases when the lower the exposure temperature coexists. The dissolution equation is stated as follows (Marchand et al. 1994):

$$2NaCl + Ca(OH)_2 \rightarrow CaCl_2 + 2NaOH \qquad \text{Eq. (2.1)}$$

Prior studies supported this view as that CH dissolution is not the main problem per se as compared to the exacerbation of other attacks such as frost damage and carbonation (Yener et al. 2015; Liu et al. 2015; Cody et al. 1994).

The soluble calcium chloride produced in the process can also react with the aluminate phases in the cement paste to form chloroaluminate phases (e.g. Eq. 2.2) (Kuzel's salt ($3CaO.Al_2O_3.0.5CaSO_4.0.5CaCl_2.11H_2O$) at low chloride concentrations (<10 mmol/l) or Friedel's salt ($3CaO.Al_2O_3.CaCl_2.10H_2O$) at high chloride concentrations (between 10 mmol/l to 3 mol/l) (Glasser et al. 2005).

$$CaCl_2 + C_3A \rightarrow C_3A.CaCl_2.10H_2O \qquad \text{Eq. (2.2)}$$

This reaction is related to the chloride ions, rather than the sodium, and can be observed with interactions with $MgCl_2$ and $CaCl_2$ solutions as well. Also, it was reported that the total amount of chloroaluminate formed is independent of the chloride concentration but depends instead on the aluminate phase's content. (Birnin-Yauri et al. 1998; Suryavanshi et al. 1996a). Very limited data in the literature was recorded regarding the pressures exerted due to precipitation of chloroaluminate crystals, and whether this contributes to the damage of concrete. In addition, it is worth noting that some industrial grades of rock salt (sodium chloride) may contain traces of calcium sulfate ($CaSO_4$), which lead to concrete damage, especially in combination with F/T cycles, due to pore filling possibly by Friedel's salt and ettringite (Arribas-Colón et al. 2012; Sutter et al. 2008; Taylor et al. 2006).

- *Magnesium Chloride (MgCl₂)*

Interactions of $MgCl_2$ with the cement hydration products in concrete are reported to cause damaging alterations to the cement paste structure, which reduce the concrete strength and increase its porosity owing to depleting CH to form brucite ($Mg(OH)_2$) and calcium chloride (Sutter et al. 2006; Lee et al. 2000), as shown in Eq. 2.3.

$$MgCl_2 + Ca(OH)_2 \rightarrow CaCl_2 + Mg(OH)_2 \qquad \text{Eq. (2.3)}$$
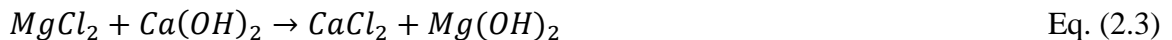
This reaction causes decalcification of the hydration product, calcium-silicate-hydrate (C-S-H), making the paste very porous and converting it to the secondary product, magnesium-silicate-hydrate (M-S-H; Eq. 2.4), which is a non-cementitious product (Sutter et al. 2006; Lee et al. 2000).

$$MgCl_2 + CSH \rightarrow CaCl_2 + MSH \qquad \text{Eq. (2.4)}$$

Such reactions were reported to be initially limited to the concrete surface layer as the brucite layer can hinder and slow down ingress of the solution into the concrete (Sutter et al. 2006; Rechenberg et al. 1996). Rechenberg et al. (1996) claimed that the formation of brucite at the surface of the concrete acts as a protective layer as no deterioration of concrete specimens were observed even after following 10 years of exposure to 2,500 mg/l $MgCl_2$ solution.

Even though less well-known, the formation of 3- or 5-form MOX could be part of the aggressive reaction products in concrete samples under the action of concentrated $MgCl_2$ solutions (Peterson et al. 2013; Sutter et al. 2006; Monosi et al. 1993). These phases have been studied under the $MgO–MgCl_2–H_2O$ system and are part of the hydrated products of magnesium oxychloride or Sorel's cement (Pannach et al. 2017; Dehua et al. 1999; Xia et al. 1991). The minimum concentration for the formation of MOX phases in the $MgO–MgCl_2–H_2O$ system was reported to be 1.96 mol/l (Dehua et al. 1999). A recent laboratory study by Peterson et al. (2013) referred the degradation in cement mortars exposed to 15% $MgCl_2$ for 500 days in 4.4 °C to the formation of MOX phase; however, no direct evidence was given for its formation (e.g. morphology) and their roles in the damage process.

Another aggressive feature of $MgCl_2$ treatment was degradation of both durable and non-durable concrete when it contains dolomite aggregates (Lee et al. 2000; Cody et al.

1994; Dubberke et al. 1985). Lee et al. (2000) reported that MgCl₂ produced distinctive alteration rims at the margins of reactive dolomite aggregate. Also, they stated that more brucite formed in the outer light-colored dolomite rim, a feature not seen in the corresponding alteration rims of untreated material; thus, further accelerates the concrete deterioration process.

- *Calcium Chloride (CaCl₂)*

Prior studies (Peterson et al. 2013; Sutter et al. 2006; Cody et al. 1996; Collepardi et al. 1994) reported that CaCl₂ salt is associated with a deleterious chemical reaction with concrete by formation of COX, as shown in Eq. 2.5.

$$CaCl_2 + 3Ca(OH)_2 + 9H_2O \rightarrow 3CaO \cdot CaCl_2 \cdot 12H_2O \qquad \text{Eq. (2.5)}$$
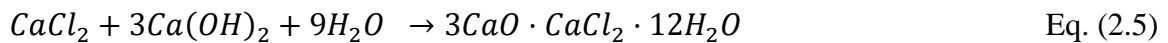
This reaction proceeds most efficiently at temperatures just above freezing point (4 to 10°C). It was speculated that COX formation generates additional stress within the concrete matrix due to the internal hydraulic pressures that may be generated (Collepardi et al. 1994). Collepardi et al. (1994) also cited a number of studies on the chemical effects of CaCl₂ on cement paste using X-ray diffraction techniques. They stated that previous researchers had not connected CaCl₂ paste/concrete damage to COX as such phases are not discernable by X-ray diffraction in dried samples. Monosi et al. (1990) reported the disappearance of oxychloride phases when the samples were washed with alcohol, filtered, heated, and dried at low RH. Also, Shi (2001) recorded the decomposition of calcium oxychloride phases when sample is air-dried at 20°C and 20% RH. Similar observations were reported by Peterson et al. (2013) upon drying of fresh calcium oxychloride crystals. Also, in a recent study by Galan et al. (2015) on the stability and coexistence of these

oxychloride phases in synthetic hydrated materials, they reported that the sensitivity of COX (3:1:12) to coating process and vacuum drying in the scanning electron microscope makes it difficult to observe their unaltered morphology.

Similar to the other salts, $CaCl_2$ can potentially affect aggregates within concrete (Lee et al. 2000; Cody et al. 1994). $CaCl_2$ solution enhances reactivity in dolomite aggregates, releasing magnesium ions, which then form destructive brucite and M-S-H, as previously discussed. It is worth noting that texture and porosity play a major role in aggregate degradation, and concrete deterioration.

2.1.1   Previous Studies on the Effects of De-icers/Anti-icers on Concrete

A number of methods have been used to simulate environmental conditions experienced by concrete pavements, which involve F/T cycles, W/D cycles, and soaking (immersion) of mortar/concrete specimens in de-icing salt solutions. F/T cycles tend to magnify the physical effects of the de-icers investigated, while W/D cycles and soaking allow chemical effects to be developed without the effects of frost action masking these reactions. A summary of the exposure regimes used in previous studies and the effects of various de-icers on concrete are presented in Table 2.1.

Table 2.1: Summary of the exposure conditions used in previous studies and the effects of common de-icers on concrete

	Exposure conditions	Temperature range/cycles	Concentration of the salt (% by weight or Mol/l)		
			NaCl	CaCl$_2$	MgCl$_2$
Collepardi et al. 1994	Immersion	Immersion at 5°C	--	30%*	--
Cody et al. 1996	W/D	Wetting at 60°C for 132 h Drying at 60°C or 90°C for 24 h	3M†	3M*	3M*
	F/T	Freezing at 0°C or -70°C for 132 h Thawing at 25°C for 24 h	3M†	3M*	3M*
	Immersion	Immersion at 60°C	3M†	3M*	3M*
Marchand et al. 1999	F/T	Freezing at -20°C for 15 h Thawing in warm water at 9 h	30%†	--	--
Lee et al. 2000	F/T	Freezing at -4°C for 24 h Thawing at 58°C for 132 h	0.75M†	0.75M†	0.75M†
Sutter et al. 2006	Immersion	Immersion at 4.4°C	27%†	17%*	15%*
Wang et al. 2006	W/D	Wetting at 4°C for 15 h Drying at 23°C for 9 h	26.5%†	37.9%*	--
	F/T	Freezing at -20°C for 15 h Thawing in warm water 9 h	13.3%†	9.5%*	--

*Significant and †Minor effects.

Table 2.1 Cont'd: Summary of the exposure conditions used in previous studies and the effects of common de-icers on concrete

	Exposure conditions	Temperature range/cycles	Concentration of the salt (% by weight or Mol/l)		
			NaCl	CaCl$_2$	MgCl$_2$
Kozikowski et al. 2007	F/T	Freezing at -18°C for 16-18 h Thawing at 23°C for 6-8 h	30%†	--	30%†
	Immersion	Immersion at 23°C	30%†	--	30%†
Drawin et al. 2008	W/D	Wetting at 23°C for 4 days Drying at 38°C for 3 days	15%†	16%*	18%*
Shi et al. 2010	F/T	Freezing at -17.8°C for 17 h Thawing at 22.8°C for 7 h	11%*	--	28%†
Shi et al. 2011	Immersion	Immersion at 23°C	7.8%†	8.2%*	8.8%*
Jain et al. 2012	W/D	Wetting at 4°C for 16 h Drying at 23°C for 8 h	23%†	28%*	25%*
	F/T	Freezing at -20°C for 5 h Thawing at 22°C for 4 h	14%†	17%*	15%*
Mori et al. 2013	F/T	Freezing at -18°C for 16 h Thawing at 23°C for 8 h	--	30%*	--
	Immersion	Immersion at 23°C	--	30%*	--
Peterson et al. 2013	Immersion	Immersion at 4.4°C or 5°C	17.8%†	15%*	17%*
Wu et al. 2015	F/T	Freezing at -17°C for 3 h Thawing at 8°C for 1 h	3*, 5*, and 20%†	--	3*, 5*, and 20%†

*Significant and †Minor effects.

While many studies have been conducted on the deterioration of concrete under de-icing salts combined with F/T cycles, limited research has been carried out on the effect of de-icing salts with W/D cycles. Also, most of the studies on the effects of W/D cycles have typically applied insufficient periods/regimes for drying the samples (Jain et al. 2012; Wang et al. 2006a; Collepardi et al. 1994) as the relative humidity (RH) used in these studies played an important role in limiting the effect of drying cycles. Moreover, the impact of these environmental conditions (W/D) on the formation/stability of complex salts (oxychloride phases) in cementitious matrices is not adequately documented in the literature, specifically regarding the explanation of the damage process/mechanism.

In addition, previous studies referred the extent of damage due to the type of de-icing salt used; however, these studies have focused on single de-icing salt solutions (NaCl, $MgCl_2$, and $CaCl_2$). In practice, transportation agencies improve the safety of roadways during wintery weather by using de-icing, anti-icing and pre-wetting strategies (combined salts). Unfortunately, no published data have been reported on the extent of damaged concrete when combined de-icing salts are used under any exposure. Also, previous studies on the effects of de-icing salts on concrete pavement used solutions that have either an equal mass of de-icing salt or an equal molar concentration (equal number of molecules for a given volume of solution). The issue with this approach is that the ice melting capability of a de-icer is better related to the number/concentration of chloride ions in a given quantity of water rather than the mass or molar concentration of the de-icer.

On the other hand, prior studies on the effect of de-icers on concrete mainly focused on conventional concrete. One of the theoretically promising strategies to mitigate the degradation by oxychloride formation is the use of SCMs. However, the nature of these interactions and how they are affected by the presence of SCMs in the cementitious system

are not well documented in the literature, specifically by direct evidence. For example, Suraneni et al. (2016) recently reported that use of 20% fly ash or slag as a replacement in synthetic hydrated materials reduces the COX amount by approximately 40% compared with plain cement pastes. However, they did not link the observed reduction in the formation of COX with physico-mechanical properties of real cementitious systems and the exact roles of SCMs in mitigating the damage of concrete.

2.2 Predicting Service-Life of Concrete Pavement Exposed to De-icers

Given the growing concern for concrete degradation in harsh environments, numerous computer-aided tools have been developed to assist engineers in the prediction of concrete service-life. Previous studies reported that laboratory and field experience indicated that the durability of cement-based composites is, in most cases, controlled by their ability to act as a barrier that can effectively impede or at least slow down the transport process. Therefore, different service-life models have been developed to calculate the transport properties of concrete, as a way of predicting its durability (Tamimi et al. 2008; Samson et al. 2007; Johannesson 2003). These studies relied on more or less complex (analytical or numerical) solutions of Fick's law of diffusion to map chloride penetration profiles in paste/concrete samples. However, this approach is based on many assumptions such as saturated conditions and simplified chemical interactions that do not reflect the actual behaviour of cementitious materials and effects of environmental conditions. Nevertheless, many studies showed the dependence of chloride diffusion in concrete on environmental conditions (Zhang et al. 2009; Nilsson et al. 2006). Consequently, it is not possible to predict the service-life of structures on the diffusion coefficients obtained for a given environment and use them for durability analyses in other environments. Also, the dissolution of existing phases (e.g. CH) and formation of complex phases (e.g. oxychloride)

during the chemical reactions may alter the transport properties of the system (paste/concrete) (Farnam et al. 2015c); thus, solutions of Fick's law cannot be expected to provide reliable results given the complexity of the phenomena involved (Marchand et al. 2009). Actually, most of these assumptions are rarely valid, particularly for concrete pavements exposed to de-icers combined with different environmental conditions. In a recent review by Marchand et al. (2009), they concluded that most service-life prediction models cannot be expected to provide reliable results given these limitations. They aimed to develop multi-ionic approaches to provide a more accurate prediction of the intricate interaction between ions and the hydrated cement paste; however, such models incorporate more detailed transport and chemistry equations and require a larger number of input parameters such as diffusion coefficient, permeability, porosity, moisture isotherm, thermal conductivity and heat capacity, as well as hydrated cement paste and pore solution compositions, which made it inapplicable for many agencies.

For complex durability problems of concrete, artificial intelligence techniques, such as fuzzy inference systems (FIS), artificial neural networks (NNs), adaptive neuro-fuzzy inference systems (ANFIS), have been successfully applied in recent years (Cho et al. 2016; Boğa et al. 2013; Štemberk et al. 2013; Bianchini et al. 2010; Bassuoni et al. 2008; Göktepe et al. 2006; Kim et al. 2006; Do et al. 2005; Haj-Ali et al. 2001).

FIS are modeling tools that can handle ambiguity and errors in complex systems. System components are mapped (fuzzified) to partial degrees of belongings or membership functions (Ross 2004). All non-linear and complex relations between system components are handled using linguistic rules in the form of IF-THEN statements in rule-based engines to convert fuzzified inputs to fuzzy outputs. Outputs of respective rules are aggregated and defuzzified to give a scalar solution. Anoop et al. (2002) used the ability of fuzzy sets in

handling uncertainties for developing a general methodology for durability-based service-life design of reinforced concrete structural members. The quality of construction, workmanship and exposure conditions were treated as fuzzy variables. They concluded that FIS addressed some of the issues that might be considered in the durability based service-life design by quantifying the environmental aggressiveness and taking into consideration the uncertainties arising due to the use of linguistic terms for quality of construction and exposure condition. Do et al. (2005) developed a fuzzy arithmetic approach to rationally estimate the time-to-corrosion initiation for reinforced concrete elements exposed to chlorides. Also, Do 2006 used FIS to determine the effects of environmental conditions accompanying chloride-rich environments on estimating the service-life of reinforced concrete structural members. Also, Kim et al. (2006) introduced a fuzzy-based assessment system for reinforced concrete structures to efficiently estimate their current state and present a guide for future maintenance and management.

ANNs are another artificial intelligence-based computational tool capable of pattern recognition and self-learning (Ross 2004; Hertz et al. 1991). The basic operations of such systems simulate that of neurons of the human brain. ANNs usually consist of input, hidden and output layers that comprise neurons (processing units). Neurons of one layer are partially or fully connected to neurons in the succeeding layer but are not connected to conjugate neurons in the same layer. Such a type of networks is classified as feed-forward ANNs. A large amount of data is usually needed to train ANNs in order to learn relationships between input parameters and their corresponding outputs. In ANNs, the back-propagation technique is commonly used for training ANNs where the convergence of ANNs is determined based on minimizing least square calculations between the output of the network and their corresponding actual values. Accordingly, the weights (strength

of connections) between connected neurons are continually updated until the global error (usually the root-mean-squared error, RMSE) reaches the desired minimum value or the number of epochs (training patterns) reaches a designated value. Several studies used ANNs to accurately estimate the properties of cement-based materials or to predict the deterioration in engineering properties of cement-based materials exposed to aggressive conditions. For example, Haj-Ali et al. (2001) and Göktepe et al. (2006) showed the capability of ANNs to reasonably estimate the expansion of mortars/concretes exposed to sulfate solutions. They concluded that ANNs can effectively learn and predict the expansion of the mortar/concrete samples within a practical range.

ANFIS is a hybrid system incorporating the learning abilities of ANNs and semantic knowledge representation and inference capabilities of FIS that have the ability to self-modify their membership functions to achieve the desired performance (Ross 2004; Brown et al. 1994; Jang 1993). This helps tailoring the membership functions of FIS to variation in given input-output data sets. In ANFIS, the FIS learn information about data to compute parameters of membership functions that best describe input-output behaviour. The algorithm works similarly to that of ANNs. Therefore, it can model the qualitative aspects of human knowledge and reasoning processes without employing precise quantitative analyses. The basic structure of ANFIS consists of four parts; fuzzification, rule base, inference engine and the de-fuzzification blocks as shown in Figure 2.4. This framework makes ANFIS modeling more systematic and less reliant on expert knowledge.
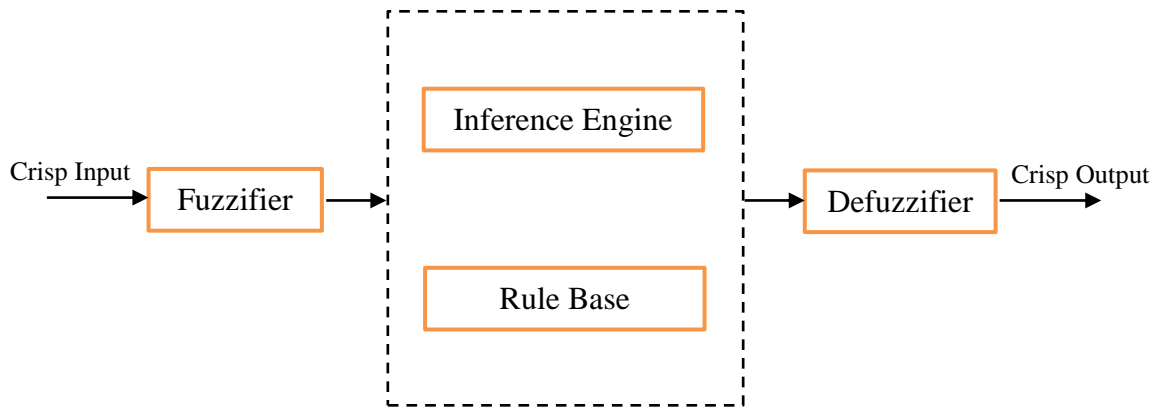
Figure 2.4: Schematic diagram of ANFIS.

ANFIS has feasibly been used to develop building management systems that are capable of analyzing the condition state of reinforced concrete structures under severe conditions of environments and loading (Kawamura et al. 2003). Also, Hu et al. (2006) successfully applied ANFIS to evaluate the effect of the composition of fly ash on suppressing the expansion of concrete due alkali-aggregate reaction. Bassuoni et al. (2008) also developed ANFIS models to predict the behaviour of a wide range of self-consolidating concrete mixtures under various sodium sulphate exposure regimes. They concluded that the sensitivity analyses for this approach had good agreement with experimental results and microstructural analysis. Bianchini et al. (2010) applied ANFIS to predict the performance of pavements using the parameters routinely collected by agencies, i.e. the development of distresses on the pavement surface by the rolling wheel deflectometer, to characterize the condition of an existing pavement. Also, Balasubramaniam et al. (2012) established an ANFIS model to estimate the performance characteristics of reinforced high-strength concrete beams subjected to different levels of corrosion damage. They concluded that ANFIS can be an alternative approach for the evaluation of such degradation as both training and testing data errors lay within reasonably small limits (RMSE $\leq 13.7\%$). ANFIS has also been successfully used for the evaluation

of chloride ions permeability in concrete containing blast furnace slag, calcium nitrite-based corrosion inhibitors, and a combination of these components with 92.2% accuracy (Boğa et al. 2013). Recently, Cho et al. (2016) also proposed ANFIS to estimate the carbonation depth of reinforced concrete members, based on the data obtained from field inspections of nine buildings. They stated that the proposed ANFIS algorithm closely estimated the carbonation depths and provided relatively good accuracy compared to the carbonation depth estimation method presented by the Korea Concrete Institute and the Japan Society of Civil Engineers. Thus, using a well-defined experimental database (input-output), ANFIS can be an efficient tool in modeling complex durability issues of concrete.

2.3 Repair of Concrete Pavements

Concrete is used in the construction of pavements because of engineering and economic considerations, including load carrying capacity, durability, local availability of constituent materials and relatively low maintenance cost. However, there have been frequent cases of concrete pavements constructed within the last 10 to 20 years showing premature deterioration, especially in the areas adjacent to longitudinal and transverse joints (Jain et al. 2012; Arribas-Colón et al. 2012). It has been estimated that almost one-half of all concrete repairs fail (Al-Ostaz et al. 2010; Vaysburd et al. 2004), leading to frequent maintenance and repair throughout the service life of concrete elements, resulting in significant life-cycle economic, social, and environmental impacts. Approximately 12 billion dollars is spent on pavements annually in Canada as indicated by Public Works Canada for innovative rehabilitation and repair of aging pavements (Transportation in Canada 2016). Also, United States Federal Highway Administration estimates that $85 billion would be needed in annual capital investment up to 2028 to be directed towards improving the physical condition of existing road assets in order to achieve the Department

of Transportation's State of good repair benchmark for a better ride quality (Report Card for America's Infrastructure 2013).

Corrective repair is used to improve the serviceability of pavement after some degree of deterioration by partial depth repairs (PDR) or full depth repair (FDR) (Frentress et al. 2012; Soliman et al. 2012; FHWA 2005; Wilson et al. 1999). PDRs are considered only if the distress is limited to the upper one-third to half of the concrete slab and the existing load-transfer devices (e.g. dowels) are still functional. When the deterioration is greater than half of the slab thickness or includes the load-transfer devices, FDRs should normally be employed. PDRs or FDRs can restore a well-defined and uniform joint system to keep incompressible materials and water out of the joint. As a result, it may restore structural integrity, improves ride quality, and extend the service life of aging pavements. The failure and subsequent repair of concrete pavements often cause traffic jams, giving rise to the need for rapid repair materials. Multiple factors (workability, hardening time, shrinkage, coefficient of thermal expansion, strength, durability, cost, service life, etc.) are considered before making a selection for the patching mixture (ACI 546.3R 2006). A variety of materials is available for use in PDRs including conventional cementitious materials, early-strength cementitious and polymeric products, latex-modified concrete, and various bituminous-based mixtures.

Portland cement concrete can be proportioned for use as a reliable patching material for concrete pavement (Delatte et al. 2014; Caltrans 2008; Emmons et al. 2006). It is most effective for FDR or complete slab replacement. Li et al. (2011) stated that if adequate early strength can be attained, a normal portland cement-based mixture is always favored over proprietary rapid hardening cement. However, conventional concretes were reported not to be the best materials for PDR of pavements due to the delay in setting time and

strength gain at early ages as well as the long curing times (Roh et al. 2015; Li et al. 2014; Li et al. 2011). Efficient repairs of concrete pavements often require a rapid setting material that can be placed, cured, and opened to traffic in a relatively short period of time. Despite that there is no general consensus on a minimum compressive strength prior traffic openings, Parker et al. (1991) suggested that for road patch repairs, a value of 13.8 MPa compressive strength was sufficient to control raveling, abrasion, deformation, and cracking. Also, California State Department of Transportation (2001) requires a minimum flexural strength of 2.8 MPa prior to opening roads to traffic. It reported that if the slab is subjected to traffic prior to obtaining this strength, the durability and life expectancy of the repaired pavement may be jeopardized. Different studies reported that approximately 75% of the premature failures of road repairs are attributed to lack of durability rather than structural failures (Li et al. 2011; Al-Ostaz et al. 2010; Wang et al. 2006b). Premature deterioration is more common for high-early-strength repair concrete because many proprietary binder systems often perform unpredictably under various construction conditions.

Over the past two decades, several high-early-strength cement-based repair material compositions (both generic and proprietary) have been successfully developed with various strength (compressive and flexural) gain rates, depending on the types of binders, i.e. high alumina cement, gypsum-based cement, magnesium phosphate cement, and accelerating admixtures used (Li et al. 2011; Wang et al. 2006b; Anderson et al. 2003; Seehra et al. 1993; Parker et al. 1991). While such materials can be placed and hardened within a relatively short period of time, many of these materials are vulnerable to cracking, poor bonding, and premature deterioration, for example, due to incompatibility with the existing concrete pavement (Soliman et al. 2014; Li et al. 2011). Such materials can also suffer from

stress concentrations, because of their susceptibility to thermal gradients and autogenous shrinkage, resulting in high levels of micro-cracking, and, in turn, durability issues (Soliman et al. 2014; Bentz et al. 2008). Additionally, reduced F/T resistance has also been found in some very high-early-strength materials, limiting their applications in cold regions (Whiting et al. 1994).

In the last decade, polymer concretes were used as an alternative repair material because they have acceptable mechanical properties and the curing time can be controlled (Jung et al. 2014; Soraru et al. 2004). Materials such as epoxies, polyesters, vinyl esters and methyl-methacrylates are the polymers commonly used in polymer concrete (Czarnecki et al. 1999). The main advantage of polymers is that they set much quicker than most of the cementitious materials (Jung et al. 2014; Soraru et al. 2004). Despite the benefits of polymer concretes, repetitive expansion and contraction of the repaired part as a result of environmental temperature changes may cause material failure at the bonding surface or the existing concrete as polymer concretes have 3 to 4 times higher coefficients of thermal expansion relative to cement-based concretes (Roh et al. 2015).

Sprinkel (1999) introduced latex-modified concrete as a repair option for PDRs of concrete pavements and bridge decks. The main advantage of latex-modified concrete is that it develops a compressive strength of 20 MPa within three hours after its placement, thus shortening traffic closure time. Also, latex-modified concrete had high resistant to the intrusion of chloride ions, and greater freeze-thaw resistance. Despite these advantages, the possibility of early-age cracking is significantly high due to its rapid hydration at the early age (Choi et al. 2014; Yun et al. 2014). Yun et al. (2014) evaluated the factors influencing thermal and autogenous shrinkages of latex-modified concrete in terms of latex-solid content, water-to-cement ratio, retarder content, and air entraining agent. They reported

that the latex-solid content is the main factor affecting the shrinkage. Also, they concluded that the risk of cracking might be higher in the field owing to the high evaporation rate, which may lead to cracking of the overlay with latex-modified concrete.

Modified bituminous materials (e.g. polymer-modified bitumen) were also introduced for repairing concrete pavements to reduce the scaling of deteriorated cracks and joints (Brown et al. 2000). These materials can be placed across transverse and longitudinal joints without the need for maintaining or reforming the joint, which helps reduce installation time. However, these materials are not recommended for permanent repairs of rigid pavements because they allow excessive horizontal movement of the slab, providing no load transfer across the joint and thus rapid deterioration (Markey et al. 2006; Silva 2005). Therefore, they should be only considered as a short-term or temporary repair.

CHAPTER 3 – PHASE I: FIELD INVESTIGATION OF JOINTS IN CONCRETE PAVEMENTS

3.1 Introduction

Condition assessment of pavement distress is generally considered relative to functional and structural performance in the decision process for maintenance. Several methods are available to measure and quantify distresses of the pavement including Roughness Index, Riding Comfort Index, and Distress Manifestation Index (DMI). The most common and simplest method is using DMI to evaluate the pavement condition (type, extent, and severity of pavement surface distress) by providing a numerical rating (e.g. 0 worst possible condition to 100 best condition) (Schlorholtz et al. 2003). A decision of maintenance requirement based on DMI ratings can vary among transportation agencies. On a small scale or in isolated cases, distress is determined through observations by two or more expert inspectors to decide on preventive maintenance that can stop a road deteriorating to the point that it needs expensive rehabilitation. Additionally, cores might be extracted for a series of macro- and micro-scale test. On the other hand, many non-destructive techniques, such as stress wave propagation, impact-echo, spectral analysis of surface waves, infrared thermography and ground penetration radar can also be used to predict the level of deterioration (ACI 228.2R 2013).

Previous in-situ evaluations in multiple sites revealed that, in many cases, the joints continued to hold water/solution (due to application of de-icing salts) long after wetting events (Arribas-Colón et al. 2012; Ranjaraju 2002). This solution is involved in the deterioration by physical actions (generation of micro- and macro-cracks by

increasing the degree of saturation) (Arribas-Colón et al. 2012; Kang et al. 2012) or chemical reactions (leaching/decomposition of hydration products and formation of expansive phases) (Kang et al. 2012; Jain et al. 2012). Currently, it has been suspected that the widespread use of specific types of de-icing salts may have played a role in either triggering or accelerating the concrete pavement distress (Wang et al. 2006a; Ramakrishna et al. 2005). Also, changes in de-icing practices such as implementation of anti-icing (to prevent the bonding of ice to the roadway before a storm) and de-icing strategies (to melt and break down the bond between the ice layer and the road surface) may impart deleterious effects on concrete pavements and reduce its integrity and durability.

From a durability perspective of concrete, the root causes behind joint deterioration are not yet fully understood since a multitude of reactions and mechanisms are responsible for this deterioration (de-icing salts, freezing/thawing (F/T) and wetting/drying (W/D) cycles, D-cracking, alkali-aggregate reaction, degree of saturation, corrosion of dowel bars at joints, drainage conditions and maintenance). Also, they may vary within the same transportation jurisdiction/city, for example, due to implementing varying winter practices (e.g. type and rate of de-icing salts) to different street zones. For better understanding of the source of this damage and identifying aspects contributing to premature joint deterioration of concrete pavement in Winnipeg, Manitoba, Canada, this chapter involved analyzing concrete core samples collected from both distressed and sound joint locations in concrete pavements. The pavement sections (regional roads and residential streets) were exposed to different winter treatments (type, rate, and application (direct/indirect) of de-icing salts) and had been in service in wet and long-freezing conditions between 15 and 20 years. This study presents the results of an evaluation for the condition of these concrete pavements through macro- and micro-scale analyses.

3.2 Description of Field Sites and Data Collection

Representative pavement sections (regional roads and residential streets) were chosen by Public Works Department, City of Winnipeg (COW) at an urban zone in the central area of Winnipeg, Manitoba. The pavement in the test location is subjected to large temperature changes, as the maximum and minimum air temperatures during the last 10 years were +36°C and –36°C, respectively. The investigation started with a detailed inventory of the pavement sections by visual examination in order to identify the type and level of deterioration for the candidate locations before extraction of the cores. Distress rating by visual examination for the extent of damage on the surface of pavement and along joints was reported and described as minimum, medium (considerable), or high (extensive) for each site, as shown later in the visual observations section. A level of distress classified as medium or high indicated that attention is required for such areas, which likely needs maintenance. The available information on the history of these pavement sections including treatment methods was documented, as listed in Table 3.1.

Generally, concrete with target performance between 30 to 35 MPa and meeting a class of exposure C-2 (plain concrete subjected to chlorides and freezing-thawing) according to CSA A23.1 was used in all roads under investigation. Typically, the concrete comprised General Use (GU) portland cement and up to 15% fly ash (Class F), as a SCMs, meeting the requirements of CSA A3001, and the water-to-cementitious materials ratio (*w/cm*) was in the range of 0.36 to 0.38.

Table 3.1: Available information on the history of the pavement sections

	Residential street I	Residential street II	Regional road I	Regional road II

Year constructed	2001	1999	1996	1996
Service years	15	17	20	20
No. of lanes	2 (traffic lane/parking lane)	2 (traffic lane/ parking lane)	3 (3 traffic lane/ parking lane)	3 (2traffic lane/ shoulder)
Average traffic/day (vehicles)	< 2500	< 2500	> 20000	> 20000
Design stress (flexural Strength, MPa)	3.8	3.8	4.5	4.5
Design speed (km/h)	40 - 50	40 - 50	60 - 80	60 - 80
Salt application (kg/lane kilometer) [Avg. frequency/winter]	Not recommended	Not recommended	160 [14]	160 [18]
Treated sand* (kg/lane kilometer)	Specific areas**	Specific areas**	320	320

*Liquid salt is added to the sand (5% by weight).
**Intersections, pedestrian corridors and crosswalks, railway crossings and inclinations.

Stresses in concrete pavements are generated by different factors such as traffic loads (flexural stresses due to cyclic wheel loads), curling (as a result of a temperature gradient, in which the surface of the slab has a temperature that is different from that at the bottom), frictional stresses (due to the contraction of slab due to shrinkage), unequal subgrade settlements stresses and stresses due to harsh service conditions (e.g. F/T cycles, W/D cycles). Therefore, the design of concrete pavement is based on the stresses that a specific pavement system can sustain before failure (capacity) as shown in Table 3.1. In this field study, crumbling and damage of joints in regional roads led to reducing the effective bearing area resisting such stresses, which would likely increase the magnitude of stresses projected in Table 3.1. However, no sensors were installed in these locations to specifically quantify the level of stresses generated in the damaged areas. The City of Winnipeg commissioned this field study based on visual classification of damage to thoroughly investigate the source of damage and identify aspects contributing to joint deterioration of regional roads compared to residential streets.

According to COW policy for ice control (Policy on Snow Clearing and Ice Control 2011), the regional roads have been classified as priority I streets where de-icers (mainly chloride-based salts: salt brine with a concentration of 23.3% of sodium chloride by weight) are directly used in winter months to provide an adequate level of service by preventing the formation of ice on the roadway surface due to freezing rain, fog, and traces of snow (anti-icing). Moreover, a liquid salt (proprietary solution comprising 26.6% calcium chloride, 3.1% magnesium chloride, 1.3% sodium chloride and 0.9% potassium chloride) are also added to abrasives (sand) or solid salts to make them easier to manage and distribute and help them stay on roads (pre-wetting). The pre-wetting chemical is applied at 40 l/ton for treated sand and 50 l/ton for road salt. The rates of application for these de-icers are shown in Table 3.1. In contrast, the existing policy for ice control states that the residential streets (priority II) are maintained to a compacted snow/ice by plowing operations without applying salts, except for specific areas as described in Table 3.1. Similar winter maintenance operations are applied by different transportations agencies in the northern United States (Minnesota Snow and Ice Control 2012) and Canada (City of Toronto 2016). However, the type and rate of de-icing salts may vary depending on the availability of the de-icing salt, the effective freezing temperature, in addition to balancing social, environmental and economic factors.

3.3 Laboratory Testing

A series of macro- and micro-scale tests were conducted to evaluate the nature of the distress, if any, in both regional roads and residential streets. A total of 48 cores were taken at multiple locations to capture the effect of different winter treatments (rate and application (direct/indirect) of de-icing salts) in the pavement sections under investigation.

The core diameters ranged from 100 mm to 150 mm. All the results in this study are averages of at least two specimens prepared from these cores.

The transport properties of concrete were assessed by capillary absorption and electro-migration of chloride ions. The absorption test was conducted on previously conditioned (dried at a temperature of 50±2 °C and a relative humidity (RH) of 40% for 72 h followed by vacuum pressure (~85 KPa) for 6 h) concrete discs (75 mm diameter and 50 mm thickness) cut from the cores. The initial mass to the nearest 0.01 g was recorded and then the specimens were submerged in 4% calcium chloride solution for up to 360 min, and the amount of absorption after 1, 5, 10, 20, 40, 80, 160 and 360 minutes were determined and normalized by the initial mass (dry mass) of the specimens (Tiznobaik et al. 2017).

Also, to evaluate the resistance of these concrete cores to the penetrability of aggressive ions, rapid chloride penetrability test (RCPT) according to ASTM C1202 was used and the penetration depth of chloride ions into concrete, which better correlates to the physical characteristics of the pore structure, was determined according to the procedure described by Bassuoni et al. (2006). After the RCPT, the specimens were axially split and sprayed with 0.1 M silver nitrate solution, which forms a white precipitate of silver chloride in approximately 15 minutes, to measure the physical penetration depth of chloride ions. The average depth of the white precipitate was determined at five different locations along the diameter of each half specimen. This depth is considered to be an indication of the ease of ingress of external fluids, and thus the continuity of microstructure.

To complement the results of the absorption and RCPT tests, the characteristics of the pore structure of concrete were determined by mercury intrusion porosimetry (MIP) with a maximum pressure of 206 MPa, allowing the detection of pore radii ranging from 3

nm up to 1000 µm. Small pea-sized chunks (around 5-10 mm in size) taken from at least two replicate cores were carefully selected to avoid the inclusion of large aggregates. The chunks were oven-dried at 45±5 °C for 72 h; they were then kept in a desiccator containing calcium sulfate for 24 h before the MIP test. This method of drying at a lower temperature for a longer period was adopted to avoid the formation of micro-cracks, which may occur at higher drying temperatures. The contact angle and the surface tension of mercury were taken as 130º and 485 dynes/cm, respectively.

To characterize the air-void system in the concrete cores, the automated flatbed scanner method described by Chatterji et al. (1977) was used on a square cross-section of 100 mm cut pieces from the cores. This method is based on painting the surface of concrete in black and then forcing white powder of wollastonite into the air-voids so that the voids are visible in scanning and image analysis. This method provides repeatability and a good level of accuracy as reported by previous studies (Zalocha et al. 2005). Finally, to understand the alteration of microstructure and thus gain a fundamental understanding of the principal mechanisms of deterioration, microscopy, thermal and mineralogical studies had been used. Fracture pieces were extracted from the top and bottom portions in the cores and examined by scanning electron microscopy (SEM) assisted with energy-dispersive X-ray analysis (EDX). The SEM samples were coated with a fine layer of carbon before performing the analysis to make the surface conductive and to improve the sample imaging. To augment the analysis from the SEM, the mineral phases within the cementitious matrix were analyzed by X-ray diffraction (XRD, Cu-Kα) and differential scanning calorimetry (DSC) on powder samples collected from the cores. This powder was prepared from carefully extracted fracture pieces (not including large coarse aggregate) of specimens, which were pulverized to fine powder passing through sieve #200 (75 μm).

3.4 Results and Discussion

3.4.1   Visual Observations

The visual inspection provided reasonable information about possible factors affecting the damage. These factors comprised collecting information about the surrounding environment, drainage conditions, maintenance, sealant condition, presence of water/solution, presence of precipitates, and any visual damage.

For regional roads, most of the sites showed distinctive signs of damage (Fig. 3.1). The visual evaluation of the condition of these sites revealed that the drainage of the joints contributed significantly to their performance. The drainage system suffered from differential movement of slabs, i.e. change of slope, in many locations, debris, natural siltation, vegetation, and lack of proper maintenance. Most joints continued to entrap water (solution) long after wetting events (Fig. 3.1a), which also can be linked to insufficient permeability within the base and sub-base layers. Thus, notable darkening (shadowing) of the concrete near the transverse and longitudinal joint was visible (Fig. 3.1b). The darkening indicated the accumulation of dirt and other road debris and high moisture content within the micro-cracks along and near the joints. In addition, narrow longitudinal cracks filled with white efflorescence with less than 2 mm in width were present along some joints (Fig. 3.1c). Joint sealants were mostly de-bonded from both sides of the saw-cut joints (Fig. 3.1d). The most intensive damage occurred at the intersection of the transverse and longitudinal joints, where these areas exhibited significant loss of material. Therefore, based on the visual evaluation of the condition of these sites, the extent of damage was considered as 'medium or high' deterioration in both longitudinal and transverse joints. Due to the differences in the pavement conditions for the streets selected, the cores had been extracted from different sections at and adjacent to the joints. In many

cases, the damage to the joints was extensive and the concrete crumbled during the coring process (Fig. 3.2a); therefore, it was not possible to obtain full cores in these locations, where they ended up into several pieces, as for example shown in Fig. 3.2b. Parallel cracks were also a common damage feature of concrete cores in these locations (e.g. Fig. 3.2c), and the damage was generally found in both top and bottom parts (Fig. 3.2d).

Figure 3.1: Evidence of joint deterioration in regional roads: (a) widening of joints and entrapment of water/solution, (b) shadowing near the joints, (c) cracks filled with white efflorescence, and (d) de-bonded sealants

Figure 3.2: An example from regional roads showing: (a) damage of concrete during the coring process, (b) fractured cores, (c) sub-parallel cracks in the extracted cores, and (d) damage of top and bottom parts.

In comparison to the regional roads, the residential streets were in excellent conditions (minimal deterioration, Fig. 3.3), except that the concrete surface occasionally exhibited surface scaling and pop-outs in the parking lane. Most of the joints were clean and sound, and there was no evidence of faulting or spalling (e.g. Figs. 3.4a-b). The pavement cross slope and drainage system appeared to be effective as water continued draining after wet events as adequately as designed. During coring, it was observed that core holes drained well compared with core holes of regional roads. Also, the cores extracted at and near joints appeared sound and intact; they were cleanly and fully drilled with excellent conditions (e.g. Fig. 3.4c).

Figure 3.3: A residential street showing surface scaling of concrete.

Figure 3.4: An example from a residential street showing: (a) sound joint without evidence of faulting or spalling, (b) joint cross-sections without damage, and (c) whole/intact core.

3.4.2   Transport Properties

Most durability issues of concrete pavements, particularly under aggressive environments such as F/T and W/D cycles, are controlled by the pore structure characteristics and transport properties of concrete. The porosity of concrete and interconnectivity of the pore structure are key parameters for understanding the transport of fluids and ionic species into concrete, which indicates the ease of saturation of concrete and in turn its vulnerability to damage. Therefore, a series of tests were carried out to identify the pore structure characteristics for the cores extracted from different locations in both regional and residential streets. All the results of absorption, RCPT, and MIP tests

were statistically evaluated by the Analysis of Variance (ANOVA) method at a significance level (α) of 0.05. According to ANOVA, exceeding the critical value (F_{cr}) of an F-distribution density function reflects that the tested variable significantly affects the mean of the results (Montgomery 2014).

Water absorption test indicates mass transport of fluids into concrete by capillary suction (Hall 1989). The rate and total absorption were determined for at least six samples from each location in both regional and residential streets, as shown in Fig. 3.5. It can be noted that the general trend of the absorption curves indicates significant (Table 3.2) difference between the cores extracted from the regional and residential streets. For example, the initial absorption, at 1 min, for the cores extracted from the residential and regional streets gained about 25% and 55%, respectively of their total absorption after 360 min. Also, the rate and total absorption values for the cores extracted from the regional streets are significantly higher (two to three times) than that of the cores extracted from the residential streets.
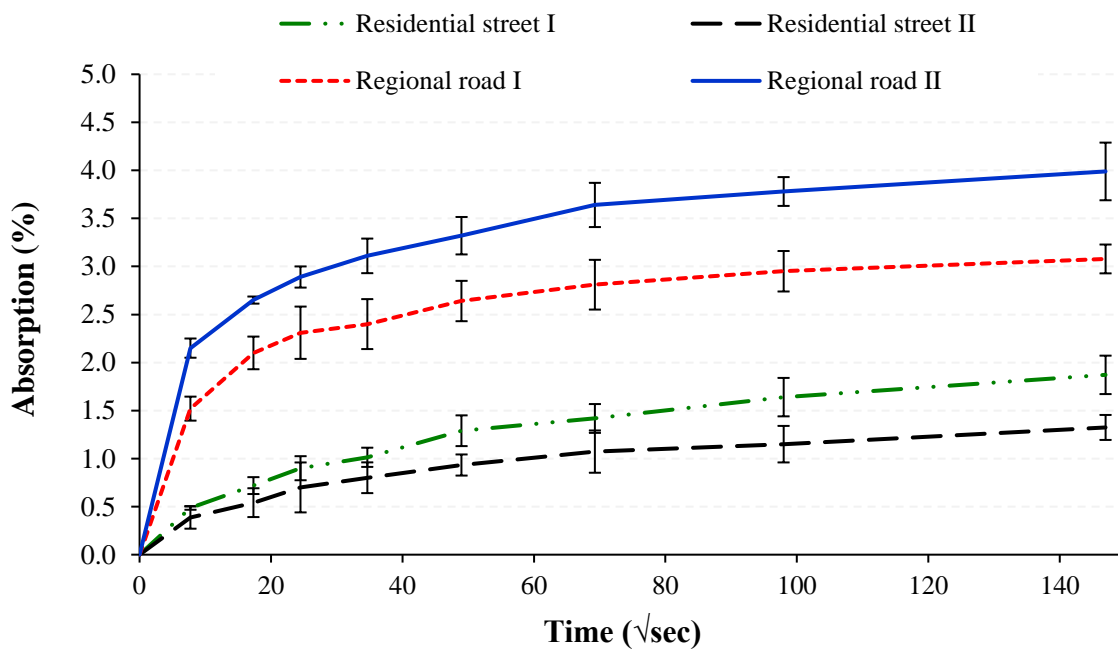
Figure 3.5: Rate of water absorption of cores extracted from different pavement sections.

Table 3.2: ANOVA for the total absorption, migration coefficient and total porosity
results of the cores extracted from different streets

Test	*F*	*P-Value*	F_{cr}	**Effect**
Absorption test				
Absorption %	90.45	0.001	4.20	Significant
RCPT				
Migration coefficient	189.12	9.95E-14	4.49	Significant
MIP				
Total Porosity %	29.68	0.003	18.51	Significant

The trends of the absorption test conformed to the measured penetrability (Table 3.3) of concrete in these locations. The cores obtained from regional streets were classified as "Moderate to High" penetrability according to ASTM C1202, indicating coarse and continuous pore structure. Comparatively, specimens from residential streets generally had "Very Low" penetrability. The classification of chloride ions penetrability was consistent with the chloride diffusion coefficients (non-steady-state migration coefficient) of these cores. The chloride migration coefficient of concrete was calculated on the basis of the penetration depth (Table 3.3 and Fig. 3.6) according to NT BUILD 492 (2011), to account for the effect of heat (Joule) and different testing durations on ionic mobility within specimens. These factors particularly affected samples with high porosity and considerable contamination with chloride ions. Among all the cores tested, cores from regional road II had the highest migration coefficient (average of 54.46 $\times 10^{-12}$ m^2/s), conforming to the earlier observations of the absorption test. Despite a "Moderate" penetrability in some cores extracted from regional roads, their penetration depth was very high (50 mm). The values of passing charges observed in these samples may be attributed to the Joule effect as these samples reached the maximum temperature (70°C) allowed by the apparatus before the end of testing; subsequently, the test stopped before collecting the actual passing charges after 6 hours. It seems that applying de-icing salts altered the transport properties

of the concrete in the regional roads. It was reported that de-icing salts may cause leaching of calcium hydroxide from the hardened cement paste, resulting in higher porosity of concrete (Wang et al. 2006a), as discussed later in the TG and microscopy section.

Table 3.3: Rapid chloride penetrability test (RCPT) results

	Passing charges (coulombs)	Chloride ion penetrability class (ASTM C1202)	Average penetration depth (mm) (standard error)	Migration coefficient ($\times 10^{-12}$ m^2/s)
Residential street I	327	Very Low	9 (0.74)	1.62
	1013	Low	15 (1.29)	5.55
	456	Very Low	10 (0.69)	2.24
	846	Very Low	12 (1.01)	3.51
Residential street II	112	Very Low	11 (0.49)	2.87
	216	Very Low	13 (0.79)	4.10
	103	Very Low	10 (1.09)	2.22
	401	Very Low	8 (0.69)	1.72
Regional road I	2864	Moderate	50 (0)	31.37
	4832	High	50 (0)	34.02
	3120	Moderate	43 (0.64)	27.30
	5143	High	50 (0)	35.39
Regional road II	4689	High	50 (0)	81.47
	4989	High	50 (0)	49.47
	5223	High	50 (0)	53.26
	4930	High	50 (0)	33.62

Figure 3.6: Whitish color showing the chloride penetration.

The MIP results (cumulative intrusions, porosity, threshold pore diameters and proportion of micro-pores (less than 0.1 µm)) for all the field cores are listed in Table 3.4. The MIP tests were done on at least four small chunks extracted from two replicate cores for each street, which were put in the same test compartment (porosimeter). Thus, the results shown in Table 3.4 can be reasonably considered the averages of representative populations to the physical features of microstructure for the concrete cores tested in this study. The trends of MIP conformed to the transport properties (absorption and penetrability/diffusivity) determined for these cores in the sense that there was a significant (Table 3.2) increase in the proportion of macro-pores, threshold pore diameter, and total porosity of the cores extracted from regional roads relative to the cores extracted from residential streets (Table 3.4). For example, the total porosity for the concrete extracted from regional roads was 58% higher than that of corresponding cores extracted from the residential streets. Also, the threshold pore diameter for these cores was, approximately, 3 µm, which was one order of magnitude higher than the lowest threshold of macro-pores (0.1 µm). Correspondingly, the proportion of micro-pores in these cores was less than 35% of the total pore volume (Table 3.4). Thus, the ease of percolation in a larger proportion of macro-pores facilitated the absorption and penetrability processes in cores extracted from the regional roads.

Table 3.4: Mercury intrusion porosimetry (MIP) test results for field cores

	Apparent total porosity (%)	Threshold pore diameter (µm)	Proportion of micro-pores (<0.1 µm) (%)
Residential street I	13.2	0.21	47.1
Residential street II	12.4	0.14	53.2
Regional road I	18.7	2.12	35.4
Regional road II	21.2	3.89	32.4

3.4.3   Air Void System

Performance of concrete subjected to F/T environments is a function of the air void system. Therefore, the quality of the air void system in terms of air content, spacing factor and specific surface area was determined (Table 3.5). Generally, the majority of the concrete cores obtained from joints in regional roads showed lack of air voids dispersed in the paste (Fig. 3.7a). For example, the total air content for these cores was approximately 2.5% which did not satisfy the limits (6.5% ±1.5%) specified by North American codes for durable concrete to F/T cycles (ACI 201.2R 2016; CSA 2014). Likewise, the key parameter of spacing factor (dispersion of air voids in the cementitious matrix) was significantly higher than that required by these codes (Table 3.5). Also, the marked drop in the specific surface area (the average air voids size) for the concrete extracted from the regional roads indicated that a significant amount of the smaller air voids diminished. This trend linked to the increase of the threshold pore diameter obtained from the MIP test (Table 3.4). Comparatively, the air void system in the residential streets did not appear to be affected (Fig. 3.7b). Adequate air content (an average of 5.4%), uniform spacing factor (an average of 0.1 mm) and high specific surface area were obtained for this concrete.

Table 3.5: Air void system characteristics for field cores

	Total air content (%) (Target: 5%-8%)	Spacing factor (mm) (Target: < 0.2 mm)	Specific surface area (mm^2/mm^3) (Target: > 25 mm^2/mm^3)
Residential street I	5.29	0.12	49
Residential street II	6.13	0.10	57
Regional road I	3.16	0.48	12
Regional road II	2.43	0.61	9

Note: The results are the average of four samples or more in each area.
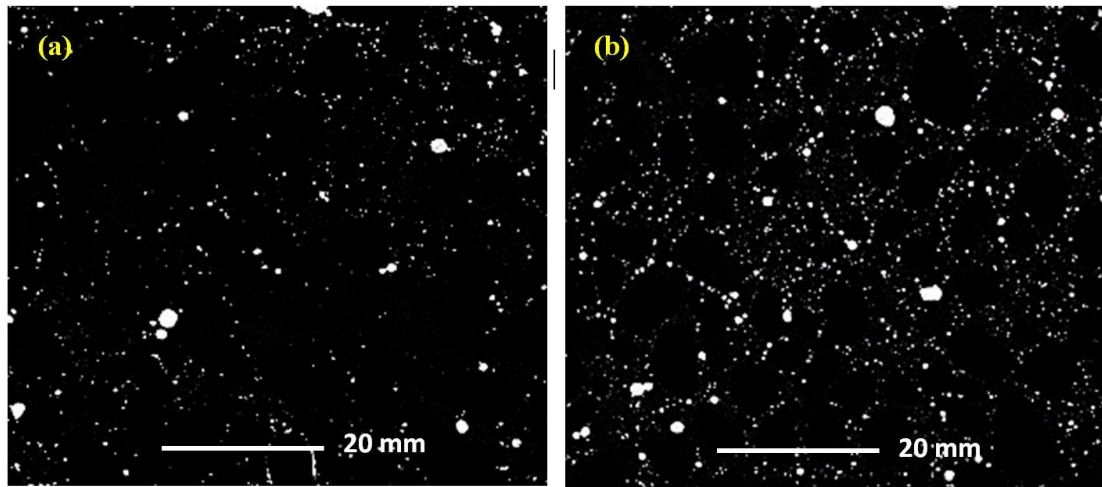
Figure 3.7: Images of polished surfaces treated with wollastonite (white spots) for: (a) regional roads, and (b) residential streets.

3.4.4   Mineralogical, Thermal and Microstructural Analyses

To characterize the microstructure of this concrete, XRD analysis was performed on powder samples collected from the cores and the results are shown in Fig. 3.8. Also, the XRD pattern for newly (28 days) cast concrete pavement in Winnipeg was used as a reference for identifying possible leaching and new crystalline reaction products. Almost all samples had generally similar dominant phases of quartz, dolomite, and calcite. The sources of quartz in the diffractograms originated from the siliceous coarse aggregate and sand, while the peaks of dolomite and calcite occurred because the coarse aggregate contained a fraction of carboniferous aggregate in addition to possible carbonation of the hydrated cement paste.

Compared to the reference sample, samples collected from the residential streets generally showed similar XRD patterns, except that portlandite ($Ca(OH)_2$) peaks diminished (Fig. 3.8). Traces of Friedel's salt and ettringite were also noted in some samples. These trends were further corroborated by DSC tests, as shown in Table 3.6. A semi-quantitative analysis based on the enthalpy concept (integration of heat flow peaks over temperature) can determine the relative phase formation, as the enthalpy of each

phase, i.e. ettringite, Friedel's salt, portlandite, is directly related to its amount (Brown et al. 2011). The consumption of portlandite in these samples might be due to the long-term pozzolanic activity as this concrete comprised 15 to 20% Type F fly ash and/or leaching/reaction of this phase. However, the bulk properties of concrete from residential streets substantiate the first hypothesis (pozzolanic activity), as this concrete had low absorption, limited penetrability/diffusivity, and an effective air void system. Also, the microscopy analysis supported this trend as homogenous matrix without micro-cracks was observed in various specimens (e.g. Fig. 3.9a), with incidental occurrence of Friedel's salt and ettringite crystals (e.g. Fig. 3.9b) in some voids near (within 10 mm) the exposed surface. The presence of Friedel's salt is likely a result of the substitution of sulfate ions by chloride ions, i.e. chloride binding, in aluminate phases such as monosulphate and unreacted tri-calcium aluminate, if any; however, this phase may not be detrimental to the integrity of concrete as no marked symptoms of cracking and softening were detected.
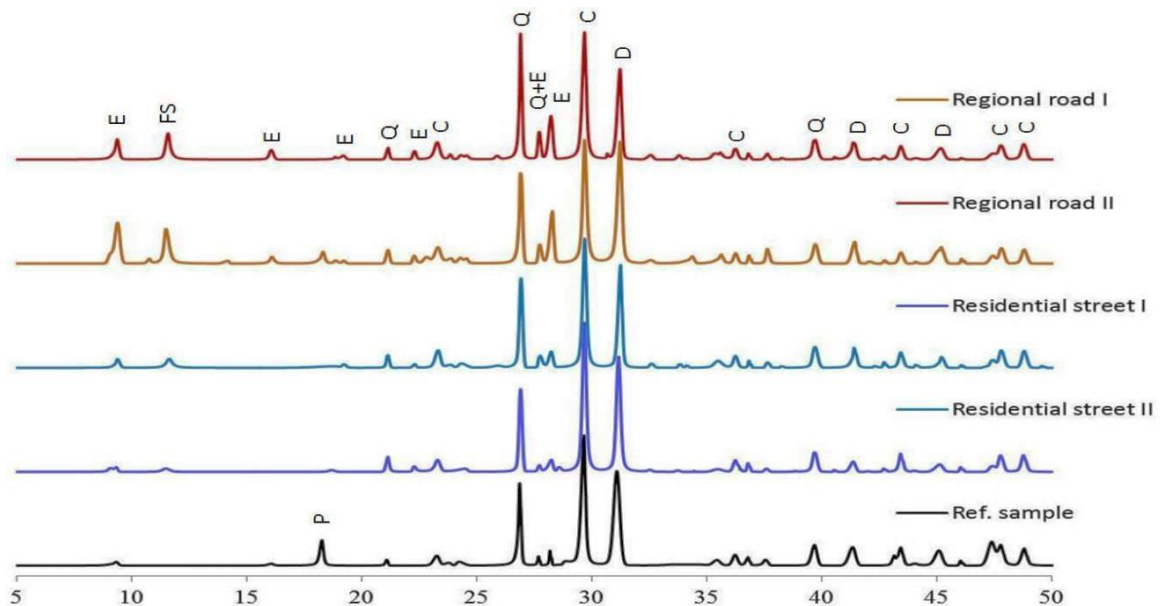
Figure 3.8: XRD patterns of samples from different roads. (Note: E = Ettringite, FS =Friedel's salt, P = Portlandite, D = Dolomite, C = Calcite, and Q = Quartz)

Table 3.6: Enthalpies (J/g) of the main phases in the cementitious matrix

	Ettringite (90-110ºC)	Friedel's salt (340-390ºC)	Portlandite (410-450ºC)
Reference sample	5.7	0.0	17.2
Residential street I	8.2	3.6	0.9
Residential street II	6.3	2.9	1.7
Regional road I	39.7	11.9	0.0
Regional road II	48.9	14.2	0.0

Note: The enthalpies results are the average of eight samples or more in each street.
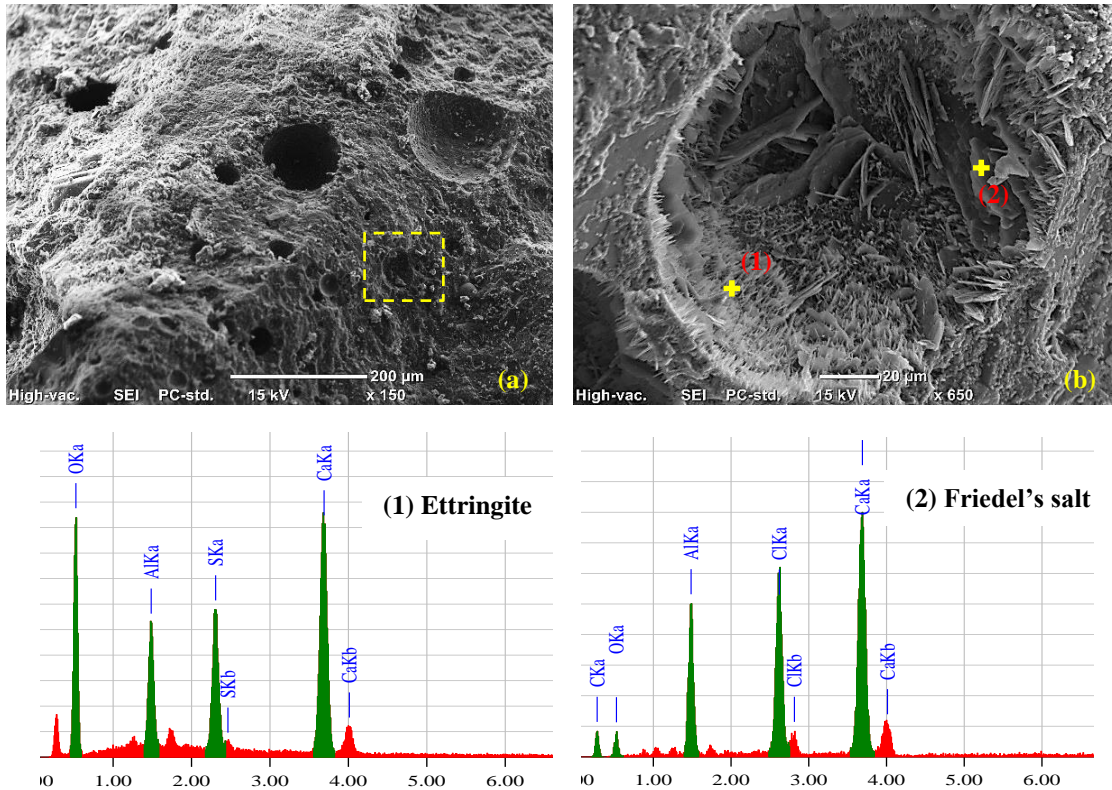
Figure 3.9: Samples collected from residential streets showing: (a) homogenous matrix; and (b) incidental occurrence of Friedel's salt and ettringite crystals precipitating in air voids with associated EDX spectra.

Conversely, samples extracted from the regional roads showed distinctive XRD pattern, as shown in Fig. 3.8. Higher intensity peaks of ettringite and Friedel's salt were detected in this concrete as the key reaction products. This trend was further supported by the DSC analysis; for instance, Table 3.6 shows that the amounts of ettringite and Friedel's salt formed in the regional roads samples were approximately 7 and 4 times, respectively that in the residential streets samples. SEM showed that this concrete had high intensity of

micro-cracks (e.g. Fig. 3.10a) and most air voids (both small and large) were filled with various levels of secondary depositions (e.g. Fig. 3.10b). Spatial elemental distribution by EDX revealed that the secondary depositions were mostly ettringite (e.g. Fig. 3.10c). This observation complies with previous studies on field performance of concrete pavements (Arribas-Colón et al. 2012; Ranjaraju 2002) which reported the presence of secondary depositions in the cementitious matrix.

Chloride ions from de-icing salts are bound by aluminate phases such as monosulphate, calcium aluminate hydrate and unreacted tri-calcium aluminate, if any, forming Friedel's salt or Kuzel's salt (depending on the chloride concentrations), which can lead to releasing sulfate ions into the pore solution. With time, the releasable sulfate ions combine with the remaining monosulphate in the presence of the moisture, precipitating ettringite. In addition, Friedel's might decompose and release chloride ions due to many factors such as acidification and carbonation, and consequently form ettringite, especially with the presence of sulfate ions in the pore solution (Brown et al. 2000; Suryavanshi et al. 1996a and 1996b). Actually, re-crystallization and/or formation of ettringite might also be attributed to different reasons (availability of the components that form ettringite, Ostwald ripening, variations in pH and temperature).

First, if external (e.g. as impurities in de-icing salts, or dissolved in groundwater) or internal (e.g. from aggregates) sources of sulfate ions are present, the sulfate would react with monosulphate to form ettringite with consequent deposition in open spaces, such as air voids. However, if no sources of sulfate are available, ettringite may form due to repetitive saturation in the system (W/D and F/T cycles), which may induce expansion due to its formation (Stark et al. 1999). However, it is not certain whether the growth of larger secondary ettringite in air voids is expansive, as expansive damage of paste is usually

attributed to micro-crystalline ettringite formed in the hydrated paste (Skalny et al. 2002; Mather 2001). Detwiler et al. (1999) reported that expansion and distress of pavements in Wisconsin occurred before much ettringite deposited in air voids. Famy et al. (2001) and Ouyang et al. (1999) stated that ettringite found in this benign state as large needle-shaped or compact crystals (Fig. 3.10b), should not necessarily be interpreted as the cause of damage of concrete since this may be just a consequence of re-crystallization. Famy et al. (2001) stated that ettringite formation in microstructural defects can be promoted by frequent drying and repeated wetting. They stated that the higher the amount of water passing into the capillary system, the higher the apparent amount of ettringite was observed (Famy et al. 2001). Small crystals (with higher specific surface and surface energy) dissolve in the pore solution and recrystallize as large crystals in available large spaces, such as pores and cracks 'Ostwald ripening' (Famy et al. 2001; Stark et al. 1999). Indeed, such moisture conditions were available in the wet joint of regional roads due to application of de-icing salt as salt solutions have lower vapor pressure than that of pure water (Mehta et al. 2014). Litvan (1976) reported that when concrete is saturated with a saline solution, evaporation will only commence at a relatively lower relative humidity, leading to high moisture content.

Whether ettringite crystals formed in air voids are expansive or not, in-filling of air voids (especially smaller air voids) with secondary products reduced their effectiveness (inadequate air-void system; Table 3.5 and Fig. 3.7) to provide an adequate level of F/T protection. In-filling of air voids with ettringite or any precipitates in concrete from regional roads may also ease reaching critical saturation levels due to higher rates of moisture ingress (Fig. 3.5) because the air voids are not available anymore to interrupt the paths of penetrability (Stark et al. 1999). This made this concrete vulnerable to progressive

F/T damage as manifested by micro- and macro-cracking and eventually crumbling (Fig. 3.2). Similar observations were reported for laboratory concrete by Ouyang et al. (1999). These trends suggest that concrete at joints in regional roads might have suffered from F/T cycles as the primary mechanism of deterioration.
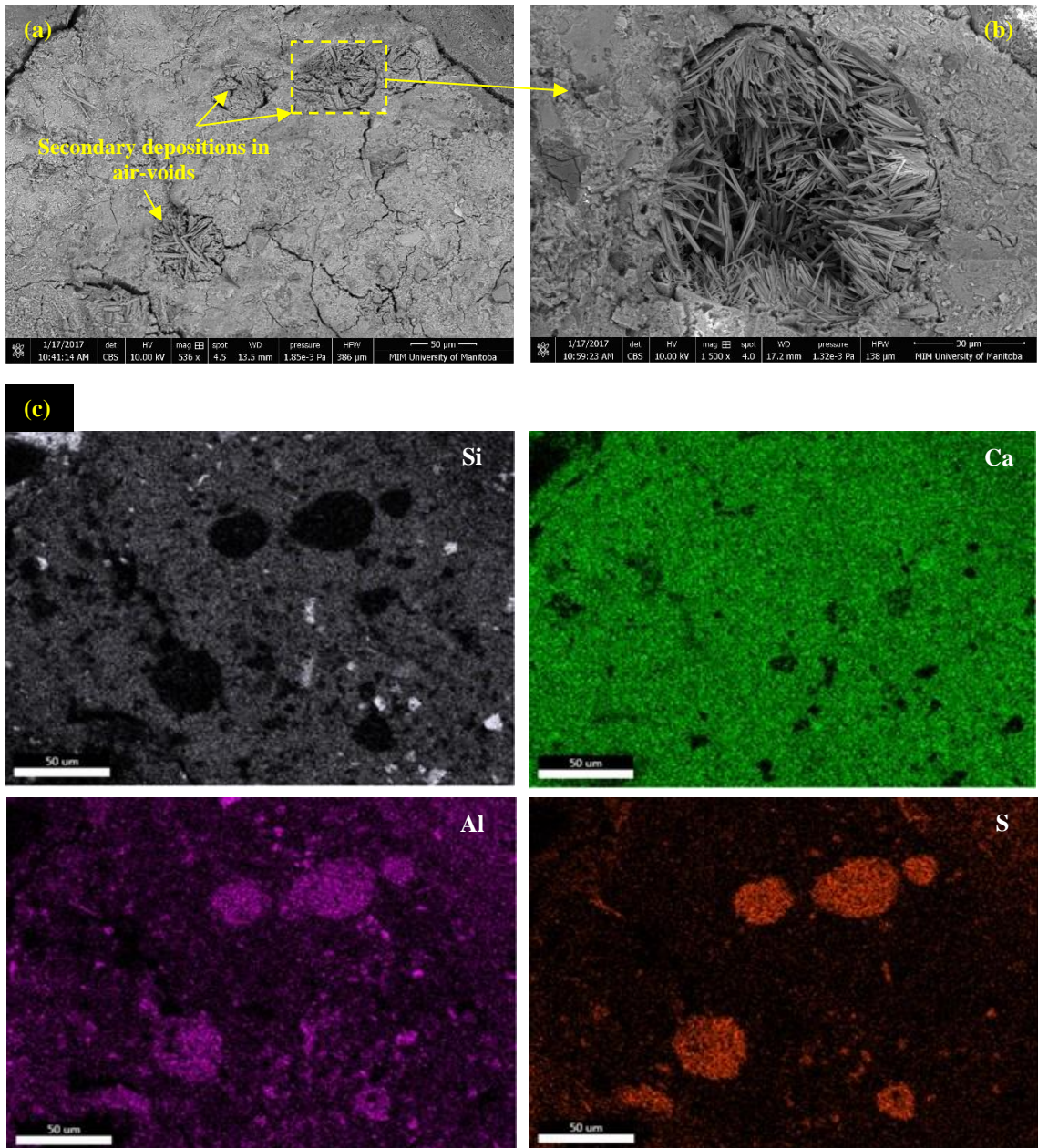
Figure 3.10: Example of microanalysis for a specimen from regional roads showing: (a) high intensity of micro-cracks, (b) secondary depositions filling air-voids, and (c) elemental spatial distribution for the field of view in (a).

CHAPTER 4 – PHASE II: RESPONSE OF CONCRETE TO CONTINUAL IMMERSION AT 5°C AND W/D EXPOSURES WITH CHLORIDE-BASED SALTS

In Chapter 3 (Phase I: assessment of joints in concrete pavements), it has been shown that de-icing salts either trigger or accelerate distress of concrete pavements, especially at joints. Hence, the present chapter investigates the damage mechanisms of concrete exposed to different de-icing salts when combined with two environmental conditions: constant low temperature and wetting/drying (W/D) cycles.

4.1 Introduction

Historically, the damage of concrete due to the presence of de-icing salts was linked to physical mechanisms such as frost damage, scaling, and salt crystallization (Valenza et al. 2006; Scherer et al. 1999; Jacobsen et al. 1997). While these physical mechanisms have been widely investigated, the chemical interactions between de-icing salts and hydrated cement paste in concrete have been studied less frequently, especially with direct microscopy techniques. At high concentrations, chloride (Cl^-) ions and cations (e.g. Na^+, Mg^{2+}, and Ca^{2+}) in de-icing salts can enter into chemical reactions with cement-based materials forming complex salts. Formation of calcium oxychloride (xCa(OH)$_2 \cdot y$CaCl$_2 \cdot z$H$_2$O (COX), where $x{:}y{:}z$ can be 3-4:1:8-15, depending on Ca(OH)$_2$/CaCl$_2$ molar ratio, surrounding temperature and relative humidity (RH), and pH of the pore solution (Galan et al. 2015; Peterson et al. 2013; Monosi et al. 1990)) and magnesium oxychloride (mMg(OH)$_2 \cdot n$MgCl$_2 \cdot 8$H$_2$O, where the ratio of $m{:}n$ is 3:1 or 5:1, termed as 3- or 5-form MOX, respectively) were suspected for causing chemical degradation of hardened concrete exposed to concentrated deicer solutions (>3 mol/l)

(Suraneni et al. 2016; Farnam et al. 2015a and 2015b; Peterson et al. 2013; Shi 2011; Julio-Betancourt et al. 2009; Sutter et al. 2006; Monosi et al. 1990).

The formation of COX/MOX has mostly been studied in synthetic hydrated materials using inferred trends from longitudinal guarded comparative calorimetry (Farnam et al. 2015a and 2015b), low-temperature differential scanning calorimetry (Suraneni et al. 2017; Monical et al. 2016), thermogravimetric analysis (Suraneni et al. 2016), and volume change measurements (Qiao et al. 2017). However, the explicit occurrence and exact nature and morphology of these phases were not unequivocally established in deteriorating concrete systems due to their instability when subjected to conditions (e.g., sawing, polishing, washing, filtering, coating) normally applied for sample preparation before direct microstructural tests (Galan et al. 2015; Peterson et al. 2013). Drying and elevated temperatures lead to losing some of or all their combined water resulting in changes in their crystal structure (Galan et al. 2015; Shi 2011; Julio-Betancourt et al. 2009). The sensitivity of these phases to vacuum drying in the scanning electron microscope makes it difficult to observe their unaltered morphology (Galan et al. 2015). Also, the instability of these phases might be the reason that fewer studies could successfully correlate the physico-mechanical damage of concrete to the formation of these complex salts (Galan et al. 2015; Peterson et al. 2013).

On the other hand, the impact of environmental conditions such as wetting/drying (W/D) cycles on the formation/stability of COX/MOX in cementitious matrices is not adequately documented so far. Galan et al. (2015) reported conversion of synthetic COX (3:1:12) to anhydrous salt $Ca(OH)_2 \cdot CaCl_2$ or $CaClOH$ by drying and wetting, respectively and this conversion was reversible (Galan et al. 2015). However, the effect of this conversion between hydrous and anhydrous oxychloride phases on the damage

66

manifestations of concrete remains unknown. Most of the reported investigations did not show the formation of such phases in field concrete exposed to highly concentrated chloride solutions (e.g. 25% salt by mass) (Ranjaraju 2002). Actually, in many of the cores taken from aged and damaged concrete pavements exposed to high concentration de-icing salts, conspicuous ettringite formation was found in-filling the majority of voids as well as interfacial transition zones in hydrated cement paste (Ranjaraju 2002; Stark et al. 1999); however, the mechanism by which chlorides influence ettringite formation and its role in the damage process is still uncertain.

Many approaches focused on improving the durability properties of concrete exposed to de-icing salts by: (i) using topical treatments (sealers) to provide a physical barrier between salt and concrete, (ii) carbonation of the concrete to form a barrier of calcite, and (iii) improving the performance of such concrete by replacing part of the cement with a pozzolan such as fly ash. The pozzolanic reaction refines the pore structure of the cementitious matrix, which reduces its permeability and ionic diffusivity. Furthermore, portlandite consumption in this reaction helps alleviating the chemical attack by chloride ions. Despite the benefits of fly ash concrete, the use of fly ash as a cement replacement in concrete pavements in North America is optional and typically limited by departments of transportation to dosages less than 15-20% (Standard Construction Specifications - Manitoba 2014; Ontario provincial standard specification 2014; Standard Specifications for Construction of Roads and Bridges on Federal Highway Projects 2014). The delay in setting time, strength gain, and microstructural development at early ages of fly ash concrete as well as vulnerability to surface scaling are considered to be the major technical issues, which deter its wider acceptance (Mehta et al. 2014; Malhotra et al. 2000). Nevertheless, these performance limitations associated with the use of slowly reactive

supplementary cementitious materials (SCMs) (e.g. Class F fly ash) can be mitigated by incorporation of nanoparticles (size scale of 1-100 billionth of a meter) in this concrete (Ghazy et al. 2016; Kong et al. 2015; Madani et al. 2012; Said et al. 2012). Nanoparticles (e.g. nanosilica) have been applied in the production of concrete and proven to enhance fresh and hardened properties by modifying the structure of the cementitious matrix at the nano and micro levels. Therefore, their application in concrete may have a great potential to produce innovative types of fly ash concrete with superior performance for concrete pavements exposed to high concentrations of de-icing salts. Yet, this needs to be experimentally verified.

4.2 Research Significance

Given the aforementioned research needs in this area, the objective of this study was to directly investigate the formation/stability of oxychloride phases in concrete under different exposure conditions when combined with chloride-based de-icing salts. Conditioned mode (controlled temperature and relative humidity) environmental scanning electron microscopy (ESEM) was specifically used to minimize changes in the crystal structure of these reaction products to explicitly capture their unaltered morphology and existence in deteriorating concrete. In addition to normal/reference concrete (ordinary and PLC), concretes incorporating nanosilica without and with different dosages of fly ash were tested in order to substantiate the potential benefits of SCMs, if any, in mitigating this type of damage.

4.3 Experimental Program

4.3.1   Materials and Mixtures

General use (GU) portland cement, portland limestone cement (PLC), and fly ash (Class F), which meet the requirements of the CAN/CSA-A3001 standard, were used as

the main components of the binder. Their chemical and physical properties are shown in

Table 4.1. In addition, a commercial nanosilica sol (50% solid content of SiO_2 dispersed in

an aqueous solution, Table 4.1) was incorporated in some binders. The target consistency

of fresh concrete was achieved by high-range water reducing admixture (HRWRA) based

on polycarboxylic acid and complying with ASTM C494, Type F. This HRWRA was

added at variable dosages (0 to 475 ml per 100 kg of the binder) to the mixtures in order to

maintain a slump range of 50 to 100 mm. In addition, an air-entraining admixture was used

to obtain a fresh air content of 6±1%. The coarse aggregate used were mostly natural gravel

(max. size of 9.5 mm) with a small proportion of carboniferous aggregate; its specific

gravity and absorption were 2.65 and 2%, respectively. The fine aggregate was well-graded

river sand with a specific gravity, absorption, and fineness modulus of 2.53, 1.5% and 2.9,

respectively.

Table 4.1: Chemical composition and physical properties of cement and SCMs

	GU	PLC	Fly Ash	Nanosilica
Chemical Composition				
SiO_2 %	19.21	18.92	55.20	99.17
Al_2O_3 %	5.01	4.41	23.13	0.38
Fe_2O_3 %	2.33	3.22	3.62	0.02
CaO %	63.22	63.42	10.81	--
MgO %	3.31	0.70	1.11	0.21
SO_3 %	3.01	2.71	0.22	--
Na_2O_{eq} %	0.12	0.31	3.21	0.20
Physical Properties				
Specific Gravity	3.15	3.11	2.12	1.40
Mean Particle Size, μm	13.15	11.81	16.56	35×10^{-3}
Fineness, m^2/kg	390[*]	460[*]	290 (1.41×10^3)[*]	80000[**]
Viscosity, Cp	--	--	--	8
pH	--	--	--	9.5

[*] Blain fineness.
[**] Fineness was determined by titration with sodium hydroxide according to the procedure described by Sears (1956).

Six concrete mixtures were tested in each group (GU and PLC); the total binder

(GU or PLC cement, fly ash and nanosilica) content in all mixtures and the water-to-binder

ratio (*w/b*) were kept constant at 400 kg/m^3 and 0.4, respectively. Single binder (control) mixtures were prepared from 100% GU cement, representing typical concrete pavements in North America, or PLC. Fly ash was used to prepare blended binders with GU and PLC cements without or with nanosilica, at dosages of 20% and 30% by the total binder content (80 and 120 kg/m^3, respectively). The nanosilica was added at a single dosage of 6% by the total binder content (solid content of 24 kg/m^3), as a replacement of the cement component in the binder, to prepare binary (comprising GU or PLC and nanosilica) and ternary binders (comprising GU or PLC cements, fly ash and nanosilica). This dosage of nanosilica sol was found to advantageously affect the fresh and hardened properties of cementitious materials (Ghazy et al. 2016; Said et al. 2012). Table 4.2 shows the mixture design proportions of the concrete tested in this study.

Table 4.2: Proportions of mixtures per cubic meter of concrete

Mixture ID.	Cement (kg/m^3)	Fly Ash (kg/m^3)	Nanosilica (kg/m^3)	Water[a] (kg/m^3)	Coarse Aggregate (kg/m^3)	Fine Aggregate (kg/m^3)	28 day Compressive Strength (MPa)
GU group							
GU	400	--	--	160	1096	590	40 (0.3)[b]
GUF20	320	80	--	160	1077	580	38 (0.7)
GUF30	280	120	--	160	1068	575	35 (1.1)
GUS	376	--	48	136	1091	587	43 (0.2)
GUF20S	296	80	48	136	1072	577	44 (0.7)
GUF30S	256	120	48	136	1063	573	46 (0.5)
PLC group							
PLC	400	--	--	160	1096	590	46 (0.4)
PLCF20	320	80	--	160	1077	580	43 (1.2)
PLCF30	280	120	--	160	1068	575	40 (0.8)
PLCS	376	--	48	136	1091	587	43 (0.3)
PLCF20S	296	80	48	136	1072	577	46 (1.0)
PLCF30S	256	120	48	136	1063	573	47 (0.3)

[a] Adjusted amount of water considering the water content of nanosilica (aqueous solution with 50% solid content of SiO_2)
[b] The values between brackets in the last column are the standard errors

Constituent materials were mixed in a mechanical mixer and cast in prismatic molds (50×50×285 mm) to prepare triplicates for each mixture. Also, eight replicate cylinders (100×200 mm) were prepared in order to evaluate the compressive strength (Table 4.2) according to ASTM C39, and the penetrability of chloride ions into concrete mixtures. The specimens were demoulded after 24 h and then cured for 28 days at standard conditions (22±2°C and 98% RH) according to ASTM C192. Recent studies have shown that the addition of nanosilica in concrete, even in mixtures containing 30% fly ash, accelerates the rate of hydration and microstructural development to a level comparable to concrete prepared from single binders containing 100% ordinary cement (Ghazy et al. 2016; Kong et al. 2015; Said et al. 2012). Hence, the curing period was kept constant to provide a uniform basis of comparison among all mixtures.

4.3.2   Exposures

To evaluate the durability of the tested mixtures to chloride-based de-icing salts, two exposure regimes were adopted:

- Exposure I is a continuous immersion exposure in which prismatic specimens were fully immersed in high concentration solutions of various de-icing salts at 5°C up to 540 days. Sodium chloride (NaCl), dihydrate form of calcium chloride ($CaCl_2 \cdot 2H_2O$) and hexahydrate form of magnesium chloride ($MgCl_2 \cdot 6H_2O$) with purity of 99, 96 and 96%, respectively were used to prepare the solutions. In addition, combined salts ($MgCl_2 \cdot 6H_2O$ and $CaCl_2 \cdot 2H_2O$) were applied to simulate anti-icing and de-icing strategies. Table 4.3 shows the concentrations of the de-icing solutions used in the present study. These types and concentrations of de-icing salts are comparable to that applied by different transportation agencies in North America (e.g. Snow and Ice Control – Ministry of Transportation – Ontario 2016; Policy on snow clearing and ice

control – City of Winnipeg 2011; Minnesota Snow and Ice Control 2012) based on factors such as the availability of the de-icing salt and effective freezing temperature in each region. Also, for better comparison between the de-icers used, an equal number of chloride ions (~160,000 ppm) among the four solutions were used. The solutions were renewed every four weeks to keep a continual supply of de-icing salts, thus providing aggravated damage conditions.

- Exposure II is a W/D exposure in which prismatic concrete specimens were subjected to wetting in salt solutions similar to the ones used in exposure I followed by drying. A W/D cycle (five days) consisted of full immersion of specimens for two days in the de-icing salt solutions at a temperature of 5°C, followed by drying at 23±2°C and 55±5% RH for two days and an additional day at 40±2°C and 30±5% RH in an environmental chamber. This cyclic exposure might mimic the consecutive built up of Cl^- ions within concrete surface from winter and wet spring conditions followed by drying periods during summer. This exposure also continued for 540 days (108 cycles).

Table 4.3: Concentration of de-icing solutions

Type of Salt	Salt Concentration Mass (%)	Chloride Concentration (mol/l)	Chloride Concentration[*] (ppm)
Sodium Chloride (NaCl)	23.3	4.52	160,071
Calcium Chloride (CaCl₂)	21.9	4.51	160,067
Magnesium Chloride (MgCl₂)	19.1	4.52	160,069
Combined Salt (MgCl₂+CaCl₂)	10.9 + 9.6	4.52	160,073

[*] The ionic concentration of Cl^- ions in each solution was verified by ion chromatography (ASTM D 4327).

4.3.3   Tests

In order to evaluate the penetrability (physical resistance) of the concrete specimens, the rapid chloride permeability test (RCPT) was performed according to ASTM C1202 on four specimens from each mixture. To alleviate the effects of electrolysis bias and temperatures on the trends, the penetration depth of chloride ions/front into concrete,

which better correlates to the physical characteristics of the pore structure, was determined. Following the RCPT, the discs were axially split and sprayed with 0.1 M silver nitrate solution which forms a white precipitate of silver chloride, to measure the average physical penetration depth of chloride ions. To complement the trends of the RCPT test, mercury intrusion porosimetry (MIP) was conducted on small pea-sized (4-7 mm) chunks (about 6-8) taken from at least two (sound/untested) concrete cylinders of each mixture at 28 days. These chunks were carefully selected so that large aggregates were not included. Preconditioning of samples was done by oven drying at 45±2°C until a constant mass is reached to reduce the potential of drying shrinkage cracks associated with higher temperatures. The apparatus had a pressure range from sub-ambient to 228 MPa. By assuming a cylindrical geometry of pores, a mercury contact angle of 130° and surface tension of 485 dynes/cm, the high-pressure limit (228 MPa) yields a pore radius of about 3 nm, implying intrusion of all capillary pores.

Before exposure, the initial physico-mechanical properties of the intact specimens were measured. For all specimens, the initial mass, length (ASTM C 157) and dynamic modulus of elasticity, E_d (ASTM C 215) were recorded. Specimens were removed from the solutions at specified time intervals (every 4 weeks), and the free expansion of prisms was immediately measured. Subsequently, debris, if any, were removed by a nylon brush, and the specimens were left to dry under 23±2°C and 50% RH for 30 min before visual inspection and measurement of mass and fundamental transverse frequency. Relative to the initial values, the changes in mass, length and dynamic modulus of elasticity (RE_d) versus time of exposure were calculated. The alteration of microstructure in deteriorating specimens was assessed by microscopy, thermal and mineralogical analyses. To minimize changes in the crystal structures of complex phases, conditioned-mode ESEM was

performed without prior specimen preparation (e.g. drying, coating) to capture unstable phases due to temperature changes, if any. For this test, fracture pieces were taken from the specimens and immediately placed inside an isothermal container to avoid the change in temperature of the samples. The samples were then put in the ESEM chamber conditioned at temperature and RH similar to that of the exposures. In addition, the mineral phases within the cementitious matrix were analyzed by X-ray diffraction (XRD, Cu-Kα) with a scanning rate of 0.5°/min, and differential scanning calorimetry (DSC) with an incremental heating rate of 10°C/min on powder samples collected from the surface of exposed and unexposed specimens. These specimens were first kept in a desiccator containing calcium sulfate for 5 days at 5±2°C. Subsequently, the powder was prepared from carefully selected fracture pieces (not including large coarse aggregate) of specimens, which were pulverized to a fine powder passing through sieve #200 (75 μm).

4.4 Results

4.4.1   Visual Assessment and Mass Change

Visual examination was regularly made to assess the conditions of the specimens (e.g. Figs. 4.1 and 4.2). Also, the mass change of specimens with time was determined and summarized in Table 4.4 and Table 4.5. The overall trends from the continuous immersion and W/D exposures indicate that the aggression of solutions, in an ascending order, is NaCl, $MgCl_2$, $CaCl_2$ and combined ($MgCl_2+CaCl_2$) salts. Up to 540 days of exposure, specimens from all mixtures subjected to continuous immersion in the NaCl solution experienced a steady mass gain (maximum of 2%) with time, without any distinctive visual features of damage (Figs. 4.1a and 4.2a).

Comparatively, the reference specimens (GU) and specimens made with binary binders containing 20% fly ash (GUF20) exposed to $MgCl_2$ solution developed blisters at

the surface, and the skin of the specimens started to peel off at approximately 90 and 180 days. With time, the deterioration was advancing with visible gel-like compound on/below the surface of the specimens accompanied by high intensity of cracks. Eventually, these specimens (GU and GUF20) were softened, disintegrated, and showed notable swelling (e.g. Fig. 4.1b and 4.2b) with a mass loss of 21% and 14%, respectively; thus, the physico-mechanical measurements were discontinued for these specimens at 150 and 330 days, respectively.

Among the individual de-icing solutions used, the $CaCl_2$ solution was the most aggressive as the rate of deterioration of specimens was very rapid. Micro-cracks along the edges of GU, GUF20 and GUF30 specimens and clear separation of the surface layer from the rest of the specimen were the main features of damage at early stages of exposure (e.g. Fig. 4.1c and 4.2c). Additional cracks parallel to the edge of prisms progressively appeared and the deterioration of these specimens proceeded until complete disintegration at 60, 180 and 360 days, respectively, due to macro-cracks with high magnitude of mass loss (Table 4.4).

The predominant features of damage of specimens under the combined salts ($MgCl_2+CaCl_2$) were similar to that in the $MgCl_2$, as shown in Figs. 4.1d and 4.2d, but the rate of damage under such conditions was significantly aggravated. Also, the specimens made with binary binders containing 30% fly ash (GUF30) failed in this solution at 300 days. Irrespective of the type of binder (binary or ternary), all the specimens comprising nanosilica and fully immersed in different salt solutions showed no visible features of damage up to the end of this exposure (Appendix A, Fig. A.1 and A.2). Generally, similar features of damage were observed for the PLC specimens in both exposures, irrespective

of the type of the solutions, except that these specimens survived longer (Table 4.5) than

the GU specimens
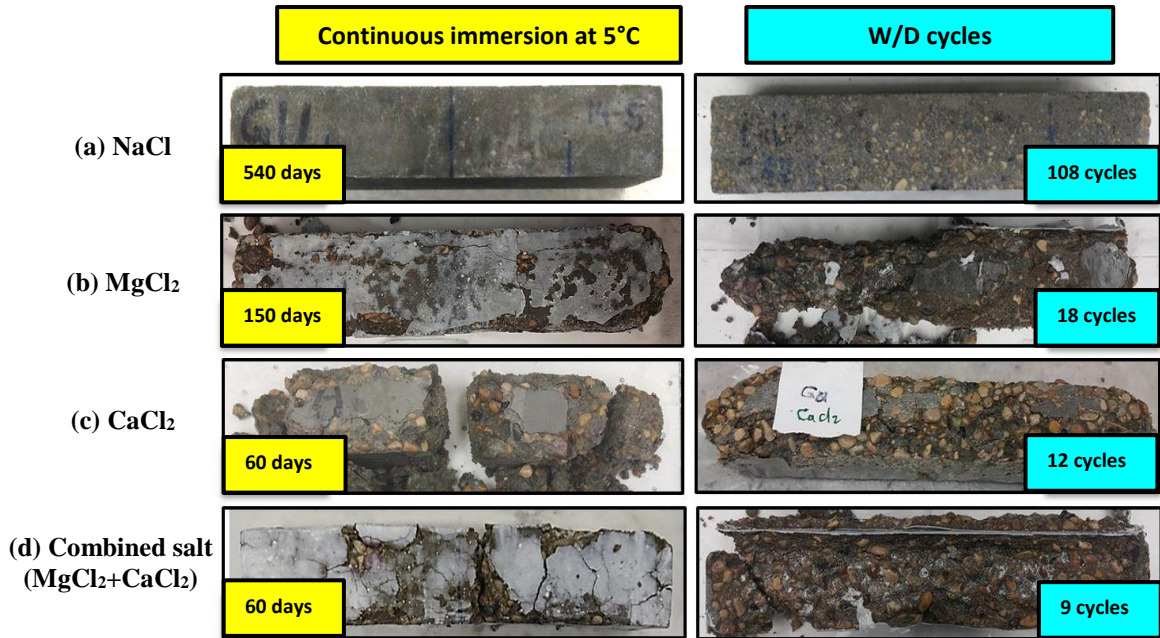
Figure 4.1: Exemplar visual features of damage for the reference specimens (GU)
exposed to different de-icing salts.
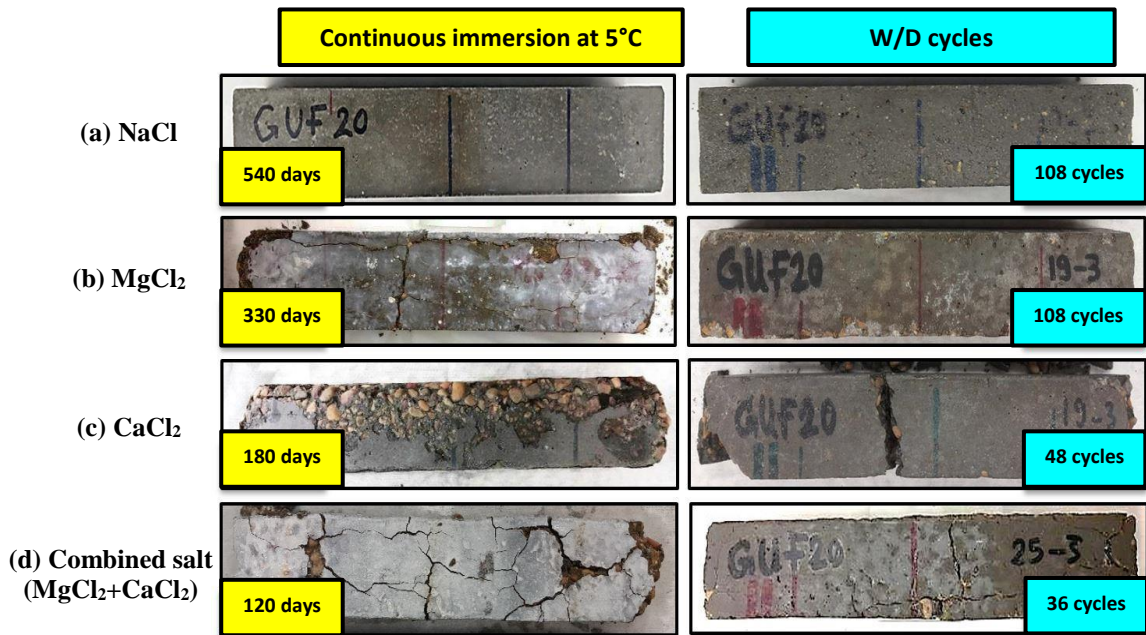
Figure 4.2: Exemplar visual features of damage for the specimens made with the binary
binder containing 20% fly ash (GUF20) exposed to different de-icing salts.

In comparison to the continuous immersion exposure, surface scaling was notable for the GU specimens under the W/D exposure during the early stages (Fig. 4.1), which was often accompanied by spalling along the edges and/or at the corners. This led to sequential destruction of the surface until eventual disintegration of specimens. Therefore, the W/D cycles had an accelerating effect on the deterioration of these specimens. For example, the GU specimens immersed in the NaCl solution showed minor scaling (mass loss of 4%) after 108 W/D cycles (540 days). Also, the GU specimens exposed to $MgCl_2$ solution suffered significant scaling after 9 cycles with mass loss of 10%. Subsequently, the cross sections of these specimens were considerably reduced until complete disintegration at 90 days (Fig. 4.1b) with a mass loss of 29%. Similar features of damage were observed for the GU specimens exposed to the $CaCl_2$ and combined salt solution (Fig. 4.1c and 4.1d). Unlike the continuous immersion exposure, specimens made with binary binders containing 20% fly ash (GUF20) exposed to the $MgCl_2$ did not fail under the W/D exposure (Fig. 4.2b). The GUF20 specimens exposed to the $CaCl_2$ and combined salts solutions with W/D conditions had abruptly failed by transverse cracks (e.g. Fig. 4.2c and 4.2d) at 240 and 180 days, respectively, without excessive mass loss (4% and 3%, respectively). However, specimens from the binary binder with 30% fly ash (GUF30) did not fail under such an exposure. Again, all specimens made with binary or ternary binders comprising nanosilica showed no visible features of damage throughout the entire W/D exposure.

Table 4.4: Results of mass change, expansion, and time of last measurement for GU specimens after the continuous immersion at 5°C and W/D exposures.

Mixture ID.	NaCl			MgCl$_2$			CaCl$_2$			Combined salt (MgCl$_2$+CaCl$_2$)		
	Mass change (%)	Expansion (%)	Time* (days)	Mass change (%)	Expansion (%)	Time* (days)	Mass change (%)	Expansion (%)	Time* (days)	Mass change (%)	Expansion (%)	Time* (days)
Exposure I: Continuous immersion at 5°C												
GU	0.0	0.02	540	- 20.6	1.56	150[†]	- 30.6	2.80	60[†]	- 26.4	2.93	60[†]
GUF20	0.0	0.021	540	- 14.0	0.64	330[†]	- 25.5	1.07	180[†]	- 11.3	1.03	120[†]
GUF30	0.0	0.03	540	1.0	0.05	540	- 17.8	0.70	360[†]	- 4.6	0.71	300[†]
GUS	0.1	0.01	540	1.1	0.02	540	0.1	0.03	540	0.8	0.03	540
GUF20S	0.3	0.01	540	1.4	0.02	540	1.0	0.02	540	0.9	0.02	540
GUF30S	0.4	0.02	540	1.1	0.02	540	0.9	0.02	540	1.0	0.03	540
Exposure II: W/D cycles												
GU	- 3.6	0.02	540	- 29.4	0.118	90[†]	- 27.3	0.102	60[†]	- 27.9	0.131	45[†]
GUF20	- 1.9	0.02	540	- 1.2	0.042	540	- 4.1	0.532	240[†]	- 3.0	0.449	180[†]
GUF30	- 2.9	0.02	540	0.7	0.031	540	0.9	0.040	540	1.0	0.042	540
GUS	0.3	0.02	540	0.9	0.023	540	1.0	0.023	540	0.8	0.012	540
GUF20S	0.2	0.03	540	0.7	0.023	540	0.2	0.031	540	0.7	0.023	540
GUF30S	0.0	0.01	540	0.9	0.023	540	0.5	0.037	540	0.9	0.024	540

*Refers to the time of the last measurement.
[†]Specimens failed after this stage.

Table 4.5: Results of mass change, expansion, and time of last measurement for PLC specimens after the continuous immersion at 5°C and W/D exposures.

Mixture ID.	NaCl				MgCl$_2$				CaCl$_2$				Combined salt (MgCl$_2$+CaCl$_2$)			
	Mass change (%)	Expansion (%)	RE_d	Time^a (days)	Mass change (%)	Expansion (%)	RE_d	Time^a (days)	Mass change (%)	Expansion (%)	RE_d	Time^a (days)	Mass change (%)	Expansion (%)	RE_d	Time^a (days)
Exposure I: Continuous immersion at 5°C																
PLC	0.0	0.02	102	540	-17.3	1.21	0	210[†]	-22.4	2.44	0	90[†]	-21.9	2.21	0	75[†]
PLCF20	0.0	0.02	101	540	-13.1	0.53	0	490[†]	-21.3	1.04	0	265[†]	-11.4	0.89	0	190[†]
PLCF30	0.0	0.03	100	540	0.0	0.03	100	540	0.0	0.62	0	495[†]	-5.3	0.53	0	395[†]
PLCS	0.0	0.01	101	540	0.0	0.02	101	540	0.0	0.02	103	540	0.0	0.03	100	540
PLCF20S	0.0	0.02	102	540	0.0	0.02	103	540	0.0	0.03	102	540	0.0	0.01	100	540
PLCF30S	0.0	0.01	103	540	0.0	0.01	102	540	0.0	0.01	102	540	0.0	0.02	103	540
Exposure II: W/D cycles																
PLC	-2.7	0.01	101	540	-23.7	0.16	0	135[†]	-26.3	2.23	0	75[†]	-11.2	2.71	0	60[†]
PLCF20	-2.3	0.02	103	540	-3.4	0.05	0	540	-4.7	1.96	0	360[†]	-3.9	2.57	0	285[†]
PLCF30	0.0	0.01	101	540	0.0	0.03	100	540	0.0	0.02	101	540	0.0	0.03	101	540
PLCS	0.0	0.03	102	540	0.0	0.02	102	540	0.0	0.01	100	540	0.0	0.03	101	540
PLCF20S	0.0	0.01	103	540	0.0	0.02	102	540	0.0	0.03	101	540	0.0	0.01	100	540
PLCF30S	0.0	0.02	101	540	0.0	0.01	103	540	0.0	0.01	103	540	0.0	0.02	102	540

[*]Refers to the time of the last measurement.
[†]Specimens failed after this stage.

4.4.2   Expansion

Table 4.4 shows the total expansion of specimens subjected to the continuous immersion and W/D exposures. The expansion was low (maximum of 0.03%) for all specimens immersed in the NaCl solution compared to other solutions under both exposures. In contrast, the GU specimens immersed in the $MgCl_2$, $CaCl_2$ and combined salts showed high expansion (1.56%, 2.80%, and 2.93%, respectively) before failure (Table 4). Incorporating fly ash in the binder notably decreased the magnitude of the expansion irrespective of the type of solution. For example, the binary binders containing 20% fly ash (GUF20) immersed in the $MgCl_2$, $CaCl_2$ and combined salts solutions yielded an expansion of 0.64%, 1.01% and 1.03% (reduction of 59%, 63% and 64%, respectively) after 330, 180, and 120 days (Table 4.4). Also, the effect of fly ash was more pronounced in the GUF30 specimens. No single mixture made with binary or ternary binders comprising nanosilica exceeded an expansion value of 0.04% throughout the entire exposure (540 days), as shown in Table 4.4.

Despite the aggravated effect of the W/D exposure on the damage of GU specimens, the expansion values of these specimens under this exposure were lower. For example, the GU specimens immersed in the $MgCl_2$, $CaCl_2$, and combined salts solutions had an expansion of 0.12%, 0.10% and 0.13% (reduction of 92%, 96% and 95%, respectively) before failure (90, 60, and 45 days, respectively) compared to the corresponding specimens in the continuous immersion exposure. This may be ascribed to the nature of the damage processes under these two exposures as discussed in the Mechanisms of Damage section. Unlike the continuous immersion exposure, specimens made with binary binders containing 20% fly ash (GUF20) exposed to the $MgCl_2$ did not show any evidence of expansion (maximum of 0.04%). Also, the magnitude of expansion was consistently lower

(an average of 53%) for the GUF20 specimens immersed in the $CaCl_2$ and combined salts solutions under such conditions compared to the corresponding specimens in the continuous immersion exposure. Likewise, specimens from the binary binder with 30% fly ash (GUF30) did not show any evidence of expansion (maximum of 0.04%) under all solutions. Again, the expansion values of all specimens comprising nanosilica did not exceed 0.03% throughout the entire exposure (540 days), as shown in Table 4.4. The expansion trends of the PLC specimens were mirrored in both exposures, but they were slightly lower compared to the GU counterparts as shown in Table 4.5.

4.4.3   Relative Dynamic Modulus of Elasticity (RE_d)

The change in RE_d with time (Fig. 4.3) should capture the internal damage of concrete specimens exposed to chemical and/or physical degradation. No single specimen immersed in the NaCl solution had reduction of RE_d, up to the end of this exposure (Fig. 4.3a). In contrast, a decreasing trend was observed with time for the GU and GUF20 specimens continuously immersed in the $MgCl_2$ solution until complete disintegration or failure, which was expressed by zero RE_d (Fig. 4.3b). Similar to the trends of mass loss and expansion, the GU, GUF20 and GUF30 specimens continuously immersed in the $CaCl_2$ solution had a marked drop (more than 30%) in RE_d after 45, 150, and 330 days followed by complete disintegration (Fig. 4.3c). A similar trend was observed for these specimens immersed in the combined salts solution but at faster rates (Fig. 4.3d). Again, the type of binder had a pronounced effect on the RE_d results. Increasing the dosage of fly ash in the binary binder generally performed better and/or survived longer than the reference specimens under continuous immersion in all salt solutions. Also, incorporation of nanosilica in the binders (binary or ternary) led to a consistently high RE_d at or slightly above 100% (Fig. 4.3) up to 540 days.
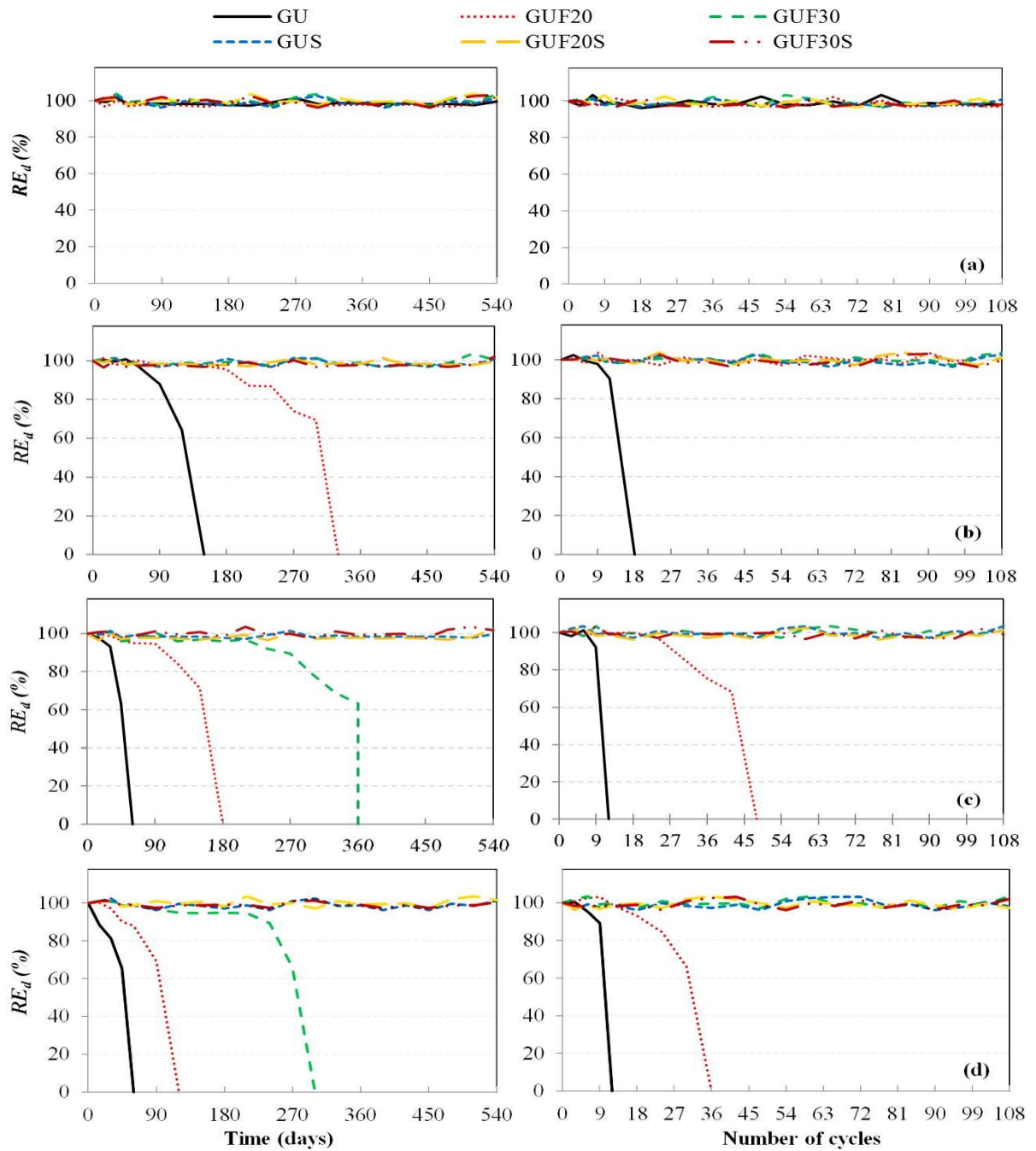
Figure 4.3: Relative dynamic modulus of elasticity vs. time of exposure for all specimens exposed to continuous immersion at 5°C (left), and W/D cycles (right): (a) NaCl, (b) MgCl$_2$, (c) CaCl$_2$, and (d) combined salt (MgCl$_2$+CaCl$_2$).

Despite that the reference specimens (GU) exposed to the W/D cycles in the NaCl had minor scaling (4%, Table 4.4), these specimens did not show any reduction in RE_d. Also, similar to the trends observed in expansion, the RE_d results of the GU specimens exposed to the W/D cycles in MgCl$_2$, CaCl$_2$, and combined salt solutions did not show

82

notable reduction (maximum of 10%) of RE_d before complete failure (crumbling). However, these specimens had significant mass losses (Table 4.4), which can be attributed to the nature of damage of the GU binder. Conversely, the drop-in RE_d was significant (more than 30%) for the specimens made with the binary binder containing 20% fly ash exposed to the W/D cycles in the $CaCl_2$ and combined salt solutions conforming to the expansion trends. Comparatively, the specimens comprising 30% fly ash and/or nanosilica maintained a high RE_d at or slightly above 100% over the entire time of the W/D exposure in all de-icing salt solutions (Fig. 4.3). Similar trends were observed for the PLC specimens in both exposures; however, the drop in RE_d was less (Table 4.5).

4.5 Discussion

4.5.1 Mechanisms of Damage

4.5.1.1 Continuous immersion at 5°C

In this exposure, the trends of physico-mechanical results of deteriorated specimens were comparable within each salt solution, which suggests that the mechanisms of damage were similar. Thus, in this section, the reference specimens (GU) are presented in order to demonstrate these mechanisms for each salt solution. Subsequently, the effect of fly ash and nanosilica on the mechanisms of damage will be discussed. Also, the potential benefits of PLC in mitigating this type of damage will be highlighted in Chapter 5 and 6.

NaCl salt seems to be benign in terms of chemical attack as no signs of deterioration were observed for all specimens immersed in this solution up to 540 days. This trend is generally consistent with previous studies (Peterson et al. 2013; Wang et al. 2006a), which reported negligible damage of concrete exposed to high concentrations (18 to 23%) of NaCl. Compared to the corresponding specimens immersed in deionized water at 5°C, the XRD patterns generally showed similar dominant phases of portlandite, calcite, quartz and

dolomite, except that Friedel's salt and ettringite peaks were observed in the specimens immersed in the NaCl solution (Fig. 4.4). Friedel's salt crystals with different morphologies and variable sizes as well as ettringite were infilling voids near (within 10 mm) the exposed surface of specimens (e.g. Fig. 4.5). The formation of Friedel's salt was likely a result of the substitution of sulfate (SO_4^{2-}) ions by Cl^- ions decomposing monosulphate, or reaction of the solution with other aluminate bearing phases, as for example summarized by Eq. (4.1). With time, the releasable SO_4^{2-} ions combine with the remaining monosulphate and a part of Friedel's salt already formed, precipitating ettringite (Eqs. 4.2 and 4.3), as substantiated by higher intensity of ettringite peaks in Fig. 4.4 compared to the corresponding specimens immersed in the deionized water at 5°C. Binding Cl^- ions by aluminate phases to form chloroaluminate phases such as Friedel's salt or Kuzel's salt ($3CaO.Al_2O_3.0.5CaSO_4.0.5CaCl_2.11H_2O$, at low chloride concentrations (< 10 mmol/l)) may not be detrimental to the integrity of the hydrated cement paste as no marked symptoms of expansion, cracking, spalling and softening were observed for the specimens. This may be attributed to the stability of these phases at high pH (~13) due to the formation of NaOH (Eq. 4.1) (Birnin-Yauri et al. 1998).

$$2NaCl + Ca(OH)_2 + 3CaO.Al_2O_3.CaSO_4.12H_2O \rightarrow$$
$$3CaO.Al_2O_3.CaCl_2.10H_2O + Ca^{2+} + SO_4^{2-} + 2NaOH + 2H_2O \quad \text{Eq. (4.1)}$$

$$3Ca^{2+} + 3SO_4^{2-} + 3CaO.Al_2O_3.CaSO_4.12H_2O + 20H_2O \rightarrow$$
$$3CaO.Al_2O_3.3CaSO_4.32H_2O \quad \text{Eq. (4.2)}$$

$$2Ca^{2+} + 3SO_4^{2-} + 3CaO.Al_2O_3.CaCl_2.10H_2O + 22H_2O \rightarrow$$
$$3CaO.Al_2O_3.3CaSO_4.32H_2O + 2Cl^- \quad \text{Eq. (4.3)}$$
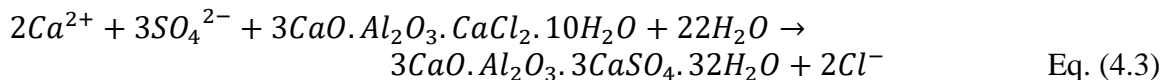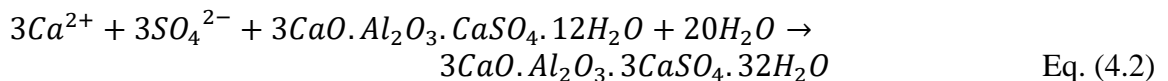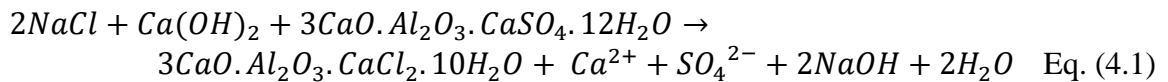
E = Ettringite
P = Portlandite
FS = Friedel's salt

COX = Calcium oxychloride
3-MOX = Magnesium oxychloride (3-form)
5-MOX = Magnesium oxychloride (5-form)
G = Gypsum

B = Brucite
D = Dolomite
C = Calcite
Q = Quartz
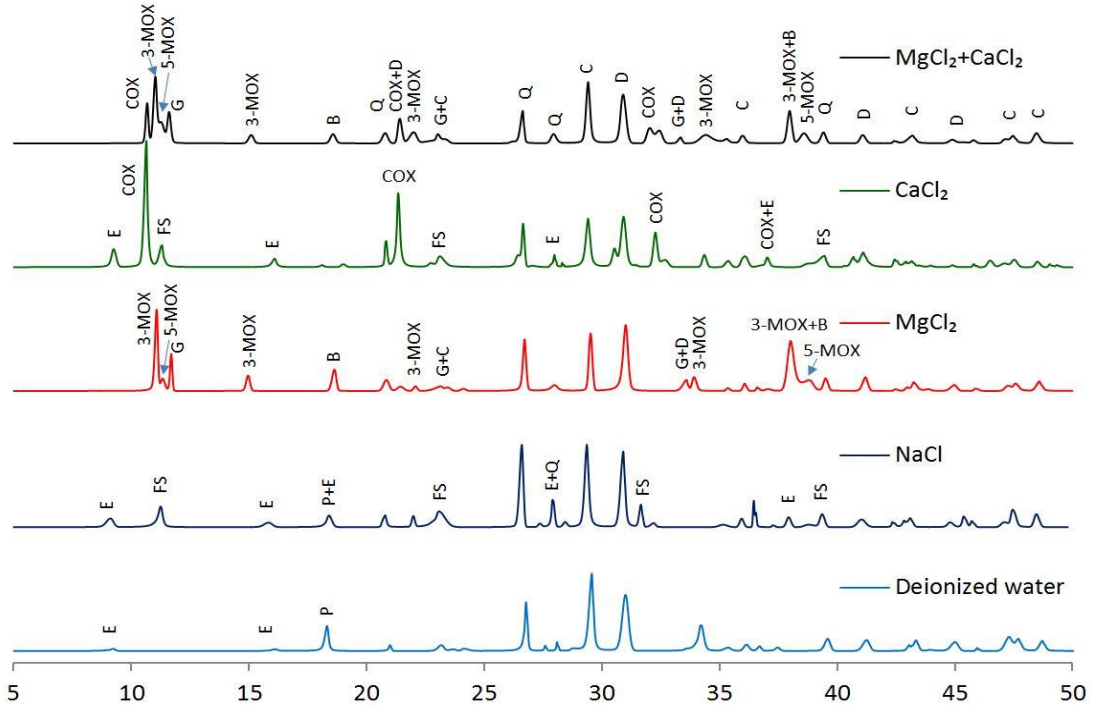
Figure 4.4: XRD patterns of the reference specimens (GU) continuously immersed in different solutions at 5°C at the time of failure listed in Table 4.4.

(1) Friedel's salt

Element	Weight%
Al K	9.8
Cl K	13.6
Ca K	25.3
O K	48.7

(2) Ettringite

Element	Weight%
Ca K	18.4
Al K	5.4
S K	7.3
O K	68.9
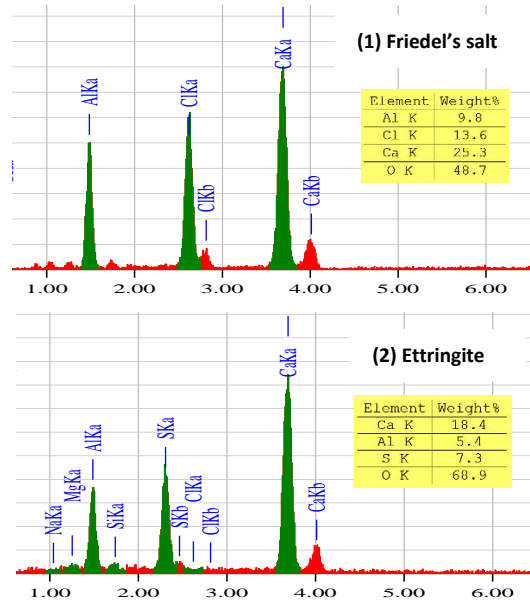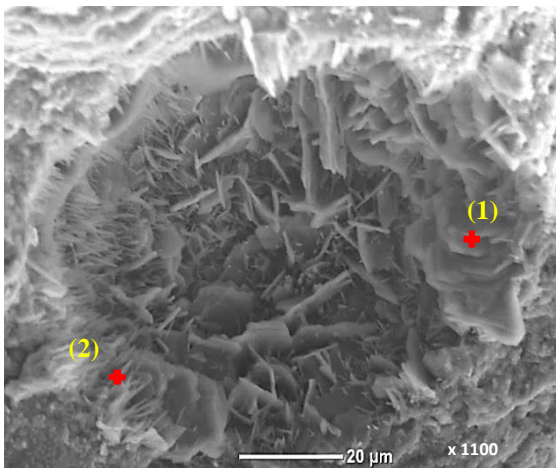
Figure 4.5: ESEM micrograph and EDX analyses of fresh fracture pieces tested at 5°C and 80% RH from the reference specimens (GU) immersed in NaCl after 540 days showing air void hosting mixed crystals of Friedel's salt and ettringite.

The mechanism induced by $MgCl_2$ is more complex. Mg^{2+} and Cl^- ions penetrate into the cementitious matrix and cause instability in the pore solution electro-neutrality due to reducing its pH. This process destabilizes the matrix by decomposing portlandite which releases OH^- ions to reestablish the pH of the solution. Increasing the concentration of Mg^{2+} and OH^- ions within the surface of the specimen forms magnesium hydroxide/brucite $(Mg(OH)_2$ according to Eq. 4.4), as a gel-like layer (Fig 4.1b and 4.2b), while Cl^- ions are bound temporarily by the aluminate phases forming Friedel's salt (e.g. Eq. 4.5).

$$Mg^{2+} + 2Cl^- + Ca(OH)_2 \rightarrow Mg(OH)_2 + Ca^{2+} + 2Cl^- \qquad \text{Eq. (4.4)}$$

$$Ca^{2+} + 2Cl^- + 3CaO.Al_2O_3.CaSO_4.12H_2O \rightarrow$$
$$3CaO.Al_2O_3.CaCl_2.10H_2O + Ca^{2+} + SO_4{}^{2-} + 2H_2O \qquad \text{Eq. (4.5)}$$
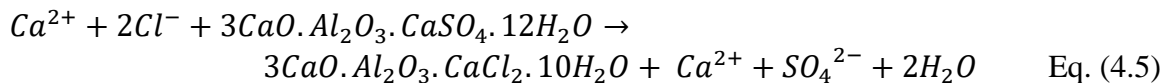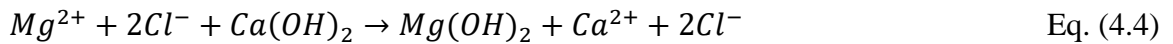
The formation of brucite may play a role in an incipient formation of COX on/underneath the surface by providing the necessary Ca^{2+} and Cl^- ions required for this reaction (Eq. 4.6). This might explain the appearance of blisters on the surface of deteriorating prisms immersed in the $MgCl_2$ solution at early-ages. Continual dissolution of portlandite and formation of brucite led to a drop in the pH of the pore solution, resulting in destabilizing Friedel's salt and incipient COX. This was indicated by the almost neutral

pH (~6.5) of the surrounding solution and absence of Friedel's salt and COX peaks in the

XRD pattern (Fig. 4.4). This observation is consistent with predictions/calculations from

thermodynamic modeling of the CaO-Al_2O_3-$CaCl_2$-H_2O system (Brown et al. 2004). With

time, the saturation of the pore fluid with respect to Mg^{2+}, Ca^{2+}, Cl^-, and OH^- ions lead to

favorable conditions for crystallization of a mixture of the 3- and 5-form MOX, according

to Eqs. 4.7 and 4.8, resulting in expansion and disintegration of concrete. The 3- and 5-

form MOX were identified by XRD (Fig. 4.4), and it was a prevailing feature observed by

ESEM (e.g. Fig. 4.6) as acicular flattened bladed crystals - several 10's of μm long by up

to 2 μm wide and approximately 1 μm thick. These crystals predominantly grew in parallel

growth bundles and occasionally as individual fibers.

$$Ca^{2+} + 2Cl^- + 3Ca(OH)_2 + 12H_2O \rightarrow 3Ca(OH)_2.CaCl_2.12H_2O \qquad \text{Eq. (4.6)}$$

$$2Mg^{2+} + 12Cl^- + 3Ca(OH)_2 + 2H_2O \rightarrow$$
$$Mg_2(OH)_3Cl.4H_2O + 3Ca^{2+} + 10Cl^- \qquad \text{Eq. (4.7)}$$

$$3Mg^{2+} + 12Cl^- + 5Ca(OH)_2 + 2H_2O \rightarrow$$
$$Mg_3(OH)_5Cl.4H_2O + 5Ca^{2+} + 10Cl^- \qquad \text{Eq. (4.8)}$$
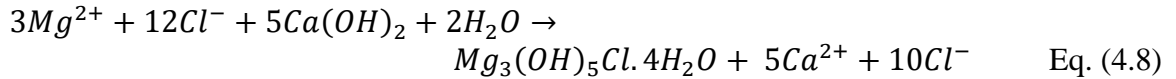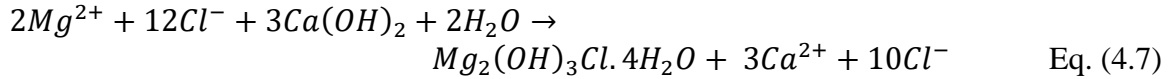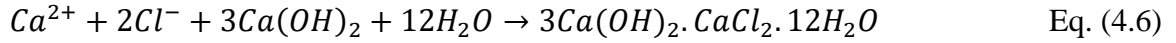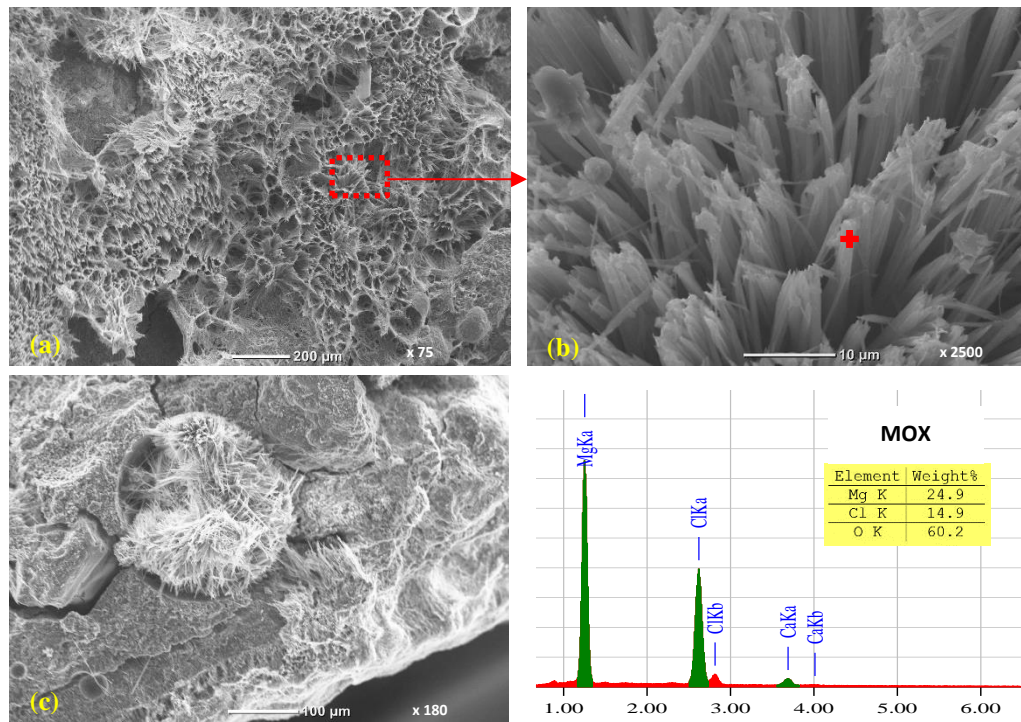
Figure 4.6: ESEM micrographs and associated EDX spectrum of fresh fracture pieces tested at 5°C and 80% RH from the reference specimens (GU) immersed in $MgCl_2$ at the time of failure listed in Table 4.4: (a) acicular flattened blades of MOX within the surface, (b) a close-up showing the morphology of the crystals, and (c) an air void hosting expansive MOX.

The presence of high concentration of Cl^- ions also encourages the formation of porous calcium-silicate-hydrate (C-S-H), due to the leaching of Ca^{2+} ions and formation of soluble $CaCl_2$. Subsequently, the leaching of Ca^{2+} ions from C-S-H promotes the penetration of Mg^{2+} ions into the cement gel converting it to non-cementitious magnesium-silicate-hydrate (M-S-H), according to Eq. 4.9. M-S-H has low crystallinity, and thus it cannot be easily resolved by XRD. This phase dominantly occurs at much advanced stages of the damage process as Mg^{2+} ions are relatively insoluble in C-S-H and must first form an independent phase containing essential Mg (e.g. $Mg(OH)_2$) and depending on the activity of silica and alumina (Brew et al. 2005). Eventually, the releasable SO_4^{2-} ions (from monosulphate, Eq. 4.5, or the dissolution of ettringite due to its instability at low pH) react

with Ca^{2+} ions in the pore solution, resulting in gypsum formation (Eq. 4.10, Figs. 4.4 and 4.7).

$$3Mg^{2+} + 6Cl^- + 3CaO.SiO_2.4H_2O + 12H_2O \rightarrow$$
$$2MgO.SiO_2.9H_2O + Mg(OH)_2 + 3CaCl_2.2H_2O \qquad \text{Eq. (4.9)}$$

$$Ca^{2+} + SO_4{}^{2-} + 2H_2O \rightarrow Ca(SO)_4.2H_2O \qquad \text{Eq. (4.10)}$$
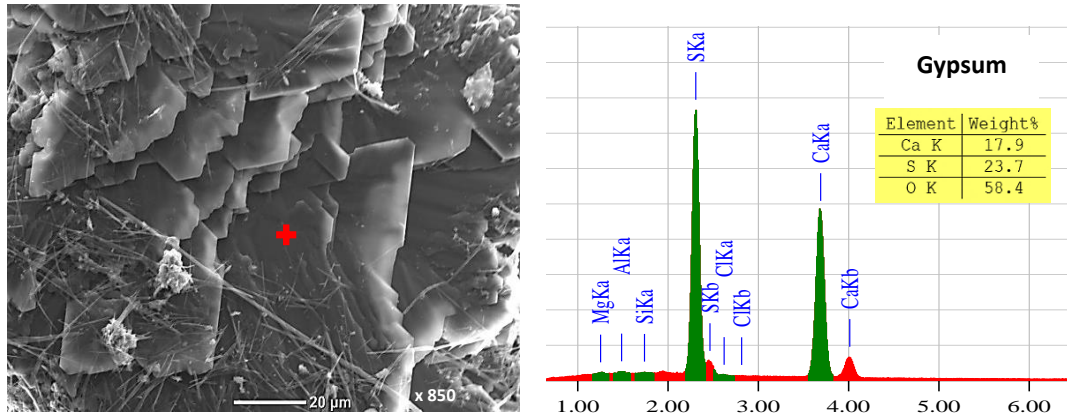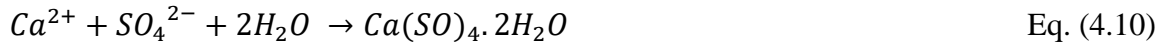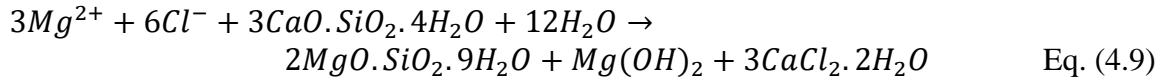
Figure 4.7**:** ESEM micrograph and associated EDX spectrum of fresh fracture piece tested at 5°C and 80% RH from the reference specimens (GU) immersed in $MgCl_2$ at the time of failure listed in Table 4.4 showing gypsum crystals.

Diaphanous crystals (Fig. 4.8) with several millimeters lengths precipitated on the surface of specimens after immersion in the $CaCl_2$ solution after two weeks. The corresponding XRD pattern for these crystals matches the pattern for the ideal composition of 3:1:12 COX as reported by (Peterson et al. 2013; Monosi et al. 1990). Also, drying these crystals over silica gel for 2 days at 40°C showed dominate phases of partially dehydrated COX ($Ca(OH)_2 \cdot CaCl_2$ (1:1:0) or $Ca(OH)_2 \cdot CaCl_2 \cdot 2H_2O$ (1:1:2)), calcite and portlandite. Similar observations were reported by Peterson et al. (2013).
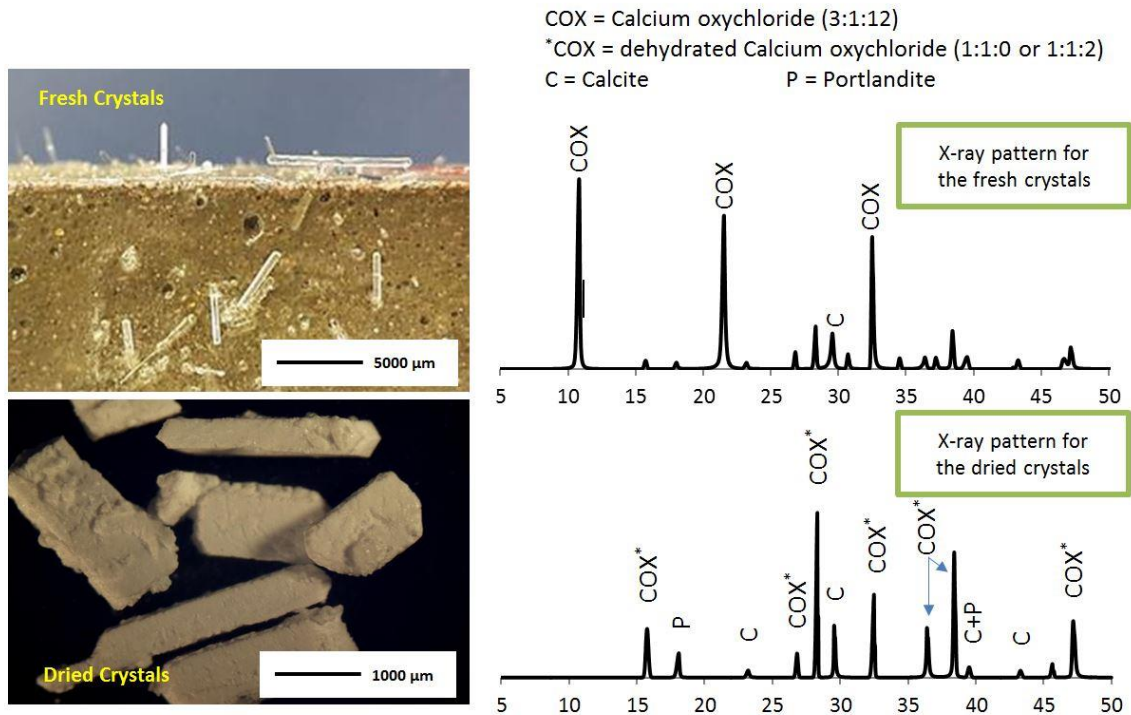
Figure 4.8: COX crystals on the surface of the reference specimens (GU) after two weeks of immersion in CaCl₂ solution at 5°C (left) and XRD pattern (right).

It seems that the high concentration of Ca^{2+}, Cl^-, and OH^- ions at the surface of specimens created favorable conditions for crystallization of COX; however, these crystals were unstable and decomposed rapidly in the solution. Within the exposed surface of concrete, diffusing Cl^- ions have a preferential reaction with aluminate bearing phases rather than portlandite to form Friedel's salt (chloride binding) as discussed earlier. With time, as penetrating ions moved inwards, the chloride concentrations increased, which created favorable conditions for crystallization of COX (Eq. 4.6), as identified by XRD (Fig. 4.4). Subhedral pseudo-hexagonal plates with up to 5 μm diameter and less than 1 μm thick were a prevailing feature observed by ESEM for 3:1:12 COX salt (e.g. Fig. 4.9a). Also, very tiny fibrous crystals, which matched the chemical elements of 3:1:15 COX, were detected (e.g. Fig. 4.9b). Formation of fibrous and platy COX was accompanied by significant expansion (Table 4.4) and cracking. Galan et al. (2015) suggested that the low

physical density of synthetic COX (3:1:12), 1.62 g/cm^3, and high water content contribute to the potential for expansion in confined space.

Data for the quaternary system CaO-Al_2O_3-$CaCl_2$-H_2O in synthetic preparations revealed invariant points involving coexistence of COX (3:1:12) with Friedel's salt and portlandite at $23\pm2°C$ (Galan et al. 2015; Damidot et al. 1994). The stability regions for these phases are related to temperature and chloride concentrations (Galan et al. 2015). The assemblage between Friedel's salt and COX (3:1:12) was also captured in this study at low temperature (5°C), as shown in the XRD pattern (Fig. 4.4), whereas the portlandite was transient due to its consumption in formation of COX (Eq. 4.6). Peaks of ettringite were also detected by XRD and rosette crystals were the direct feature observed by ESEM (Fig. 4.10). It appears that partial substitution of Cl^- ions in the existing ettringite structure took place, precipitating such stubby rosette crystals. This provides direct evidence for the hypothesis proposed by Galan et al. (2015) as chloride substitution into ettringite could be more extensive, when chloride activities become sufficient to stabilise COX phases.
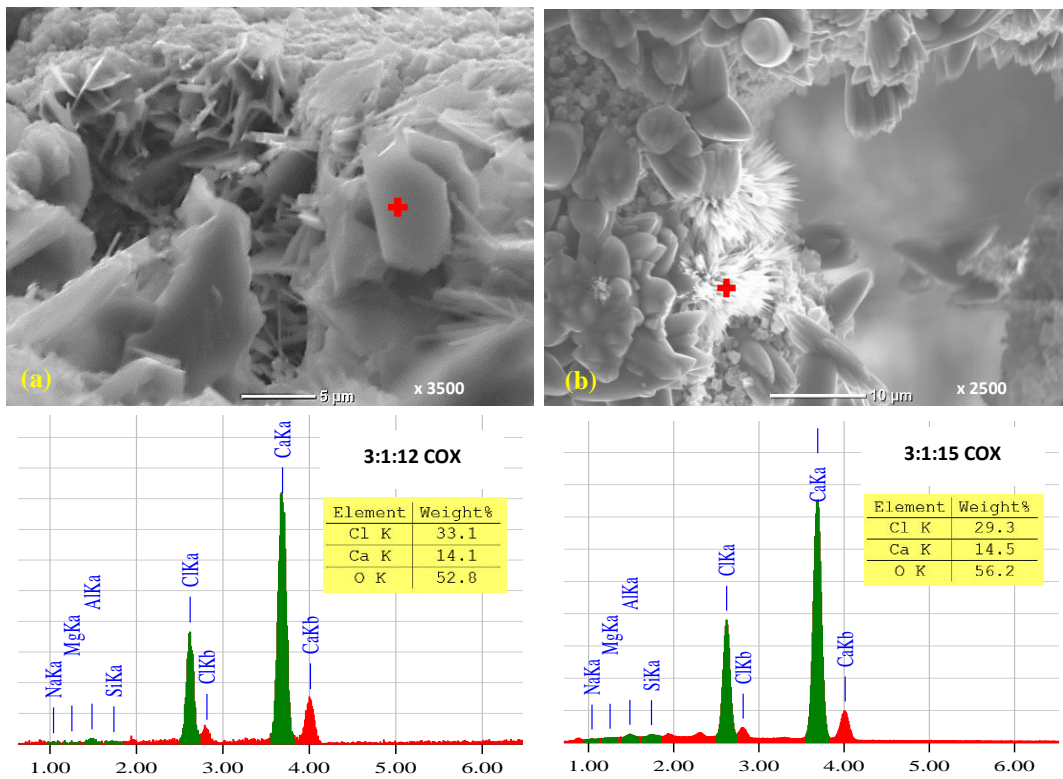
Figure 4.9**:** ESEM micrographs and associated EDX spectra of a fresh fracture piece at 5°C and 80% RH from the reference specimens (GU) immersed in $CaCl_2$ at the time of failure listed in Table 4.4 showing: (a) platy and (b) fibrous COX crystals.
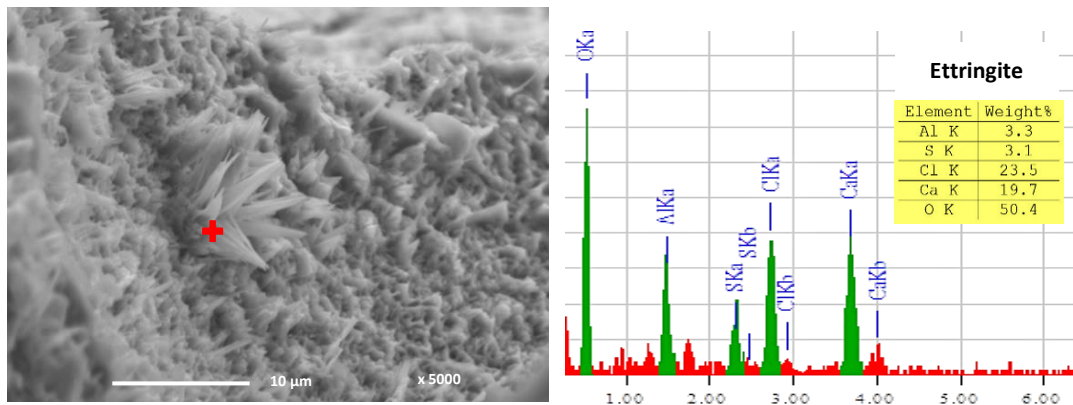
Figure 4.10**:** Exemplar micrograph of ESEM and EDX analyses of a fresh fracture piece at 5°C and 80% RH from the reference specimens (GU) immersed in $CaCl_2$ at the time of failure listed in Table 4.4 showing ettringite rosettes (left) with corresponding EDX (right).

As mentioned earlier, the predominant feature of damage by the combined salt ($MgCl_2$+$CaCl_2$) was similar to $MgCl_2$, as shown by the XRD patterns in Fig. 4.4. However**,** the propagation of the damage of specimens under the combined salt was significantly accelerated. This may be attributed to the limited gel-like compound (brucite) formed during this exposure, facilitating the ingress of the solution into concrete. Likewise, the presence of $CaCl_2$ might countervail the drop in the pH of the pore solution, as indicated by the relatively high pH (~10) of the surrounding solution, and provoke the damage by direct formation of COX, as suggested by the intense and sharp peaks of COX in the XRD (Fig. 4.4) compared to the $MgCl_2$ solution. However, at this pH level of the surrounding solution and brucite formation within the reaction zone, gypsum rather than ettringite was the stable phase, as shown by the XRD patterns in Fig. 4.4.

4.5.1.2 Wetting/drying exposure

Figures 4.11a-b show the XRD patterns for the GU specimens exposed to the W/D cycles and salt solutions after the drying and wetting events, respectively. The W/D case contrary to previous studies which used a W/D exposure (Jain et al. 2012; Wang et al. 2006a; Collepardi et al. 1994) that reported decelerated damage kinetics due to applying insufficient periods/regimes for drying the samples as the relative humidity (RH) used in these studies played an important role in limiting the effect of drying cycles.

E = Ettringite　　　　G = Gypsum　　　　3-MOX = Magnesium oxychloride (3-form)
P = Portlandite　　　 C = Calcite　　　　 5-MOX = Magnesium oxychloride (5-form)
FS = Friedel's salt　 B = Brucite　　　　 COX = Calcium oxychloride
D = Dolomite　　　　 N = Nepskoeite　　 *COX = Anhydrous calcium oxychloride (1:1:0 or 1:1:2)
Q = Quartz　　　　　　　　　　　　　　　　CACl = Calcium aluminum hydroxide chloride hydrate
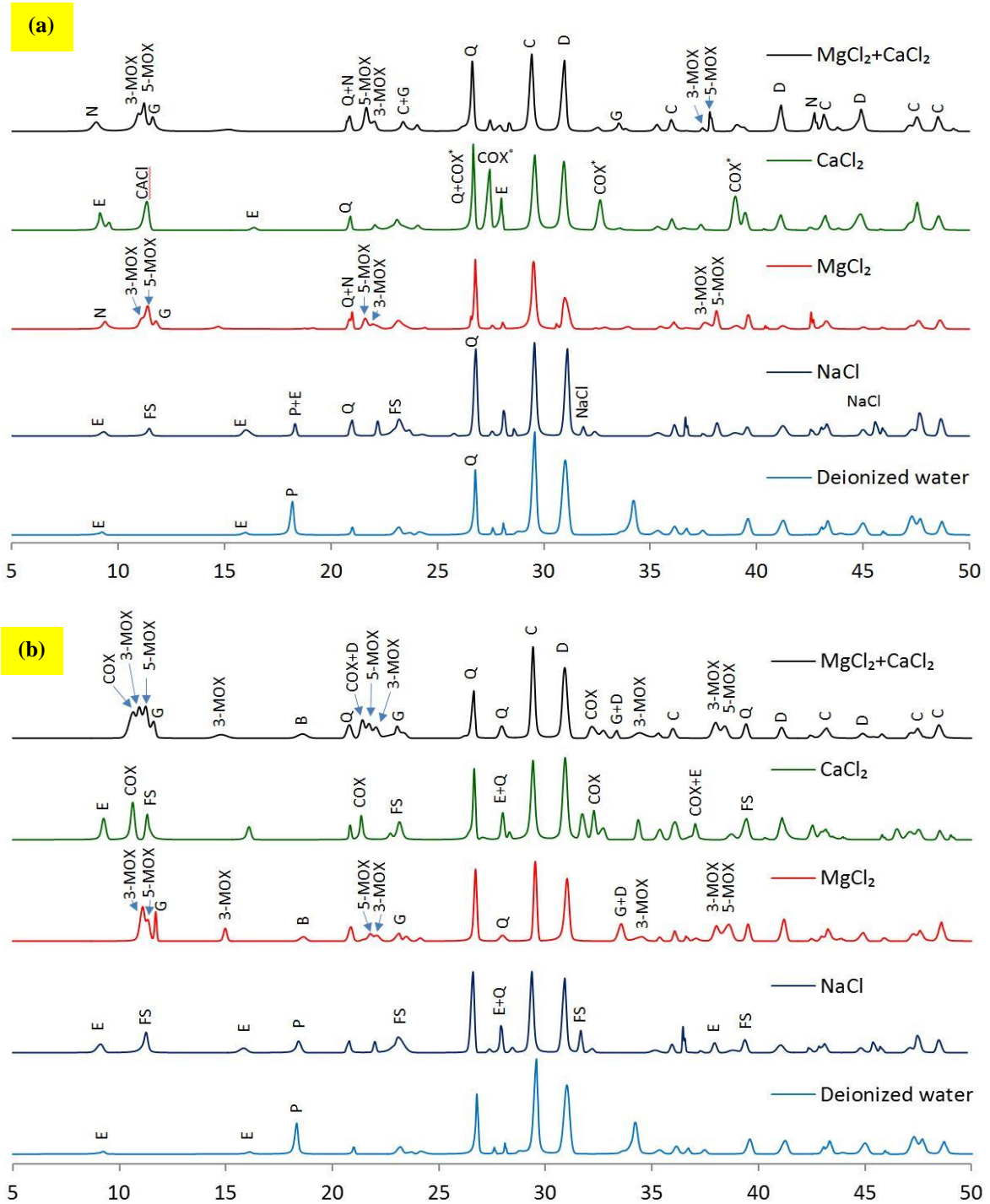
Figure 4.11: XRD patterns of the reference specimens (GU) exposed to W/D cycles in different solutions at the time of failure listed in Table 4.4 after: (a) drying, and (b) wetting events.

Compared to the corresponding specimens fully immersed in the NaCl solution at 5°C, the XRD patterns of the GU specimens exposed to W/D cycles indicate that NaCl did not induce any detectable change in the matrix. Similar phases of portlandite, calcite, quartz, dolomite, ettringite, and Friedel's salt were identified, except that halite (NaCl) peaks were identified after the drying period (Fig. 4.11a). Generally, the results indicate that NaCl is not aggressive with respect to the chemical degradation of concrete. However, the subsequent evaporation of solution and nucleation and growth of salt due to W/D cycles (e.g. Fig. 4.12) may result in enough crystallization pressure to cause surface scaling of concrete, as shown earlier in the results section.
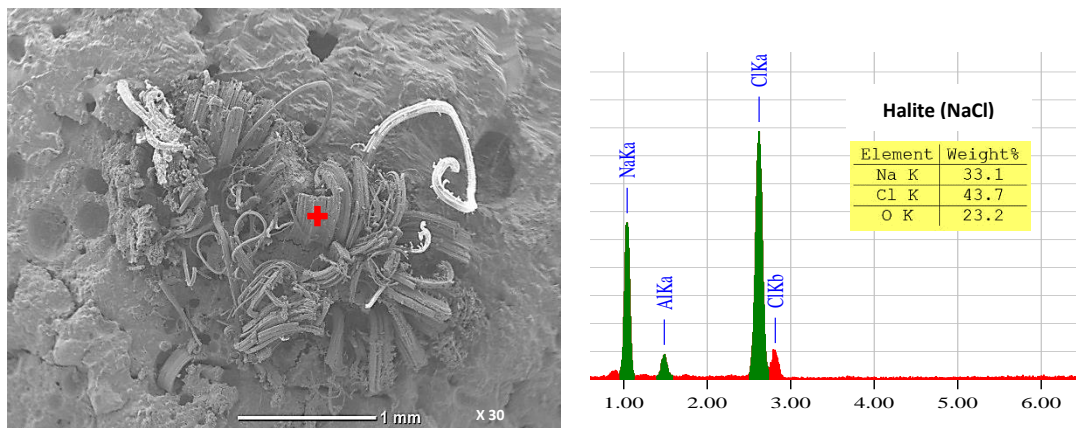
Figure 4.12**:** ESEM and associated EDX spectrum at 23°C and 50% RH for fracture surfaces from the reference specimens (GU) exposed to W/D cycles (after a drying event) and NaCl at 540 days showing crystallization of salt within the exposed surface.

In the $MgCl_2$ and combined salts solutions, the XRD patterns were comparable to that of the continuous exposure at 5°C (Fig. 4.4) after the W/D events (Figs. 4.11a-b), except that the 5-form MOX was well-defined after the drying period. Sglavo et al. (2011) reported that at low temperature (up to 10°C), the 3-form MOX was produced in place of the 5-form as the temperature influences the chemical reactions (Eqs. 4.5 and 4.6).

Nepskoeite ($Mg_4Cl(OH)_7 \cdot 6H_2O$), which is a crystalline compound associated with $MgCl_2$ salt, was also observed in the XRD patterns after the drying period. It seems that consecutive cycles of W/D caused crystallization of salts in a convective zone near-in the exposed surface, which led to micro-cracks in the cementitious matrix facilitating further penetrability of the solution and elevating the salt concentration in the specimens. These factors provided favorable conditions with respect to Mg^{2+}, Ca^{2+}, and Cl^- ions for formation of COX, 3- and 5-form MOX and gypsum (Figs. 4.11b and 4.13) during the wetting and lower temperature periods with consequent deposition in open spaces (cracks), thus accelerating rate of deterioration.
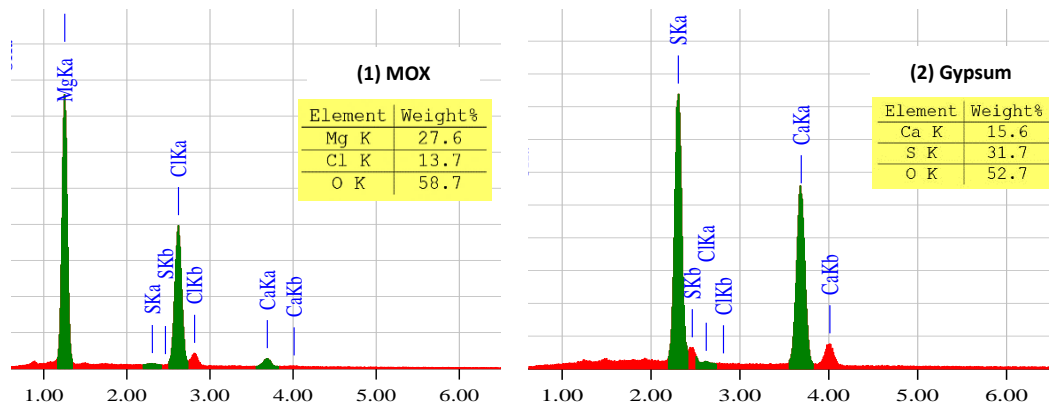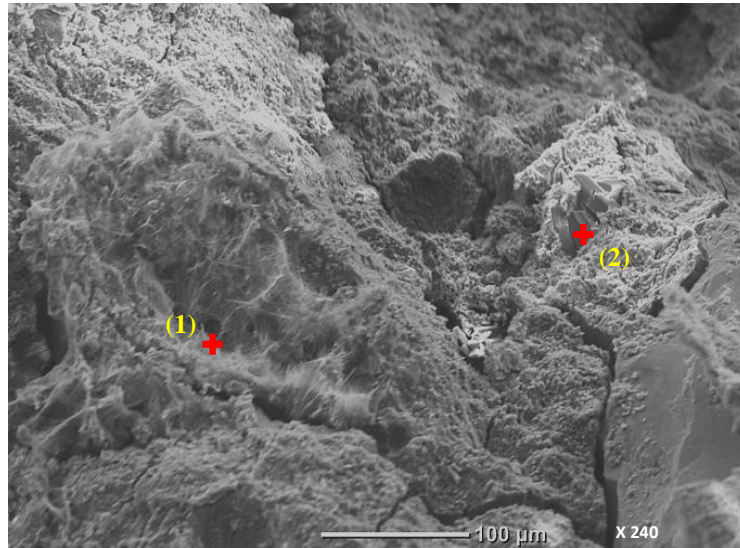
Figure 4.13: Exemplar micrographs of ESEM and EDX analyses of a reference specimen (GU) at 5°C and 80% RH exposed to W/D cycles in $MgCl_2$ at the time of failure listed in Table 4.4 showing MOX and gypsum growth in the cracks after the wetting event.

For the $CaCl_2$ solution, when the samples were collected after the wetting period (Fig. 4.11b), the XRD patterns were comparable to that of the continuous exposure at 5°C (Fig. 4.4). COX (3:1:12), Friedel's salt and ettringite were the main reaction phases detected at this stage. On the other hand, anhydrous COX (1:1:2 or 1:1:0) and calcium aluminum hydroxide chloride hydrate (CACl: $Ca_2Al(OH)_6Cl \cdot 2H_2O$) were the phases detected after the drying periods (Fig. 4.11a). Elongated, bladed, prismatic and tiny needle-like crystals were a ubiquitous feature for these phases observed by ESEM at hot-dry conditions (e.g. Fig. 4.14 and Fig 4.15a). The fine needle-like crystals are likely a polymorph of Friedel's salt due to dry conditions. Since the reaction patterns in specimens during the wetting periods were similar to the full immersion exposure, it can be deduced that the hot-dry periods (especially at 23°C and 50% RH) led to conversion of 3:1:12 COX to anhydrous COX (1:1:0 or 1:1:2) and the conversion was reversible upon wetting at 5°C. Similar observations were reported by Galan et al. (2015) upon drying synthetic 3:1:12 COX samples over silica gel for 2 weeks at 20°C by XRD. Also, they stated that wetting at 20°C for three weeks converted this dried form to 3:1:12 COX. However, in the current study, the low temperature (5°C) during the wetting events accelerated this conversion (e.g Fig 4.15b) and consequently the kinetics of damage, as substantiated by the results. As for

the role of anhydrous COX (1:1:0 or 1:1:2) in the expansion of GU specimens, it is

suggested that the relatively high density, 2.4 g/cm^3 (Galan et al. 2015), and limited water

content in these compounds reduced the expansion of specimens in this exposure. These

observations suggest that the damage of specimens herein was aggravated due to the

synergistic actions of W/D, salt crystallization and reversible formation of high and low-

density reaction products, resulting in disintegration of the cementitious matrix prepared

with GU cement.
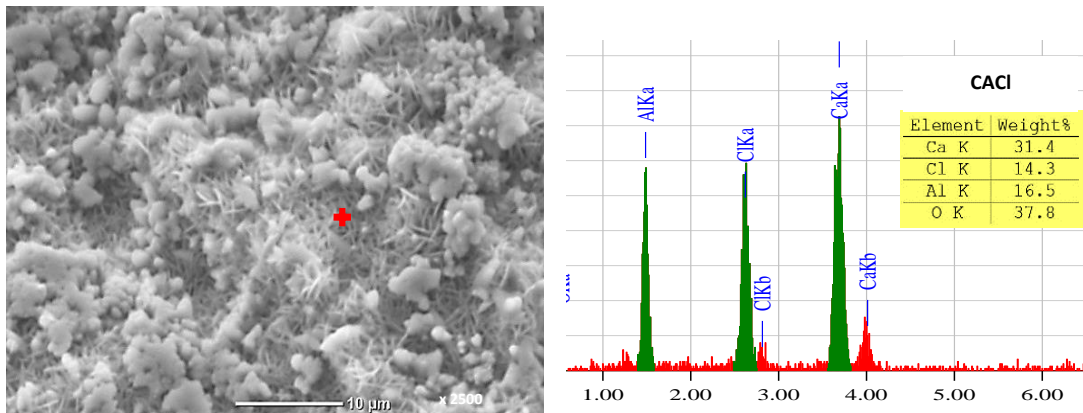
Figure 4.14**:** ESEM micrograph and associated EDX spectrum of a fracture piece at 23°C and 50% RH from the reference specimens (GU) exposed to W/D cycles (after the drying events) in $CaCl_2$ at the time of failure listed in Table 4.4 showing tiny needle-like crystals of CACl (Calcium aluminum hydroxide chloride hydrate).
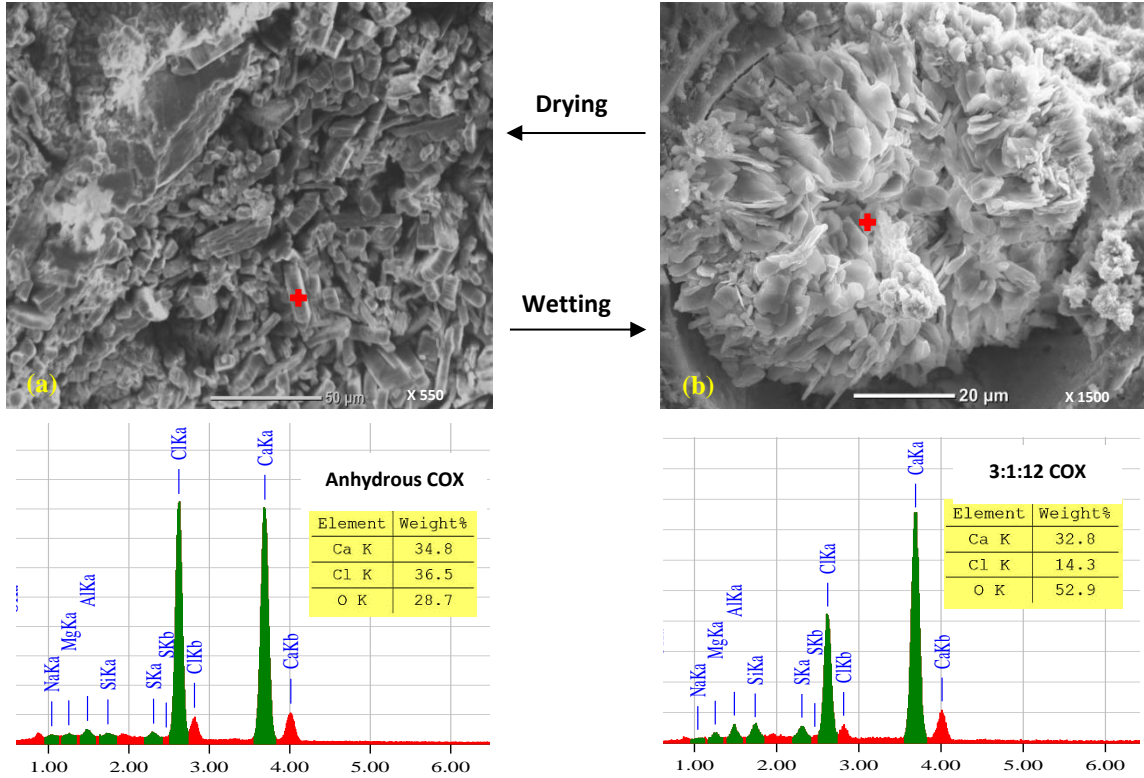
Figure 4.15**:** ESEM micrographs and associated EDX spectra of fracture pieces from the reference specimens (GU) exposed to W/D cycles and $CaCl_2$ at the time of failure listed in Table 4.4 showing: (a) anhydrous COX (1:1:0 or 1:1:2), and (b) 3:1:12 COX crystals.

4.5.2 Effect of Fly Ash and Nanosilica

4.5.2.1 Physical resistance

The physical resistance of all specimens after curing (28 days) was evaluated by the RCPT and MIP and the results are listed in Table 4.6. After completing the RCPT, the physical penetration depth of chloride front was measured for concrete specimens as indicated by the whitish precipitate (e.g. Fig. 4.16). Also, the non-steady-state migration coefficient was calculated based on the penetration depth, geometry of specimen, applied voltage, temperature of the anolyte solution and test duration, according to NT BUILD 492

99

(2011), to account for the heat (Joule) effect and different testing durations, if any, on ionic mobility within specimens. However, the concrete mixtures tested herein had *w/b* of 0.4 and contained SCMs (except for the reference GU mixture). Therefore, the cell compartments showed small temperature rise (maximum of 4°C) and the test duration was constant (6 h). In addition, MIP was conducted at 28 days to determine the apparent porosity, threshold pore diameter, average pore size and proportion of micro-pores (less than 0.1 µm) of these concrete specimens. From Table 4.6, it can be noted that the trends of RCPT were consistent with that of MIP in the sense that small penetration depths/migration coefficients corresponded to low cumulative intrusion (apparent total porosity) and/or further pore size refinement and vice versa.

Table 4.6: Results from RCPT and MIP

Mixture ID.	**RCPT results**				**MIP results**			
	Charges Passed, coulombs	Chloride Ions Penetrability Class, ASTM C1202	Average Penetration Depth, mm	Migration Coefficient, $\times10^{-12}$m^2/s	Apparent Total Porosity, %	Threshold Pore Diameter, µm	Average Pore Size, µm	Proportion of Micro-Pores (<0.1 µm), %
GU	2142	Moderate	17.9 (0.32)*	17.32	16.1	0.120	0.173	64.1
GUF20	1515	Low	13.0 (0.64)	10.12	17.5	0.117	0.114	72.2
GUF30	1244	Low	10.3 (0.57)	8.23	18.7	0.113	0.087	74.7
GUS	723	Very Low	5.7 (0.60)	4.74	10.3	0.067	0.015	78.3
GUF20S	586	Very Low	5.2 (0.73)	3.86	10.7	0.065	0.013	79.1
GUF30S	476	Very Low	3.9 (0.64)	2.84	8.3	0.053	0.008	80.8

*Standard error is shown between brackets

17.9 mm

10.3 mm

100
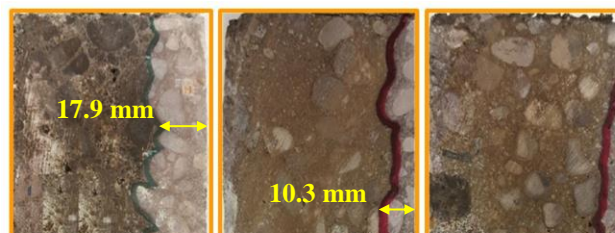
Figure 4.16: Whitish precipitate showing the average penetration depth of chloride ions in specimens from: (a) single binder (GU), (b) binary binder containing 30% fly ash (GUF30), and (c) ternary binder comprising 64% GU cement, 30% fly ash and 6% nanosilica (GUF30S).

Compared to the single binder (GU) mixture, the incorporation of fly ash in binary binders significantly reduced the migration coefficient of concrete. For instance, adding 20 and 30 % fly ash in binary binders (GUF20 and GUF30) led to approximately 42 and 52% reduction in the migration coefficient of specimens compared to that of the corresponding specimens prepared with the GU cement only, which was 17.32×10^{-12} m^2/s. The reduction of the penetration depth/migration coefficient, despite the increase of apparent porosity (9 and 16%, respectively), can be attributed to the notable reduction of the average pore size (Table 4.6) and correspondingly the effective porosity, thus reducing the penetrability of the matrix. Accordingly, fly ash mixtures had reduced ingress of salt solutions and consequently better resistance to chemical degradation by de-icing salts, which generally performed better and/or survived longer than the GU specimens as shown earlier in the Results section. Also, the effect of fly ash was enhanced in the W/D exposure compared to the continuous immersion at 5°C due to the continual pozzolanic activity of these mixtures with time, as will be discussed in the next section (Chemical Resistance), which further reduced the effective porosity and in turn penetrability of specimens. These trends were corroborated by the smaller whitish precipitate indicating the penetration depth of chloride

ions in the cross-section of the fly ash specimens in the W/D exposure compared to that of

the corresponding specimens in the continuous immersion at 5°C for all salt solutions (e.g.

Fig. 4.17).
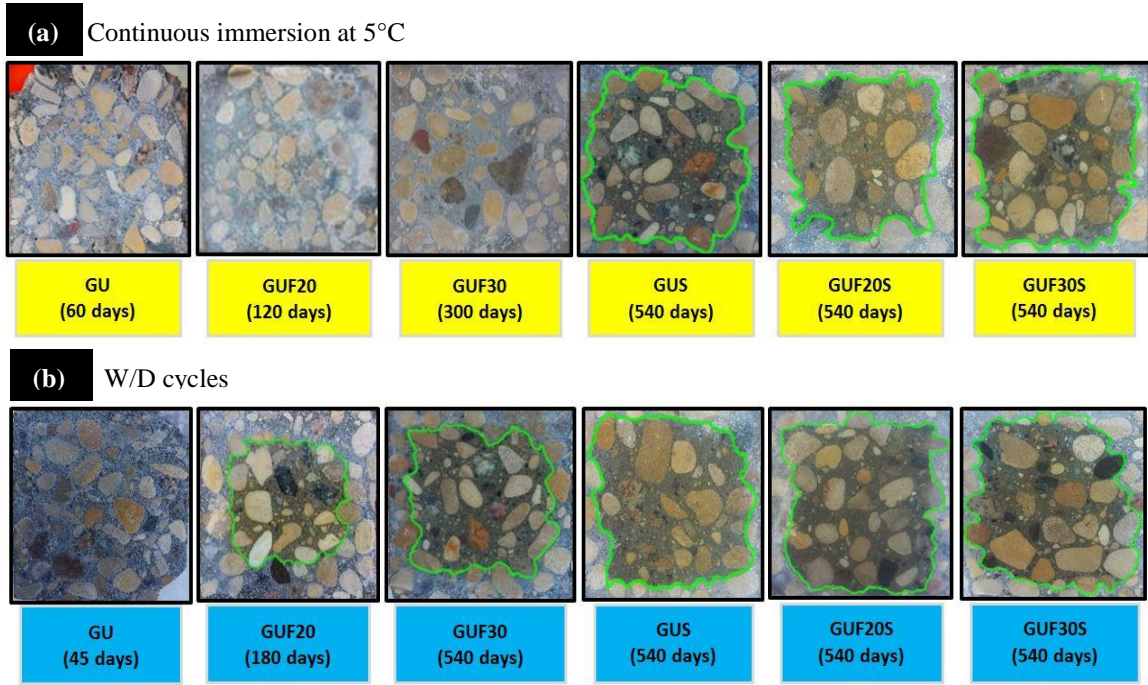
Figure 4.17: Example of whitish precipitate of silver chloride showing the ingress of chloride ions in the cross-section of specimens exposed to $CaCl_2$ solution at failure or at end of exposure. (*Note: the green boundary shows the depth of the chloride ions from the exposed surface*)

Using an ultrafine pozzolan such as nanosilica (specific surface of 80,000 m^2/kg) in the binary (GUS) and/or ternary binders (GUF20S and GUF30S) produced significantly refined microstructure, irrespective of the dosage of fly ash, as indicated by reducing the penetration depth/migration coefficient and total porosity (Table 4.6). Incorporation of 6% nanosilica in concrete led to an average reduction of the migration coefficient by 73% and total porosity by 36%, compared to the reference GU concrete. The proportion of the micro-pores in these systems comprising nanosilica was increased, which led to smaller threshold pore diameters (an average of 45% reduction relative to the GU specimens), and in turn reduced penetrability of these matrices and consequently less solution uptake and no damage (Table 4.6). These trends were corroborated by the significantly smaller whitish precipitate of chloride ions after 28 days (e.g. Fig. 4.16) and in the cross-section of the specimens containing nanosilica after 540 days in both exposures (Fig. 4.17) compared to the reference (GU) or the binary binder specimens with fly ash. These results are consistent with the effects of nanosilica on cementitious systems, which contribute to the microstructural development of cement-based materials through multiple mechanisms, including accelerated pozzolanic activity, filler effect, and water absorption into the high surface area of silica aggregates/agglomerates, i.e. reduction of *w/b* in the paste. Details of such mechanisms were previously described in other studies (Ghazy et al. 2016; Kong et al. 2015; Madani et al. 2012; Said et al. 2012), and they are beyond the scope of this work.

4.5.2.2 Chemical resistance

Portlandite is a key component in the reaction of hydrated paste with de-icing salts as discussed earlier. Table 4.7 provides a summary of the DSC results of the portlandite contents in the cementitious matrix of all mixtures with their corresponding enthalpies before (at 28 days) and after the exposures (540 days or 108 W/D cycles) or at the time of

failure. Semi-quantitative analysis based on the enthalpy concept (integration of heat flow peaks over temperature) can determine the relative phase formation, as the enthalpy of the phase is directly related to its amount (Brown et al. 2011). There was no efficient later-age pozzolanic activity of Type F fly ash in the binary specimens exposed to continuous immersion in deionized water at 5°C as indicated by the presence of portlandite (maximum consumption of 7% after 540 days, Table 4.7) in these specimens. This implies that the long-term activity of fly ash was hindered at this low temperature (5°C), especially that these specimens were initially cured for 28 days. Hence, the binary fly ash specimens generally failed (but after the GU specimens with higher initial portlandite contents and penetrability) under this exposure before 540 days, especially with the aggressive types of salt solutions (Table 4.4).

Perhaps, if the binary specimens comprising 20 and 30% fly ash were initially cured for longer periods (56 days or more) before exposure, the effect of fly ash might have been more improved. This is suggested by the behaviour of ternary binders comprising 20 and 30% fly ash combined with a more reactive pozzolanic material (nanosilica). In addition to the improved physical resistance, nanosilica vigorously sped-up the kinetics of cement hydration and fly ash reactivity. This was substantiated by the DSC results as the incorporation of nanosilica catalyzed the reactivity of fly ash, resulting in an average reduction of the initial portlandite content in the ternary mixtures (GUF20S and GUF30S) by 83 and 86%, respectively, compared to the corresponding binary mixtures (GUF20 and GUF30). Also, the action of W/D cycles increased the long-term efficiency of pozzolanic reactivity of Type F fly ash, as particularly indicated by the marked consumption of portlandite in specimens GUF20 and GUF30 after 540 days of repetitive wetting in deionized water at a low temperature and drying at higher temperatures (Table 4.7); this

was reflected by the better performance of these specimens, as shown in Table 4.4. Correspondingly, nil portlandite content was observed in ternary cementitious systems comprising GU, fly ash and nanosilica under the W/D exposure, which was corresponded to sound mechanical properties (e.g. Fig. 4.3) and longevity (Table 4.4), irrespective of the type of solution.

Table 4.7: Enthalpies (J/g) of portlandite in the cementitious matrix

Mixture ID.	After 28 days in the curing chamber	After 540 days immersed in deionized water	After 540 days or at the failure point* immersed in the de-icing salts			
			NaCl	MgCl$_2$	CaCl$_2$	MgCl$_2$+ CaCl$_2$
Exposure I: continuous immersion at 5 °C						
GU	63.6	62.1	42.3	0.0*	0.0*	0.0*
GUF20	56.8	50.4	38.9	0.0*	0.0*	0.0*
GUF30	45.8	39.7	31.8	22.9	0.0*	0.0*
GUS	23.9	19.9	16.4	15.6	11.9	13.1
GUF20S	8.9	5.7	3.6	2.4	3.1	1.7
GUF30S	7.0	5.3	2.9	0.7	2.2	1.1
Exposure II: W/D cycles						
GU	63.6	60.2	54.8	0.0*	0.0*	0.0*
GUF20	56.8	24.7	23.7	21.9	0.0*	0.0*
GUF30	45.8	16.4	14.1	17.8	12.2	13.3
GUS	23.9	17.9	13.7	15.9	16.1	17.1
GUF20S	8.9	0.0	0.0	0.8	0.0	0.0
GUF30S	7.0	0.0	0.0	0.0	0.0	0.0

Spatial elemental distribution of Cl⁻ ions by EDX for billets extracted from some specimens in the W/D exposure was conducted. Figure 4.18 shows an example of the Cl⁻ and Cl/Ca of billets extracted from single (GU), binary (GUF20), and ternary (GUF30S) specimens exposed to W/D and CaCl$_2$ solution. The GU specimens showed the highest Cl/Ca and intensity of micro-cracks throughout the depth of billets, which corresponded to high intensity of damage observed in these specimens due to formation of complex compounds, as discussed earlier. Comparatively, in the binary (GUF20) specimens, the Cl/Ca showed high values within 6 mm near the exposed surface (convective zone) with a reducing gradient of Cl⁻ ions inwards. This may be due to the densification of

microstructure and pozzolanic activity (reduction of portlandite) of fly ash, which may explain the notable delay in the initial damage for specimens containing 20 and 30% fly ash compared to their corresponding GU specimens. Once considerable amounts of expansive phases were formed within the reaction zone, significant swelling of this zone underneath the surface relative to the restraining (non-expanding) core might have led to abrupt failure as observed for GUF20 specimens in the W/D exposure with the $CaCl_2$ and combined salts solutions (Fig. 4.3 and Table 4.4). It is worth noting that such gradient/zonation diminished in the specimens containing nanosilica, primarily due to the significant physical resistance and reduction of portlandite when combined with fly ash (e.g. Fig. 4.18c).

Figure 4.18**:** Example of chlorine and Cl/Ca maps of billets exposed to W/D cycles at the
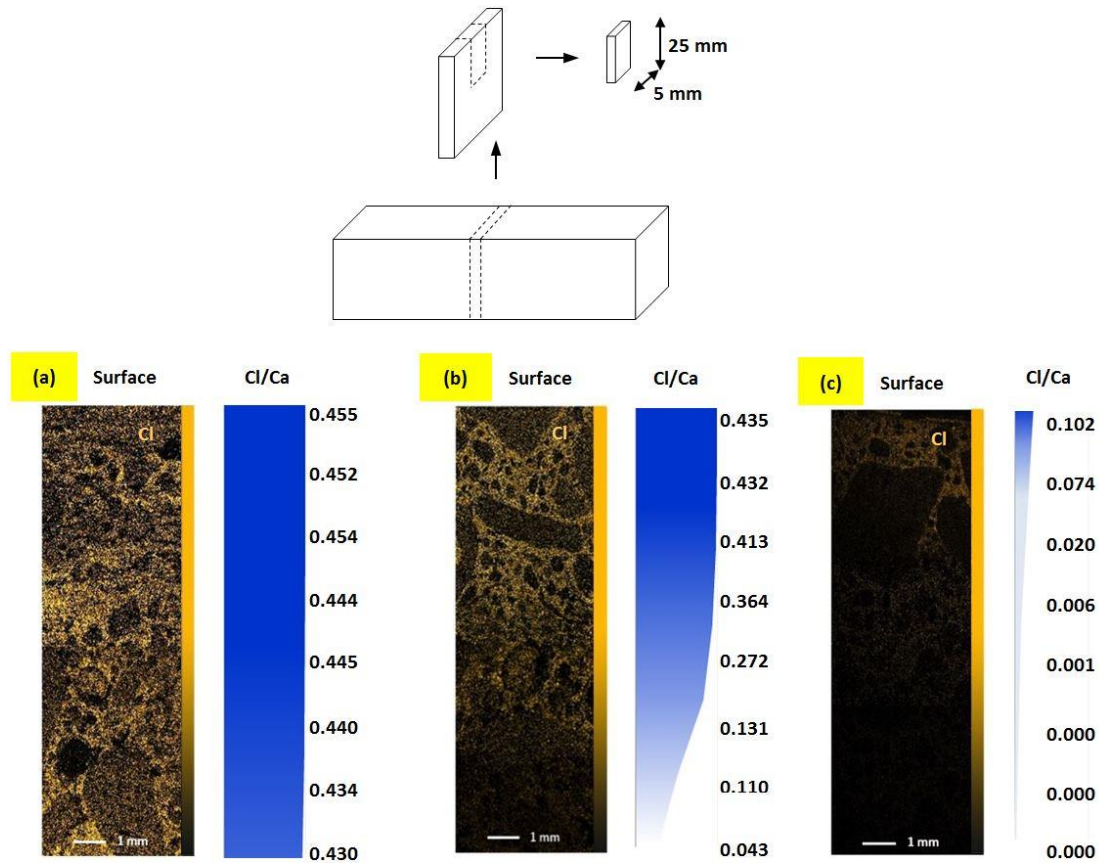
time of failure listed in Table 4.4 from: (a) single binder (GU), (b) binary binder (GUF20), and (c) ternary binder (GUF30S).

CHAPTER 5 – PHASE II: RESPONSE OF CONCRETE TO FREEZING-THAWING CYCLES AND DIFFERENT CONCENTRATIONS OF DE-ICING SALTS

The preceding chapter has elucidated the damage mechanisms of concrete under de-icing solutions when combined with constant low temperature (5°C) and wetting/drying (W/D) cycles. In addition, it documented the potential benefits of supplementary cementitious materials (SCMs: fly ash and nanosilica) in mitigating/preventing the damage under these conditions. The current chapter provides additional information on the performance of the developed mixtures under freezing/thawing (F/T) cycles combined with different concentrations of the most individual aggressive de-icing salts ($MgCl_2$ and $CaCl_2$). Also, it substantiates the potential benefits of portland limestone cement (PLC), in mitigating this type of damage.

5.1 Introduction

In cold weather environments, concrete deterioration is accelerated when it is subjected to de-icing salts and freezing/thawing (F/T) cycles. The deterioration due to de-icing salts erosive effects can develop rather rapidly compared with the destructive effects of normal F/T cycles on concrete (Penttala 2006; Litvan 1976). Studies on frost damage of concrete typically classify the problem into internal frost damage, a bulk cracking problem, and salt-frost scaling, a superficial damage (Sun et al. 2010; Valenza et al. 2006; Penttala 2006; Litvan 1976; Powers 1975). Salts can also chemically interact with concrete, resulting in leaching and decomposition of the hydrated cement products (Peterson et al. 2013; Wang et al. 2006a). Formation of oxychloride phases was suspected

107

for causing the chemical degradation of hardened concrete exposed to concentrated de-icing salts combined with F/T cycles; however, these phases were mostly reported in synthetic hydrated materials (Suraneni et al. 2016; Farnam et al. 2015a and 2015b Peterson et al. 2013).

Many studies have been conducted to evaluate the effect of different de-icing salt (NaCl, $MgCl_2$, $CaCl_2$) concentrations, ranging between 3 to 20%, on ice-formation pressure and volume expansion of concrete using accelerated F/T tests (Wu et al. 2015; Liu et al. 2015; Marchand et al. 1999). At intermediate salt concentration (3 to 10% by mass), the most deleterious effects with respect to salt frost scaling of concrete surface were reported due to the instant expulsion of liquid towards the unfrozen zone and persistent ice accretion in capillaries or air voids (Yener et al. 2015; Liu et al. 2015; Powers 1975; Powers 1945). Several mechanisms may be associated with frost damage of concrete including hydraulic, osmosis, and crystallization pressures (Liu et al. 2015; Litvan 1976; Powers 1975; Powers et al. 1953; Powers 1945). The gradual build-up of ice in capillary pores exerts tensile stresses on pore walls, and consequently micro-cracking of the hardened cement paste. De-icing salts also aggravate the risk of frost damage due to the increase in the degree of saturation and moisture distribution in the pore structure of the cementitious system (Sun et al. 2010; Penttala 2006; Litvan 1976).

Figure 5.1 shows a generic phase diagram to highlight the possible scenarios in which two or more phases of matter exist together in pure substances or in solutions. The curved lines represent the freezing points as a function of temperature and the solute concentration. When the temperature declines, more solute is required to melt the ice until the eutectic temperature is reached. The differences in the amount of de-icing salts needed to melt ice at a given temperature are explained by the amount of charge contributed by the

ions in the solution. Therefore, typical maintenance strategies for transportation infrastructure in North America have recently included using higher concentration of solute, at lower temperatures, to maintain the chemical potential gradient needed to melt the ice which might aggravate the chemical activity in concrete (Snow and Ice Control – Ontario 2016; Policy on snow clearing and ice control – City of Winnipeg 2011; Minnesota Snow and Ice Control 2012). The majority of the studies on F/T damage of concrete focused on low or moderate solute concentrations (up to 10% by mass) which might mainly provoke salt frost scaling of concrete (physical damage) (Wu et al. 2015; Liu et al. 2015; Marchand et al. 1999). However, at high concentrations, chemical degradation of concrete might be the dominant mode of damage, which has been less documented in the technical literature (Peterson et al. 2013). In this context, it is noteworthy that the previous Chapter shows that only exposure to solutions of $MgCl_2$ and $CaCl_2$ led to chemical degradation of concrete, and there is no evidence of a similar damage in NaCl solutions.
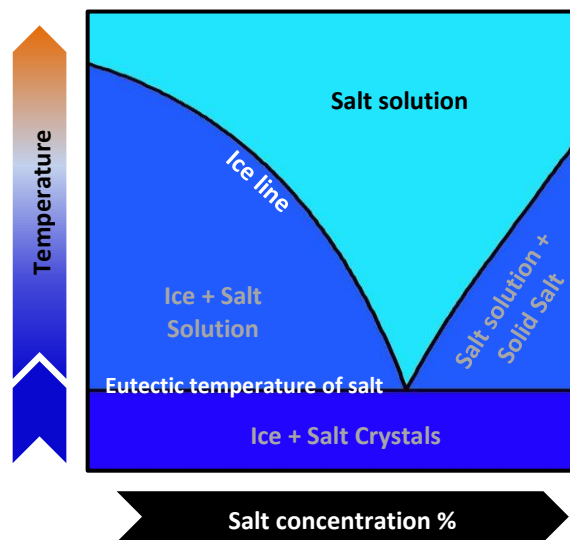
Figure 5.1: Generic phase diagram of the de-icing salts.

Extensive research on the use of supplementary cementitious materials (SCMs) such as fly ash showed that incorporation of Class F fly ash generally improves the long-

term performance and durability of concrete (Mehta et al. 2014). Despite the benefits of fly ash concrete, many government agencies limited the maximum replacement amount of fly ash to 20% or less in the concrete mixtures exposed to F/T combined with de-icing salts due to their unsatisfactory performance (Ontario provincial standard specification 2014; Standard Specifications for Construction of Roads and Bridges on Federal Highway Projects 2014). The delay in setting time, strength gain, and microstructural development at early ages of fly ash concrete, as well as vulnerability to surface scaling, are considered to be the major issues, which deter its wider acceptance (Malhotra et al. 2000). Nevertheless, these performance limitations associated with the use of slowly reactive materials (e.g. fly ash) can be mitigated by incorporation of nanoparticles (size scale of 1-100 billionth of a meter) in concrete (Ghazy et al. 2016; Said et al. 2012). Nanoparticles (e.g. nanosilica) have been applied in concrete research and proven to enhance fresh and hardened properties by modifying the structure of the cementitious matrix at the nano and micro levels (Ghazy et al. 2016; Zadeh et al. 2013; Madani et al. 2012; Said et al. 2012). Therefore, their application in concrete may have a great potential to produce innovative types of fly ash concrete with superior performance for applications exposed to harsh environments.

Recently, a new type of portland cement has been introduced to the North American market which contains 6 to 15% of interground limestone powder (portland limestone cement: PLC) with clinker due to their technical, economic, and ecological benefits. Limestone substitution significantly affects the physical and mechanical properties of cement. While there are a number of studies on the hydration and strength characterization of concrete made from PLC (e.g. Marzouki et al. 2013) and its response to durability issues such as sulfate attack (e.g. Ramezanianpour et al. 2013), alkali-aggregate reactions and

chloride ions penetration (Thomas et al. 2010; Tsivilis et al. 2003), there has been dearth of information and field experience on the effect of PLC on performance of concrete subjected to F/T cycles combined with de-icing salts; hence, the wider use of PLC in transportation infrastructure remains limited.

5.2 Research Significance

Given the dearth of information on the combined effects of fly ash, nanosilica and PLC on the physical and chemical resistances of concrete subjected F/T and de-icing salts, the objective of the current study was to investigate the response, in terms of physico-mechanical properties and microstructural features, of concrete made with different types of cement (ordinary and PLC) without or with SCMs (fly ash and nanosilica) to F/T cycles combined with different concentrations of the most aggressive chloride-based de-icing salts. Results from this investigation should contribute better understanding of the underlying mechanisms of concrete degradation under such conditions; in addition, they would substantiate the potential benefits of nanoparticles and PLC, if any, in mitigating this type of damage, and hence, improve the current specifications and guidance for concrete exposed to extensive use of de-icing salts combined with F/T cycles.

5.3 Experimental Program

5.3.1 Materials and Mixtures

The materials and mixtures used in this Chapter were similar to that used in Chapter 4 (refer to Section 4.3.1).

5.3.2 Exposure

The findings from Chapter 4 showed that only $MgCl_2$ and $CaCl_2$ led to chemical degradation of concrete among the individual de-icing solutions used, and there is no

evidence of a similar damage under NaCl solutions. Therefore, these salts ($MgCl_2$ and $CaCl_2$) were only used in this section. Hexahydrate form of magnesium chloride ($MgCl_2 \cdot 6H_2O$) and dihydrate form of calcium chloride ($CaCl_2 \cdot 2H_2O$) with purity of 94% and 96%, respectively, were used to prepare the solutions. Moderate and high concentrations were used to cover two different states (solution with and without ice, Fig. 5.1) according to the phase diagrams for these salts (Fig. 2.3), as shown in Table 5.1. The solutions were renewed every two weeks (15 F/T cycles) to keep a continual supply of Cl^- ions, thus providing aggravated damage conditions. The specimens were immersed in the respective solutions for 2 days before starting the F/T exposure. The specimens were then subjected to de-icing salts combined with F/T cycles according to the general procedures of ASTM C666 test procedure A, expect that de-icing solutions were used instead of water and the frequency of F/T cycles per day was less to allow the chemical reactions to exist, if any. The duration of one F/T cycle was 12 hours: freezing at $-18\pm1°C$ for 7 h and thawing at $4\pm1°C$ for 3.5 h, and 45 min. to ramp to the minimum freezing temperature or the maximum thawing temperature. This exposure continued for up to 600 cycles.

Table 5.1: Concentration of de-icing solutions

Type of Salt	Moderate concentration			High concentration		
	Salt Concentration Mass (%)	Chloride Concentration (mol/l)	Chloride Concentration[a] (ppm)	Salt Concentration Mass (%)	Chloride Concentration (mol/l)	Chloride Concentration* (ppm)
$MgCl_2$	11.9	2.82	100,735	19.1	4.52	160,069
$CaCl_2$	13.6	2.81	100,731	21.9	4.51	160,067

[a] The ionic concentration of Cl^- ions in each solution was verified by ion chromatography (ASTM D 4327).

5.3.3 Tests

Similar to Chapter 4, the physical resistance of the concrete specimens was evaluated by the rapid chloride penetrability test (RCPT) and mercury intrusion porosimetry (MIP). Also, the physico-mechanical properties (mass, length (ASTM C 157)

and dynamic modulus of elasticity, E_d (ASTM C 215)) of the specimens were measured versus time of exposure. In addition, the alteration of microstructure in deteriorating specimens was assessed by microscopy, thermal and mineralogical analyses (refer to Section 4.3.3).

5.4 Results

5.4.1 Visual Assessment and Mass Change

Close examination was regularly made to assess the condition of the specimens (e.g. Figs. 5.2 and 5.3). Also, the mass change of specimens with time was measured and summarized in Table 5.2. Under moderate and high concentrations of $MgCl_2$, the GU specimens were softened, disintegrated, and showed notable swelling (e.g. Fig. 5.2a), with mass losses of 32% and 26%, respectively; thus, the physico-mechanical measurements were discontinued for these specimens at 375 and 465 cycles, respectively. Similar features of damage were observed for the GUF20 specimens exposed to the high concentration of $MgCl_2$ solution (Fig. 5.2a), except the magnitude of the damage was less (mass loss of 11%). Comparatively, GUF20 specimens exposed to the moderate concentration of $MgCl_2$ solution did not fail (Fig. 5.2a). Specimens from the binary binder with 30% fly ash (GUF30) did not show any evidence of damage under both concentrations of $MgCl_2$. On the other hand, except specimens from the single binder in the PLC group exposed to the high concentration $MgCl_2$ solution (Fig. 5.3a), no single specimen had any evidence of damage or reduction in engineering properties (Table 5.2) at both concentrations of $MgCl_2$ up to 600 cycles.

The $CaCl_2$ was more aggressive than $MgCl_2$ as the rate of deterioration of specimens was very rapid at both concentrations. For the moderate concentration, the reference specimens (GU) and specimens made with binary binders containing 20% and

30% fly ash (GUF20 and GUF30) suffered notable surface scaling on all faces as well as swelling (e.g. Fig. 5.2b), with mass losses of 21%, 22% and 10%, respectively. Specimens made with 100% PLC and binary binders containing 20% fly ash (PLCF20) were quite intact with less surface scaling (7% and 4%, respectively) and minor pop-outs and no evidence of significant degradation. Comparatively, micro-cracks along the edges and/or at the corners of GU, GUF20, PLC and PLCF20 specimens accompanied by spalling and clear separation of the surface layer from the rest of the specimen were the main features of damage at the high concentration $CaCl_2$ until complete disintegration at 285, 495, 510 and 600 cycles with mass losses of 31%, 19%, 14% and 13%, respectively. Unlike the moderate concentration exposure, specimens made with binary binders containing 30% fly ash (GUF30 and PLCF30) exposed to high concentration of $CaCl_2$ solution did not fail under such exposure (Table 5.2). Irrespective of the type of cement (GU or PLC) and binder (binary or ternary), all specimens comprising nanosilica exposed to $MgCl_2$ or $CaCl_2$ solutions showed no visible features of damage up to the end of the exposure (600 F/T cycles) (Appendix A, Fig. A.3 and A.4).
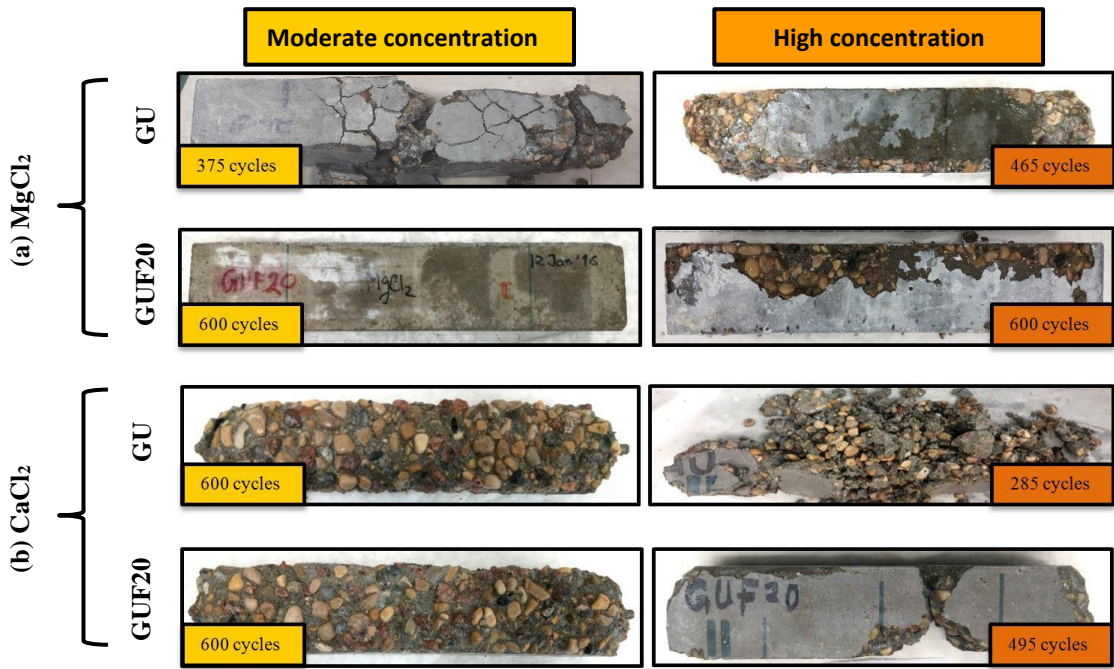
Figure 5.2: Exemplar visual features of damage for the GU and GUF20 specimens exposed to: (a) MgCl$_2$ and (b) CaCl$_2$ salts.
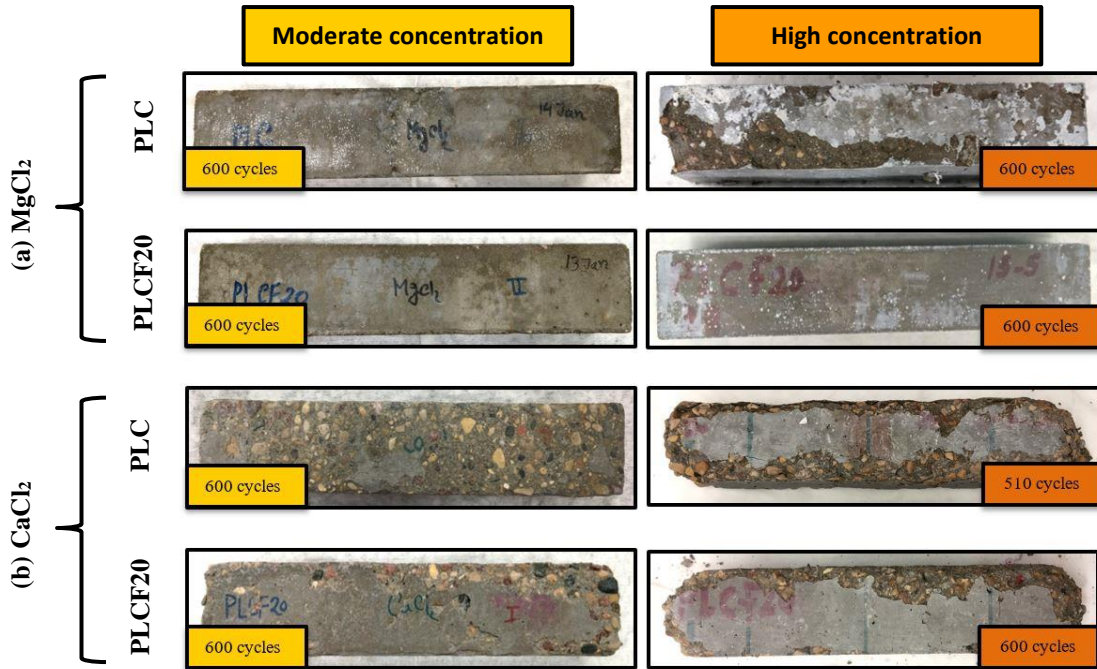
Figure 5.3: Exemplar visual features of damage for the PLC and PLCF20 specimens exposed to: (a) $MgCl_2$ and (b) $CaCl_2$ salts.

Table 5.2: Results of mass loss, expansion, RE_d and the time of the last measurement for specimens exposed to moderate concentration of de-icing salts

Mixture ID.	Moderate concentration								High concentration							
	MgCl$_2$				CaCl$_2$				MgCl$_2$				CaCl$_2$			
	Mass change (%)	Expansion (%)	RE_d	Time[a] (No. of cycles)	Mass change (%)	Expansion (%)	RE_d	Time[a] (No. of cycles)	Mass change (%)	Expansion (%)	RE_d	Time[a] (No. of cycles)	Mass change (%)	Expansion (%)	RE_d	Time[a] (No. of cycles)
GU group																
GU	-26.7	2.56	0	375	-20.8	0.04	82	600	-26.4	1.66	0	465	-27.9	2.89	0	285
GUF20	-0.2	0.02	100	600	-22.1	0.02	85	600	-11.3	0.72	0	600	-19.4	1.69	0	495
GUF30	-0.1	0.01	101	600	-11.6	0.03	89	600	-0.1	0.02	100	600	0.0	0.03	102	600
GUS	0.0	0.03	102	600	0.0	0.03	101	600	0.0	0.02	101	600	0.0	0.03	100	600
GUF20S	0.0	0.02	100	600	0.0	0.01	100	600	0.0	0.03	102	600	0.0	0.01	101	600
GUF30S	0.0	0.03	101	600	0.0	0.02	102	600	0.0	0.01	102	600	0.0	0.02	103	600
PLC group																
PLC	0.0	0.01	100	600	-6.7	0.03	94	600	-8.9	0.43	81	600	14.2	0.71	0	510
PLCF20	-0.1	0.03	100	600	-4.4	0.04	97	600	0.0	0.03	100	600	13.1	0.57	78	600
PLCF30	-0.1	0.01	101	600	0.0	0.03	100	600	0.0	0.02	101	600	0.0	0.03	100	600
PLCS	0.0	0.02	102	600	0.0	0.01	101	600	0.0	0.01	102	600	0.0	0.01	101	600
PLCF20S	0.0	0.01	100	600	0.0	0.02	102	600	0.0	0.02	100	600	0.0	0.02	102	600
PLCF30S	0.0	0.01	101	600	0.0	0.01	100	600	0.0	0.01	103	600	0.0	0.01	101	600

[a] Refers to the time of the last measurement.

5.4.2   Expansion

Table 5.2 shows the total expansion of specimens subjected to both exposures. Complying with the visual assessment and mass loss results, the magnitude of expansion was negligible (maximum of 0.04%) for all specimens in both GU and PLC groups exposed to moderate concentration of $MgCl_2$, except the specimens prepared with the GU cement only, which was 2.56%. Despite the aggravated effect of the moderate concentration of $CaCl_2$ solution on the deterioration of specimens (e.g. GU, PLC, GUF20, PLCF20 and GUF30 specimens), no marked symptoms of expansion were recorded (maximum of 0.04%).

The GU specimens exposed to the high concentration of $MgCl_2$ or $CaCl_2$ solutions showed high expansion (1.66% and 2.89%, respectively) before failure (Table 5.2). Incorporating fly ash in the binder notably decreased the magnitude of the expansion irrespective of the type of solution. For example, the binary binders containing 20% fly ash (GUF20) exposed to the high concentration of $MgCl_2$ or $CaCl_2$ solutions yielded an expansion of 0.72% and 1.69% (reduction of 56% and 42%, respectively, compared to the GU counterparts) after 600 and 495 cycles, respectively. Also, the effect of fly ash was more pronounced in the GUF30 specimens as no marked expansion was recorded.

The expansion trends in the PLC group were mirrored, but were notably lower, compared to the GU counterparts. For example, the PLC specimens exposed to high concentration of $MgCl_2$ or $CaCl_2$ solutions yielded an expansion of 0.43% and 0.71% (reduction of 74% and 76%, respectively) after 600 and 510 cycles, respectively (Table 5.2). Also, the magnitude of expansion was consistently lower (an average of 66%) for the PLCF20 specimens exposed to the high concentration $CaCl_2$ solution compared to the corresponding GUF20 specimens. In addition, the PLCF20 specimens exposed to the high

concentration of $MgCl_2$ did not show any evidence of expansion (maximum of 0.03%). Specimens from the binary binder with 30% fly ash (PLCF30) did not show any evidence of expansion (maximum of 0.03%) under both solutions. Irrespective of the type and concentration of solution, no single mixture made with binary or ternary binders comprising nanosilica exceeded an expansion value of 0.02% throughout the entire exposure (600 cycles), as shown in Table 5.2.

5.4.3 Relative Dynamic Modulus of Elasticity (RE_d)

The results of the drop in RE_d after the exposure (600 F/T cycles) or at the time of failure are listed in Table 5.2. The change in RE_d should capture the internal damage of concrete specimens exposed to chemical and/or physical degradation. Similar to the trends of mass loss and expansion, all specimens in both GU and PLC groups exposed to moderate concentration of $MgCl_2$ solution did not show any drop in the RE_d up to 600 F/T cycles, except the specimens prepared with the GU cement only. These specimens had significant drop in RE_d at 375 cycles, which was expressed by zero RE_d in Table 5.2. The RE_d results of the GU, GUF20 and GUF30 specimens exposed to moderate concentration of $CaCl_2$ solution did not show notable reduction (maximum of 18%) of RE_d up to 600 F/T cycles. However, these specimens had significant mass losses (Table 5.2), which can be attributed to the nature of damage (surface damage).

A similar trend was observed for the PLC and PLCF20 specimens exposed to the moderate concentration of $CaCl_2$; however, the drop in RE_d was notably less (Table 5.2). Conversely, a decreasing trend in RE_d was observed till complete disintegration or failure for the GU and GUF20 specimens exposed to high concentration $MgCl_2$ or $CaCl_2$ solutions, which was expressed by zero RE_d in Table 5.2. A similar trend was observed for the PLC specimens exposed to the high concentration $CaCl_2$ solution. Except for the PLC specimens

exposed to the high concentration $CaCl_2$ solution, the PLC group had lower losses in RE_d after 600 F/T cycles compared to the GU counterparts. Increasing the dosage of fly ash (30%) in the binary binder led to better performance and/or longevity than the reference specimens under both solutions. Again, incorporation of nanosilica in the binders (binary or ternary) led to a consistently high RE_d at or slightly above 100% (Table 5.2) over the entire time of the exposures, irrespective of the type and concentration of solutions.

5.5 Discussion

5.5.1 Effect of the Solution Type and Concentration

In this section, the single binder (GU) specimens are presented as an example in order to demonstrate the effect of the solution type and concentration on the damage mechanisms. Subsequently, the effects of the type of cement, fly ash and nanosilica on the performance of concrete will be discussed. For the $MgCl_2$ salt, the trends of physico-mechanical results of deteriorated specimens were comparable at both concentrations (moderate or high), which suggest that the mechanisms of damage were similar. The XRD results in Fig. 5.4a show that almost both GU specimens exposed to moderate or high concentrations of $MgCl_2$ had similar dominant phases of magnesium oxychloride (in various forms; 3- or 5-form MOX), brucite, gypsum, quartz, dolomite and calcite, except that the intensity of the MOX and gypsum peaks was notably higher in the high concentration solution. This might be attributed to the saturation of the pore fluid with respect to magnesium, calcium, chloride, and hydroxyl ions that lead to favorable conditions for crystallization of a mixture of the 3- and 5-form MOX. The peaks of dolomite and calcite might have occurred because the coarse aggregate contained a fraction (about 10 to 15%) of carboniferous aggregate, while the sources of quartz in the diffractograms originated from the siliceous coarse aggregate and sand in all mixtures.
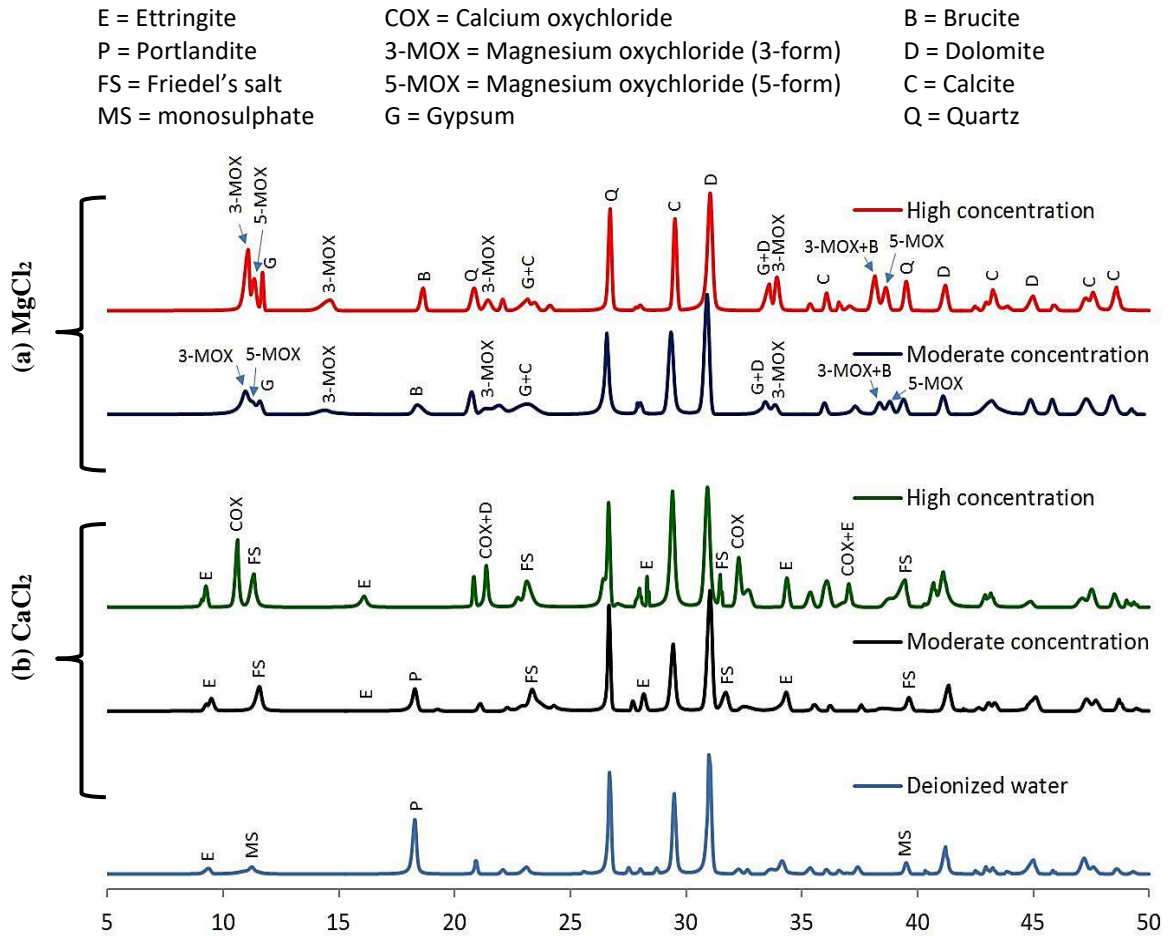
Figure 5.4: XRD analysis of GU specimens exposed to different concentrations of: (a) MgCl₂ and (b) CaCl₂ salts.

The major cause of deterioration by MgCl₂ in both cases (moderate and high concentrations) is likely the chemical activity resulting in formation of relatively expansive (MOX, Fig. 5.5) and softening (gypsum, Fig. 5.6) phases. In the case of moderate

121

concentration, the damage was also aggravated due to the synergistic action of formation of these reaction products and F/T cycles (micro-cracking due to ice formation). These micro-cracks might facilitate further penetrability of the solution, an, in turn, increasing the salt concentration in the specimens. These factors provided favorable conditions for formation of MOX and gypsum in open spaces (cracks, Fig. 5.7a) and air voids (Fig. 5.7b), which impaired their effectiveness (inadequate air-void system) to provide an adequate level of F/T protection, and thus accelerating rate of deterioration compared to that of the corresponding specimens exposed to the high concentration (Table 5.4), where ice formation was not expected (Fig. 5.1).
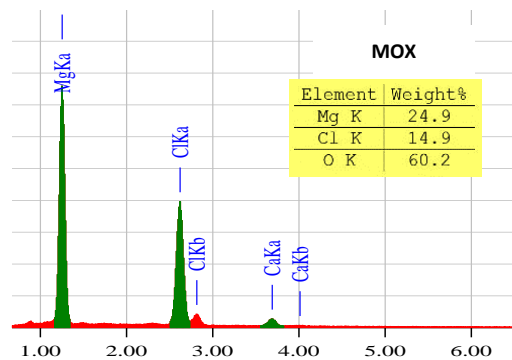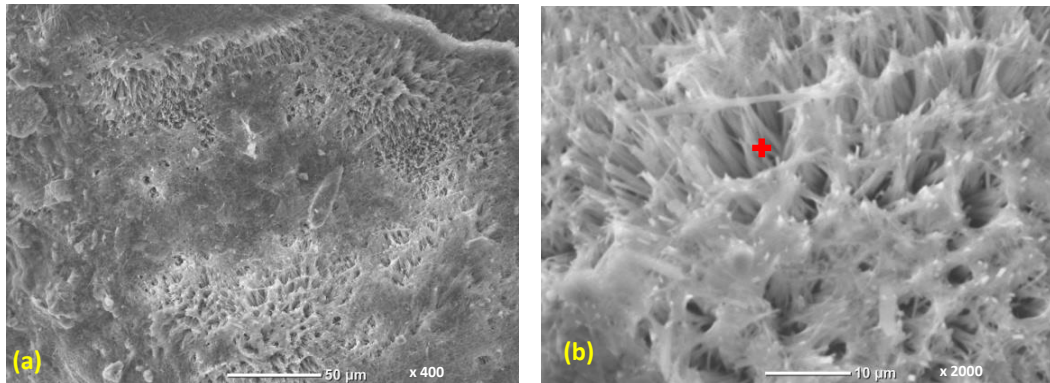
Figure 5.5**:** ESEM micrographs and associated EDX spectrum of fresh fracture pieces tested at 4°C and 80% RH from GU specimens exposed to high concentration of MgCl₂ at the time of failure (Table 5.2) showing: (a) acicular MOX within the surface, and (b) a close-up showing the morphology of the crystals.
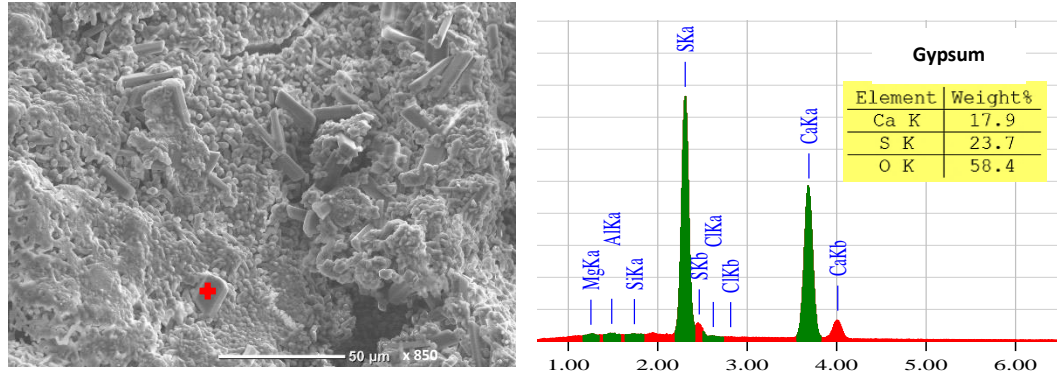
Figure 5.6**:** ESEM micrograph and associated EDX spectrum of fresh fracture piece tested at 4°C and 80-90% RH from GU specimens exposed to high concentration of MgCl₂ at the time of failure (Table 5.2) showing gypsum crystals.
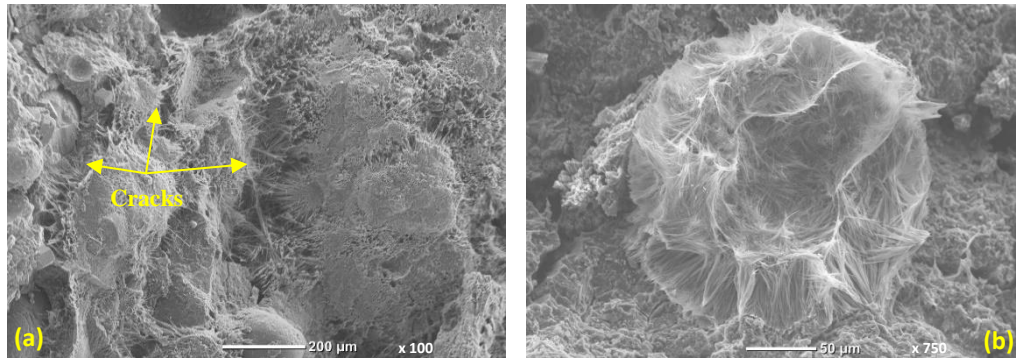
Figure 5.7: Exemplar micrographs of ESEM of a GU specimen at 4°C and 80% RH exposed to moderate concentration of MgCl₂ after 150 F/T cycles showing: (a) reaction products growth in the cracks, and (b) an air void hosting expansive MOX.

The XRD patterns of the specimens exposed to moderate and high concentrations of $CaCl_2$ were different from that in the $MgCl_2$ solutions. At the moderate concentration, Friedel's salt and ettringite were detected in the deteriorated specimens as the main reaction products (e.g. Fig. 5.4b). Also, portlandite peaks were clearly identified. These observations suggest that the chemical activity between the salt and cementitious matrix was not sufficiently triggered at this concentration as portlandite should be significantly consumed in the chemical degradation (formation of calcium oxychloride: COX) process, as shown in Chapter 4. The damage of specimens, in this case, was characterized by paste swelling and spalling (e.g. Fig. 5.8). The swelling of the whole paste around the periphery of coarse aggregate might suggest excessive pore pressure built-up beneath the concrete surface. Friedel's salt and ettringite crystals were observed infilling voids near (within 5 mm) the surface of specimens (e.g. Fig. 5.8). The formation of Friedel's salt was likely a result of the substitution of sulfate ions by chloride ions decomposing monosulphate, or reaction of the solution with other aluminate phases (chloride binding). The releasable sulfate ions may combine with the remaining monosulphate and a part of Friedel's salt already formed in the presence of moisture, precipitating ettringite. This was supported by the higher intensity of the ettringite peaks compared to the reference sample exposed to deionized water (Fig. 5.4). The deposition of these crystals in confined space (especially smaller air voids, e.g. Fig. 5.9) could generate pressure and cause spalling of the surface of concrete during the F/T cycles. Goni et al. (2003) also stated that there might be a link between surface scaling damage and precipitation of Friedel's salt as concrete prepared by cements containing higher aluminate contents (C_3A and C_4AF) were more susceptible to scaling.

The other possible cause of scaling was the large mismatch in the thermal expansion of the ice ($\sim50\times10^{-6}$/°C before melting) and concrete ($\sim10\times10^{-6}$/°C), which might cause excessive tensile stresses and eventually led to scaling of the concrete according to the "glue-spall theory" forwarded by Valenza et al. (2006). A mixture of solid ice and liquid brine was possible in the moderate concentration case as long as its temperature stayed between the freezing and eutectic points (Fig. 5.1). Thus, unfrozen liquid might create pockets of brine, which acted as stress concentrators and promoted cracking of the ice and consequent damage to the underlying concrete. For the high concentration $CaCl_2$ solution, the XRD pattern was comparable to that of the moderate exposure, except that intense peaks of COX were detected (e.g. Fig. 5.4b). In addition, portlandite peaks diminished due to its consumption in the formation of COX. Subhedral pseudo-hexagonal plates and very tiny fibrous crystals were a prevailing feature observed by ESEM for the COX phase (e.g. Fig. 5.10). Formation of fibrous and platy COX was accompanied by significant expansion (Table 5.2) and cracking, which led to complete disintegration of specimens, even without freezing (chemical degradation).
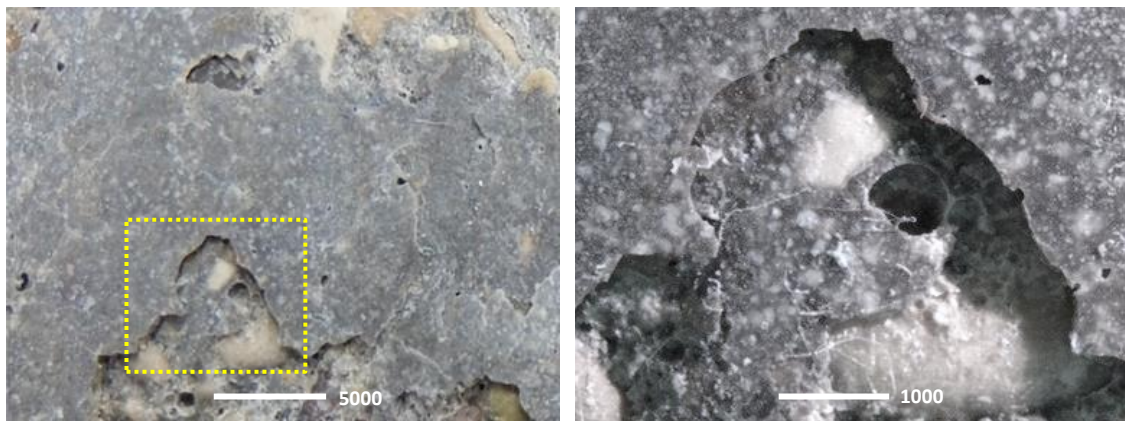
Figure 5.8: Paste swelling on the surface of GU specimens exposed to moderate concentration of $CaCl_2$ after 50 F/T cycles.
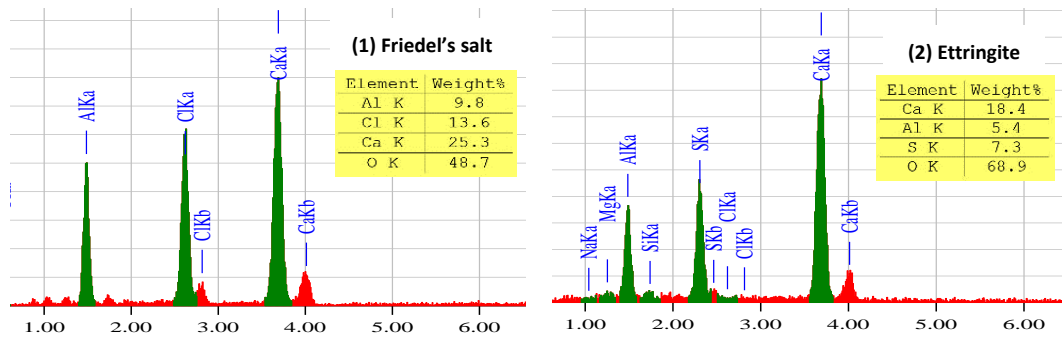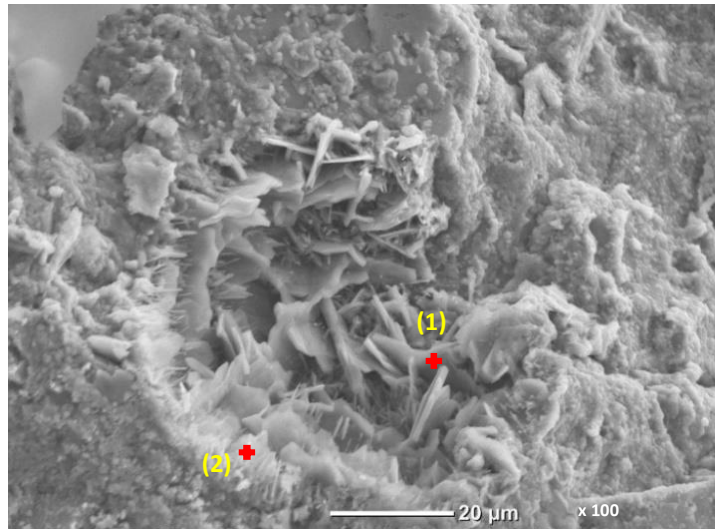
Figure 5.9: ESEM micrograph and EDX analyses of fresh fracture pieces tested at 4°C and 80% RH from GU specimens exposed to moderate concentration of $CaCl_2$ after 600 F/T cycles showing air void hosting mixed crystals of Friedel's salt and ettringite.
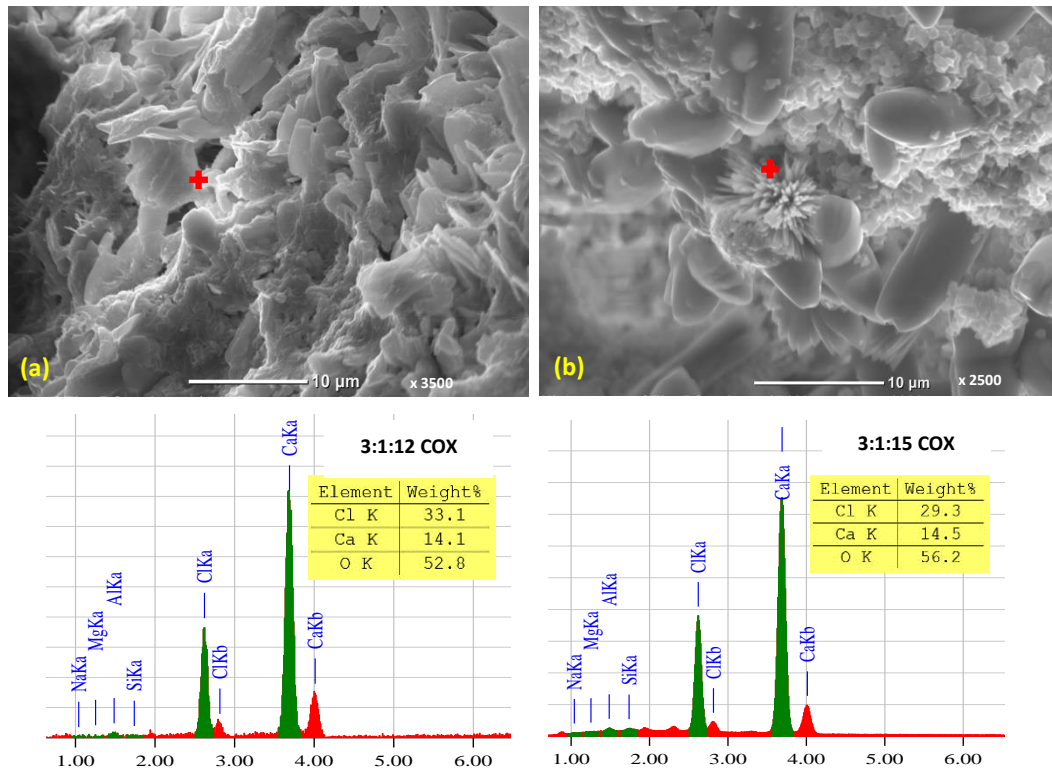
Figure 5.10**:** ESEM micrographs and associated EDX spectra of fresh fracture piece at 4°C and 80% RH from GU specimens exposed to high concentration of $CaCl_2$ at the time of failure (Table 5.2) showing: (a) platy and (b) fibrous COX crystals.

5.5.2   Effect of Type of Cement

Generally, the physico-mechanical results showed similar performance among the GU mixtures and corresponding PLC mixtures, with some improvement in the retention of stiffness and mass (less mass loss, Table 5.2) for the PLC mixtures. The physical resistance of all specimens after curing (28 days) was evaluated by the RCPT and MIP and the results are listed in Table 5.3. After completing the RCPT, the physical penetration depth of chloride front was measured for concrete specimens as indicated by the whitish precipitate (e.g. Fig. 5.11). Also, the non-steady-state migration coefficient was calculated based on the penetration depth, geometry of specimen, applied voltage, temperature of the anolyte solution and test duration, according to NT BUILD 492 (2011), to account for the heat (Joule) effect and different testing durations, if any, on ionic mobility within specimens. However, the concrete mixtures tested herein had *w/b* of 0.40 and comprised SCMs (except for the reference GU and PLC mixtures). Therefore, the cell compartments showed small temperature rise (maximum of 4°C) and the test duration was constant (6 h). From Table 5.3, it can be noted that the trends of RCPT were consistent with that of MIP in the sense that small penetration depths/migration coefficients corresponded to low cumulative intrusion (apparent total porosity) and/or further pore size refinement and vice versa.

Table 5.3: Results from RCPT and MIP

Mixture ID.	RCPT				MIP			
	Charges Passed, coulombs	Chloride Ions Penetrability Class, ASTM C1202	Average Penetration Depth, mm	Migration Coefficient, $\times 10^{-12} m^2/s$	Apparent Total Porosity, %	Threshold Pore Diameter, μm	Average Pore Size, μm	Proportion of Micro-Pores (<0.1 um), %
GU group								
GU	2248	Moderate	17.6 (0.94)[a]	17.67	15.3	0.120	0.189	63.3
GUF20	1527	Low	12.8 (0.64)	10.16	15.6	0.112	0.115	71.2
GUF30	1253	Low	10.1 (0.57)	8.16	16.2	0.103	0.093	73.4
GUS	743	Very Low	5.3 (0.60)	4.24	10.4	0.060	0.013	78.2

GUF20S	556	Very Low	5.1 (0.73)	4.01	10.1	0.075	0.014	78.2
GUF30S	463	Very Low	4.2 (0.64)	2.85	8.7	0.055	0.009	79.4
PLC group								
PLC	1867	Low	13.1 (1.07)	12.93	12.6	0.100	0.178	71.1
PLCF20	1370	Low	11.4 (1.14)	9.81	12.7	0.115	0.111	73.4
PLCF30	917	Very Low	9.4 (0.96)	8.01	13.1	0.105	0.086	74.0
PLCS	871	Very Low	6.3 (0.81)	5.61	10.6	0.073	0.013	79.3
PLCF20S	447	Very Low	4.6 (0.38)	3.86	9.8	0.070	0.012	78.6
PLCF30S	375	Very Low	4.3 (0.53)	3.01	7.2	0.043	0.007	81.1

[a] Standard error is shown between brackets.
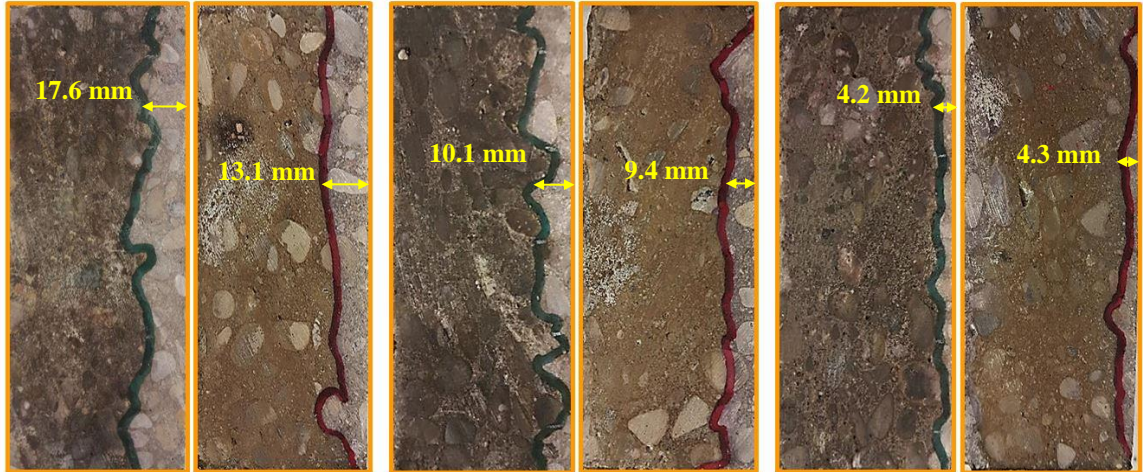
Figure 5.11: Whitish precipitates showing the average penetration depth of chloride ions in specimens (GU left and PLC right): (a) single binder, (b) binary binder (30% fly ash), and (c) ternary binder (30% fly ash with nanosilica).

The control specimens from PLC mixture showed about 26% reduction in the penetration depth relative to the control GU specimens. This might be ascribed to the higher fineness of the PLC (460 m^2/kg) in comparison to the GU cement (390 m^2/kg) due to intergrinding limestone powder with clinker, which can improve the hydration process and microstructural evolution of concrete. In addition, the filler effect resulting from the continuous particle size distribution of PLC may yield better particle packing in the matrix (Marzouki et al. 2013). Accordingly, PLC mixtures had reduced ingress of salt solutions and consequently better resistance to physical/chemical degradation by de-icing salts, which generally performed better and/or survived longer than the GU specimens as shown earlier in the Results section, irrespective of the type and concentration of the solutions.

The limestone component in PLC also changed the hydration pattern of the binder as shown by the XRD for the reference sample exposed to deionized water in Fig. 5.12. Carboaluminate appeared as a distinctive reaction product between limestone powder and various aluminate compounds (e.g. hydroxy-AFm and monosulphate). The formation of carboaluminate-type compounds in portland-limestone cements was also observed in previous studies (Lothenbach et al. 2008; Ipavec et al. 2013). The ability of carboaluminate hydrates to bind chloride was reported to be significantly less than other AFm compounds (e.g. monosulphate) (Ipavec et al. 2013). This was corroborated herein by the lower intensities of Friedel's salt peaks in the XRD pattern, as for example noted in the PLC specimens exposed to moderate concentration of $CaCl_2$ solution (Fig. 5.12), compared to their corresponding GU specimens (Fig. 5.4).

The liberated carbonate ions might also be bound in calcite. The sources of calcite herein could not be definitively resolved as the coarse aggregate initially contained a fraction (about 10 to 15%) of carboniferous aggregate; however, the intensities of the calcite peaks were more pronounced than their corresponding peaks in the GU specimens. Balonis et al. (2010) proved this conversion among monocarboaluminate, Friedel's salt and calcite in synthetic hydrated materials due to $CaCl_2$ solution. Also, they reported that the volume changes, in this case, were much reduced relative to those in the carbonate-free system. These physical and chemical effects of limestone might explain the significant improvement in the resistance of PLC mixtures to surface scaling in the moderate concentration cases (an average of 67% reduction in the mass loss relative to the GU specimens exposed to moderate concentration $CaCl_2$, Table 5.2).

On the other hand, the lower clinker component (due to dilution by 12% interground limestone) in the PLC cement reduced the initial portlandite (at 28 days) in these mixtures;

subsequently, the potential for the chemical activity under both high concentration salts.

These trends were supported by DSC results for the portlandite contents at 28 days (before

exposure), as shown in Table 5.4. Moreover, the PLC mixtures had lower C_3A content

relative to the GU mixtures resulting in slower chemical activity (incipient formation of

Friedel's salt). This trend was supported by the XRD analysis (Fig. 5.12) as the intensities

of the reaction products (COX, Friedel's salt, ettringite, MOX, and gypsum) for the PLC

specimens exposed to high concentration $MgCl_2$ and $CaCl_2$ solutions were notably lower

than their corresponding GU specimens. Hence, PLC specimens performed better and/or

survived longer than the GU specimens exposed to high salt concentrations.
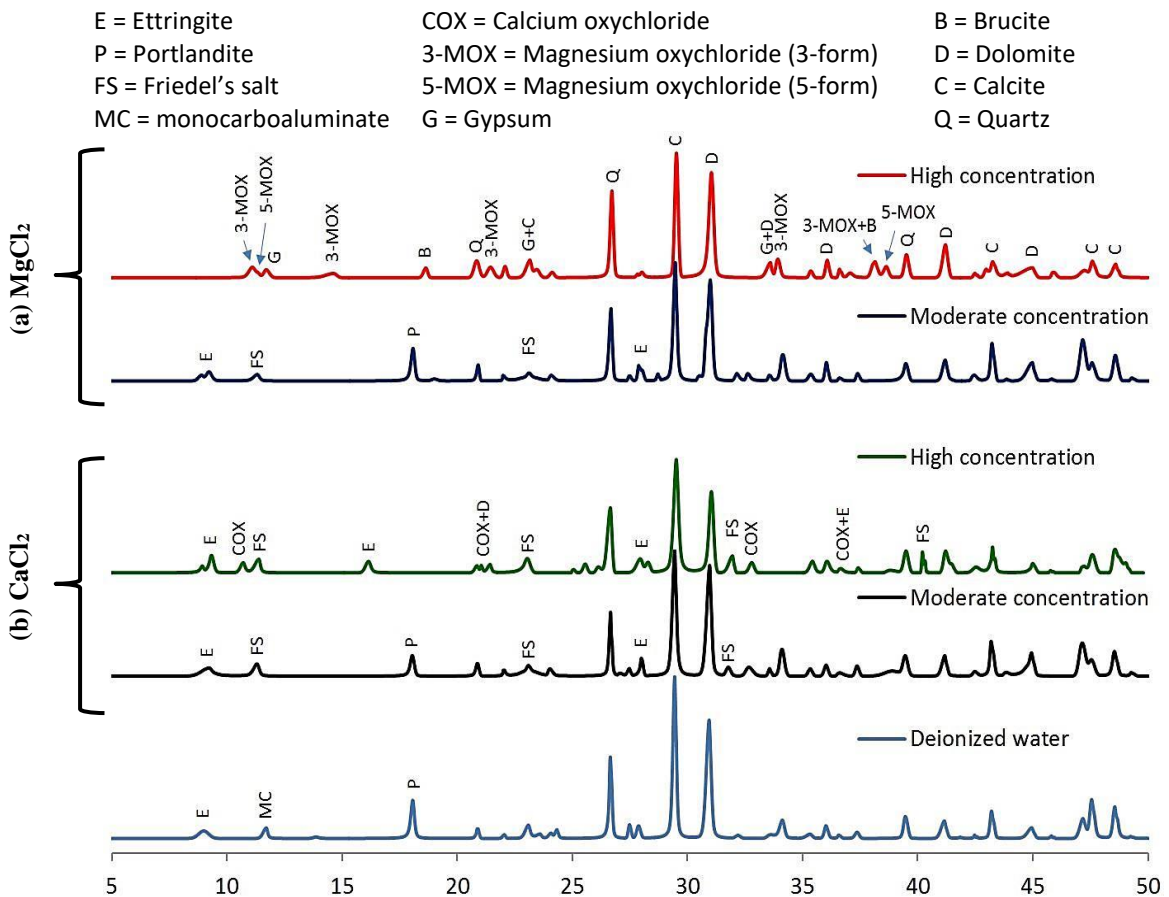
Figure 5.12: XRD analysis of PLC specimens exposed to different concentrations of: (a) $MgCl_2$ and (b) $CaCl_2$ salts.

5.5.3   Effects of Fly Ash and Nanosilica

Compared to the single binder (GU and PLC) mixtures, the incorporation of fly ash in binary binders reduced the penetrability of concrete. For instance, adding 20 and 30 % fly ash in binary binders (GUF20 and GUF30) led to approximately 43 and 54% reduction in the migration coefficient of specimens compared to that of the corresponding specimens prepared with the GU cement only, which was 17.67×10^{-12} m^2/s. The reduction of the penetration depth/migration coefficient, despite the increase of apparent porosity (by 10 and 15%, respectively), can be attributed to the notable reduction of the average pore size (Table 5.3) and correspondingly, the effective porosity; thus, reducing the penetrability of the matrix (increased physical resistance). In addition, the initial portlandite content in these specimens decreased with increasing the dosage of fly ash in the binders (Table 5.4) owing to the dilution of the cement component, consequently limiting the chemical activity. Hence, fly ash mixtures performed better and/or survived longer than the reference GU or PLC specimens, especially the mixture containing 30% fly ash, as shown earlier in the Results section.

Table 5.4: Enthalpies (J/g) of portlandite in the cementitious matrix

Mixture ID.	After 28 days in the	After 600 F/T cycles in	After 600 F/T cycles or at the failure point[a] in the de-icing salts	
			Moderate concentration	High concentration

	curing chamber	deionized water	MgCl$_2$	CaCl$_2$	MgCl$_2$	CaCl$_2$
GU group						
GU	63.6	62.1	0.0[a]	52.6	0.0[a]	0.0[a]
GUF20	56.8	50.4	47.9	49.2	0.0[a]	0.0[a]
GUF30	44.8	39.7	39.8	40.1	38.9	37.3
GUS	23.9	17.9	17.4	16.6	16.9	18.1
GUF20S	8.9	5.7	3.6	4.4	3.1	2.7
GUF30S	7.0	5.3	0.9	0.7	0.2	0.3
PLC group						
PLC	53.6	46.8	47.8	46.1	0.0[a]	0.0[a]
PLCF20	48.3	43.3	44.9	45.3	43.3	0.0[a]
PLCF30	38.8	32.7	34.7	35.3	33.2	32.1
PLCS	20.4	14.6	17.2	19.1	16.1	17.2
PLCF20S	9.1	3.9	5.1	3.1	2.9	3.0
PLCF30S	5.8	4.1	0.8	0.1	0.0	0.0

The DSC results showed that there was no efficient later-age pozzolanic activity of Type F fly ash in the binary specimens as indicated by the presence of high portlandite contents at the end of the exposure (average consumption of 10% after 600 F/T cycles in deionized water or in the intact specimens, Table 5.4). This implies that the long-term activity of fly ash was hindered at this range of low temperature (4°C to -18°C), especially that these specimens were initially cured for 28 days. This might explain the degradation observed in the specimens comprising 20% fly ash exposed to the high concentration of MgCl$_2$ and CaCl$_2$ solutions (but after the GU specimens with higher initial portlandite contents and penetrability). Comparatively, the specimens comprising 30% fly ash did not fail under such exposure (high concentrations of de-icing salts) due to the improved physical (low penetrability) and chemical (low initial portlandite) resistances.

Perhaps, if the binary specimens comprising 20% fly ash were initially cured for longer periods (56 days or more) before exposure, the effect of 20% fly ash might have been more improved. This is suggested by the behaviour of ternary binders comprising 20% fly ash combined with a more reactive pozzolanic material (nanosilica), as discussed later in this section. At moderate concentrations (MgCl$_2$ or CaCl$_2$), the portlandite contents

in the binary specimens incorporating 20 and 30% fly ash after 600 F/T cycles were close to their initial values before exposure (at 28 days), which suggested limited chemical activity for these mixtures (Table 5.4). It seems that the amount of solution absorbed and content of $Ca(OH)_2$ initially present in these specimens were insufficient to trigger the chemical reactions necessary for forming the complex salts of MOX or COX. However, the unbound fly ash particles in these matrices, especially with the hindered long-term pozzolanic activity, led to notable surface scaling under the aggressive de-icing salt ($CaCl_2$) and F/T cycles. This trend diminished in the $MgCl_2$ case, likely due to the formation of a thin film of magnesium hydroxide ($Mg(OH)_2$) on the surface of the specimens which acted as a partial barrier to deeper penetration of the salt. The effect of fly ash was magnified in the PLC group for both concentrations (moderate and high) owing to the improvement effect of the limestone component in cement, as discussed earlier.

The trends of specimens containing nanosilica are consistent with the effects of nanosilica on cementitious systems, which contribute to microstructural development of cement-based materials through multiple mechanisms, including accelerated pozzolanic activity, filler effect, and water absorption into the high surface area of silica aggregates/agglomerates (reduction of *w/b* in the paste). Details of such mechanisms were previously described in other studies (Ghazy et al. 2016; Zadeh et al. 2013; Said et al. 2012; Madani et al. 2012). Using nanosilica with a specific surface of 80,000 m^2/kg in the binary and/or ternary binders led to speeding up the rate of hydration and pozzolanic reactions, resulting in refined microstructure, as reflected by the results in Table 5.3. For example, incorporation of 6% nanosilica in the binary system (GUS) led to an average reduction of the migration coefficient by 76% and total porosity by 36%, compared to the reference GU concrete. Also, the proportion of the micro-pores in these systems comprising nanosilica

was notably increased, which led to smaller threshold pore diameters (an average of 47% reduction relative to the GU specimens), and in turn reduced penetrability of these matrices and solution uptake with no signs of damage irrespective of the type and concentration of solution, as shown earlier in the Results sections.

In addition to the much improved physical resistance, nanosilica vigorously sped-up the kinetics of cement hydration and fly ash reactivity. This was substantiated by the DSC results (Table 5.4) as the incorporation of nanosilica catalyzed the reactivity of fly ash, resulting in an average reduction of the initial portlandite contents in the ternary mixtures (GUF20S and GUF30S) by 83 and 86%, respectively, compared to the corresponding binary mixtures (GUF20 and GUF30), and consequently better resistance to chemical degradation by high concentrations of de-icing salts. Also, no surface scaling was observed under the moderate concentration $CaCl_2$ when the ternary binders were modified with nanosilica due to binding of fly ash in the system. The combination of fly ash with nanosilica led to a dense matrix, as reflected by the RCPT and MIP results in Table 5.3, which might discount the process of crack propagation in the surface of concrete in such an exposure (moderate concentration), and thus increasing its resistance to salt-frost scaling.

CHAPTER 6 – PHASE II: RESPONSE OF CONCRETE TO CYCLIC ENVIRONMENTS AND CHLORIDE-BASED SALTS

In the previous chapters (4 and 5), separate exposure regimes (constant low temperature, W/D, or F/T) were used to evaluate the performance of a wide range of concrete mixture under de-icing salts. Considering the demand for 'holistic' tests to improve the reliability of assessment of concrete performance, combinations of exposure procedures should be also explored. Hence, the present chapter investigates the resistance of concrete, studied in the previous chapters, to the concomitant action of de-icing salts and cyclic (alternating W/D and F/T) environments, which simulates real field conditions.

6.1 Introduction

The adverse effects of de-icing salts on concrete have been a key durability issue and a subject of extensive investigation for many decades. In laboratory-simulated conditions, different exposure schemes have been used to mimic concrete exposed to environmental conditions combined with de-icing salts. Previous studies focused on individual exposure regimes such as continuous immersion, wetting/drying (W/D) cycles or freezing/thawing (F/T) cycles, to evaluate the performance of concrete to de-icing salts (Wu et al. 2015; Darwin et al. 2008; Wang et al. 2006a; Lee et al. 2000). However, there have been instances of different performance of concrete in such individual testing regimes from that observed in the field due to overlooking some important parameters existing in the field (Bouzoubaâ et al. 2011; Marchand et al. 2005; Bilodeau et al. 1992). The damage process disintegrates the hydrated cement paste to various levels

---

based on the prevailing exposure conditions and key mixture design parameters of concrete. For example, in Chapter 4, testing/evaluating mixtures with slow reactivity materials (e.g. fly ash or slag) under continuous immersion at low temperatures (4 to 10°C), the frequently used exposure to evaluate the chemical effect of de-icing salts on concrete (Peterson et al. 2013; Cody et al. 1996), may give erroneous conclusions as this exposure hinders the long-term activity of these materials. Thus, there is need to develop performance-based tests comprising multiple damage mechanisms as well as field parameters to improve the understanding of their combined effects on normal and emerging concretes.

Prior studies on the effect of de-icers on concrete mainly focused on conventional concrete (Wu et al. 2015; Peterson et al. 2013; Darwin et al. 2008; Wang et al. 2006a; Cody et al. 1996). One of the theoretically promising strategies to mitigate the degradation of concrete by de-icing salts is the use of supplementary cementitious materials (SCMs). However, the nature of physical and chemical interactions in the damage process, and how they are affected by the presence of SCMs in the cementitious system are still uncertain. For example, some laboratory studies indicated that concrete containing more than 20% fly ash often performs unsatisfactorily when exposed to F/T cycles in the presence of de-icing salts (Wu et al. 2014; Marchand et al. 2005; Malhotra et al. 2000; Bilodeau et al. 1992). However, there are several cases reported of concrete incorporating similar amounts of such SCMs that have performed well in the field (e.g. Bouzoubaâ et al. 2011; Marchand et al. 2005). These discrepancies between experimental and field data as well as unresolved practical limitations in field applications such as delay in setting time, strength gain, and microstructural development, led to limiting the dosage of fly ash to less than 15-20% by many departments of transportation in North America (Material Specification for Concrete

– Ontario, 2014; Standard Specifications for Construction of Roads and Bridges on Federal Highway Projects 2014). Nevertheless, these performance limitations associated with the use of slowly reactive SCMs (e.g. Class F fly ash) can be mitigated by incorporation of nanoparticles (size scale of 1-100 billionth of a meter) in this concrete (Ghazy et al. 2016; Belkowitz et al. 2015; Said et al. 2012). As a promising emerging material in construction, nanoparticles (e.g. nanosilica) have been applied in the production of concrete and proven to enhance fresh and hardened properties by modifying the structure of the cementitious matrix at the nano- and micro-levels. Therefore, their application in concrete may have a great potential to produce innovative types of fly ash concrete with superior performance for concrete pavements and bridges exposed to concentrated de-icing salts.

Recently, portland limestone cement (PLC), containing up to 15% limestone powder, has been introduced in the North American market due to their economic and ecological benefits. While there are a number of studies on the hydration and strength characterization of concrete made from PLC (Li et al. 2017; Marzouki et al. 2013; Ramezanianpour et al. 2013) and its response to durability issues such as sulfate attack (Ramezanianpour et al. 2013) and chloride ions penetration (Thomas et al. 2010), there has been dearth of information and field experience on the effect of PLC on the performance of concrete exposed to de-icing salts; hence, the wider use of PLC in transportation infrastructure remains limited in North America.

6.2 Research Significance

The ongoing international shift to performance-based standards and specifications for concrete demands the development of new approaches that better correlate to service conditions. Given the aforementioned research needs, in this study, a combination of exposure procedures (alternating W/D and F/T cycles) with the most widely used chloride-

based de-icing salts (individual and combined) was designed to mimic the field performance of the concrete pavements and bridges. Such combinations are more relevant to in-service conditions than their individual effects on concrete. In addition to normal/reference concrete (ordinary and PLC), concretes incorporating nanosilica without and with different dosages of fly ash were tested. The physico-mechanical properties and alteration of microstructure were used to evaluate the performance of the mixtures. Results from this investigation should contribute fundamental understanding of the underlying mechanisms of concrete degradation under such conditions. In addition, they would substantiate the potential benefits of nanoparticles and PLC, if any, in mitigating this type of damage and hence improve the current specifications and guidance for concrete exposed to extensive use of de-icing salts.

6.3 Experimental Program

6.3.1 Materials and Mixtures

The materials and mixtures used in this Chapter were similar to that used in Chapter 4 (refer to Section 4.3.1).

6.3.2 Exposures

Alternating W/D and F/T cycles were applied in order to simulate successive spring/summer and winter seasons, respectively. This cyclic exposure might mimic the annual built up of Cl⁻ ions within the surface of concrete pavements. A spring/summer season was simulated by six W/D cycles, while a winter season consisted of 30 successive F/T cycles. A W/D cycle (five days) consisted of full immersion of specimens for two days in the de-icing salt solutions at a temperature of 5°C, followed by drying at 23 ± 2°C and $55\pm5\%$ RH for two days and an additional day at 40 ± 2°C and $30\pm5\%$ RH in an environmental chamber. The specimens were then subjected to de-icing slats combined

with F/T cycles according to the general procedures of ASTM C666 test procedure A, expect that de-icing salt solutions were used instead of water and the frequency of F/T per day was less to allow chemical reactions, if any, with hydrated paste. The duration of one F/T cycles was 12 hours: freezing at $-18\pm1°C$ for 7 h and thawing at $4\pm1°C$ for 3.5 h, and 45 min to ramp to the minimum freezing temperature or the maximum thawing temperature. This regime of exposure has been applied for 540 days (12 spring/summer alternating with 12 winter seasons).

Sodium chloride (NaCl), dihydrate form of calcium chloride ($CaCl_2·2H_2O$) and hexahydrate form of magnesium chloride ($MgCl_2·6H_2O$) with purity of 99, 96 and 96%, respectively were used to prepare the solutions. In addition, combined salts ($MgCl_2·6H_2O$ and $CaCl_2·2H_2O$) were applied to simulate anti-icing and de-icing strategies. Table 6.1 shows the concentrations of the de-icing solutions used in the present study. High concentrations of de-icing salts solutions were applied during the W/D exposure to maximize the potential chemical interactions between the de-icers and concrete, while lower concentrations were used during the F/T regime to incorporate the effect of physical degradation (solution with ice) according to the phase diagrams for these salts (Kelting et al. 2010). These concentrations had been selected to maintain similar ionic concentration of chloride (Cl^-) ions in each solution for each state. The solutions were renewed before each exposure (W/D and F/T) to keep a continual supply of de-icing salts, thus providing aggravated damage conditions.

Table 6.1: Concentration of de-icing salt solutions

Type of Salt	Concentrations during F/T cycles			Concentration during W/D cycles		
	Salt Concentration Mass (%)	Chloride Concentration (mol/l)	Chloride Concentration[a] (ppm)	Salt Concentration Mass (%)	Chloride Concentration (mol/l)	Chloride Concentration[a] (ppm)
NaCl	14.2	2.83	100,630	23.3	4.52	160,071
MgCl₂	11.9	2.82	100,735	19.1	4.52	160,069
CaCl₂	13.6	2.81	100,731	21.9	4.51	160,067
MgCl₂+CaCl₂	5.9+6.8	2.82	100,733	9.6+10.9	4.52	160,073

[a] The ionic concentration of Cl⁻ ions in each solution was verified by ion chromatography according to ASTM D4327.

6.3.3   Tests

Similar to Chapters 4 and 5, the physical resistance of the concrete specimens was evaluated by the rapid chloride penetrability test (RCPT) and mercury intrusion porosimetry (MIP). Also, the physico-mechanical properties (mass, length (ASTM C 157) and dynamic modulus of elasticity, E_d (ASTM C 215)) of the specimens were measured versus time of exposure. In addition, the alteration of microstructure in deteriorating specimens was assessed by microscopy, thermal and mineralogical analyses (refer to Section 4.3.3).

6.4 Results

6.4.1   Visual Assessment and Mass Change

Visual examination was regularly made to assess the condition of the specimens (e.g. Figs. 6.1 and 6.2). Also, the mass change of specimens with time was determined and summarized in Table 6.2. For the NaCl solution, specimens made with the single (GU and PLC) and binary binders containing 20% fly ash (GUF20 and PLCF20) were intact with limited surface scaling (maximum of 5%, Table 6.2), minor pop-outs and no evidence of significant degradation (Figs. 6.1a and 6.2a). Also, no specimens from the other binders had any evidence of damage or reduction in the engineering properties up to 540 days (Table 6.2). Comparatively, the GU specimens exposed to the MgCl₂ solution suffered

141

notable scaling within the first 6 W/D cycles (spring/summer season) with mass loss of 8%. Subsequently, micro-cracks along the edges and/or at the corners of these specimens accompanied by spalling as well as swelling were the main features of damage during the subsequent winter season (first 30 F/T cycles). These features of damage were repeated until complete disintegration at 90 days with a mass loss of 18%. Similar features of damage were observed for the PLC specimens, except that these specimens survived longer (135 days) than the GU specimens (Fig. 6.1a). On the other hand, specimens from the binary binder with 20% fly ash (GUF20 and PLCF20) had abruptly failed by transverse cracks (e.g. Fig. 6.2b) at 150 and 240 days, respectively, without excessive mass loss (7% and 3%, respectively).

The $CaCl_2$ solution was more aggressive than the $MgCl_2$ solution as the rate of deterioration of specimens was very rapid. The GU and PLC specimens exhibited significant surface scaling on all faces after 45 days, with mass losses of 11 and 9%, respectively. Subsequently, these specimens suffered significant degradation with visible macro-cracks on the surface which led to complete disintegration at 60 and 105 days, respectively (e.g. Fig. 6.1c). Unlike the reference specimens (GU and PLC), specimens made with binary binders containing 20% fly ash (GUF20 and PLCF20) exposed to the $CaCl_2$ failed by transverse cracks (e.g. Fig. 6.2c) at 105 and 150 days, respectively, without excessive mass loss (maximum of 5%).

Among all the de-icing salt solutions used, the combined salt ($MgCl_2$+$CaCl_2$) was the most aggressive. For example, the reference specimens (GU and PLC) failed within 45 days by widespread transverse cracks (Fig. 6.1d). Also, the GUF20 and PLCF20 abruptly failed after 90 and 135 days, respectively due to significant swelling with visible macro-cracks (Fig. 6.2d). Generally, all specimens made with binary binders containing 30% fly

ash (GUF30 and PLCF30) and exposed to different salt solutions were intact with no evidence of degradation up to 540 days. Also, irrespective of the type of binder (binary or ternary), all the specimens comprising nanosilica and exposed to different salt solutions showed no visible features of damage up to the end of this combined exposure (Appendix A, Fig. A.5 and A.6).
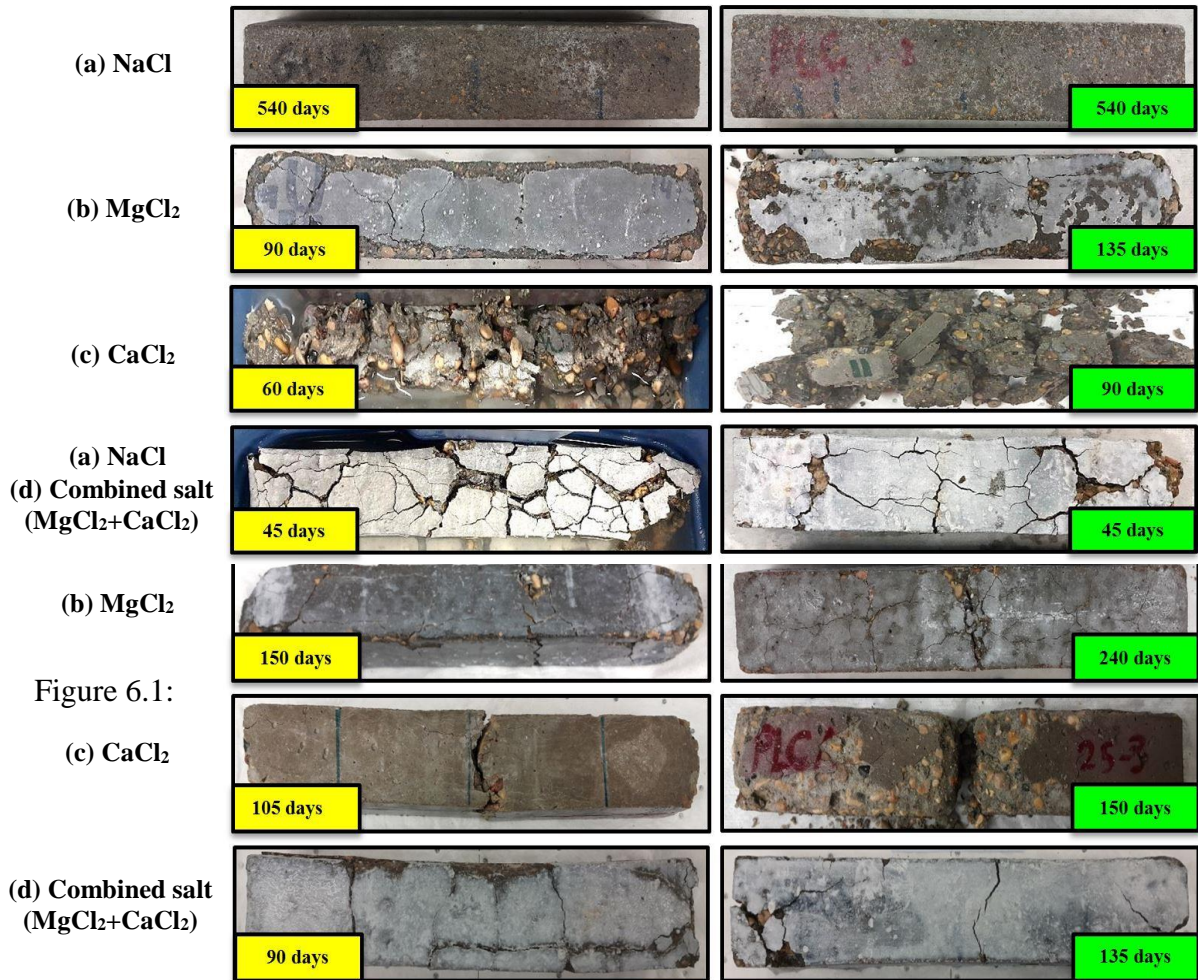
Figure 6.1:

Exemplar visual features of damage for the GU (left) and PLC (right) specimens exposed to different de-icing salts.

Figure 6.2: Exemplar visual features of damage for the GUF20 (left) and PLCF20 (right) specimens exposed to different de-icing salts.

Table 6.2: Results of mass loss, expansion, RE_d and the time of the last measurement for all specimens

Mixture ID.	NaCl				MgCl₂				CaCl₂				Combined salt (MgCl₂+CaCl₂)			
	Mass change (%)	Expansion (%)	RE_d	Time[a] (days)	Mass change (%)	Expansion (%)	RE_d	Time[a] (days)	Mass change (%)	Expansion (%)	RE_d	Time[a] (days)	Mass change (%)	Expansion (%)	RE_d	Time[a] (days)
GU group																
GU	-5.3	0.03	99	540	-18.3	1.91	0	90[†]	-28.4	2.84	0	60[†]	-17.9	3.21	0	45[†]
GUF20	-4.6	0.02	101	540	-7.1	1.73	0	150[†]	-2.3	2.44	0	105[†]	-7.4	2.49	0	90[†]
GUF30	0.0	0.01	99	540	0.0	0.03	100	540	0.0	0.02	100	540	0.0	0.03	102	540
GUS	0.0	0.03	101	540	0.0	0.02	101	540	0.0	0.02	103	540	0.0	0.03	100	540
GUF20S	0.0	0.02	102	540	0.0	0.02	103	540	0.0	0.03	102	540	0.0	0.01	100	540
GUF30S	0.0	0.03	101	540	0.0	0.01	102	540	0.0	0.01	102	540	0.0	0.02	103	540
PLC group																
PLC	-4.4	0.01	100	540	-16.7	1.62	0	135[†]	-26.3	2.23	0	90[†]	-11.2	2.71	0	45[†]
PLCF20	-3.2	0.03	101	540	-3.4	1.56	0	240[†]	-4.7	1.96	0	150[†]	-3.9	2.57	0	135[†]
PLCF30	0.0	0.01	101	540	0.0	0.03	100	540	0.0	0.02	101	540	0.0	0.03	101	540
PLCS	0.0	0.02	102	540	0.0	0.02	102	540	0.0	0.01	100	540	0.0	0.03	101	540
PLCF20S	0.0	0.01	101	540	0.0	0.02	102	540	0.0	0.03	101	540	0.0	0.01	100	540
PLCF30S	0.0	0.01	102	540	0.0	0.01	103	540	0.0	0.01	103	540	0.0	0.02	102	540

[a] Refers to the time of the last measurement.
[†] Specimens failed after this stage.

6.4.2   Expansion

Table 6.2 shows the total expansion of specimens. Complying with the visual assessment and mass loss results, the magnitude of expansion was negligible (maximum of 0.03%) for all specimens from the GU and PLC groups exposed to the NaCl solution. In contrast, the reference specimens (GU) immersed in the $MgCl_2$, $CaCl_2$ and combined salts showed high expansion (1.91%, 2.84%, and 3.21%, respectively) before failure. Also, the expansion trends of the PLC specimens were mirrored, but they were slightly lower compared to the GU counterparts as shown in Table 6.2. Generally, incorporating fly ash in the binder decreased the rate of expansion irrespective of the type of solution. For example, the binary binders containing 20% fly ash (GUF20) immersed in the $MgCl_2$, $CaCl_2$, and combined salts solutions yielded an expansion of 1.73%, 2.44%, and 2.49% (reduction of 10%, 14%, and 22%, respectively, compared to the GU counterparts, Table 6.2). Also, the effect of fly ash was more pronounced in the GUF30 and PLCF30 specimens as no marked expansions were recorded (maximum of 0.03%). Irrespective of the type of solution, no single mixture made with binary or ternary binders comprising nanosilica exceeded an expansion value of 0.03% throughout the entire exposure (540 days), as shown in Table 6.2.

6.4.3   Relative Dynamic Modulus of Elasticity (RE_d)

The results of the drop in RE_d after the exposure (540 days) or at the time of failure are listed in Table 6.2. The change in RE_d should capture the internal damage of concrete specimens exposed to chemical and/or physical degradation. Despite that the reference specimens (GU and PLC) exposed to NaCl solution had minor scaling (4% and 3%, Table 6.2), these specimens did not show any reduction in RE_d. Conversely, a decreasing trend in RE_d was observed till complete disintegration or failure for the GU and PLC specimens

exposed to the $MgCl_2$, $CaCl_2$ and combined salts, which was expressed by zero RE_d in Table 6.2. Also, a drop of RE_d was recorded for the specimens made with the binary binder containing 20% fly ash (GUF20 and PLCF20) exposed to the $MgCl_2$, $CaCl_2$ and combined salts conforming to the expansion trends. However, these specimens did not show significant mass losses (Table 6.2), which can be attributed to the nature of damage (internal damage), as explained in the discussion section. Comparatively, the specimens comprising 30% fly ash and/or nanosilica maintained a high RE_d at or slightly above 100% over the entire time of the exposure in all de-icing salt solutions (Table 6.2).

6.5 Discussion

6.5.1 Effect of Type of Solution

In this section, the single binder (GU) specimens are presented as an example in order to demonstrate the effect of the solution type on the damage mechanisms. Subsequently, the effects of the type of cement, fly ash and nanosilica on the performance of concrete will be discussed.

Compared to the corresponding specimens exposed to deionized water, the XRD patterns generally showed similar dominant phases of portlandite, calcite, quartz, and dolomite, except that Friedel's salt and ettringite peaks were observed in the specimens exposed to the NaCl solution in all stages (wetting, drying, and thawing events; Fig. 6.3). Also, halite (NaCl) peaks were identified when the samples were collected after the drying period during the W/D cycles. The peaks of dolomite and calcite might have occurred because the coarse aggregate contained a fraction (about 10 to 15%) of carboniferous aggregate, while the sources of quartz in the diffractograms originated from the siliceous coarse aggregate and sand in all mixtures. Friedel's salt crystals and ettringite were infilling voids near (within 5 mm) the exposed surface of specimens (e.g. Fig. 6.4). The formation

of Friedel's salt was likely a result of the substitution of sulfate ions by chloride ions decomposing monosulphate, or reaction of the solution with other aluminate bearing phases (chloride binding). The releasable sulfate ions may combine with the remaining monosulphate and a part of Friedel's salt already formed in the presence of moisture, precipitating ettringite. This was supported by the higher intensity of the ettringite peaks compared to the reference sample exposed to deionized water (Fig. 6.3).

Previous studies reported that the maximum scaling damage of concrete occurs at a concentration range of 1 to 6%, which is known as the pessimum salt concentration, due to ice formation and thus internal pore pressure build-up within the surface of the sample (Liu et al. 2015; Valenza et al. 2006). Also, it was stated that the presence of excessive salt ions (more than the pessimum concentration) in the concrete pores has a counter-balancing effect on specimen scaling associated with ice-growth. However, in the current case (with concentrations well above the pessimum level), the deposition of chemical products (Friedel's salt and ettringite) rather than ice formation can also provoke the scaling. This might be attributed to the deposition of these crystals in confined space (especially in smaller air voids, e.g. Fig. 6.4), which might generate pressure and cause spalling of the surface of concrete, especially during the F/T cycles. A similar observation was reported by Goñi et al. (2003) in concrete prepared by cements containing different aluminate contents (C_3A and C_4AF) due to higher precipitation of Friedel's salt. Likewise, the subsequent evaporation of solution and nucleation and growth of NaCl salt due to W/D cycles (Fig. 6.5) may result in enough crystallization pressure to provoke surface scaling of concrete, as shown in the results section.
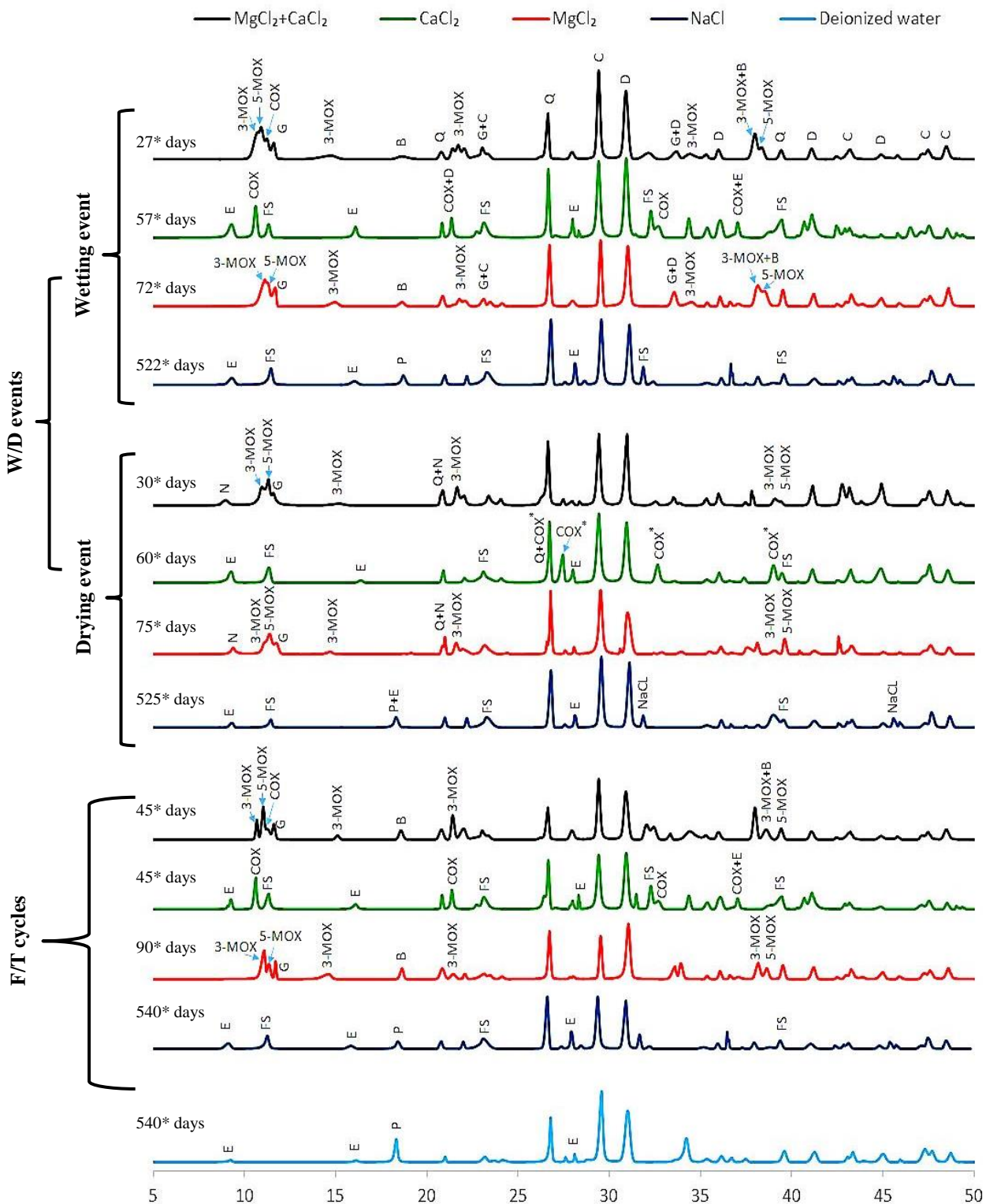
Figure 6.3: XRD analysis of GU specimens exposed to different solutions at each stage during the exposure. *(Note:* Refer to the time of collecting the samples for the test; E=Ettringite, P=Portlandite, FS=Friedel's salt, COX=Calcium oxychloride (3:1:12), COX*=Anhydrous calcium oxychloride (1:1:0 or 1:1:2), 3-MOX=3-Form Magnesium oxychloride, 5-MOX=5-Form Magnesium oxychloride, B=Brucite, N=Nepskoeite, D=Dolomite, C=Calcite, Q=Quartz, G=Gypsum)*
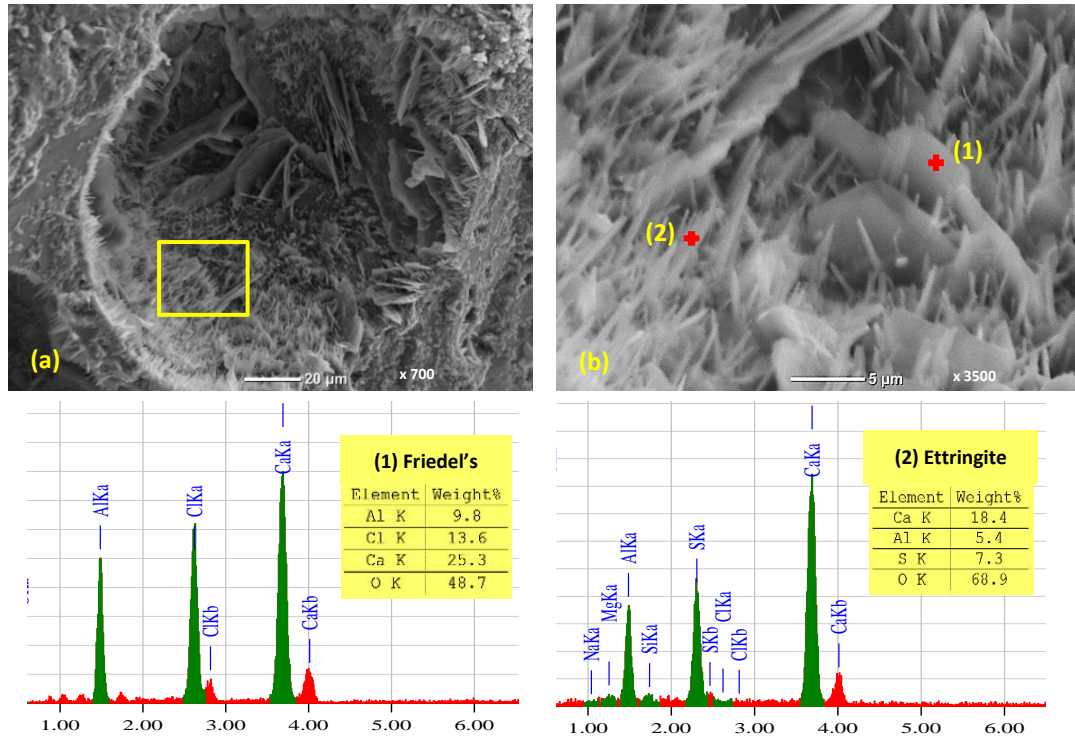
Figure 6.4: ESEM micrograph and EDX analyses of fresh fracture pieces tested at 5°C and 80% RH from GU specimen exposed to NaCl after 522 days (wetting event, Fig. 6.3) showing: (a) air void hosting mixed crystals of Friedel's salt and ettringite and (b) a close-up for the morphology of the crystals.

149
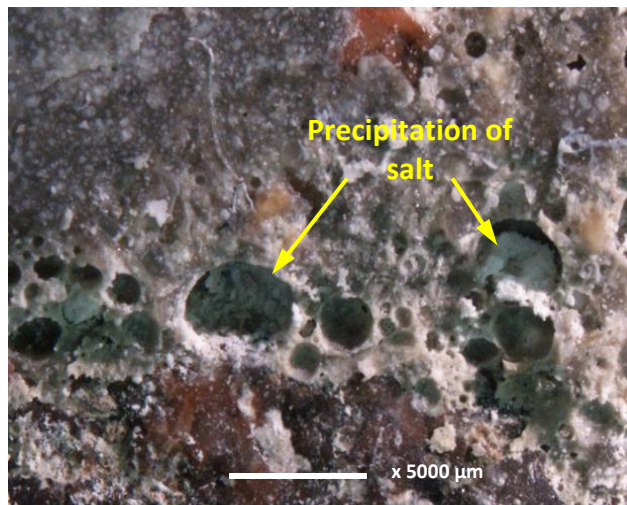
Figure 6.5: Crystallization of salt within the surface of GU specimens exposed to NaCl after 525 days (drying event in Fig. 6.3).

For the $MgCl_2$ salt, the XRD patterns in Fig. 6.3 show that the GU specimens exposed to $MgCl_2$ at different stages (W/D and F/T) had similar dominant phases of magnesium oxychloride (3- or 5-form MOX), brucite, gypsum, quartz, dolomite, and calcite. $MgCl_2$ solution penetrates into the cementitious matrix and causes instability in the pore solution electro-neutrality due to reducing its pH, as implicated by the almost neutral pH (~6.5) in the surrounding solution. Also, brucite formed due to increasing the concentration of magnesium and hydroxyl ions within the surface of the specimens. Moreover, the saturation of the pore fluid with respect to magnesium, calcium, chloride, and hydroxyl ions led to favorable conditions for crystallization of a mixture of the 3- and 5-form MOX that grew in bundles and occasionally as individual fibers, as observed by ESEM (Fig. 6.6). The releasable sulfate ions (from monosulphate, or the dissolution of initial ettringite due to its instability at low pH) reacted with calcium ions in the pore solution, resulting in gypsum formation (Fig. 6.7). Eventually, non-cementitious magnesium-silicate-hydrate (M-S-H) might be formed by replacing the calcium in calcium-silicate-hydrate (C-S-H) by magnesium ions; however, M-S-H cannot be easily resolved by XRD due to its low crystallinity. Therefore, the chemical activity was likely the major cause of deterioration by $MgCl_2$ resulting in formation of relatively expansive (3- or 5-form MOX) and softening (gypsum) phases.

During the drying events (Fig. 6.3), Nepskoeite ($Mg_4Cl(OH)_7 \cdot 6H_2O$), which is a crystalline compound associated with $MgCl_2$ salt, was observed. Thereby, the consecutive cycles of W/D also caused crystallization of salts in the convective zone near-in the exposed surface. The chemical activity (during all stages), as well as the salt crystallization (within drying events), led to micro-cracks in the cementitious matrix (e.g. Fig. 6.6a) facilitating further penetrability of the solution and elevating the salt concentration in the

specimens. These factors provided favorable conditions for formation of a mixture of products, with consequent deposition in open spaces (voids or cracks), thus accelerating the rate of deterioration during the subsequent F/T cycles.
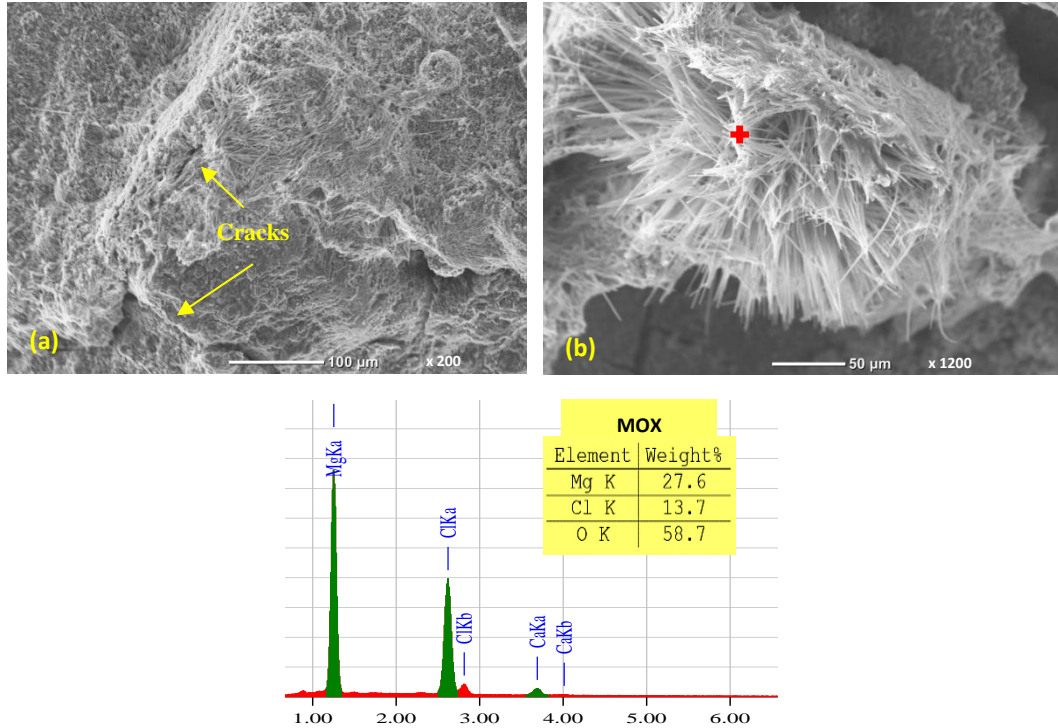
Figure 6.6: ESEM micrographs and associated EDX spectrum of fresh fracture pieces tested at 5°C and 80% RH from GU specimens exposed to $MgCl_2$ at 90 days (thawing event, Fig. 6.3) showing: (a) acicular MOX within the surface, and (b) a close-up showing the morphology of the crystals.
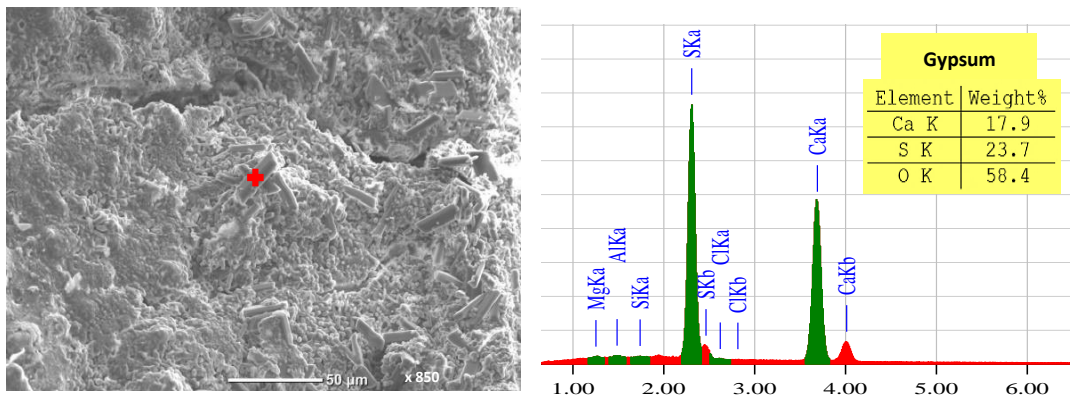
Figure 6.7: ESEM micrograph and associated EDX spectrum of fresh fracture piece tested at 5°C and 80% RH from GU specimens exposed to $MgCl_2$ at 90 days (thawing event, Fig. 6.3) showing gypsum crystals.

Unlike the $MgCl_2$, the XRD patterns of the GU specimens exposed to $CaCl_2$ were different after the wetting or thawing periods compared to the drying events (Fig. 6.3). Within the wetting or thawing events, calcium oxychloride (COX), Friedel's salt and ettringite were the main reaction phases detected. The chloride ions were initially bound to aluminate bearing phases rather than portlandite to form Friedel's salt (chloride binding) as discussed earlier. When Friedel's salt becomes essentially chloride saturated, favorable conditions (high concentration of calcium, chloride, and hydroxyl ions) for crystallization of COX phases existed. Subhedral pseudo-hexagonal plates and very tiny fibrous crystals were a prevailing feature observed by ESEM for 3:1:12 and 3:1:15 COX phases, respectively (e.g. Fig. 6.8). Formation of fibrous and platy COX was accompanied by significant expansion and cracking, which led to the notable disintegration of specimens, even without freezing (chemical degradation within the first 6 W/D cycles). Also, anhydrous COX (1:1:2 or 1:1:0), which was the main phase detected after the drying periods (Fig. 6.3), might engage in the degradation process by reversible formation of high and low-density reaction products (hydrous and anhydrous oxychloride phases). Galan et al. (2015) suspected that the conversion between hydrous and anhydrous COX might contribute to the potential of damage due to the high (2.40 g/cm^3) and low (1.62 g/cm^3) density for these products. Formation of these mixtures of products led to micro-cracks in the cementitious matrix (e.g. Fig. 6.8a), thus, accelerating rate of deterioration in this alternating exposure.
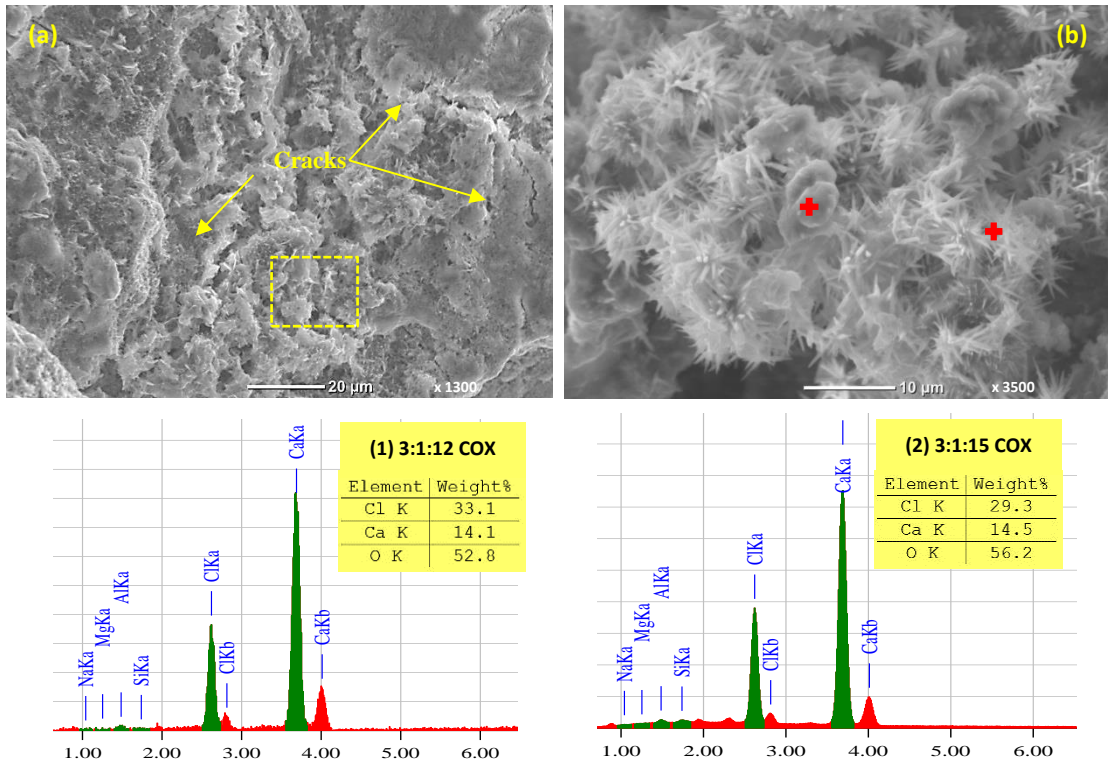
Figure 6.8: ESEM micrographs and associated EDX spectra of fresh fracture piece at 5°C and 80% RH from GU specimens exposed to $CaCl_2$ at 57 days (wetting event, Fig. 6.3) showing: (a) mixed platy and fibrous COX crystals within the surface, and (b) a close-up showing the morphology of the crystals.

The predominant feature of damage by the combined salt ($MgCl_2$+$CaCl_2$) was similar in all stages to $MgCl_2$, as shown by the XRD patterns in Fig. 6.3, except that COX was also identified after the wetting and thawing events. The presence of $CaCl_2$ might countervail the drop in the pH of the pore solution, as indicated by the relatively high pH (~9.5) of the surrounding solution compared to the $MgCl_2$ solution (~6.5), which aggravated the damage by direct formation of COX, as suggested by the intense and sharp peaks of COX in the XRD (Fig. 6.3) compared to the $MgCl_2$ solution (after the wetting and thawing events). Also, the limited gel-like compound (brucite) formed during this exposure facilitated the ingress of the solution into concrete. This made this concrete vulnerable to progressive F/T damage as manifested by micro- and macro-cracking and eventually

crumbling after the 30 F/T cycles (Fig. 6.1d).

6.5.2 Effect of Type of Cement

The physico-mechanical results generally showed similar performance among the GU mixtures and corresponding PLC mixtures, with some improvement in the retention of stiffness and longevity (Table 6.2) for the PLC mixtures. The physical resistance of all specimens after curing was assessed by the RCPT and MIP and the results are listed in Table 6.3. After completing the RCPT, the physical penetration depth of chloride front was measured for concrete specimens as indicated by the whitish precipitate (e.g. Fig. 6.9). Also, the non-steady-state migration coefficient was calculated based on the penetration depth, geometry of specimen, applied voltage, temperature of the anolyte solution and test duration, according to NT BUILD 492 (2011), to account for the heat (Joule) effect and different testing durations, if any, on ionic mobility within specimens. From Table 6.3, it can be noted that the trends of RCPT were consistent with that of MIP in the sense that small penetration depths/migration coefficients corresponded to low cumulative intrusion (apparent total porosity) and/or further pore size refinement and vice versa.

Table 6.3 shows that the PLC specimens showed about 26% reduction in the penetration depth relative to the GU specimens. This might be ascribed to the higher fineness of the PLC (460 m^2/kg) in comparison to the GU cement (390 m^2/kg) due to intergrinding limestone powder with clinker, which can improve the hydration process and microstructural evolution of concrete. Also, the continuous particle size distribution of PLC may yield better particle packing (filler effect) in the matrix (Li et al. 2017; Marzouki et al. 2013). Hence, the PLC mixtures had reduced ingress of salt solutions and consequently better resistance to physical/chemical degradation by de-icing salts, which generally performed better and/or survived longer than the GU specimens as shown earlier in the

Results section, irrespective of the type of the solutions.

Table 6.3: Results from RCPT and MIP

Mixture ID.	RCPT				MIP			
	Charges Passed, coulombs	Chloride Ions Penetrability Class, ASTM C1202	Average Penetration Depth, mm	Migration Coefficient, $\times 10^{-12} m^2/s$	Apparent Total Porosity, %	Threshold Pore Diameter, µm	Average Pore Size, µm	Proportion of Micro-Pores (<0.1 um), %
GU group								
GU	2326	Moderate	17.9 (0.84)[a]	17.67	15.4	0.122	0.191	63.0
GUF20	1483	Low	12.6 (0.52)	10.16	15.9	0.113	0.117	71.1
GUF30	1264	Low	10.8 (0.63)	8.16	16.5	0.107	0.098	74.3
GUS	803	Very Low	5.2 (1.01)	4.24	10.5	0.061	0.014	79.4
GUF20S	541	Very Low	5.0 (0.72)	4.01	10.0	0.080	0.014	78.8
GUF30S	482	Very Low	4.3 (0.63)	2.85	9.0	0.051	0.008	80.1
PLC group								
PLC	1977	Low	13.2 (1.12)	12.93	12.9	0.112	0.181	69.3
PLCF20	1463	Low	11.9 (0.54)	9.81	12.7	0.110	0.110	73.2
PLCF30	901	Very Low	10.1 (0.86)	8.01	13.3	0.101	0.081	75.0
PLCS	769	Very Low	6.4 (0.82)	5.61	10.1	0.075	0.014	78.4
PLCF20S	431	Very Low	4.5 (0.68)	3.86	10.0	0.071	0.010	77.6
PLCF30S	403	Very Low	4.1 (0.43)	3.01	7.6	0.042	0.006	82.2

[a] Standard error is shown between brackets.
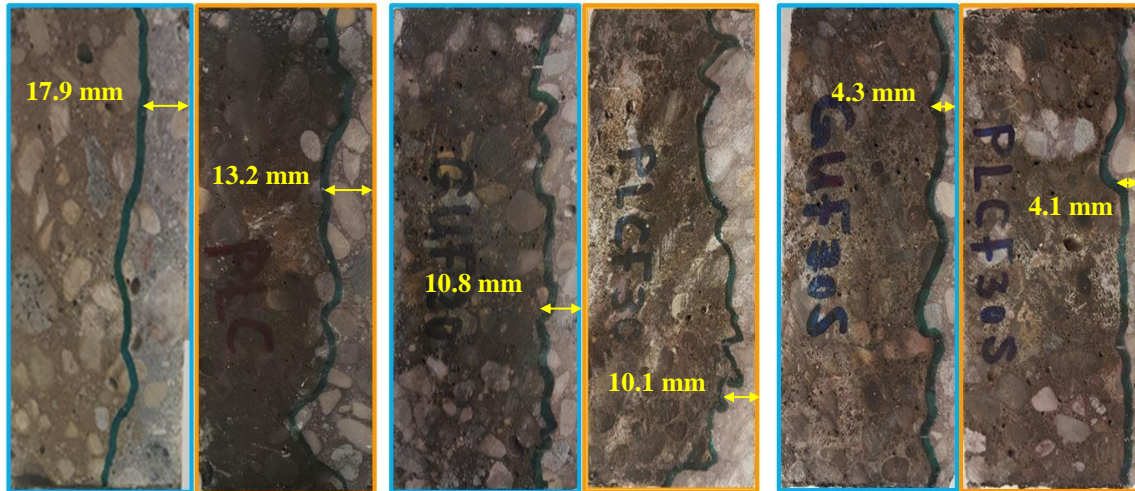
Figure 6.9: Whitish precipitates showing the average penetration depth of chloride ions in specimens (GU left and PLC right): (a) single binder, (b) binary binder (30% fly ash), and (c) ternary binder (30% fly ash with nanosilica).

In addition to the physical effect, the limestone component changed the hydration pattern of the binder as shown by the XRD for the reference sample exposed to deionized water in Fig. 6.10. The formation of carboaluminate-type compounds was detected rather than the other various aluminate compounds (e.g. hydroxy-AFm and monosulphate). Similar observations were reported by Ipavec et al. (2013). Such compounds reduced the ability to bind chloride ions in the system and consequently limited the chemical activity. These trends were corroborated by the XRD analysis as for example shown in Fig. 6.10. In this figure, the intensities of the reaction products (COX, Friedel's salt, ettringite, MOX, and gypsum) for the PLC specimens exposed to all salt solutions after the wetting were notably lower than their corresponding GU specimens. Also, the intensities of the calcite peaks were more pronounced in the PLC specimens than their corresponding peaks in the GU specimens as the liberated carbonate ions might be bound in calcite. Similar observations were reported for this conversion among monocarboaluminate, Friedel's salt and calcite in synthetic hydrated materials (Balonis et al. 2010). These physical and chemical effects of limestone might explain the improvement in the resistance of PLC mixtures to degradation.

On the other hand, the lower clinker component (due to dilution by 12% interground limestone) in the PLC cement reduced the initial portlandite (at 28 days) in these mixtures, and thus discounted the potential for the chemical activity with de-icing salts. These trends were supported by DSC results for the portlandite contents at 28 days (before exposure), as shown in Table 6.4. Also, the PLC mixtures had lower C_3A content relative to the GU mixtures resulting in slower chemical activity (incipient formation of Friedel's salt). Hence, PLC specimens performed better and/or survived longer than the GU specimens in all solutions.

Table 6.4: Enthalpies (J/g) of portlandite in the cementitious matrix

Mixture ID.	After 28 days in the curing chamber	After 540 days exposed to alternating W/D and F/T cycles in deionized water	After 540 days or at the failure point[*] exposed to alternating W/D and F/T cycles in the de-icing salts			
			NaCl	MgCl$_2$	CaCl$_2$	Combined salt (MgCl$_2$+CaCl$_2$)
GU group						
GU	63.6	60.2	46.4	0.0[*]	0.0[*]	0.0[*]
GUF20	56.8	29.7	28.9	0.0[*]	0.0[*]	0.0[*]
GUF30	44.8	13.4	14.1	11.8	12.2	11.3
GUS	23.9	13.9	13.7	14.9	13.1	13.1
GUF20S	8.9	0.0	0.0	0.0	0.0	0.0
GUF30S	7.0	0.0	0.0	0.0	0.0	0.0
PLC group						
PLC	53.6	48.3	35.4	0.0[*]	0.0[*]	0.0[*]
PLCF20	48.3	22.7	23.9	0.0[*]	0.0[*]	0.0[*]
PLCF30	38.8	12.3	11.1	11.7	12.2	11.7
PLCS	20.4	11.8	13.3	11.3	12.8	12.2
PLCF20S	9.1	0.0	0.0	0.0	0.0	0.0
PLCF30S	5.8	0.0	0.0	0.0	0.0	0.0
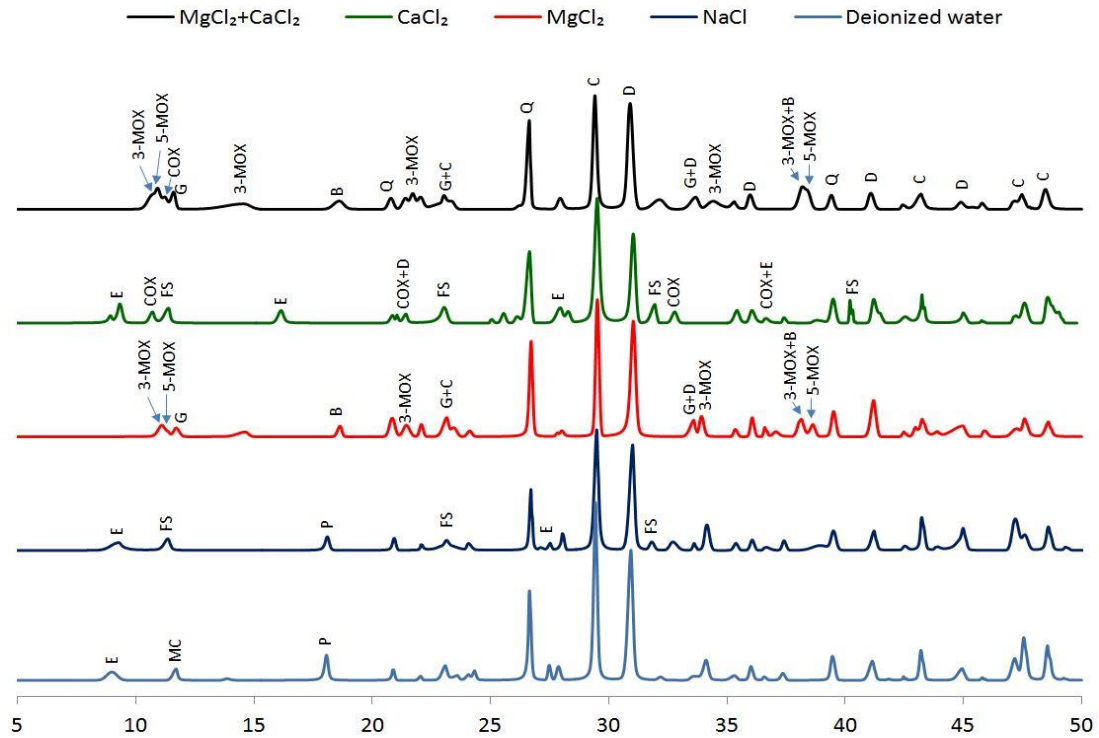
Figure 6.10: XRD analysis of PLC specimens exposed to different solutions at the time of failure (Table 6.2). *(Note: E=Ettringite, P=Portlandite, FS=Friedel's salt, MC=Monocarboaluminate, COX=Calcium oxychloride (3:1:12), 3-MOX=3-Form Magnesium oxychloride, 5-MOX=5-Form Magnesium oxychloride, B=Brucite, D=Dolomite, C=Calcite, Q=Quartz, G=Gypsum)*

6.5.3   Effects of Fly Ash and Nanosilica

Compared to the single binder (GU and PLC) mixtures, the incorporation of fly ash in binary binders notably enhanced the physical resistance (reduced its penetrability) of concrete (Fig. 6.9). For example, the binary binders containing 20 and 30 % fly ash (GUF20 and GUF30) had a penetration depth of 12.6 and 10.8 mm (reduction of 30% and 40%, respectively, compared to the GU counterparts, Table 6.3). The reduction of the penetration depth/migration coefficient, despite the increase of apparent porosity (by 4 and 7%, respectively), can be attributed to the notable reduction of the average pore size (Table 6.3) and correspondingly, the effective porosity; thus, reducing the penetrability of the matrix. In addition to the physical effects, the dilution of the cement component led to decreasing the initial portlandite content (Table 6.4), consequently limiting the chemical activity. These effects of fly ash were more pronounced in the GUF30 specimens as no marked symptoms of degradation were recorded (Table 6.2) due to the improved physical (low penetrability) and chemical (low initial portlandite) resistances. Eventually, the effect of fly ash was magnified in the PLC group owing to the improvement effect of the limestone component in cement, as discussed earlier.

The trends of specimens containing nanosilica are consistent with the effects of nanosilica on cementitious systems, which contribute to microstructural development of cement-based materials through multiple mechanisms, including accelerated pozzolanic activity, filler effect, and water absorption into the high surface area of silica aggregates/agglomerates, i.e. reduction of water-to-binder ratio in the paste. Details of such mechanisms were previously described in other studies (Ghazy et al. 2016; Belkowitz et al. 2015; Said et al. 2012). Using nanosilica with a specific surface of 80,000 m^2/kg in the binary and/or ternary binders led to speeding up the rate of hydration and pozzolanic

reactions, resulting in the refined microstructure, as reflected by the results in Table 6.3. For example, incorporation of 6% nanosilica in the binary system (GUS) led to an average reduction of the penetration depth by 71% and total porosity by 32%, compared to the reference GU concrete. Also, the proportion of the micro-pores in these systems comprising nanosilica was notably increased, which led to smaller threshold pore diameters (an average of 50% reduction relative to the GU specimens), and in turn reduced penetrability of these matrices and solution uptake with no signs of damage irrespective of the type of solution, as shown earlier in the Results sections.

In addition to the much improved physical resistance, nanosilica vigorously sped-up the kinetics of cement hydration and fly ash reactivity. This was substantiated by the DSC results (Table 6.4) as the incorporation of nanosilica catalyzed the reactivity of fly ash, resulting in an average reduction of the initial portlandite contents in the ternary mixtures (GUF20S and GUF30S) by 83 and 86%, respectively, compared to the corresponding binary mixtures (GUF20 and GUF30), and consequently better resistance to chemical degradation by de-icing salts.

CHAPTER 7 – PHASE II: MODELING OF THE DURABILITY OF CONCRETE TO VARIOUS EXPOSURES COMBINED WITH DE-ICING SALTS

In this chapter, adaptive neuro-fuzzy inference systems (ANFIS) was used to predict the behaviour of the concrete mixtures, within the range of training data studied throughout the thesis, under the various exposure regimes described in Chapters 4 through 6. This smart system was trained using the comprehensive information from the integrated testing approach developed in the current thesis.

7.1 Introduction

In cold regions, concrete infrastructure (e.g. roads, bridges) are typically exposed to aggressive service conditions due to harsh climates, particularly when combined with de-icing salts. The damage disintegrates the hydrated cement paste to various levels based on the prevailing exposure conditions and key mixture design parameters of concrete (Ghazy et al. 2017a). Studies on the extent of damage typically classified the problem into physical and chemical natures (Cody et al. 1996; Litvan 1976). Physical damage can occur due to a number of processes such as high degree of saturation, crystallization of salt in concrete pores and thermal mismatches during freeze/thaw cycles, while the chemical effects include detrimental reactions between the de-icers and the cement paste or aggravation of expansive aggregate reactions, i.e. alkali-aggregate reactions. (Ghazy et al. 2017a; Heisig et al. 2016; Wang et al. 2006a).

While enormous efforts have been expended in laboratory and field studies on the physical and chemical mechanisms of damage of concrete, only a few computer-based models have been developed to assist engineers in the prediction of the service life of

concrete exposed to harsh environments (e.g. freezing-thawing (F/T) cycles, wetting-drying (W/D) cycles) combined with de-icing salts (Tamimi et al. 2008). In particular, modeling the transport properties of concrete has received much attention, to indicate the ease of saturation of concrete and in turn its vulnerability to damage (Tamimi et al. 2008; Johannesson et al. 2003). Despite the significant improvements and sophistication of computer models for the transport processes in concrete, it is still challenging to predict the behaviour of concrete exposed to aggressive environments including chemical and physical parameters based only on transport properties. This is due to the simplified assumptions in these models such as the saturated condition of concrete and overlooking the effect of environmental conditions (temperature, relative humidity) existing in the field (Marchand et al. 2009; Tamimi et al. 2008; Johannesson et al. 2003). In addition, excluding the chemical interactions in these ions transport models, especially in the presence of de-icing salts, does not reflect the behaviour of cementitious materials because the damage process of concrete is dynamically complex due to the dissolution of existing phases (e.g. calcium hydroxide (CH) and calcium silicate hydrate (C-S-H)) and formation of new products (e.g. Kuzel's salts, Friedel's salt, ettringite, gypsum and oxychloride phases), which alter the characteristics of the cementitious paste (Ghazy et al. 2017a).

Recently, multi-ionic modeling approaches have been developed to provide more reliable service-life predictions of the complicated interactions between ions and hydrated cement paste (Marchand et al. 2009). Furthermore, Song et al. (2016) reported that the dual/multi cation (e.g. Na^+, Mg^{2+}, and Ca^{2+}) in de-icing salts, due to applying combined chloride-based ice control chemicals, alter the binding rates of chloride ions in concrete, which is not considered in most of these ions transport models. However, these approaches may not be easily applicable by transportation agencies as a result of long computational

time and/or the complex nature of input data required, i.e. diffusion coefficient, permeability, porosity, moisture isotherm, thermal conductivity and heat capacity, and hydrated cement paste and pore solution compositions.

For these complex durability issues, which involves physical and chemical interactions, artificial intelligent techniques, such as neural networks (NNs), fuzzy inference systems (FIS), adaptive neuro-fuzzy inference systems (ANFIS), have been promisingly applied in concrete research. Using a well-defined experimental database (input-output), artificial intelligence can be an efficient tool in modeling complex durability issues such as chloride-induced corrosion, alkali-aggregate reaction, carbonation depth and sulfate attack of concrete (Cho et al. 2016; Štemberk et al. 2013; Boğa et al. 2013; Bianchini et al. 2010; Balasubramaniam et al. 2012; Bassuoni et al. 2008; Göktepe et al. 2006; Kim et al. 2006; Do et al. 2005; Haj-Ali et al. 2001). ANNs are information-processing algorithms, which are composed of a number of interconnected processing elements analogous to neurons resulting in high learning capabilities (Haykin 1999). Comparatively, FIS allows a stochastic data-driven modeling approach, which uses IF-THEN rules and logical operators to establish qualitative relationships among the variables in the model (Ross 2004). Therefore, ANFIS is a hybrid system incorporating the learning abilities of ANNs and semantic knowledge representation and inference capabilities of FIS that have the ability to self-modify their membership functions to achieve a desired performance (Ross 2004; Brown et al. 1994). It can model the qualitative aspects of human knowledge and reasoning processes without employing precise quantitative analyses. This framework makes ANFIS modeling more systematic and less reliant on expert knowledge.

Hu et al. (2006) successfully applied ANFIS to evaluate the effect of composition of fly ash on suppressing the expansion of concrete due alkali-aggregate reaction. Also,

Bassuoni et al. (2008) developed ANFIS models to predict the behaviour of a wide range of self-consolidating concrete mixtures under various sodium sulfate exposure regimes. They showed that the sensitivity analyses for such approach had good agreement with experimental results and microstructural analysis. Bianchini et al. (2010) applied ANFIS to predict the performance of pavements using the parameters routinely collected by transportation agencies (e.g. the development of distresses on the pavement surface by a rolling wheel deflectometer) to characterize the condition of an existing pavement. Also, Balasubramaniam et al. (2012) established an ANFIS model to estimate the performance characteristics of reinforced high-strength concrete beams subjected to different levels of corrosion damage. They concluded that ANFIS can be an alternative approach for the evaluation of degradation as both training and testing data errors were within reasonably small limits (RMSE ≤ 13.7%).

An ANFIS model had been successfully used for the evaluation of chloride ions permeability in concrete containing blast furnace slag, calcium nitrite-based corrosion inhibitors, and a combination of these components with 92.2% accuracy (Boğa et al. 2013). Recently, Cho et al. (2016) also proposed ANFIS to estimate the carbonation depth of reinforced concrete members, in which deterioration was reflected based on data obtained from field inspections of nine buildings. They stated that the proposed ANFIS algorithm closely estimated the carbonation depths and provided relatively good accuracy compared to the carbonation depth estimation methods of the Korea Concrete Institute and the Japan Society of Civil Engineers. Based on the promising use of this approach in modeling complex durability issues of concrete, the present study aims at predicting the time of failure (*TF*) for a variable range of concrete mixtures made with different types of cement without or with supplementary cementitious materials (SCMs: fly ash and nanosilica)

under various exposure regimes combined with the most widely used chloride-based de-icing salts (individual and combined) using ANFIS. The ANFIS model was developed, trained, and tested using experimental data from Chapters 4, 5, and 6. In the prequalification stage of a construction project, this model can effectively assist in selecting optimum mixtures proposed for a specified exposure.

7.2 Experimental Program

7.2.1 Materials and Mixtures

The materials and mixtures used in this Chapter were similar to that used in Chapters 4, 5, and 6 (refer to Section 4.3.1).

7.2.2 Procedures

Detailed experimental procedures of the testing approaches have been given in Chapters 4 through 6. In summary, to reliably evaluate the durability of the tested mixtures to de-icing salts, four exposure regimes were adopted in the current thesis:

- Exposure I (Chapter 4) is a continuous immersion exposure in which prismatic specimens were fully immersed in the high concentration solutions (Table 7.1) of various de-icing salts at 5°C up to 540 days. The solutions were renewed every two weeks to keep a continual supply of de-icing salts, thus providing aggravated damage conditions.

- Exposure II (Chapter 4) is a wetting/drying (W/D) exposure in which prismatic concrete specimens were subjected to wetting in the high concentration solutions (Table 7.1) followed by drying. A W/D cycle (five days) consisted of full immersion of specimens for two days in the de-icing salt solutions at a temperature of 5°C, followed by drying at 23±2°C and 55±5% RH for two days and an additional day at 40±2°C and 30±5% RH in an environmental chamber. This cyclic

165

exposure might mimic the consecutive built up of Cl⁻ ions within concrete surface from winter and wet spring conditions followed by drying periods during summer. The solutions were also renewed every two weeks and this exposure continued for 540 days (108 cycles).

- Exposure III (Chapter 5) is a freezing/thawing (F/T) exposure according to the general procedures of ASTM C666 test procedure A, expect that de-icing solutions were used instead of water and the frequency of F/T cycles per day was less to allow chemical reactions, if any. The duration of one F/T cycle was 12 hours: freezing at $-18\pm1°C$ for 7 h and thawing at $4\pm1°C$ for 3.5 h, and 45 min. to ramp to the minimum freezing temperature or the maximum thawing temperature. Moderate and high concentrations (Table 7.1) were used in this exposure to cover two different states (solution with and without ice) according to the phase diagrams for these salts (Kelting et al. 2010). The solutions were renewed every two weeks and the exposure continued for 540 days (1080 cycles).

- Exposure IV (Chapter 6) is a combination of W/D followed by F/T procedures to mimic the field performance of concrete pavements (successive spring/summer and winter seasons, respectively). A spring/summer season was simulated by 6 W/D cycles similar to exposure III, while a winter season was composed of 30 successive F/T cycles similar to exposure IV with moderate concentration solutions. This regime of exposure has been applied for 540 days (12 spring/summer alternating with 12 winter seasons).

Table 7.1: Concentration of de-icing salt solutions

	Moderate concentration	High concentration

Type of Salt	Salt Concentration Mass (%)	Chloride Concentration (mol/l)	Chloride Concentration[a] (ppm)	Salt Concentration Mass (%)	Chloride Concentration (mol/l)	Chloride Concentration[*] (ppm)
NaCl	14.2	2.83	100,630	23.3	4.52	160,071
MgCl₂	11.9	2.82	100,735	19.1	4.52	160,069
CaCl₂	13.6	2.81	100,731	21.9	4.51	160,067
MgCl₂+CaCl₂	5.9+6.8	2.82	100,733	9.6+10.9	4.52	160,073

[a]The ionic concentration of Cl⁻ ions in each solution was verified by ion chromatography according to ASTM D4327.

Before any exposure, the initial physico-mechanical properties of the intact specimens were measured. For all specimens, the initial mass, length (ASTM C 157) and dynamic modulus of elasticity, E_d (ASTM C 215) were recorded. Specimens were removed from the solutions at specified time intervals (every 2 weeks), and the free expansion of prisms was immediately measured. Subsequently, debris, if any, were removed by a nylon brush, and the specimens were left to dry under $23\pm2°C$ and 50% RH for 30 min before visual inspection and measurement of mass and fundamental transverse frequency. Relative to the initial values, the changes in mass, length and dynamic modulus of elasticity (RE_d) versus time of exposure were calculated.

In order to evaluate the physical resistance (penetrability) of the concrete specimens, the RCPT was performed according to ASTM C1202. To alleviate the effects of electrolysis bias and temperatures on the trends, the penetration depth of chloride ions/front into concrete, which better correlates to the physical characteristics of the pore structure, was determined (Bassuoni et al. 2006). The average depth was determined at five different locations along the diameter of each half specimen. This depth is considered to be an indication of the ease of ingress of external fluids, and thus the continuity of microstructure.

7.3 ANFIS Model

7.3.1   Database

The database for training and testing the model developed herein comprised 480 data points from 12 mixtures (Table 4.2) used in Chapters 4, 5, and 6 (Tables 4.4, 4.5, 5.2, and 6.2) that were exposed to four de-icing salt solutions with different concentrations under four exposure regimes (full immersion at 5°C, W/D, F/T, and cyclic W/D alternating with F/T). The experimental results revealed that the resistance of concrete exposed to these environments combined with de-icing salts is a function of physical penetrability (magnitude of intruding chloride), aluminate content in cement and content of portlandite available for chemical reactions in the hydrated paste. Also, the interground limestone content in PLC contributed to improving the resistance of concrete to de-icing salts due to synergistic physical and chemical actions of limestone in the matrix. Therefore, the model and database had input variables to cover both physical and chemical parameters: penetration depth of chloride ions, interground limestone content, aluminate content (C_3A), and portlandite content at 28 days (before exposure), as well as the type and concentration of the de-icing salt and code of environmental exposure. The latter code was arbitrarily assigned with numbers from 1 to 4 to designate the sequence of experiments (Table 7.2), and it does not implicate the weight or aggression level of a specific exposure. The *TF* was the determined experimental parameter in the database and hence the predicted output of the model.

Currently, there is no failure limit for evaluating the resistance of concrete exposed to de-icing salts under different environmental conditions. Therefore, in this paper, the *TF* was determined based on an increase in expansion beyond 0.25%, considerable mass loss (more than 20%), decline in RE_d below 60%, and/or breakage of specimens by transverse

macro-cracks as each of these criteria were observed to present complete disintegration or failure of the specimens. 345 data points of the data set were randomly assigned to the training set, while the remaining (135) data points was employed for testing the model's performance. The properties of the training and testing data for the model are listed in Table 7.3. The average expansion, mass loss, and RE_d (failure limits) for the minimum TF (45 days; Table 7.3) were 2.8%, 25%, and 45%, respectively, while these limits were 0.02%, 0.05%, and 98% for the maximum TF (540 days).

Table 7.2: Coding of exposure regimes

Description of Exposure	Designated Code
Full immersion at 5°C	I
Wetting/Drying (W/D)	II
Freezing/Thawing (F/T)	III
Cyclic of W/D followed by F/T	IV

Table 7.3: Range of time to failure (TF) for training and testing

Training Data			Testing Data		
Min.	Max.	Avg.	Min.	Max.	Avg.
45	540	463	45	540	446

7.3.2 Approach for Developing ANFIS Models

7.3.2.1 Clustering

The ANFIS model was developed in MATLAB environment (2016). Subtractive fuzzy clustering was generated to establish rule-based relationships among the input and output parameters. The data was divided into clusters to generate the fuzzy inference system. Subtractive clustering was used to initialize the ANFIS model instead of grid partitioning due to a large number of input parameters that might have led to an excessive number of rules which makes the calculations of the ANFIS network extremely slow and perhaps without convergence of the global error. Clustering methods convert a universe of

data into homogenous groups classified according to cluster centers from which the distance of data points is computed (Brown et al. 1994). This method considers that each data point can act as a candidate for the center of clusters; thus, a density measure, D_i, at data point x_i is defined as:

$$D_i = \sum_{j=1}^{n} exp\left(-\frac{\|x_i - x_j\|^2}{\left(\frac{r_a}{2}\right)^2}\right) \qquad Eq.\,(7.1)$$

where, a is a collection of n data points $\{x_1, x_2, x_3, ..., x_i\}$ in an M-dimensional space, r_a is the radius of cluster, and (x_i and x_j) are data vectors in the data space including both input and output dimensions. A data point will have a high-density value if it has many neighboring data points. In contrast, data points outside the r_a contribute only slightly to the density measure.

After the density measure of each data point had been calculated, the data point with the highest density measure was selected as the first cluster center. Then, the density measure for the next cluster center had been revised as follows:

$$D_i = D_i - D_i\, exp\left(-\frac{\|x_i - x_{cj}\|^2}{\left(\frac{r_b}{2}\right)^2}\right) \qquad Eq.\,(7.2)$$

where, r_b is a positive constant that is relatively greater than the r_a by the squash factor (η), which is a positive constant greater than 1 to avoid closely spaced cluster centers. Once the density calculation for each data point was revised, the next cluster center was selected and so on. This process was repeated until a sufficient number of cluster centers had been generated. The acceptance of a cluster center based on the density value was determined according to an acceptance threshold (ε) and rejection threshold ($\acute{\varepsilon}$). The process continued until all possible clusters in the input-output spaces were found. The number of clusters

defines the number of membership functions in the input-output space. Subtractive clustering has four parameters (acceptance threshold (ε), rejection threshold ($\acute{\varepsilon}$), the radius of cluster (r_a), and the squash factor (η) affecting the resultant number of rules for an ANFIS model. In the present study, these values were selected as 0.5, 0.15, 0.5 and 1.25, respectively, as these values led to small numbers of rules and satisfactory performance of the ANFIS model as will be shown later in the text.

7.3.2.2 Fuzzy inference method

The Sugeno inference method was used in the present study to develop the ANFIS model as this method was reported to be particularly effective for ANFIS models with given input-output data sets (Ross 2004; Jang 1993). For a first-order Sugeno fuzzy model, a typical rule set with two fuzzy IF-THEN conditions can be expressed as:

Rule₁: IF x is A_1 and y is B_1 THEN $z_1 = p_1 x + q_1 y + r_1$ $\qquad\qquad Eq. (7.3)$

Rule₂: IF x is A_2 and y is B_2 THEN $z_2 = p_2 x + q_2 y + r_2$ $\qquad\qquad Eq. (7.4)$

where, A_i and B_i are the fuzzy sets in the antecedent, and p_i, q_i, and r_i are the design parameters which are determined during the training process. The overall output (z) was obtained by a weighted average defuzzification method as follow:

$$z = \frac{\sum_{i=1}^{N} z_i \cdot w_i}{\sum_{i=1}^{N} w_i} \qquad\qquad Eq. (7.5)$$

where, N is the number of rules, z_i is the output of the ith rule, and w_i is the weight (consequent) of the ith rule.

7.3.2.3 Process

Referring to Fig. 7.1, the ANFIS architecture had five layers. The first and fourth layers contained an adaptive node, while the other layers contained a fixed node. A brief description of each layer is as follows:

- **Layer 1**: Each node (i) generates a membership function of a linguistic category (high, medium, low). The outputs from this layer are the fuzzy membership grade of the inputs, which are given by the following equations:

$$Q_i^1 = \mu_{A_i}(x) \qquad\qquad Eq.\,(7.6)$$

where, x is the input to node i, and $\mu_{A_i}(x)$ is the membership function (which can be triangular, trapezoidal, gaussian functions or other shapes) of the linguistic label A_i associated with this node and Q_i is the degree of match to which the input x satisfies the quantifier A_i. Gaussian membership functions are the most popular shape for specifying the fuzzy set because of their smoothness and concise notation (Cho et al. 2016; Štemberk et al. 2013; Boğa et al. 2013; Balasubramaniam et al. 2012; Bianchini et al. 2010; Bassuoni et al. 2008). Therefore, this function was utilized in the current study, as expressed by:

$$\mu_{A_i}(x) = exp\left[-\left(\frac{x-v_i}{2\sigma_i}\right)^2\right] \qquad\qquad Eq.\,(7.7)$$

where, v_i and σ_i are the parameters defining the shape of the membership function (premise parameters).

- **Layer 2**: Every node multiplies the input signals from layer 1, and represents the rule nodes and the output Q_i^2 that represents the firing strength of a rule and is computed as:

$$Q_i^2 = w_i = \mu_{A_i}(x) \cdot \mu_{B_i}(y) \quad : \quad i = 1,2 \qquad\qquad Eq.\,(7.8)$$

- **Layer 3**: The ith node of this layer calculates the ratio of the ith rule's firing strength to the sum of all rules' firing strengths:

$$Q_i^3 = \overline{W}_i = \frac{w_i}{\sum_{j=1}^{2} w_j} \quad : \quad i = 1,2 \qquad\qquad Eq.\,(7.9)$$

where, $\overline{W}_i$ represents the normalized firing strengths.

- **Layer 4**: Every node i is a linear function and the coefficients of the function are adapted through a combination of least squares approximation and back-propagation of the form:

$$Q_i^4 = \overline{W}_i \cdot z_i = \overline{W}_i \cdot (p_i x + q_i y + r_i) \qquad\qquad Eq.\,(7.10)$$

where, $p_i, q_i \;and\; r_i$ are a set of consequent parameters of rule i. Thus, the components of the fuzzy rules (premise and consequent parameters) in the rule-based engine are constantly changing at each training epoch until a stable error decrement minimum root mean-squared error (RMSE; 0.05 in the present study) or desired number of epochs (1000 in the present study) is reached.

- **Layer 5**: The result of this layer is obtained as a summation of the outputs of the nodes of the defuzzification layer to produce the overall ANFIS output as shown in Equation (7.5).
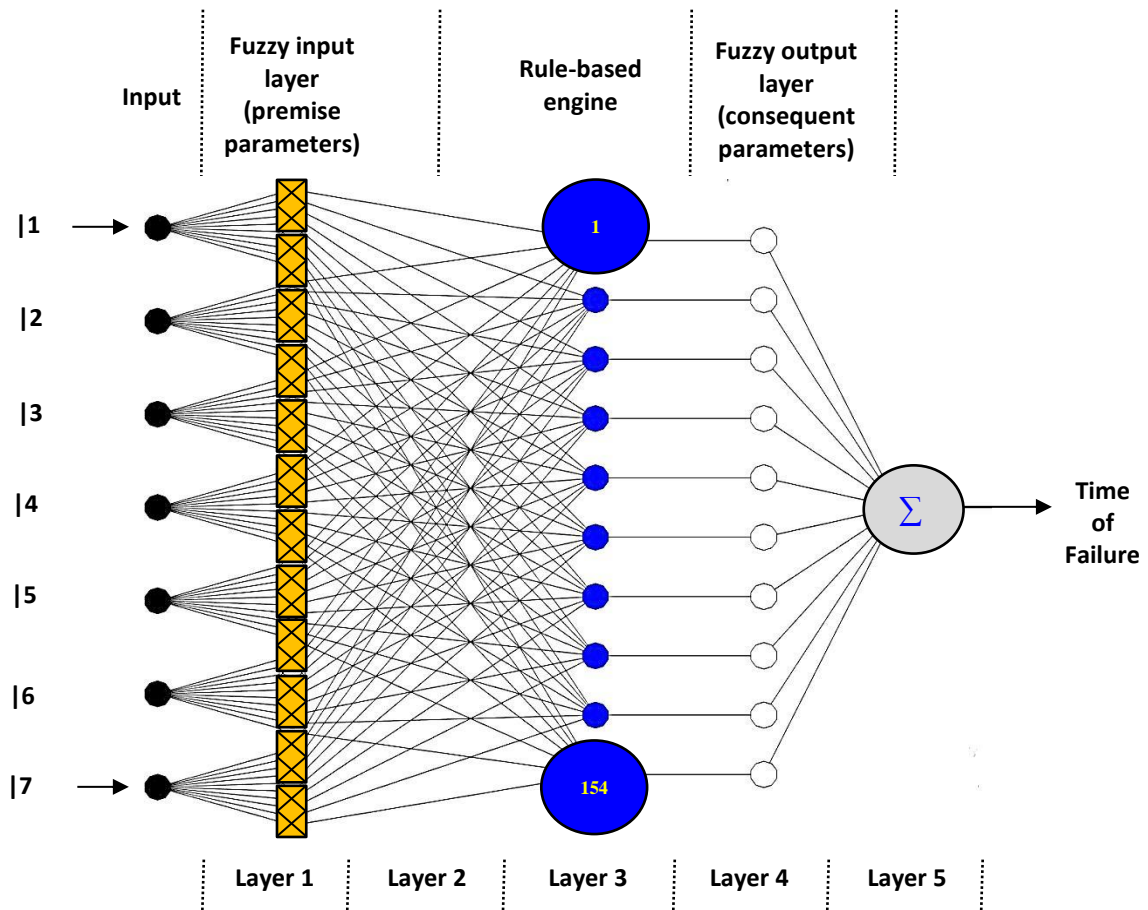
Figure 7.1**:** Architecture of the ANFIS model. (*Note*: |1: interground limestone content, |2: C_3A content, |3: penetration depth of chloride ions, |4: portlandite content |5: type of de-icing salt, |6: concentration of de-icing salt, |7: code of environmental exposure)

7.3.3 Model's Description

ANFIS was developed to predict the *TF* for concrete under various exposure regimes combined with different de-icing salts from the seven input parameters. For the training database, subtractive clustering was applied to the 345 data sets which led to producing 154 fuzzy membership functions for the seven input variables and consequently 154 rules in the rule-based engine were generated. As mentioned previously, the Gaussian membership function was selected, and first-order Sugeno model was adopted as the fuzzy inference method. In the rule-based engine, the fuzzified input variables were connected by T-norm (logical "and") with a minimization operator. The hybrid learning algorithm of

the ANFIS combined the gradient method with the least-square and back-propagation techniques to optimize the membership functions and the parameters. At each epoch, an error measure, usually defined as the sum of the squared difference between actual and desired output, was reduced. Training stopped when either the predefined epoch number or a stable error decrement was obtained. In the current study, the number of iterations (training) continued until a stable error decrement (after 288 epochs) was observed. Finally, defuzzification of the output (*TF*) was done by the weighted average method, as described earlier.

7.4 Results and Discussion

After successful training, testing data (not included in the training data) were applied to gauge the ANFIS predictions for unknown data, and thus its generalization. The performance of the ANFIS model was assessed based on the variance accounted for (VAF), average absolute error (AAE) and root mean square error (RMSE) according to the following equations, respectively:

$$\text{VAF} = \left(1 - \frac{var(f_i - z_i)}{var(f_i)} \right) \times 100\% \qquad\qquad Eq.\,(7.11)$$

$$\text{AAE} = \frac{1}{n} \sum_{i=1}^{n} \frac{|f_i - z_i|}{f_i} \times 100\% \qquad\qquad Eq.\,(7.12)$$

$$\text{RMSE} = \sqrt{\frac{1}{n} \sum_{i=1}^{n} (f_i - z_i)^2} \qquad\qquad Eq.\,(7.13)$$

where, f_i and z_i is the measured and predicted values, respectively and n is the number of data points. The higher the VAF, the better the model performance is and vice versa. For instance, a VAF of 100% means that the measured output has been predicted exactly

(perfect model). The AAE is defined as the average magnitude of the errors in a set of predictions, which indicates how close the predictions are to the eventual outcomes. Also, the RMSE has a quadratic error rule; as a result, a relatively high weight is given to large errors which are useful when large errors are undesirable in a statistical model. Table 7.4 summarizes the statistical parameters for the response of the ANFIS model. Also, the ratio of experimental-to-predicted *TF* for the training and testing data and its coefficient of variation (COV) are tabulated. All these indices indicated that the performance of ANFIS Model was satisfactory. For example, the VAF was 98.7 and 94.3% for the training and testing data, respectively with AAE less than 5%. These trends were substantiated as the ANFIS model reliably captured the input-output relationships since the points are mostly located on or slightly under/above the equity line between the experimental and predicted *TF* values for the training and testing data, as shown in Fig. 7.2. The coefficients of determination (R^2) for the training and testing data were 0.99 and 0.93, respectively, indicating strong association between the predicted and experimental *TF* values. Therefore, it can be deduced that the model has a satisfactory generalization capacity for predicting the *TF* values of other concrete mixtures exposed to various exposure regimes combined with different types and concentrations of chloride-based de-icing salts (within the range of training data).

Table 7.4: Performance indices of the ANFIS model

Training Data						Testing Data					
VAF %	AAE %	RMSE	Average of experimental-to-predicted *TF*		R^2	VAF %	AAE %	RMSE	Average of experimental-to-predicted *TF*		R^2
			Value	COV					Value	COV	
98.7	2.32	0.06	1.00	2.03	0.99	94.3	4.31	0.11	1.03	4.38	0.93
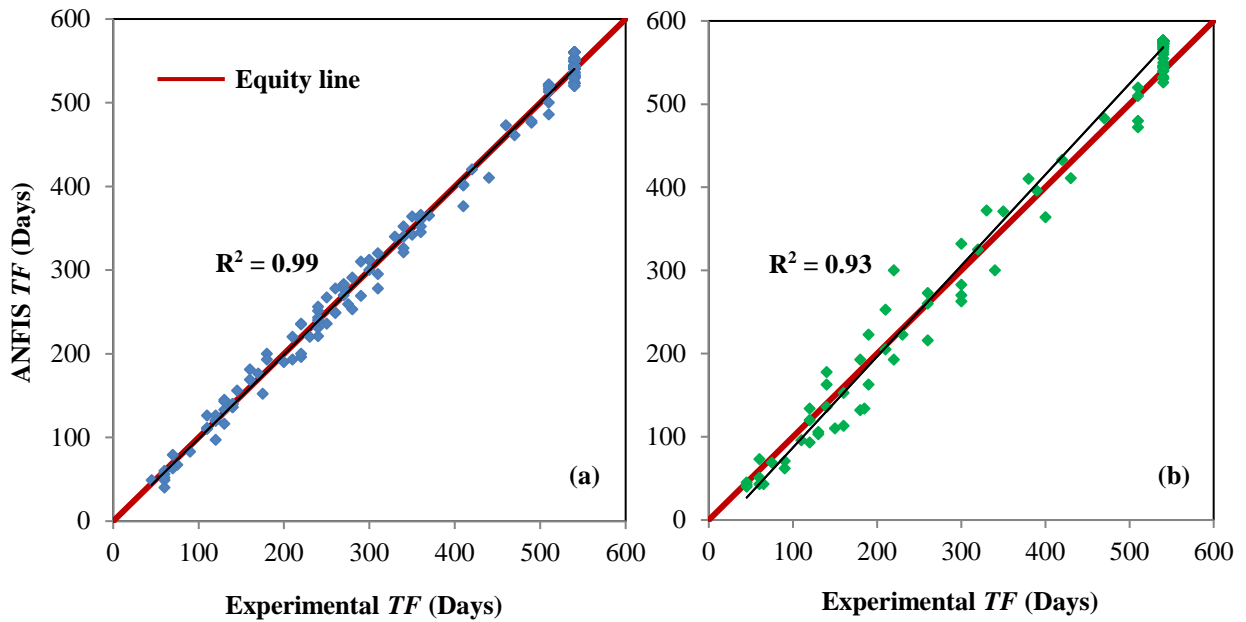
Figure 7.2: Response of ANFIS model in predicting *TF* values of specimens: (a) training data and (b) testing data.

7.5 Effect of the Solution Type and Environmental Conditions

In this section, the effect of the solution type on the damage of concrete is evaluated. The overall trends from experimental database and predictions of the ANFIS model in all exposure regimes indicated that the aggression of solutions, in an ascending order, was NaCl, $MgCl_2$, $CaCl_2$ and combined ($MgCl_2+CaCl_2$) salts, as shown in Fig. 7.3. It can be noted that the combined salt ($MgCl_2+CaCl_2$) solution, which simulates a synergistic maintenance and protective strategy in winter for concrete pavements and bridges, showed the most severe damage to concrete under all exposures. Thus, this practice should be cautiously reconsidered by transportation agencies.
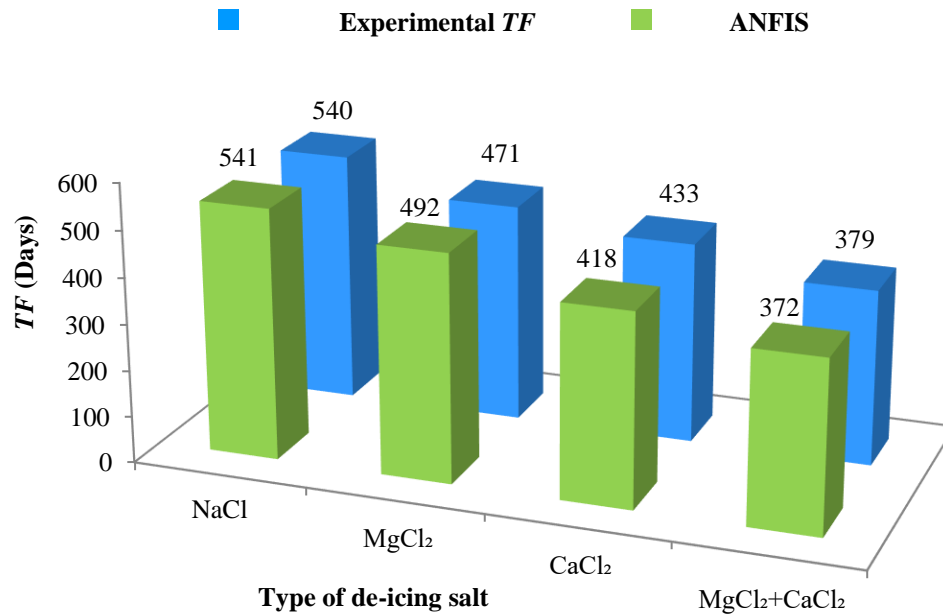
Figure 7.3: Average experimental and predicted *TF* of concrete specimens exposed to different de-icing salts under all the environmental conditions.

From the experimental database and predictions of the ANFIS model, it can be noted that the environmental exposure had a pronounced effect on the degree of deterioration of the specimens. Figure 7.4, which depicts the average *TF* of the specimens tested in each exposure under the most aggressive salt solution (combined salts), substantiates this observation. Exposure III (F/T cycles) was the least aggressive

178

(experimental and predicted *TF* of 434 and 431 days, respectively) relative to the other exposures, while exposure IV (consecutive W/D and F/T cycles), which represents alternating seasonal climatic conditions, was the most aggressive (experimental and predicted *TF* of 356 and 343 days, respectively). Overall, the results of the four exposure regimes correlated well with their corresponding average predicted *TF* values. The field-like combined exposure of cyclic environments had additive and perhaps synergistic effects on the specimens, causing the coexistence of complex degradation mechanisms (salt crystallization, surface scaling, frost damage and chemical degradation) depending on the solution type and concentration as well as the mixtures design variables. Thus, such cyclic environmental conditions should also be considered besides individual testing approaches for developing performance tests that provoke multiple damage mechanisms to improve the understanding of their combined effects on normal and emerging concretes, and hence allow a better modeling of the life-cycle performance of concrete in the field.
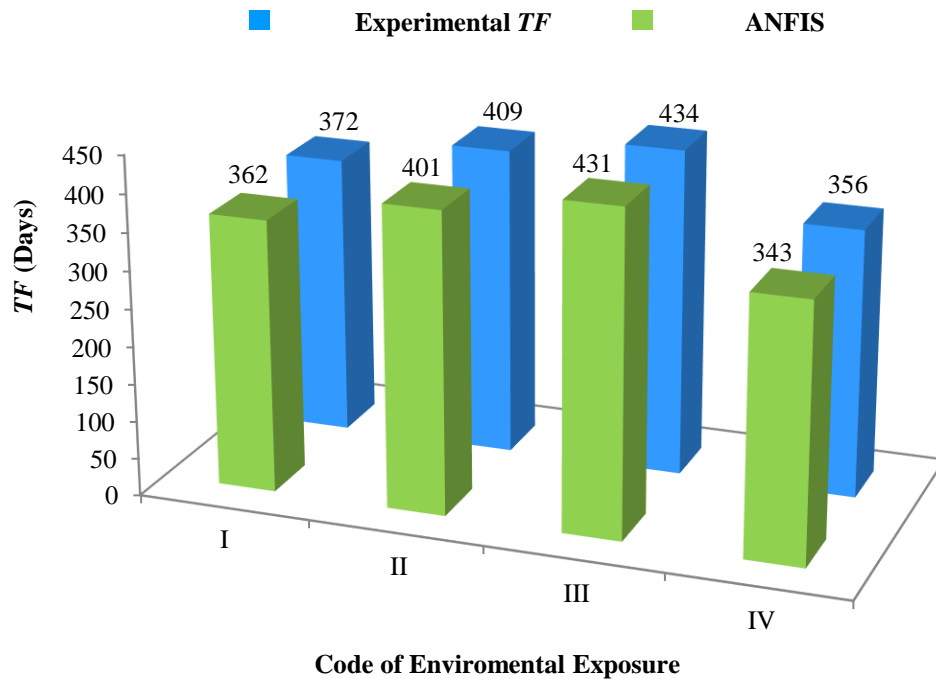
Figure 7.4: Average experimental and predicted *TF* of the specimens exposed to
combined salts under all exposure regimes.

7.6 Sensitivity Analyses

The purpose of this section is to investigate the ability of the model to capture the sensitivity of the predicted properties to individual input parameters. The sensitivity analysis was done by fixing all the input parameters except the variable of interest (Table 7.5) to evaluate its effect within the range of training data. The selected parameters of interest were the physical penetration depth of chloride, initial portlandite content, C_3A content, and interground limestone powder content in the cement. For all the parameters tested, the combined salt $(MgCl_2+CaCl_2)$ solution, which simulates a synergistic maintenance and protective strategy in winter for concrete pavements and bridges, was used as this combination provoked the most severe damage to concrete under all exposure regimes. Also, the combined exposure procedure (alternating W/D with F/T cycles), which mimics field conditions of concrete (successive spring/summer and winter seasons), was implemented in the analysis.

Table 7.5: Levels of the parameters of interest used in the sensitivity analysis

Parameter of Interest	Variation
Penetration depth (mm)	5, 10, 15, 20, 30, 40, 50
Initial portlandite content (J/g)	5, 10, 15, 20, 30, 40, 50, 60
C_3A content (%)	3, 5, 7, 9, 11
Interground limestone powder in cement (%)	3, 5, 7, 9, 11, 13, 15

7.6.1 Sensitivity to Physical Penetration Depth

The sensitivity of the ANFIS model to the penetration depth of chloride ions (physical resistance of concrete to ingress of aggressive fluids) was investigated. For the concrete mixture used in this analysis, the C_3A and interground limestone powder contents were 9 and 4% similar to the GU mixture. Also, the enthalpy of initial portlandite was 63.6

J/g. Figure 7.5 shows the ANFIS model predictions of the *TF*. The responses of the model indicated that as the depth of penetration increased, the durability of the specimens decreased. This trend complied with the experimental results as the specimens with smaller whitish precipitate indicating smaller penetration depth of chloride ions in the cross section had better resistance to degradation, which generally performed better and/or survived longer (Ghazy et al. 2017a). For instance, the binary binder containing nanosilica (GUS) primarily resists the degradation due to its significant physical resistance. Using an ultrafine pozzolan such as nanosilica (specific surface of 80,000 m^2/kg) in the binary and/or ternary binders produced significantly refined microstructure, and in turn reduced penetrability of these matrices and consequently less solution uptake and less damage (Ghazy et al. 2017a; Ghazy et al. 2016). This was clearly captured by the ANFIS model, which showed notable improvement of the *TF* by approximately 160 days when the penetration depth dropped from 50 mm to 10 mm and by more than 500 days when the penetration depth was lower than 10 mm (Fig. 7.5) when the other parameters were kept constant.
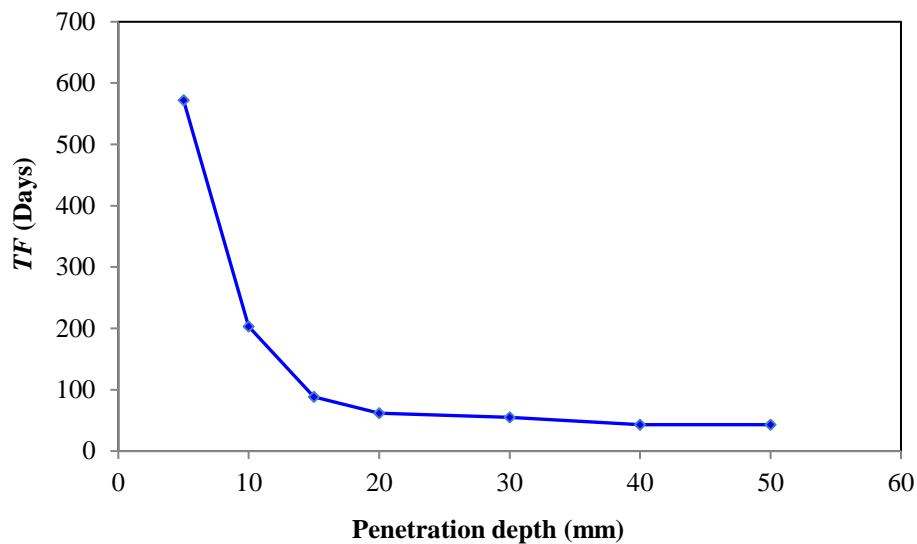
Figure 7.5: Sensitivity of ANFIS model to the penetration depth of chloride ions.

7.6.2   Sensitivity to Initial Portlandite Content

Portlandite is a key component in the chemical reaction of hydrated paste with de-icing salts, forming complex compounds (oxychloride phases), resulting in chemical degradation of hardened concrete (Ghazy et al. 2017a; Wang et al. 2006a; Cody et al. 1996). To test the sensitivity of the ANFIS model to the initial portlandite content in the binder (before exposure), the C_3A content, interground limestone powder and physical resistance for the created mixtures were kept constant at 9%, 4% and 20 mm, respectively. Figure 7.6 shows the ANFIS model predictions of the *TF*. It can be noted that the model was sensitive to the initial portlandite content in the cementitious matrix, as it showed poor performance (early *TF*) for the mixtures containing high portlandite contents and vice versa. This complies with thermal, mineralogical and microscopy analyses which showed that the degradation of the specimens exposed to de-icing salts under such exposure regimes was mainly controlled by the availability of portlandite with respect to the infiltration of chloride ions in the matrix to stimulate chemical degradation (Chapters 4, 5, and 6). This complies with the experimental observations as the W/D (II) or combined exposures (IV) increased the long-term efficiency of pozzolanic reactivity of Type F fly ash, and thus the better performance of specimens comprising fly ash. In contrast, the long-term activity of fly ash was hindered in binary specimens exposed to continuous immersion at 5°C (exposure I) or F/T cycles (exposure III) as indicated by the abundance of portlandite in these specimens. Hence, the binary fly ash specimens generally failed (but after the GU specimens with higher initial portlandite contents) under regimes I and III. Conversely, nil portlandite content was observed in ternary cementitious systems comprising GU, fly ash

and nanosilica, which corresponded to sound mechanical properties and longevity. Using nanosilica with a specific surface of 80,000 m^2/kg in the ternary binders led to speeding up the rate of hydration and pozzolanic reactions (fly ash reactivity) which led to significant reduction of the initial portlandite contents (Ghazy et al. 2016; Belkowitz et al. 2015; Said et al. 2012).
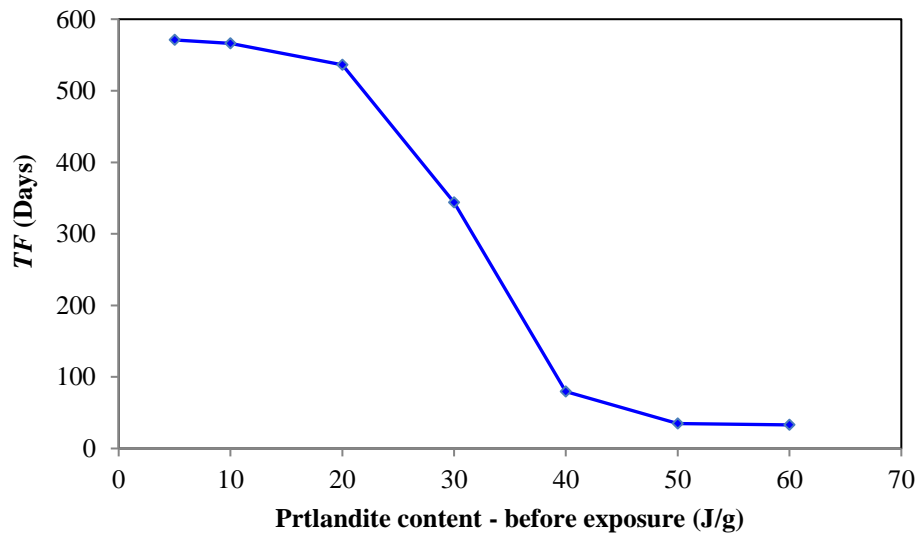
Figure 7.6: Sensitivity of ANFIS model to the portlandite content in the binders.

7.6.3 Sensitivity to C_3A Content

To test the sensitivity of the ANFIS model to the C_3A content in the binder, the interground limestone powder, initial portlandite content, and physical resistance for the created mixtures were fixed at 4%, 63.6 J/g, and 20 mm, respectively. Figure 7.7 shows the

predictions of the ANFIS model reflecting the variations in the C_3A content between 3 to 9% (within the range of training data). The responses of the model indicated that as the C_3A content decreased, the durability of the specimens notably improved. This was exhibited by a delay of the *TF* by more than 300 days when the C_3A content dropped to 5%. This agrees with experimental observations, as the mixtures containing low C_3A content (e.g. PLC specimens) had slower chemical activity and less quantities of the reaction products (calcium oxychloride, Friedel's salt, ettringite, magnesium oxychloride, and gypsum, irrespective of the type of solution) as observed in the mineralogical analysis (Ghazy et al. 2017a). Therefore, specimens with low C_3A content in the binder performed better and/or survived longer than the specimens with high C_3A content.
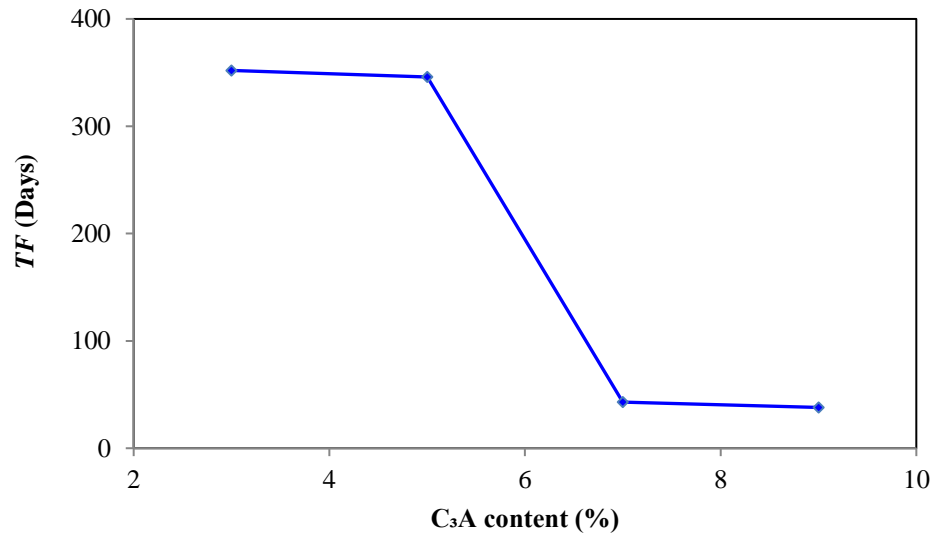
Figure 7.7: Sensitivity of ANFIS model to the C_3A content.

7.6.4   Sensitivity to Limestone Content

To examine the effect of variation in interground limestone content in cement on the responses of the ANFIS model, the C_3A content, portlandite content, and physical resistance for the created mixture were fixed at 9%, 63.3 J/g, and 20 mm, respectively.

Figure 7.8 shows that the prediction of the ANFIS model was relatively sensitive to the transition from low (4% in the GU mixtures) to high (12% in the PLC mixtures) contents of limestone in the cementitious matrix. This complies with thermal, mineralogical and microscopy analyses which showed that the higher limestone component in PLC mixtures changed the hydration pattern of the binder due to formation of carboaluminate-type compounds rather than other aluminate compounds (e.g. hydroxy-AFm and monosulphate) (Ipavec et al. 2013; Lothenbach et al. 2008). The ability of carboaluminate phases to bind chloride was reported to be significantly less than other aluminate compounds (Ipavec et al. 2013). Subsequently, the system with high interground limestone content had slow chemical activity (limited formation of Friedel's salt). This chemical effect of limestone explains the notable improvement in the resistance of the mixtures containing high interground limestone content (within the range of training data; up to 12%) exposed to chloride-rich environments, which generally performed better and/or survived longer than the specimens with low interground limestone content as exhibited by a delay of *TF* by more than 150 days in the ANFIS model (Fig. 7.8).
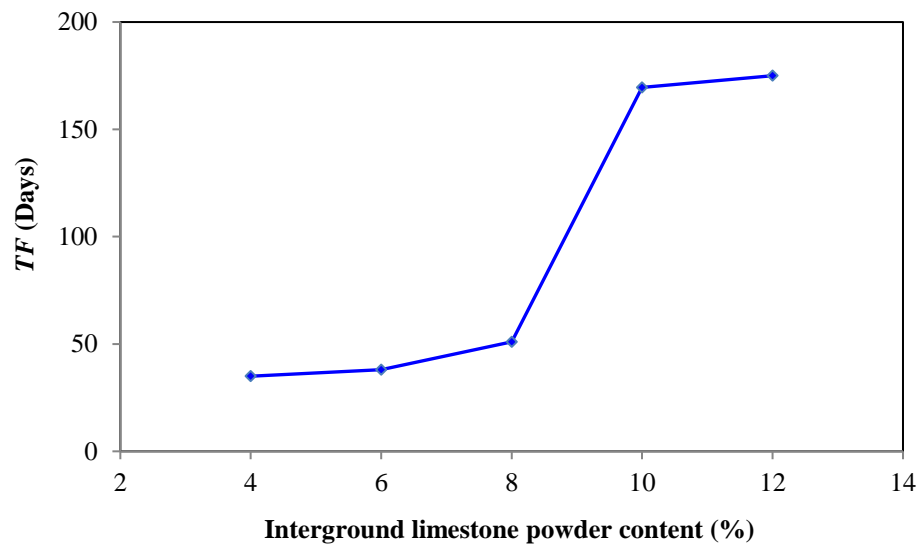
Figure 7.8: Sensitivity of ANFIS model to the interground limestone powder content in cement.

CHAPTER 8 – PHASE III: NANO-MODIFIED FLY ASH CONCRETE AS A REPAIR MATERIAL

Premature failure of repairs in concrete pavements is frequently observed (e.g. Chapter 3) resulting in significant life-cycle, economic, and social losses. Therefore, in the next three chapters (8, 9, and 10), an effort was made to develop nano-modified fly ash concrete (NMFC) as a repair material for concrete pavements. A series of tests were conducted to evaluate their early-age and long-term performance as well as their compatibility with the substrate concrete. The NMFC mixtures were then applied in a field trial as a partial-depth repair (PDR) material to repair transverse joints located on a major urban arterial road in Winnipeg to document its performance under real service conditions.

8.1 Introduction

Premature failure of repairs in concrete pavements and bridge decks is frequently observed, resulting in significant life-cycle, economic and social losses (Li et al. 2011; Al-Ostaz et al. 2010). Efficient repair of concrete pavements typically requires a rapid setting material that can be placed and hardened within a relatively short period of time for quick opening to traffic. While numerous high early-strength cementitious repair materials are commercially available, many of these materials are vulnerable to cracking, poor bonding, and premature deterioration, for example due to incompatibility with the existing concrete pavement (Soliman et al. 2014; Li et al. 2011). In addition, some studies have shown concerns of using high early-strength concrete in repair applications for pavements (Bentz et al. 2008). These materials can lead to stress concentrations,

---

because of their susceptibility to thermal gradients and autogenous shrinkage, resulting in high levels of micro-cracking, and in turn durability issues. Extensive research on the use of supplementary SCMs such as fly ash showed that incorporation of Class F fly ash generally improves the long-term performance and durability of concrete (Huang et al. 2013; Ondova et al. 2013; Malhotra et al. 2000). Despite the benefits of fly ash concrete, practical limitations remain unresolved in field applications. The delay in setting time, strength gain and microstructural development at early-age of fly ash concrete are considered to be the major issues, which deter its wider acceptance as a repair material (Huang et al. 2013; Ondova et al. 2013; Said et al. 2012; Madani et al. 2012). Also, a number of laboratory studies have indicated inferior scaling resistance of concrete containing dosages of fly ash in excess of 25 to 30% of the binder when subjected to cycles of freezing and thawing in the presence of de-icing chemicals (Ondova et al. 2013; Malhotra et al. 2000).

Recently, nanomaterials have been progressively applied in the field of concrete research, attracting considerable scientific interest due to the new potential uses of nanometer-sized particles in cementitious binders. Concrete with superior properties can be produced by incorporating nanoparticles with fly ash (Belkowitz et al. 2015; Hou et al. 2013; Said et al. 2012; Madani et al. 2012). As a result of their ultrafine nature (size scale of 1-100 billionth of a meter), nanoparticles can vigorously speed-up the kinetics of cement hydration in concrete. Hence, the delay in setting time, strength gain and microstructural development of fly ash concrete may be mitigated.

8.2 Research Significance

Carefully balancing the early-age and long-term performance of cement-based repair materials remains a challenging task, which warrants further investigation. In

comparison to two cementitious products extensively used by transportation agencies in Manitoba for partial depth repair of concrete pavements, an effort was made in the present study to develop nano-modified fly ash concrete as a repair material for concrete pavements, to achieve balanced performance in terms of hardening time, strength development, bonding with substrate concrete and durability to infiltration of fluids and salt-frost scaling.

8.3 Experimental Program

8.3.1 Materials

General use (GU) portland cement and fly ash (Class F), which meet the requirements of CAN/CSA-A3001 standard, were used as the main components of the binder. Their chemical and physical properties have been shown previously in Table 4.1. In addition, a commercial nano-silica sol (Table 4.1) was incorporated in all binders. Six concrete mixtures were prepared and a non-chloride accelerator, complying with ASTM C494/C494M Type E, was used in three mixtures to accelerate the setting time. Natural gravel with maximum aggregate size of 9.5 mm and well-graded river sand with fineness modulus 2.9 were used. Their specific gravity and absorption were 2.65 and 2%, respectively for gravel and 2.53 and 1.5%, respectively for sand. A high-range water reducing admixture (HRWRA) based on polycarboxylic acid and complying with ASTM C494 Type F was added to maintain a slump range of 50 to 100 mm. In addition, an air-entraining admixture was used to provide a fresh air content of 6±1%. For comparison purposes, two commercial cementitious repair materials were evaluated. These products are extensively used in the province of Manitoba based on the premise that they achieve early-age performance and adequate service life. Table 8.1 shows their composition and physical properties according to each manufacturer's datasheet.

Table 8.1: Composition and properties of the commercial products according to the manufacturers' datasheets

	A	B
Composition, % by mass		
Hydraulic cement	✓*	7-13
Silica sand, crystalline	✓	>60
Titanium dioxide	✓	0.1-1
Borax	✓	1-5
Physical properties		
Specific gravity	2.7	2.75
Water content, l/22.7 kg	2.1-2.8	1.6-1.8
Mixing time (min)	4-5	4
Extension**	50%	50%
Curing procedures	Wet cure the surface with water and polyethylene sheets at least one day, or use a curing compound	

*The range is not specified in the datasheet.
**Coarse aggregate extension by mass of repair material per bag, 22.7 kg.

8.3.2 Procedures

The formulations of the nano-modified fly ash concrete stem from a compatibility perspective between repair and parent concrete; thus, all the repair mixtures comprised fly ash comparable to concrete pavements in Manitoba, in which 15% fly ash is typically used. Three normal setting concrete mixtures (designated as N) were prepared with GU cement and variable dosages of fly ash (15%, 22.5% and 30% replacement by mass of the base binder (385 kg/m^3) comprising GU cement and fly ash); nano-silica was added to the mixtures at a single dosage of 6% by mass of the base binder, i.e. a solid content of 23 kg/m^3. In addition, three corresponding rapid setting concrete mixtures (designated as R) were produced with an accelerating admixture. For all mixtures, the total cementitious materials (ternary binder: GU cement, fly ash and nano-silica) content and water-to-cementitious materials ratio (*w/cm*) were kept constant at 408 kg/m^3 and 0.38, respectively.

Constituent materials were mixed in a concrete mixer with a speed of 60 RPM. To attain homogenous dispersion of components, a specific sequence of mixing was adopted based on experimental trials. First, approximately 15% of the mixing water was added to

the aggregate while mixing for 30 s. The cement and fly ash were then added to the aggregate and mixed together for 60 s. The nano-silica and the admixtures (air-entraining admixture, HRWRA, and accelerator) were added to the remaining water while stirring vigorously for 45 s to obtain a liquid phase containing well-dispersed nanoparticles and admixtures. Finally, the liquid phase was added to the mixture and mixing continued for 2 min. After mixing and casting the concrete, a vibrating table was used to ensure good compaction of specimens. Polyethylene sheets were used to cover the surface of specimens for 24 h. The specimens were then demolded and cured in a standard curing room (maintained at a temperature of 22±2°C and a relative humidity of more than 95%) until testing. The proportions of the nano-modified mixtures are shown in Table 8.2. For the commercial products, the manufactures' recommendations were carefully followed in the proportioning, mixing, casting and curing procedures (Table 8.1).

Table 8.2: Proportions of mixtures per cubic meter of concrete

Mixture ID.	Cement (kg)	Fly ash (kg)	Nano-silica (Kg)	Water* (kg)	Coarse aggregate (kg)	Fine aggregate (kg)	HRWRA (l/m³)	Accelerator (l/m³)
F15	327	58	0	147	858	858	0.7	0
F30	269	116	0	147	850	850	0.4	0
NF15	327	58	46	131	830	830	2.3	0
NF22.5	298	87	46	131	830	830	2.1	0
NF30	269	116	46	131	830	830	1.9	0
RF15	327	58	46	131	830	830	1.8	6.9
RF22.5	298	87	46	131	830	830	1.7	6.9
RF30	269	116	46	131	830	830	1.5	6.9

*Adjusted amount of mixing water considering the water content of nano-silica (aqueous solution with 50% solid content of SiO_2);

8.3.3 Testing Methods

To determine the setting time, the mortar fraction of each mixture (portion passing sieve #4 (4.75 mm)) was placed in a container at room temperature as specified by ASTM C403. At regular time intervals, the penetration resistance was determined by standard needles. In addition, paste samples with identical proportions to the paste fraction in the

concrete mixtures (Table 8.2) were prepared to measure the heat released from the hydration reactions by an isothermal calorimeter kept at 23°C following the general guidelines of ASTM C1679. The rate of heat generated was monitored and recorded every minute continuously for 100 h, and it was normalized by the mass of the sample. Also, the cumulative heat released was determined.

For each mixture, triplicate 100×200 mm concrete cylinders were prepared for the compressive strength test according to ASTM C39 and splitting tensile strength test according to ASTM C496, respectively which were performed at different ages. To evaluate the bond between the repair mixtures and concrete substrate along with the resistance of the composite assembly to environmental conditioning, the pull-off test was used according to CSA A23.2-6B. Concrete slabs of 300×400 mm surface area and 140 mm thickness were used as a concrete substrate (350 kg GU cement with 15% fly ash as a binder replacement and 0.38 *w/cm*). After casting, the slabs were demolded and moist cured for 7 days in the curing room and then maintained in normal laboratory conditions. At 90 days, the top surface (finished surface) was wire brushed and cleaned; subsequently, the repair mixtures were placed on the top surface with a thickness of 80 mm. After moist curing for 28 days, the slabs were partially cored to determine the pull-off strength according to CSA A23.2-6B. Furthermore, the bond strength of companion slabs was evaluated after consecutive F/T and W/D cycles. A total of 25 F/T cycles followed by 25 W/D cycles were applied. This customized procedure simulates climatic conditions of successive winter and summer seasons, which correlates to in-service conditions. For the F/T stage, ASTM C672 regime was applied for 25 cycles. Subsequently, the specimens were exposed to 25 W/D cycles, where each cycle consisted of ponding (3 to 5 mm) the

surface of specimens with 4% calcium chloride solution for 16 h at a temperature of 22±2°C, followed by drying at 40±2°C and 40±5% RH for 8 h.

At 28 days, the resistance of the mixtures to the penetrability of aggressive ions was evaluated by the rapid chloride penetrability test (RCPT) according to ASTM C1202. To avoid the electrolysis bias of this method, the penetration depth of chloride ions into concrete was determined according to the procedure described previously by Bassuoni et al. (2006). In addition, ASTM C672 was conducted for all the mixtures to evaluate their resistance to surface scaling due to de-icing salts (4% calcium chloride) and freezing-thawing cycles. The specimens have a minimum surface area of $0.045m^2$ and thickness of 75mm. The resistance to surface scaling was evaluated when the curing method (by a chemical compound or a standard curing room) and time (3 to 14 days) were varied. Moreover, the resistance to surface scaling was evaluated qualitatively by visual examination, and quantitatively by mass of scaled materials.

Thermal and microscopy studies were conducted to evaluate the evolution of microstructure in the concrete mixtures. The quantity of portlandite (calcium hydroxide) in the matrix was determined up to 90 days to assess the effect of nano-silica and fly ash on the hydration and pozzolanic reactions. Thermogravimetry (TG) at a heating rate of 10°C/min was used for this purpose on powder samples extracted from the concrete mixtures. The content of portlandite was calculated by determining the percentage drop in an ignited mass of the TG curves at a temperature range of 400 to 450°C and multiplying it by 4.11 (ratio of the molecular mass of portlandite to that of water). Backscattered scanning electron microscopy (BSEM) with elemental dispersive X-ray (EDX) was conducted on polished thin sections from the concrete mixtures. At 28 days, slices were cut from specimens, which were then dried and impregnated by a low-viscosity epoxy resin

under vacuum pressure and polished by successive diamond surface-grinding to a thickness of 30 to 50 µm. The sections were coated with carbon to enhance the conductivity for the BSEM analysis. Finally, selected tests (setting time, heat of hydration and thermal analysis) were also done on reference fly ash concrete mixtures (without nano-silica) comprising 15% and 30% fly ash (F15 and F30) to exemplify the difference in behaviour relative to the nano-modified fly ash concrete.

8.4 Results and Discussion

8.4.1 Fresh Properties and Heat of Hydration

Table 8.3 shows the properties of fresh concrete including density, slump and setting times (initial and final). Products A and B showed very dry consistency (zero slump) and had very short hardening times (40 to 60 min), as indicated by the acute increase of the penetration resistance curves (Fig. 8.1). This may imply critical placement, consolidation, and finishing since all these procedures should be completed within 40 min. Also, when large patches are repaired, there will be a high potential for cold joints as repair mortars/concretes are typically mixed on-site in small batches. Comparatively, the nano-modified fly ash concrete mixtures had better workability, especially the R mixtures owing to the effect of Type E (water reducer and accelerator) admixture combined with the HRWRA. Also, they had ample setting times (Fig. 8.1), which would allow more flexibility in the repair process, especially for large or multiple patches.

Table 8.3: Density, slump, initial and final setting times

Mixture ID.	A	B	F15	F30	NF15	NF22.5	NF30	RF15	RF22.5	RF30
Density, kg/m³	2312	2280	2249	2233	2224	2224	2224	2231	2231	2230
Slump, mm	0	0	75	95	55	65	80	75	90	100
Initial, min	40	40	450	550	270	345	360	165	175	210
Final, min	45	60	605	830	415	475	505	285	295	340
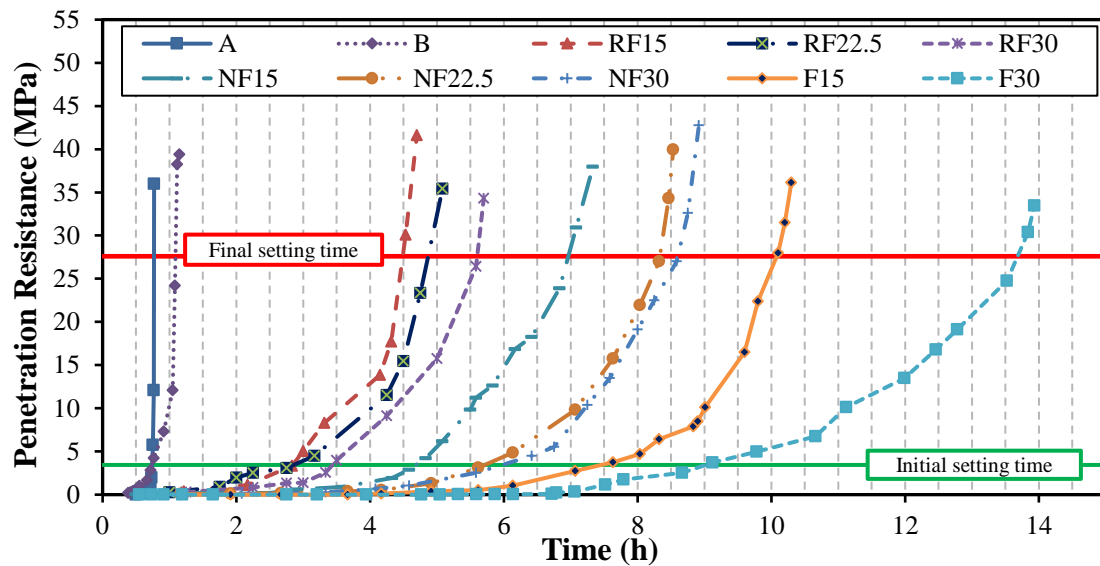
Figure 8.1: Penetration resistance versus time.

The effect of higher dosages of fly ash on retarding the setting time of concrete is well-documented (Huang et al. 2013; Ondova et al. 2013; Malhotra et al. 2000), as depicted in Fig. 8.1. For example, the reference concrete mixture containing 30% fly ash (F30) exhibited initial and final setting times of 100 and 225 min, respectively longer than that of the reference mixture with 15% fly ash (F15). However, the setting times of the nano-modified mixtures were significantly shortened relative to the reference mixtures. For example, the initial setting times for NF15 and RF15 were 270 and 165 min, respectively compared to 450 min for the corresponding reference mixture F15. Also at a higher dosage of fly ash, mixtures NF30 and RF30 exhibited final setting times 40% and 60%, respectively shorter than the reference mixture F30. This is ascribed to the addition of ultrafine silica particles, which accelerated the kinetics of hydration and pozzolanic reactions (Hou et al. 2013; Said et al. 2012; Madani et al. 2012). This effect was magnified with the incorporation of an accelerating admixture. For example, RF15 and RF30

exhibited final setting times of 130 and 165 min shorter than that of NF15 and NF30, respectively.

Isothermal calorimetry was conducted on paste samples to complement the trends observed in the setting time test. A rapid rise in the first segment of the heat flow curve may indicate initial setting (end of the dormant period) of the paste, while the peak of the curve indicates its final setting (end of acceleration stage) (Mehta et al. 2014; Nevile 2011). For comparison purposes, the heat flow data presented herein are shown over 48 to 80 h; however, the steady state stage was developed up to 100 h. The heat flow and cumulative heat released at 23°C for the reference pastes as well as the N and R mixtures are shown in Fig. 8.2. It can be noted that the heat of hydration curves for the reference samples (without nano-silica) were different from that for the fly ash pastes with nano-silica. The curves for the reference cement pastes were likely dominated by hydration of tricalcium silicate (C_3S), similar to the hydration features observed for neat portland cement pastes (Mehta et al. 2014; Nevile 2011); however, the nano-modified fly ash pastes (both the N and R mixtures) were typified by a second peak (Figs. 8.2b-c) with a higher magnitude of heat flow, likely due to the accelerating effect of nano-silica particles on the reactions.

Previous studies attributed the accelerated hydration of C_3S to the higher conversion rate of the protective hydrate layer formed close to the C_3S surface to a less permeable form due to the abundance of silicate ions (Stein et al. 1964) from nano-silica aggregates (agglomerates of nano-silica in the pore solution, for example due to high pH (Depasse 1999) or bridging of silica particles by calcium ions (Zerrouk et al. 1990)) and reduction of calcium ions through fast pozzolanic activity (within a few hours) (Madani et al. 2012; Korpa et al. 2008). This led to shortening the induction period and initial setting time of nano-modified fly ash concrete. In addition, it has been postulated that silica

aggregates can accelerate the hydration of cement by creating additional surfaces for early precipitation of hydration products, and thus reducing the final setting time (Hou et al. 2013; Madani et al. 2012; Korpa et al. 2008).

For the reference pastes, the peak of the heat flow curve was observed at 615and 675 min for the reference pastes comprising 15% and 30% fly ash, respectively (Fig. 8.2a). Comparatively, the hydration of the N nano-modified fly ash pastes was significantly accelerated (Fig. 8.2b) and the length of the dormant period was markedly shortened (by about 120 min). At a dosage of 6% nano-silica, the first peaks of the hydration curves for NF15, NF22.5 and NF30 were obtained at approximately 150, 165 and 180 min, respectively earlier than that of the corresponding reference pastes. In addition, the total heat evolved over 80 h was 12-18% higher for the N nano-modified fly ash pastes relative to the reference pastes. Again, this catalytic effect of nano-silica was magnified with the incorporation of the accelerating admixture (Fig. 8.2c). For instance, the first peaks of the normalized heat flow curves of the RF15, RF22.5 and RF30 mixtures were obtained at approximately 175, 155 and 130 min, respectively earlier than that of the corresponding N mixtures (shifted to the left), and the total cumulative heat of the R mixtures was higher (16-21%) than that of the N mixtures.

In compliance with the setting time trends that captured the retarding effect of the higher dosage of fly ash, it can be noted that there is a slight delay in the hydration of the mixtures containing 30% fly ash (Figs. 8.2b and 8.2c). The first hydration peaks of mixtures NF30 and RF30 were shifted to the right by approximately 30 and 15 min, respectively relative to that of mixtures NF15 and RF15. Correspondingly, at 80 h, the total cumulative heat released from the pastes comprising 30% fly ash was lower than that from pastes with 15% fly ash by 18% and 12% for the N and R mixtures, respectively. These results suggest

that this retarding effect was marginal since it was discounted by the addition of nano-silica, which markedly sped up the kinetics of reactions as discussed earlier. Hence, the addition of nano-silica to the fly ash binders enhanced the hydration level and shortened the hardening time, which affects the early-age strength as will be discussed in the next section.

197
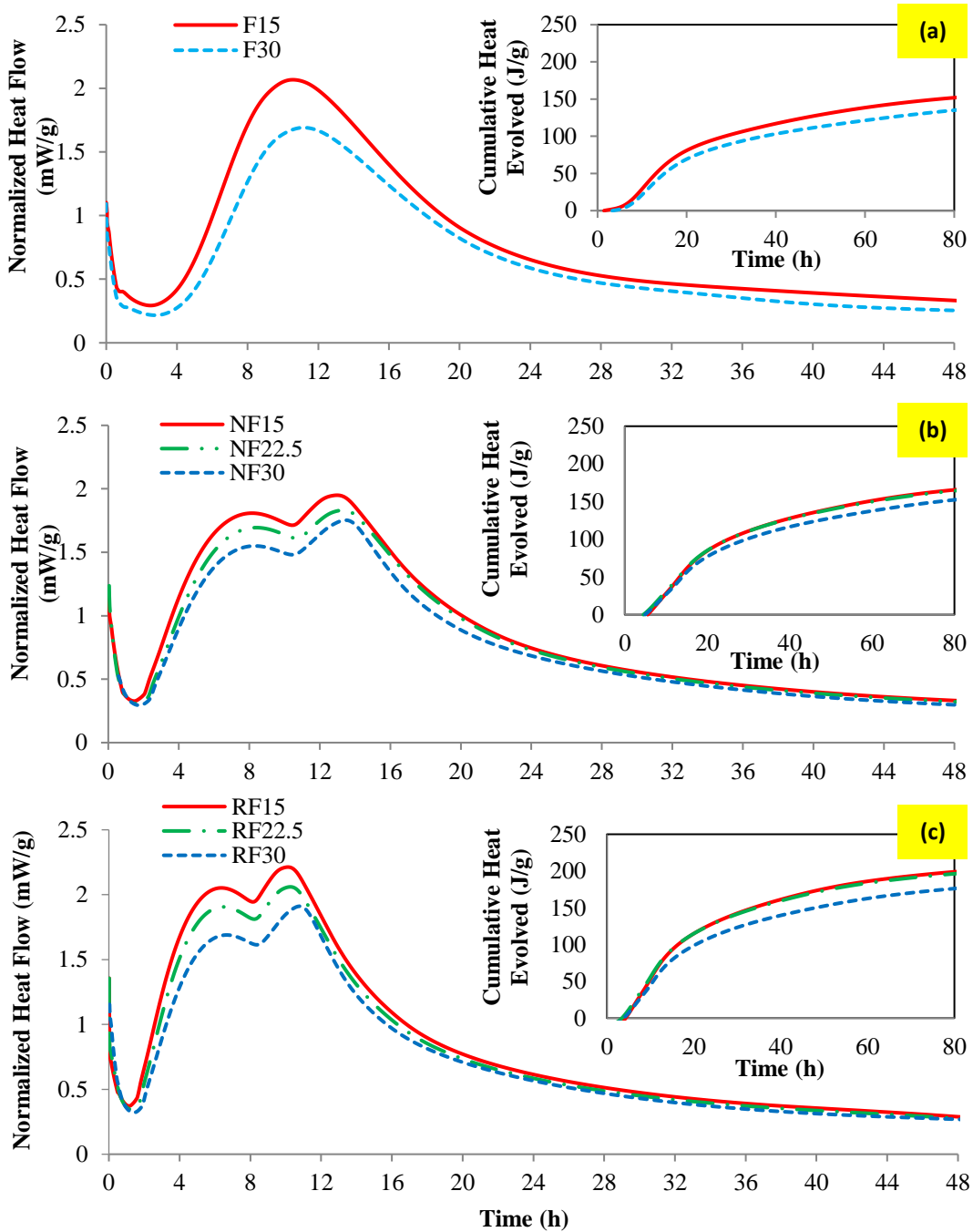
Figure 8.2: Isothermal calorimetry curves (normalized heat flow, and cumulative heat released) at 23ºC: (a) reference mixtures, (b) N mixtures, and (c) R mixtures.

8.4.2   Strength

Table 8.4 shows the average compressive and splitting tensile strengths of specimens from all mixtures at different ages. The results generally indicated that the commercial products (A and B) gained the highest compressive strength at 8 h; however, the increase in strength for these products was not significant until 1 day, while the RF15 and RF22.5 specimens achieved higher or comparable compressive strengths of 20 and 17 MPa, respectively at 1 day. In addition, the rate of strength development for products A and B was insignificant up to 3 days. This was statistically supported by the analysis of variance (ANOVA) at a significance level $\alpha = 0.05$ (Montgomery 2014). ANOVA is a statistical model used to analyze the differences between group means and their variation among and between groups. The variance of a specific parameter is separated into components attributed to different sources of variation. Exceeding the critical value of an F-distribution density function reflects that the tested variable significantly affects the mean of the results (defined as the null hypothesis). The results were statistically evaluated by the ANOVA method at a significance level (α) of 0.05, i.e. 95% confidence level. The 'α' term is the probability of rejecting the null hypothesis when it is true. Also, the p-value

is the probability of obtaining a result as extreme as, or more extreme than, the result actually obtained when the null hypothesis is true. If the *p*-value is very small, there is only a very small chance that the null hypothesis is false. For example, for product A, ANOVA for the compressive results at 8 h and 3 days had *F* value of 6.71 which is smaller than the critical value (F_{cr}) of 7.71. This insignificant change in compressive strength up to 3 days may be attributed to the very rapid reactions during the first 8 h, which might have formed thick hydration shells that discounted the diffusion of water and kinetics of hydration afterwards.

Comparatively, the rate of strength development of the nano-modified mixtures was significant (an increase of 53 to 80%) up to 3 days. For instance, ANOVA for the compressive strength at 1 and 3 days for the NF15 and RF15 specimens yielded *F* values of 28.6 and 33.7, respectively, which are larger than the corresponding F_{cr} of 7.71. The results of the nano-modified mixtures at 28 and 56 days indicated that there was continuous and significant improvement in strength beyond 7 days in comparison to the commercial products. The significant increase in strength of these mixtures with time can be ascribed to the synergistic effects of nano-silica and fly ash, as will be discussed later in the TG results.

Table 8.4: Results of compressive and tensile strengths

Mixtures	A	B	NF15	NF22.5	NF30	RF15	RF22.5	RF30
Compressive strength, MPa								
8 h	15	16	--	--	--	10	8	--
1 day	16	18	14	13	10	20	17	13
3 days	21	25	24	20	18	32	30	22
7 days	28	35	31	30	27	38	37	31
28 days	34	38	41	43	36	42	41	38
56 days	35	43	43	45	47	44	45	42
Tensile strength, MPa								
1 day	1.1	1.8	1.4	1.3	0.9	2.1	1.9	1.2
3 days	1.9	2.8	2.6	2.7	1.9	2.8	2.8	2.3
7 days	2.8	3.1	3.8	3.7	3.5	3.8	3.2	2.7

| 28 days | 3.2 | 4.1 | 5.1 | 5.3 | 5.7 | 4.9 | 5.2 | 5.5 |

For specimens from the R mixtures, the average early-age (up to 7 days) strength significantly increased (15 to 43%) in comparison to the N mixtures. This is ascribed to the presence of the accelerating admixture, which sped up the rate of hydration reactions, and consequently increased the early-age strength. However, this trend diminished between 7 to 56 days for the R mixtures, which conforms to effect of accelerators on the compressive strength development of concrete at later ages due to the slower diffusion of water through thicker hydration products (Mehta et al. 2014; Nevile 2011). Although increasing the dosage of fly ash in the mixtures led to reducing the compressive strength at early-age, the N and R specimens with 30% fly ash (NF30 and RF30) had compressive strength values of 18 and 22 MPa at 3 days, respectively. For the NF30 mixture, the compressive development was significant after 7 days (70% increase between 7 to 56 days) and achieved the highest strength at 56 days (47 MPa), which is consistent with the well-known effect of Class F fly ash on compressive strength of concrete (Malhotra et al. 2000).

The early-age (1-7 days) results generally indicate that the compressive strength of the N and R nano-modified fly ash mixtures markedly improved with the addition of nano-silica, as no low values were observed for any mixture. These results are consistent with other studies (Belkowitz et al. 2015; Said e al. 2012). Hence, the slow rate of strength development for concrete incorporating Class F fly ash can be controlled by the addition of a small dosage of nano-silica. It appears that nano-silica aggregates effectively contributed to the strength development of the mixtures up to 7 days through high pozzolanic activity (Hou et al. 2013), filler effect (Oertel et al. 2013), and water absorption (Kong et al. 2012). Moreover, nano-silica can catalyze the reactivity of fly ash at early-age (Said e al. 2012), while the long-term improvement in strength of the mixtures can be

ascribed to the continual pozzolanic effect of fly ash with time (Malhotra et al. 2000). These mechanisms are discussed in detail later in the TG and microscopy analyses section.

The splitting tensile strength of concrete mixtures was determined at different ages as listed in Table 8.4. The early-age tensile strength of product A was low, and this product had the lowest tensile strength at 28 days. Comparatively, product B gained higher tensile strength (1.8 MPa) at 1 day; in addition, the increase of tensile strength for product B was significant up to 28 days. Complying with the compressive strength results, all the nano-modified fly ash concrete mixtures exhibited comparable or higher tensile strength up to 7 days (2.7-3.8 MPa) and 28 days (4.9-5.7 MPa) with a significant rate of increase. The effect of the accelerating admixture on the early-age results of tensile strength was similar to that of the compressive strength. Also, it was observed that the tensile strength slightly decreased with the fly ash content at early-age; however, this trend was reversed at 28 days due to the continual reactivity of fly ash, as the N and R specimens with 30% fly ash had the highest tensile strength (Table 8.4). This behaviour may be attributable to the densification of the interfacial transition zone (ITZ) between aggregate and cement paste as a result of the combined effects of nano-silica and fly ash, as shown later in the microscopy analysis section.

8.4.3 Bonding

Bond failure is a critical cause of deterioration in pavement repairs. Therefore, the pull-off test was used to assess the bond strength of the repair mixtures with substrate concrete; this represents a severe scenario for the assembly, as it is subjected to a direct tension configuration. Also, the pull-off test was used to evaluate the residual bond strength of the mixtures to substrate concrete after combined cyclic environments, which should capture performance risks originating from incompatibility between the repair mixtures

and substrate concrete. Therefore, a combined exposure protocol was adopted in order to replicate consecutive winter and summer seasons, which correlate to in-service conditions. Li et al. (1999) used a similar technique to evaluate the bonding performance of rapid setting repair materials subjected to F/T cycles.

The average bond strength values before and after the combined exposure are shown in Fig. 8.3. The average value of pull-off strength from specimens (4 cores) produced a coefficient of variation of less than 20% (except for product A). The results showed that the commercial products A and B had bond strength of 1.3 and 1.6 MPa, respectively. The bond strength of these products decreased significantly after the combined exposure by 48 and 31%, respectively relative to the initial values. The failure of these specimens occurred mainly at the interface between the repair products and substrate concrete (reflecting some level of incompatibility), or in the repair products due to their lower tensile capacity (Table 8.4).

Comparatively, the bond strength for the N and R mixtures ranged between 1.9 to 3.3 MPa, and it significantly increased by 23% to 43% after the combined exposure. In addition, the failure in specimens prepared with the N and R mixtures shifted towards the substrate concrete, suggesting that the assembly behaved as an integral system with a high degree of compatibility. Unlike the commercial products, the nano-modified fly ash system
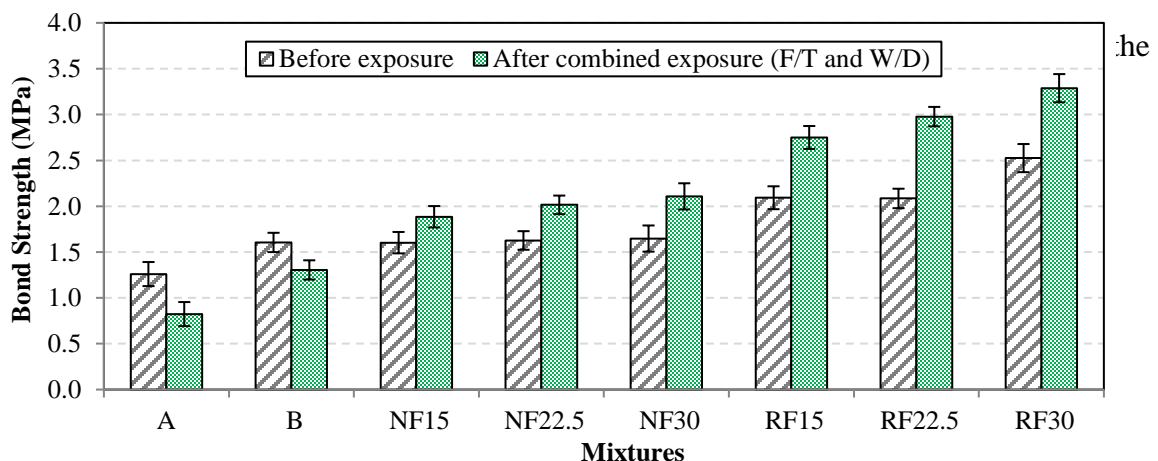
deleterious debonding effects induced by cyclic environments and improved the later-age bonding with substrate concrete. This improvement in the bond strength after the combined exposure is thought to be attributed to the continual reactivity of the ternary binder with time of exposure, which might be facilitated by the enhanced moisture level in the repair concrete due to the use of a salt solution rather than fresh water (Spragg et al. 2011).

Figure 8.3: Bond strength of the repair assembly from the pull-off test.

The evolution of the bond strength significantly increased (by 45% to 57%) for the R mixtures in comparison to corresponding specimens from the N mixtures. This may be ascribed to the presence of the accelerating admixture, which sped up the rate of hydration reactions and consequently improved the bond at the interface with substrate concrete since early stage. In addition, increasing the dosage of fly ash led to increasing the bond strength notably, especially for the R mixtures, as depicted in Fig. 8.3. This improvement in bonding of the assembly might stem from the chemical interaction between nano-silica and fly ash with the available $Ca(OH)_2$ in the substrate concrete forming secondary C-S-H at the bond interface, and thus enhancing the mechanical interlock between the two layers. The latter argument is substantiated by the efficient reactivity of binder and densified microstructure observed for mixtures comprising higher dosages of fly ash as shown by the RCPT, thermal and microscopy tests.

8.4.4   Penetrability

The penetrability of all repair mixtures was evaluated by the RCPT at 28 days and the results of passing charges and physical penetration depth are listed in Table 8.5. The commercial product A had a high passing charge value indicating coarse and continuous pore structure despite achieving a compressive strength of 34 MPa at this age. According to the classification of ASTM C1202, all the nano-modified fly ash concrete mixtures had 'very low' penetrability as their passing charges were below 1000 coulombs, with comparable performance among the N and R mixtures incorporating similar dosages of fly ash. Correspondingly, these mixtures had markedly lower penetration depths (less than 10 mm) relative to that of the repair products A (50 mm) and B (15 mm).

Table 8.5: Rapid chloride penetrability test (RCPT) results

Mixtures ID.	Passing Charges, coulombs	Chloride Ions Penetrability Class (ASTM C1202)	Average Penetration Depth, mm, (Standard Error)
A	> 4000	High	50 (0.0)
B	1443	Low	15 (1.0)
NF15	772	Very Low	8 (0.4)
NF22.5	621	Very Low	5 (0.7)
NF30	522	Very Low	3 (0.3)
RF15	921	Very Low	9 (0.7)
RF22.5	644	Very Low	6 (0.7)
RF30	602	Very Low	5 (0.4)

The dosage of fly ash in the mixtures had a significant effect on the penetration depth. Considerable reduction of penetrability was achieved for the N and R mixtures containing 30% fly ash, which had comparable compressive strength to that of the commercial repair products at 28 days. ANOVA for the penetration depth results showed that increasing the fly ash content from 15% to 30% in the N and R mixtures had *F* values 50.3 and 46.2, which are more than the critical value (F_{cr}) of 4.1. This trend indicates the

densification and discontinuity of the pore structure, which can be explained by the effects of nano-silica and fly ash as shown later in the thermal and microscopy analyses section, thus improving the durability of the mixtures to the ingress of fluids, and in turn, their projected long-term performance.

8.4.5   Surface Scaling

The results of surface scaling due to the combined action of de-icing salt and F/T cycles (ASTM C672) are shown in Figs. 8.4 and 8.5. Product A showed a high tendency to surface scaling after about 10 cycles. After 50 cycles, products A and B had cumulative mass losses of 2.4 kg/m^2 (visual rating of 4-5) and 0.5 kg/m^2 (visual rating of 1-2), receptively. Bureau du normalization du Quebec (BNQ 2002) and Ministry of Transportation, Ontario (MTO 1997) stipulate that the failure limits in salt-frost scaling tests are 0.50 and 0.80 kg/m^2, respectively. According to these criteria, considering the difference in procedures among the three tests (e.g. BNQ and MTO use a less aggressive solution of 3% sodium chloride), products A and B are deemed unacceptable as they will likely have surface scaling issues in the field. In contrast, all the nano-modified concrete mixtures had limited surface scaling (maximum mass loss of 0.25 kg/m^2, Fig. 8.4) and low visual ratings (0-1, Fig. 8.5), without a significant difference between the N and corresponding R mixtures. Minor pop-outs were observed likely due to the deterioration of some porous aggregates near the surface of concrete.
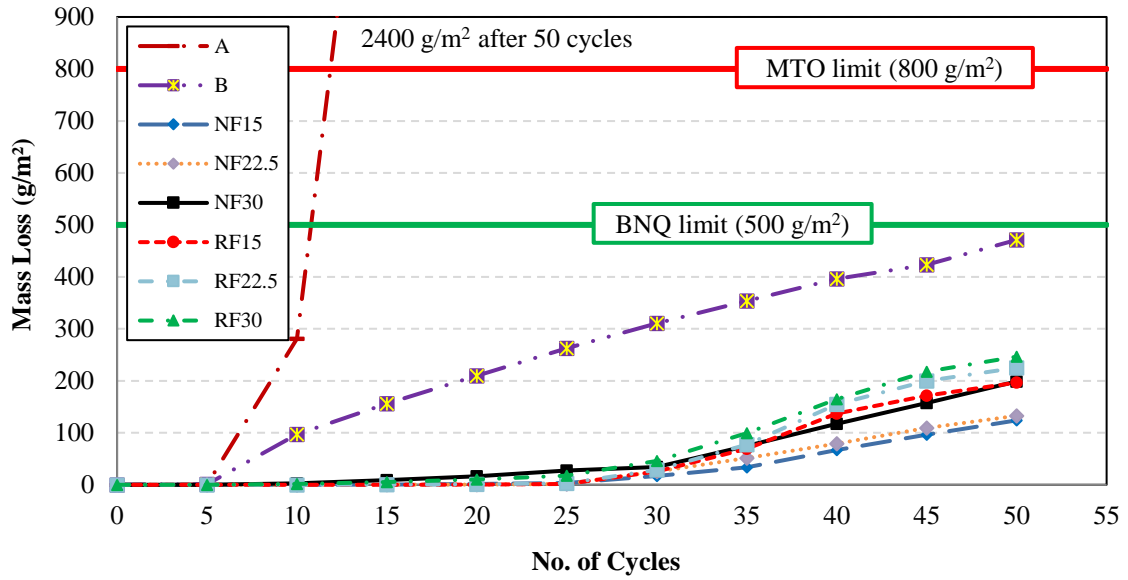
Figure 8.4: Mass loss of slabs tested according to ASTM C672.
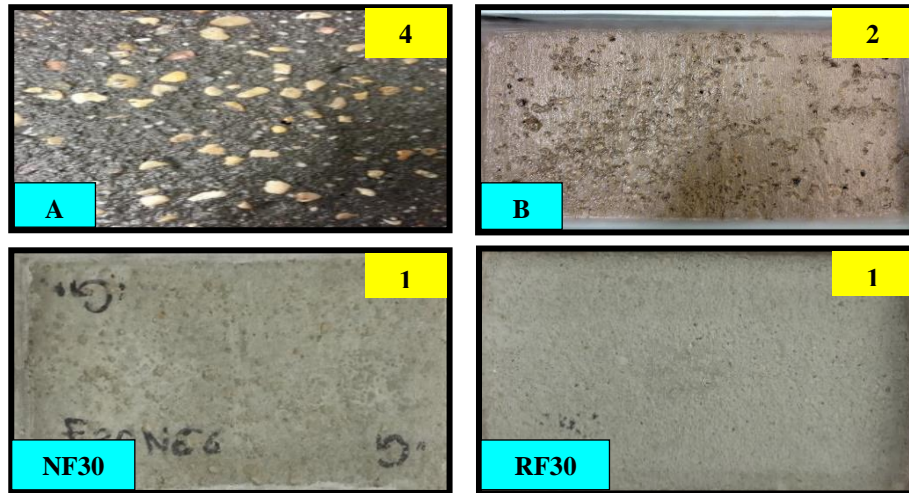
Figure 8.5: Exemplar visual ratings of slabs after 50 freezing-thawing cycles.

It has been reported that the resistance to salt-frost scaling decreases with increasing the dosage of fly ash in concrete, which is among the key reasons that deter the wider use of higher dosages of fly ash in concrete pavements (Malhotra et al. 2000). High contents of Class F fly ash in concrete may lead to significant proportions of unbound fly ash

particles in the paste, resulting in coarse microstructure and higher tendency to surface scaling. In the current study, incorporation of 30% fly ash in concrete led to a marginal increase in surface scaling as the binders were modified with nano-silica, indicating improved durability. This was shown by ANOVA, for the results of surface scaling which showed statistically insignificant difference between 15% and 30% fly ash in the N and R mixtures at 50 F/T cycles, as the *F* values were 3.8 and 9.4, respectively which are less than the F_{cr} of 18.51. In addition, when the curing method and time were varied (Table 8.6), the mass loss results for mixtures NF30 and RF30 were still below 0.5 kg/m^2. The limited surface scaling of the concrete mixtures can be attributed to the incorporation of nano-silica with fly ash, which enhanced the reactivity and binding of Class F fly ash, as indicated for example by the evolution of compressive and tensile strengths.

According to the glue-spall theory (Valenza et al. 2006 and 2007), which employs fracture mechanics to explain the process of salt-frost scaling by crack propagation into the surface of concrete, the strength of cementitious matrix substantially controls its resistance to scaling. Combination of fly ash with nano-silica led to a dense matrix/ITZ (further densifying with time) and higher tensile capacity as shown by various tests (e.g. bonding, RCPT, BSEM) which might discount the process of crack propagation in the surface of concrete, and thus improving its resistance to salt-frost scaling.

Table 8.6: Effect of curing time and method on the mass loss results after 50 F/T cycles

Curing Method	Mass loss, g/m^2					
	NF15	NF22.5	NF30	RF15	RF22.5	RF30
14 days curing[*] and 14 days in air (ASTM C672)	123	132	189	196	226	247
3 days curing[*] and 14 days in air	147	229	398	152	248	410
Curing[*] the concrete until a strength of 20 MPa and 14 days in air	142	221	331	210	363	489
Curing by a chemical compound[**] and 14 days in air	163	177	236	241	274	376

*Maintained at a temperature of 23 ± 2 °C (73.4 ± 35.6 °F) and relative humidity of more than 95%.
**The curing compound met CSA A23.1-14 (Clause 7.7.2.2) specifications.

8.4.6 Thermal and Microscopy Analyses

The consumption of portlandite (CH) in the cementitious matrix was determined at different ages to capture the evolution of hydration and pozzolanic reactions, as shown in Fig. 8.6. At a constant dosage of nano-silica (6%), consumption of CH in the N and R mixtures started at very early-age. For example, at one day, the normalized CH contents for NF15 and NF30 relative to the corresponding reference mixtures were less than 1.0 (Fig. 8.6), which may be linked to a vigorous pozzolanic activity at early-age as observed in the heat of hydration (Fig. 8.2) and strength tests (Table 8.4)**.** It has been postulated that a very rapid pozzolanic activity is possible as silicate ions from nano-silica aggregates engage with CH forming pozzolanic C-S-H gel, which subsequently precipitate on the surface of silica aggregates, resulting in slower reactivity at later ages (Kong et al. 2012; Korpa et al. 2008). Whether this mechanism is a through-solution process (Madani et al. 2012) or topochemical (Kong et al. 2012) growth is still debatable. Moreover, nano-silica can accelerate the hydration of cement by creating additional surfaces for early precipitation of hydration products (Hou et al. 2013; Korpa et al. 2008). Also, it has been shown that commercial nano-silica sols (originally dispersed to their primary sizes) form small enough agglomerates to impart a filler effect in the cementitious matrix (Oertel et al. 2013; Kong et al. 2012). All these factors might have contributed to improving the early-

age strength (up to 7 days) of nano-modified fly ash concrete even for mixtures incorporating 30% fly ash (Table 8.4).
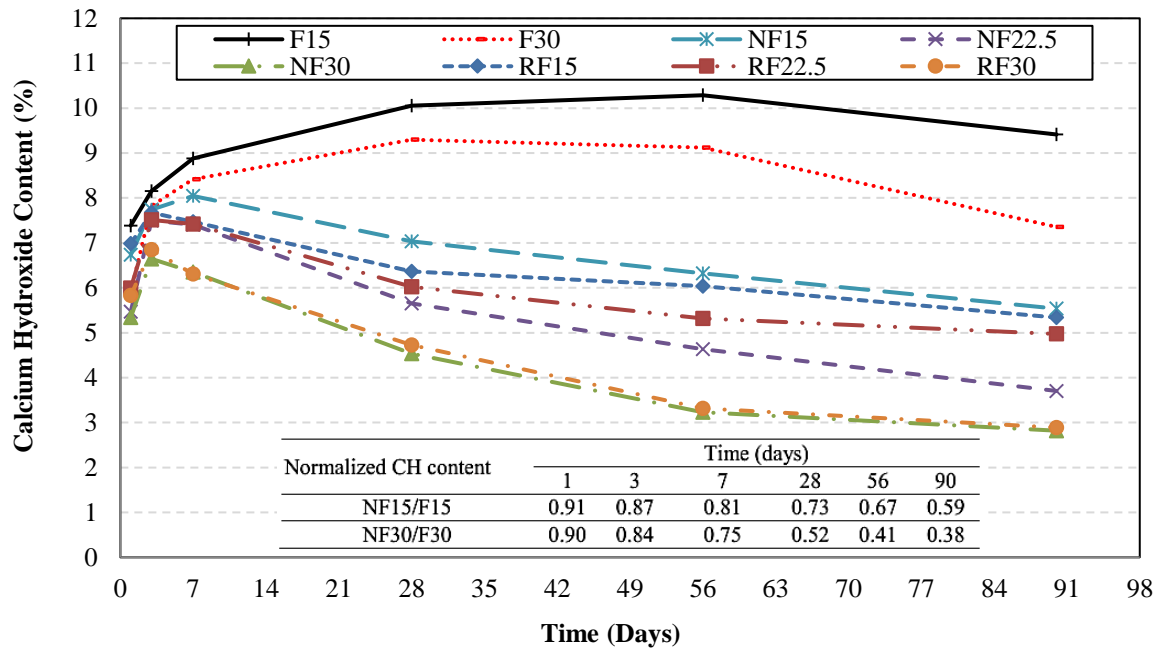
Figure 8.6: Thermogravimetry results for the portlandite content (at a temperature range 400-450ºC) in the nano-modified fly ash concrete mixtures.

It has been documented that the pozzolanic effect of fly ash in concrete starts at later ages (typically after 28 days, F15 and F30 in Fig. 8.6); therefore, most standard codes for concrete (e.g. CSA A23.1) require the properties of fly ash concrete to be assessed at 56 or 91 days (Mehta et al. 2014; Nevile 2011; Malhotra et al. 2000). It was reported that the pozzolanic action of nano-silica aggregates is completed within 7 days (Hou et al. 2013); however, Fig. 8.6 shows a significant consumption in CH in the N and R mixtures from 7 to 90 days relative to the reference mixtures, especially at higher dosages of fly ash (NF30 and RF30). This pinpoints that the presence of nano-silica catalyzed the reactivity of fly in concrete, resulting in an improved level of hydration and evolution of microstructure. The continual reactivity of the ternary binder up to 90 days is attributed to the pozzolanic activity of fly ash with time, as for example noted in the results of later-age

strength (Table 8.4) and bonding after the combined exposure (Fig. 8.3). This explains the significant densification and refinement of the pore structure at 28 days in the nano-modified fly ash concrete mixtures, which had limited penetration depth (average of 6 mm).

BSEM was conducted on thin sections to complement the trends observed in the mechanical, durability and TG tests. In comparison to the commercial product A, all the nano-modified fly ash mixtures had a significant degree of refinement and densification in the hydrated paste and ITZ at 28 days. Product A (Fig. 8.7) showed coarse microstructure in addition to micro-cracks in the paste and ITZ; the EDX analysis for C-S-H in the ITZ showed a high calcium-to-silicate (C/S) ratio (average of 2.0). These features reflect an insufficient level of hydration conforming to the inferior performance observed for this product in the mechanical and durability tests. On the contrary, homogenous and dense matrix in various specimens from the N and R mixtures with low (15%) and high (30%) dosages of fly ash were observed. For instance, Fig. 8.8 shows dense microstructure and refined ITZ at 28 days of a specimen from NF30 owing to the synergistic effects of nano-silica and fly ash, as described earlier. EDX analysis for C-S-H in the ITZ in this specimen showed that the average C/S was 1.05 indicating an efficient pozzolanic activity and densification of ITZ with secondary C-S-H. It was reported that the C/S of secondary C-S-H from pozzolanic reactions is lower than that of conventional C-S-H produced from cement hydration reactions, the former has a ratio of about 1.1, while the latter has a ratio of about 1.7 (Detwiler et al. 1996). In addition, Kong et al. (2012) stated that when small agglomerates of nano-silica form, water absorption into their ultra-high nano-porosity can reduce the *w/b* in the paste, and thus improving the microstructure of the matrix.
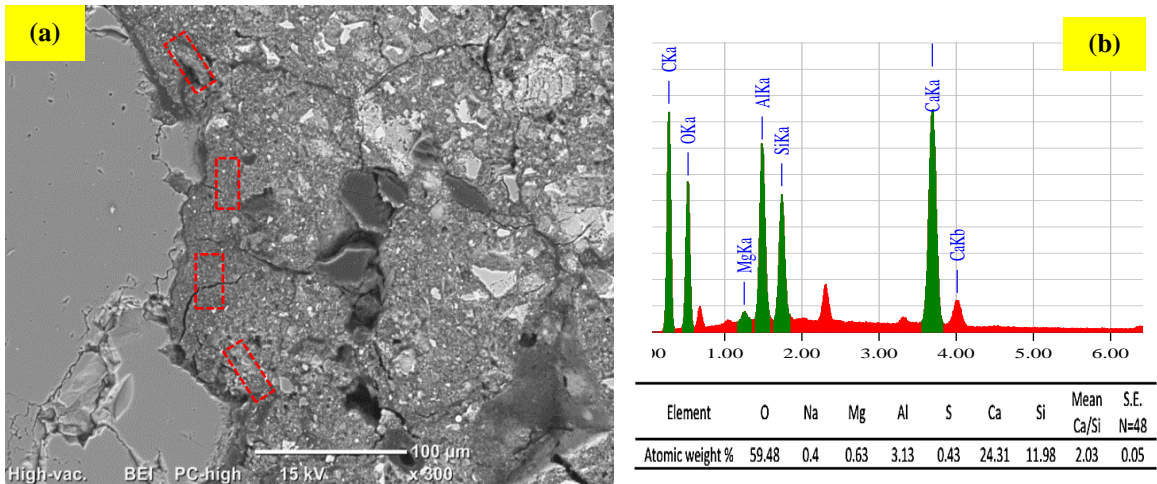
Figure 8.7: BSEM analysis for a thin section from product A showing: (a) porous ITZ and coarse microstructure, and (b) associated EDX spectrum of C-S-H in the locations indicated in (a). (Note: S.E. is the standard error)
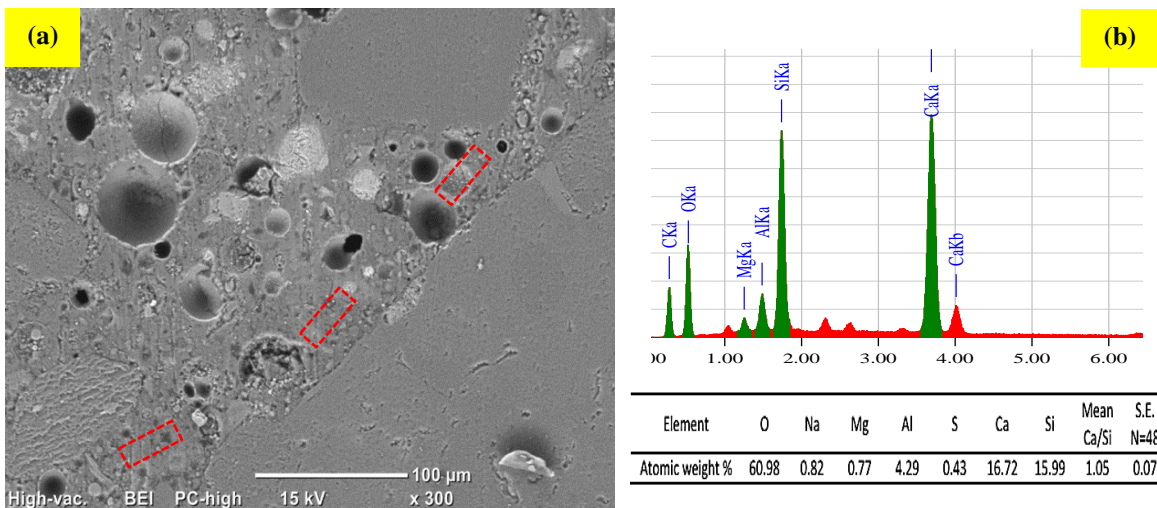
Figure 8.8: BSEM analysis for a thin section from NF30 showing: (a) refined ITZ and dense microstructure, and (b) associated EDX spectrum of C-S-H in the locations indicated in (a). (Note: S.E. is the standard error)

CHAPTER 9 – PHASE III: SHRINKAGE OF NANO-MODIFIED FLY ASH CONCRETE AS A REPAIR MATERIAL

9.1 Introduction

A key issue for many rapid setting repair materials for concrete pavements is the inability to achieve their target service lives, resulting in significant economic and social losses (Li et al. 2011; Al-Ostaz et al. 2010). This is particularly critical as United States Federal Highway Administration estimates that $85 billion would be needed in annual capital investment up to 2028 to be directed towards improving the physical condition of existing road assets in order to achieve the Department of Transportation's State of good repair benchmark for a better ride quality (Report Card for America's Infrastructure 2013). Proprietary repair materials seldom fail due to lack of intrinsic strength, per se; in fact, the failure mechanisms for many of these materials are linked to incompatibility (e.g. higher rates of shrinkage) with existing/parent concrete (Beushausen 2016; Ghazy et al. 2016; Bentz et al. 2008). Stresses due to differential shrinkage rates have long been recognized as a major problem for the performance of bonded/repair concrete (e.g. partial depth repair (PDR) applications in concrete pavements), resulting in extensive cracking (Beushausen 2016). These cracks compromise the durability of cement-based materials by introducing direct pathways for deleterious substances (e.g. de-icing salts), thus impairing the integrity of the matrix. Therefore, particular attention is required to select repair materials that properly address dimensional stability and behave similar to substrate concrete, especially when subjected to temperature and moisture changes.

The use of nanoparticles in concrete research, including repair applications, has been progressively growing in recent years (Ghazy et al. 2016; Belkowitz et al. 2015;

Zadeh et al. 2013; Said et al. 2012). Nanosilica (small sized particles of 1-100 nm with high content of amorphous silica (>99%)) is one of the most widely used nanomaterials in cementitious materials research as a result of their ability to improve fresh and hardened properties of concrete by modifying the structure of the cementitious matrix at the nano and micro levels as shown in the previous Chapter (Ghazy et al. 2016). Owing to their ultrafine nature, well-dispersed nanosilica can vigorously speed-up the kinetics of cement hydration, especially at early ages, by creating additional surfaces for early precipitation of hydration products (Kong et al. 2015; Madani et al. 2012). Moreover, a very rapid pozzolanic activity is possible as silicate ions from nanosilica aggregates engage with calcium hydroxide (CH) forming pozzolanic calcium-silicate-hydrate (C-S-H) (Ghazy et al. 2016; Zadeh et al. 2013; Said et al. 2012). It has been shown that nanosilica sols (originally dispersed to their primary sizes) form small enough agglomerates to impart a filler action in the cementitious matrix (Kong et al. 2015; Madani et al. 2012).

A number of studies aimed at producing nano-modified concrete with superior hardened and durability properties (Ghazy et al. 2016). For example, in the previous Chapter 8, a nanosilica sol was used to mitigate the limitations of early-age properties (hydration, setting time, and strength development) of cementitious binders containing Class F fly ash; the nano-modified fly ash concrete produced in this study had balanced early-age and durability properties suitable for PDR applications of concrete pavements. Yet, there is dearth of information on the shrinkage behaviour of cementitious systems containing nanosilica. Early-age cracking, for example due to physico-chemical interactions such as shrinkage, is of great concern for such binders containing ultrafine particles (Sonebi et al. 2015; Aly et al. 2009). Using nanoparticles can alter the water-to-binder ratio (w/b) when small agglomerates of nanoparticles form due to water absorption

213

into their ultra-high nano-porosity, increasing the possibility of self-desiccation of the matrix (Kong et al. 2015). Hence, shrinkage cracking of concrete comprising highly reactive materials such as nanosilica may increase (depending on curing conditions) (Mehta et al. 2014), which can defeat the purpose of using such materials to produce concrete with superior performance and longevity.

9.2 Research Significance

In the previous Chapter 8, it has been shown that nano-modified fly ash concrete may be used as a repair material for concrete pavements since it can achieve balanced early-age and long-term performance. However, with the advent of nanomaterials in concrete, it is imperative to understand its shrinkage behaviour due to the very rapid hydration and pozzolanic reactions at early-age, which warrants further investigation. Thus, in this present Chapter, the autogenous, free and restrained shrinkage behaviour of nano-modified fly ash concrete was studied to capture performance risks (in terms of dimensional stability) associated with this concrete as a repair material.

9.3 Experimental Program

9.3.1 Materials and Procedures

The materials and procedures used to develop the nano-modified fly ash concrete in this Chapter were similar to that used in Chapter 8 (refer to Section 9.3.1 and 9.3.2).

9.3.2 Testing Methods

9.3.2.1 Autogenous shrinkage test

Many studies in the literature (Loser et al. 2010; Holt 2005) refer to the volumetric change of paste from the method described by Justnes et al. (1994) adopted herein, as autogenous shrinkage irrespective of the *w/b* (less or more than 0.40). Therefore, the same

terminology is used in this paper. Paste samples with identical proportions to the paste

fraction of the concrete mixtures described in Table 8.2 were prepared. Approximately 150

g of cement paste was sealed in a polyurethane membrane, submerged in a beaker filled with

paraffin oil, and suspended from a high-precision balance (±0.001 g). The bath temperature

was controlled by a cryothermostat with an accuracy of 0.1°C at a desired temperature

(23°C), since the density of the liquid is a function of temperature (Loser et al. 2010). After

about 60 min of mixing the paste (to allow for sample preparation and test-setup), the

submerged mass of the sealed paste sample was recorded every 10 minutes for the first 4 h

and then every 2 h up to 24 h. The volumetric strain of the sample (ε_{Vol}) was calculated by:

$$\varepsilon_{Vol} = \frac{\Delta V_{paste(t)}}{V_{paste(t_0)}} = \frac{M_{sub(t)} - M_{sub(t_0)}}{\rho_L . V_{paste(t_0)}} = \frac{M_{sub(t)} - M_{sub(t_0)}}{M_{air(t_0)} - M_{sub(t_0)}} \qquad \text{Eq. (9.1)}$$

where, $V_{paste(t_0)}$ is the initial volume of the paste, $\Delta V_{paste(t)}$ is the change of the paste

volume at time (t), $M_{air(t_0)}$ and $M_{sub(t_0)}$ are the initial mass of sample measured in air and

in the buoyancy liquid (paraffin oil), respectively, $M_{sub(t)}$ is the mass of the sample in the

buoyancy liquid at time (t) and ρ_L is the density of the buoyancy liquid at 23°C. Assuming

an isotropic behaviour of the paste, the linear strain (ε_{Linear}) could be approximated by

dividing ε_{Vol} by 3 (Loser et al. 2010; Justnes et al. 1994).

9.3.2.2 Free shrinkage tests

Duplicate prisms (76×76×285 mm) were cast and stored in a standard curing room

for different durations (3, 7 and 28 days). The specimens cured for 3 and 7 days were stored

thereafter in a controlled laboratory environment (23±2°C and 55±5% RH) for 25 and 21

days, respectively. Additionally, to mimic curing conditions in the field, a curing

compound (CC) made of high-grade hydrocarbon resins in a water-based emulsion

conforming to ASTM C309 was applied to another set of companions (duplicate) prisms.

After casting, the top surface of specimens was sprayed by the CC and the specimens were left in the molds for 24 h. After demolding, the specimens were coated by the CC onto the remaining surfaces and kept in laboratory conditions for 27 days. After 28 days, all specimens were exposed to hot-dry conditions (40±2°C and 35±5% RH) for 152 days to monitor their free length change (using a digital comparator) versus time, following the general guidelines of ASTM C157. The initial comparator reading (ICR) measurements were recorded immediately after demolding, and the length change at a given age was calculated as the difference between the comparator reading at that age and ICR divided by the gauge length.

The mechanical properties and pore structure were determined for all the mixtures to complement the free shrinkage trends. Triplicate 100×200 mm concrete cylinders were prepared for the splitting tensile strength test according to ASTM C496. After casting, the cylinders were demolded and cured under similar conditions to the free shrinkage specimens and tested at 28 days; another set of cylinders were exposed to the same hot-dry conditions described earlier and their splitting tensile strength was determined at 180 days. The prisms used for the free shrinkage test were also evaluated for their dynamic modulus of elasticity at 28 and 180 days using the resonance frequency method (transverse mode) according to ASTM C215. The features of pore structure for the mixtures were determined by MIP with a maximum pressure of 206 MPa, allowing the detection of pore radii ranging from 3 nm up to 1000 µm.

9.3.2.3 Restrained shrinkage test

Many studies have reported various restrained shrinkage tests and different specimen geometries to assess the cracking potential for repair materials including the ring-test and/or end-restraint configurations (Beushausen 2016; Abbasnia et al. 2005; Weiss et

al. 1998). However, repair materials in concrete pavements are restrained by substrate (parent) concrete at the interface and/or the periphery of an enclosed patch repair; this restrained shrinkage configuration promotes formation of multiple cracks at the surface of concrete relative to the end-restraint case 'single crack' (Abbasnia et al. 2005), and thus it has been adopted in the current study to simulate Type I (square/rectangular) patch repair in concrete pavements (Frentress et al. 2012).

Concrete slabs of 300×260 mm surface area and 140 mm thickness were used as concrete substrate (350 kg/m^3 GU cement with 15% fly ash as a binder replacement and 0.38 *w/b*, which is typical of existing/parent concrete pavement). After casting, the slabs were demolded and moist cured for 7 days in the curing room and then maintained under normal laboratory conditions (23±2°C and 55±5% RH). After six months (to minimize the residual shrinkage in the substrate concrete) the top surface (finished surface) was wire brushed and cleaned; subsequently, the tested mixtures were placed on the top surface with a thickness of 30 mm. At the initial setting, the top surface of the mixtures was sprayed by the CC and the slabs were left in the formwork for 24 h. After demolding, four pairs of Demec points were attached to the surface and sides of each slab across a length of 200 mm (Fig. 9.1). The vertical surfaces of the repair sections were then cured by the CC and left under laboratory conditions for 27 days. At 28 days, the slabs were exposed to hot-dry conditions similar to the free shrinkage regime for 152 days, and the length change was measured by a dial gauge extensometer to record the average shrinkage of two slabs for each mixture.
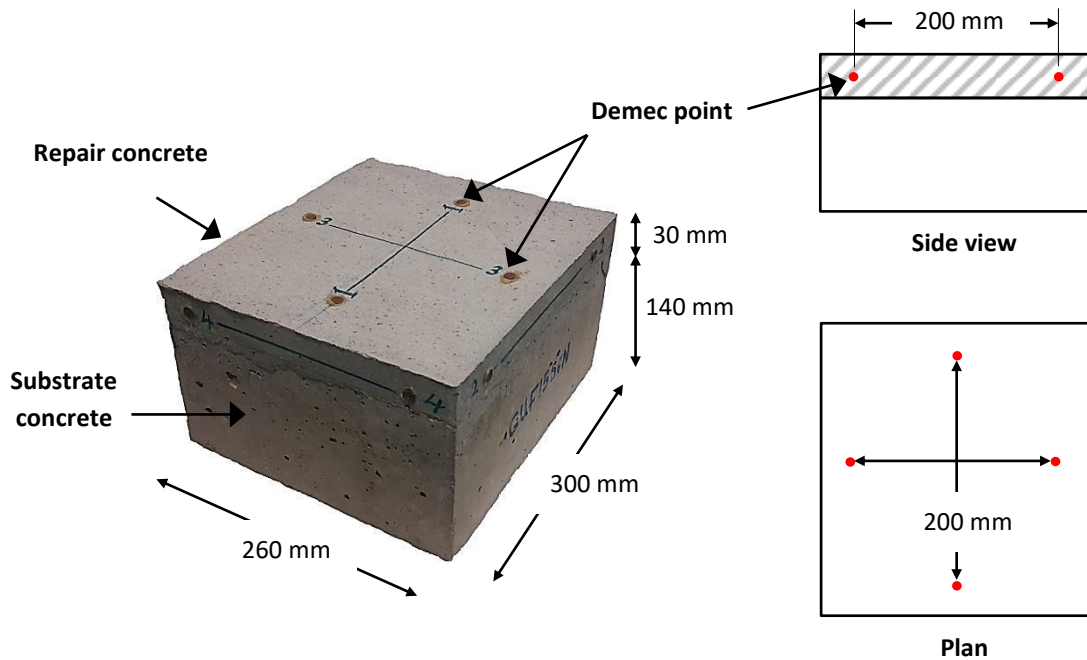
Figure 9.1: Configuration of the repair and substrate concrete assembly (left), and the locations of Demec points (right).

9.4 Results and Discussion

9.4.1 Autogenous Shrinkage

Since different definitions of autogenous shrinkage are reported in literature, it is necessary to specify the terminology used in this paper. The volumetric autogenous shrinkage herein is considered as the internal volume reduction of the paste in an isolated system (no moisture transfer) and at a constant temperature (no thermal contraction or expansion). Under this condition, the volumetric change is mainly the sum of hydration shrinkage, self-desiccation (if any), crystallization swelling, and the shrinkage due to phase transition, which is directly related to the degree of cement hydration (Yodsudjai et al. 2013; Slatnick et al. 2011). During the first few hours of hydration, negative volumetric

218

variations are critical since the induced internal tensile stresses within the cementitious matrix are often higher than its capacity; consequently, cement-based materials shrink and possibly crack. The heat of hydration data for the mixtures tested was reported previously in Chapter 8 and a summary of these results is given in Table 9.1, as these data are strongly associated with the autogenous shrinkage behaviour of these mixtures. Generally, the results showed that the presence of nanosilica accelerated the kinetics of hydration, shortened the hardening times and enhanced the level of hydration of the N mixtures at early-age. These catalytic effects of nanosilica were further magnified with the incorporation of the accelerating admixture (R mixtures), which conforms to the well-documented effect of these chemical admixtures on speeding up the kinetics of hydration of cementitious materials, accompanied by releasing higher amounts of heat (Mehta et al. 2014; Nevile 2011).

Table 9.1: Summary of the heat of hydration results

Mixture ID.	Acceleration period, h		Max. heat flow value (first peak), mW/g	Cumulative heat at steady state, J/g
	Start[*]	End		
F15	3.35	10.15	1.60	136
F30	4.15	11.40	1.45	110
NF15	1.83	7.05	1.75	138
NF30	2.08	8.15	1.50	124
RF15	1.22	5.90	2.05	171
RF30	1.40	6.60	1.75	142

[*]Denotes the end of the dormant period.

The results of autogenous shrinkage of the sealed paste samples are presented in Fig. 9.2, where each curve is the average of two measurements obtained from two replicate samples of the same mixture. The rates of shrinkage were variable with time, but it may be split into two or three stages depending on the time interval, where each interval can be roughly expressed by a constant rate of shrinkage (microstrain/h). This can ease the description of the general trends observed in the shrinkage graphs of the mixtures tested.

The rates of autogenous shrinkage were generally high during the first 10 h; subsequently, these rates decreased until reaching a small/nil value starting from 6 to 13 h, depending on the type of binder, up to 24 h. As a result of the rapid change from the plastic to pseudo-rigid state, especially in the case of mixtures comprising nanosilica during the first 4 h, the critical radius of the capillary pores may reduce rapidly with a correspondingly fast growth of capillary forces due to water menisci, thereby increasing autogenous shrinkage of the paste (Yodsudjai et al. 2013; Slatnick et al. 2011; Holt 2005). The onset of cluster formation of the hydration products marks the start of internal stress evolution due to autogenous shrinkage; in addition, the autogenous shrinkage increases rapidly as the hydration activity becomes more intense (Holt 2005). However, once the cement paste solidifies, the autogenous shrinkage seems not to be significantly affected by the formation of additional hydration products. This may be explained by the formation of interconnected hydrates creating both a solid skeleton with a considerable tensile capacity and a pore network containing the remaining water. Consequently, the internal stresses (which are generated by the lack of water in the system) would diminish when equilibrium with the tensile capacity of the matrix is reached. This argument is substantiated by the variable rate of autogenous shrinkage in Fig 9.2. The autogenous shrinkage mainly occurs before the rigid state (the end of acceleration period (6 to 12 h), Table 9.1), which generally coincides with the onset of negligible change of autogenous shrinkage with time up to 24 h.

In comparison to the reference fly ash mixtures (F15 and F30), the rates of autogenous shrinkage were higher (76.2 and 26.8 microstrain/h, respectively) between 1 to 5 h for the N mixtures containing nanosilica (NF15 and NF30). For instance, at 5 h, the autogenous shrinkage for the NF15 specimens gained about 75% of their total autogenous shrinkage after 24 h. Also, this catalytic effect of nanosilica was magnified with the

incorporation of the accelerating admixture. For example, the autogenous shrinkage for the R mixtures containing 15% and 30% fly ash (RF15 and RF30) was significantly higher (an increase of 85% to 260%) than that of the corresponding N mixtures (NF15 and NF30) at 5 h, and RF15 exhibited the highest autogenous shrinkage of 690 microstrain after 24 h. This increase of the rate of shrinkage corresponds to the acceleration stage in the hydration process, as reflected by the occurrence of the first peak at an earlier time (5.90 to 6.60 h) coupled with the highest heat flow values (1.75 to 2.05 mW/g, Table 9.1), which corresponds to water consumption and internal drying processes in these binders containing the accelerator. This was statistically supported by the analysis of variance (ANOVA), as shown in Table 9.2.
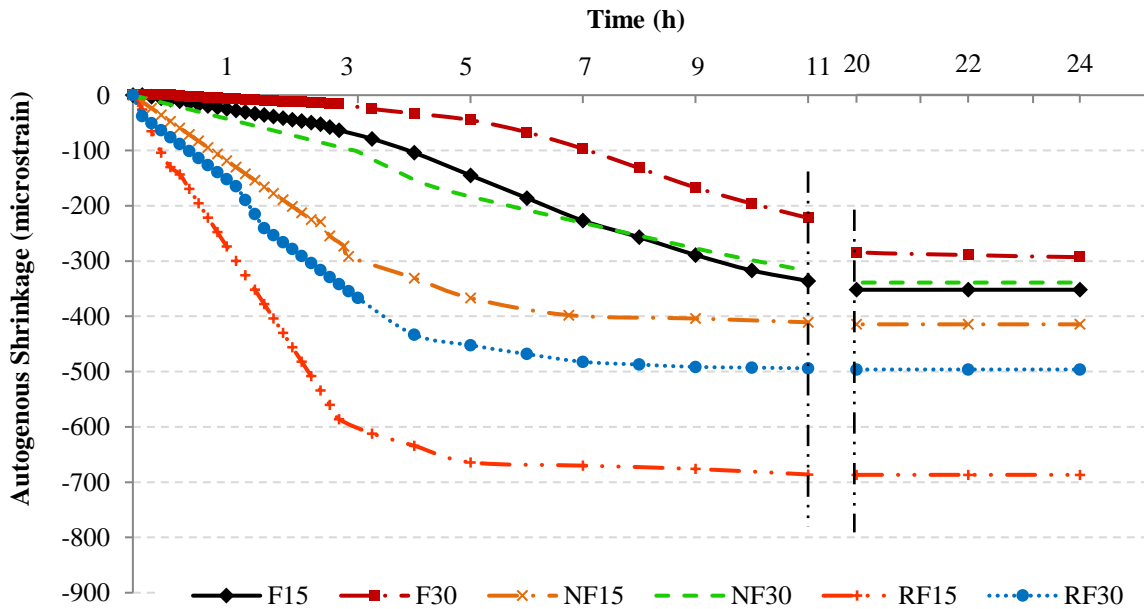
Figure 9.2: Autogenous shrinkage of the paste mixtures. (Note: Measurements started 60 min after mixing)

The effect of increasing the dosage of fly ash up to 30% on reducing the rate and total autogenous shrinkage of cementitious paste is depicted in Fig. 9.2. The reference mixture containing 30% fly ash (F30) exhibited the lowest rate (19 microstrain/h) of autogenous shrinkage within the first 13 h, and the lowest cumulative shrinkage of 295 microstrain at 24 h. Increasing the fly ash content from 15% to 30% in the N mixtures comprising 6% nanosilica (NF15 and NF30) led to a significant (Table 9.2) reduction (66%) in the rate of autogenous shrinkage up to 5 h, and the cumulative autogenous shrinkage (after 24 h) for NF30 was 341 microstrain, which was slightly higher (11%) than that of the reference mixtures without nanosilica (F30). Similarly, the higher dosage of fly ash (30%) was effective at reducing the autogenous shrinkage (by approximately 28%) of the paste containing 6% nanosilica with the accelerator (RF30). The role of fly ash in reducing autogenous shrinkage of the paste can be attributed to its dilution effect (reduction of the cement component) that led to a slower reactivity of these binders, as reflected by the heat of hydration results (Table 9.1). In addition, unhydrated fly ash particles may serve as restraining particles, similar to aggregates, which can discount shrinkage deformations at this stage (Mehta et al. 2014; Nevile 2011). Thus, addition of 30% fly ash could effectively balance the effect of 6% nanosilica on increasing autogenous shrinkage of cement paste, even with the addition of the accelerator.

Table 9.2: ANOVA for the results of autogenous, free and restrained shrinkage tests

	Autogenous shrinkage (1 day)			Free shrinkage (180 days)				Restrained shrinkage (180 days)		
	F	F_{cr}	P-value		F	F_{cr}	P-value	F	F_{cr}	P-value
Effect of nanosilica										
NF15 vs. F15	19.5	18.5	0.063[*]	3 days moist curing	0.9	18.5	0.429	91.8	4.6	1.58E-7[*]
					2.4	18.5	0.262			
				7 days moist curing	53.2	18.5	0.004[*]			
					32.6	18.5	0.002[*]			
NF30 vs. F30	2.6	18.5	0.342	28 days moist curing	120.2	18.5	0.001[*]	31.3	4.6	6.63E-5[*]
					76.7	18.5	0.001[*]			
				CC	56.2	18.5	0.001[*]			
					43.8	18.5	0.001[*]			
Effect of accelerator										
RF15 vs. NF15	102.7	18.5	0.010[*]	3 days moist curing	1.2	18.5	0.399	260.2	4.6	1.94E-10[*]
					0.9	18.5	0.436			
				7 days moist curing	40.1	18.5	0.024[*]			
					23.5	18.5	0.040[*]			
				28 days moist curing	27.3	18.5	0.035[*]			
RF30 vs. NF30	49.9	18.5	0.019[*]		73.1	18.5	0.013[*]	62.7	4.6	1.54E-6[*]
				CC	126.5	18.5	0.008[*]			
					36.5	18.5	0.026[*]			
Effect of fly ash dosage										
NF30 vs. NF15	127.5	18.5	0.008[*]	3 days moist curing	1.2	18.5	0.391	19.1	4.6	6.43E-8[*]
					7.3	18.5	0.114			
				7 days moist curing	3.9	18.5	0.185			
					0.4	18.5	0.588			
				28 days moist curing	93.2	18.5	0.001[*]			
RF30 vs. RF15	118.5	18.5	0.008[*]		72.7	18.5	0.001[*]	109.9	4.6	5.18E-8[*]
				CC	115.1	18.5	0.001[*]			
					83.8	18.5	0.001[*]			

[*]Indicates statistical significance.

9.4.2   Free Shrinkage

The term "free shrinkage" in this study comprises deformations from autogenous shrinkage (at early-age), chemical shrinkage and moisture loss (drying) from the paste to surrounding environment under hot-dry conditions. Mechanisms that induce drying shrinkage of cement paste in concrete over time include capillary stress, surface tension, and disjoining pressure, where these mechanisms can be predominant within RH range of 35 to 50% (Mehta et al. 2014; Nevile 2011; Aly et al. 2009; Holt 2005). The removal of water held by hydrostatic tension in small capillaries (mesopores: <50 nm) and loss of physically adsorbed water from C-S-H induce high capillary stresses, resulting in marked levels of drying shrinkage (Slatnick et al. 2011; Aly et al. 2009; Holt 2005). Also, other factors (e.g. water content, aggregates) including the mechanical characteristics (tensile capacity and stiffness) of the matrix influence the resistance of concrete to shrinkage stresses (Mehta et al. 2014; Soliman et al. 2014). Thus, the net effect of shrinkage of concrete is due to the combination of these factors. Table 9.3 presents the proportion of mesopores, tensile strength, and stiffness of all the specimens, considering the curing method and age of testing. The shorter curing durations (3 and 7 days) led to reduction of the degree of hydration, especially for the reference mixtures (F15 and F30), as reflected by lower proportion of mesopores, tensile strength and dynamic modulus of elasticity relative to the corresponding specimens cured for 28 days or by the CC. The effect of each curing method on the free shrinkage results is discussed below.

Table 9.3: Results of MIP, tensile strength and dynamic modulus of elasticity

Mixture ID.	Proportion of mesopores (<50 nm), %				Splitting tensile strength, MPa								Dynamic modulus, GPa							
					Curing Method															
	$3d^*$	$7d^*$	$28d^*$	CC^{**}	$3d^*$		$7d^*$		$28d^*$		CC^{**}		$3d^*$		$7d^*$		$28d^*$		CC^{**}	
Age (days)	28	28	28	28	28	180	28	180	28	180	28	180	28	180	28	180	28	180	28	180
F15	16.4	16.6	22.3	16.6	2.2	2.1	2.4	2.6	3.5	3.8	2.1	2.2	22.9	22.5	25.0	25.3	36.3	37.8	24.8	25.3
F30	10.7	14.3	24.6	18.7	1.7	2.0	2.1	2.4	3.8	4.2	2.3	2.5	20.2	21.3	22.9	23.0	37.7	40.7	27.6	30.1
NF15	36.6	49.2	75.3	46.2	3.1	3.4	3.8	4.7	5.1	5.4	3.9	4.1	27.7	31.0	39.1	42.5	50.2	54.4	42.1	44.6
NF30	24.3	37.2	82.1	49.1	2.5	3.1	3.5	4.1	5.7	5.9	4.2	4.5	25.1	27.4	35.3	39.8	56.3	59.3	45.9	47.9
RF15	39.6	42.7	47.8	41.6	3.4	3.5	4.1	4.3	4.9	5.1	3.6	3.7	30.6	30.9	41.8	42.3	43.3	44.1	37.8	37.1
RF30	33.4	41.5	58.4	43.1	3.0	3.3	3.6	3.9	5.5	5.5	3.8	4.0	27.9	28.8	36.2	37.1	51.3	53.7	40.2	41.8

* Moist Curing,
** Curing Compound (CC)

9.4.2.1 Moist curing for 3 and 7 days

Figures 9.3 shows the results of the free shrinkage test for the specimens cured for 3 days. There was a high rate of shrinkage for all specimens, especially the ones comprising nanosilica before the drying exposure (up to 28 days), followed by a higher rate of shrinkage from the start of the hot-dry exposure up to 140 days; subsequently, the rate of shrinkage for all the specimens decreased to a small or negligible value up to 180 days. In comparison to the reference specimens (F15 and F30), the rates of shrinkage for the NF15 and NF30 specimens were higher (7.7 to 10.5 microstrain/day) up to 28 days, at which they gained about 35% of their total (at 180 days) free shrinkage values that were 285 and 215 microstrain, respectively. This catalytic effect of nanosilica was further magnified (7% to 17%) with the incorporation of the accelerator in the R mixtures. This increase of the rates of shrinkage before the hot-dry exposure corresponds to the higher rates of autogenous shrinkage (within the first day) (Fig. 9.2) and chemical reactivity (hydraulic and pozzolanic) within 28 days, as shown in Chapter 8, including 25 days air-drying at 23±2°C and 55±5% RH. During the hot-dry exposure, the reference, N and R specimens showed comparably high rates of shrinkage, although for different reasons, and the total shrinkage of all specimens was in the narrow range of 715 to 805 microstrain, without statistical significance among the variables tested (Table 9.2).

For the reference specimens, insufficient curing produced a concrete matrix with lower tensile capacity (maximum of 2.2 MPa) and stiffness (maximum of 23 GPa), which led to high rates of shrinkage. Comparatively, the N and R specimens developed relatively higher mechanical properties (Table 9.3); however, these specimens had a higher proportion (25 to 40%) of mesopores (higher capillary stresses) at 28 days, and thus the rates of shrinkage were high. Therefore, curing the specimens for 3 days was insufficient

to control the rate of shrinkage of fly ash concrete without or with nanosilica.
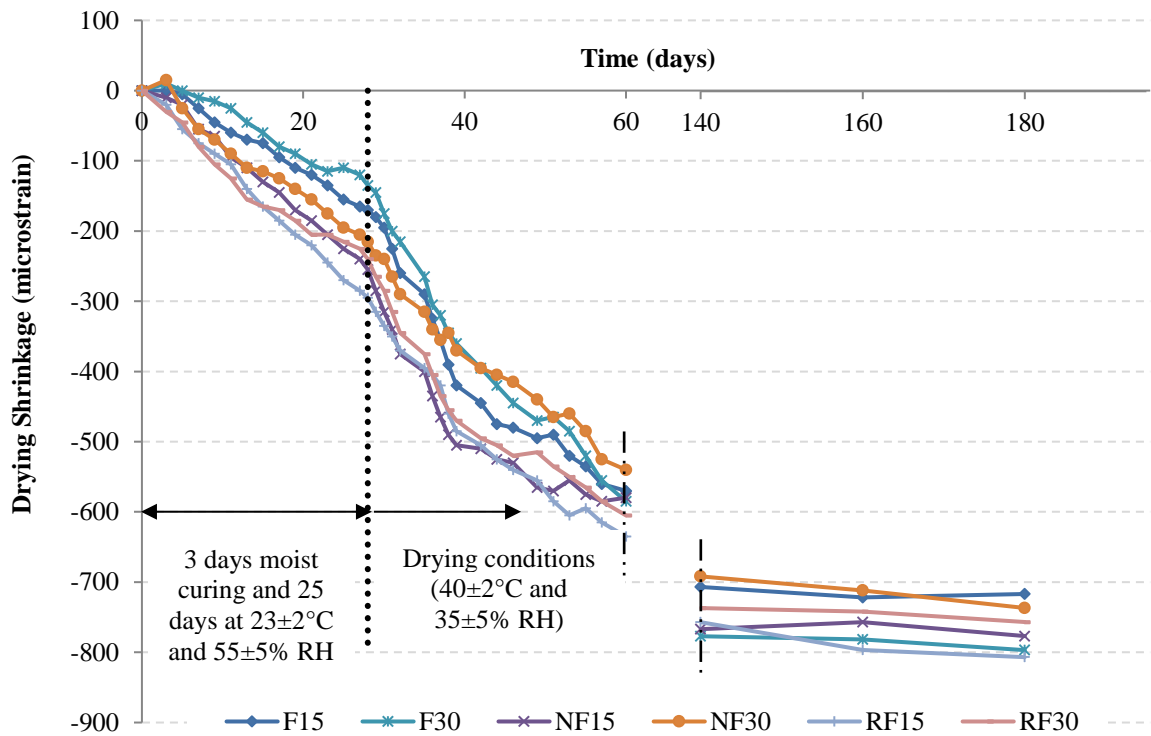
Figure 9.3: Free shrinkage of the concrete prims (3 days moist curing).

The results of specimens cured for 7 days (Fig. 9.4) show that the trends of drying shrinkage over time are similar to that of specimens cured for 3 days, except that the rates of deformation were lower. For instance, before the hot-dry exposure, the shrinkage rates for the N and R specimens decreased by 1 to 2 microstrain/day than that of the corresponding specimens cured for 3 days. Also, at 180 days, these specimens exhibited markedly lower drying shrinkage (by 15% to 37%) than that of the corresponding specimens cured for 3 days. This is ascribed to the increase of the mechanical properties (tensile capacity by 20 to 31% and stiffness by 30 to 51%, Table 9.3) due to the longer moist curing period. In comparison to the reference specimens (F15 and F30), the NF15 and NF30 specimens exhibited comparable or slightly higher rates (average of 11%) of

shrinkage up to 28 days with a significant (Table 9.2) reduction in the rate of shrinkage afterwards up to a total shrinkage of 515 and 555 microstrain, respectively.

As explained earlier, the shrinkage behaviour of the specimens comprising nanosilica may be driven by their higher autogenous shrinkage and chemical reactivity before the hot-dry exposure. Subsequently, the reduction of the total shrinkage of these specimens, despite a higher proportion of mesopores (37 to 49%), may be attributed to the significant enhancement of the mechanical properties (54% to 73%, Table 9.3). Again, the presence of the accelerator in RF15 and RF30 specimens significantly (Table 9.2) increased the rates of shrinkage and the total shrinkage values before and after the hot-dry conditions, and these mixtures gained the highest drying shrinkage of 655 and 675 microstrain, respectively. This complies with previous studies (Soliman et al. 2014; Juengera et al. 2002), which also reported the adverse effect of accelerators on increasing the shrinkage of normal and high-performance concrete.
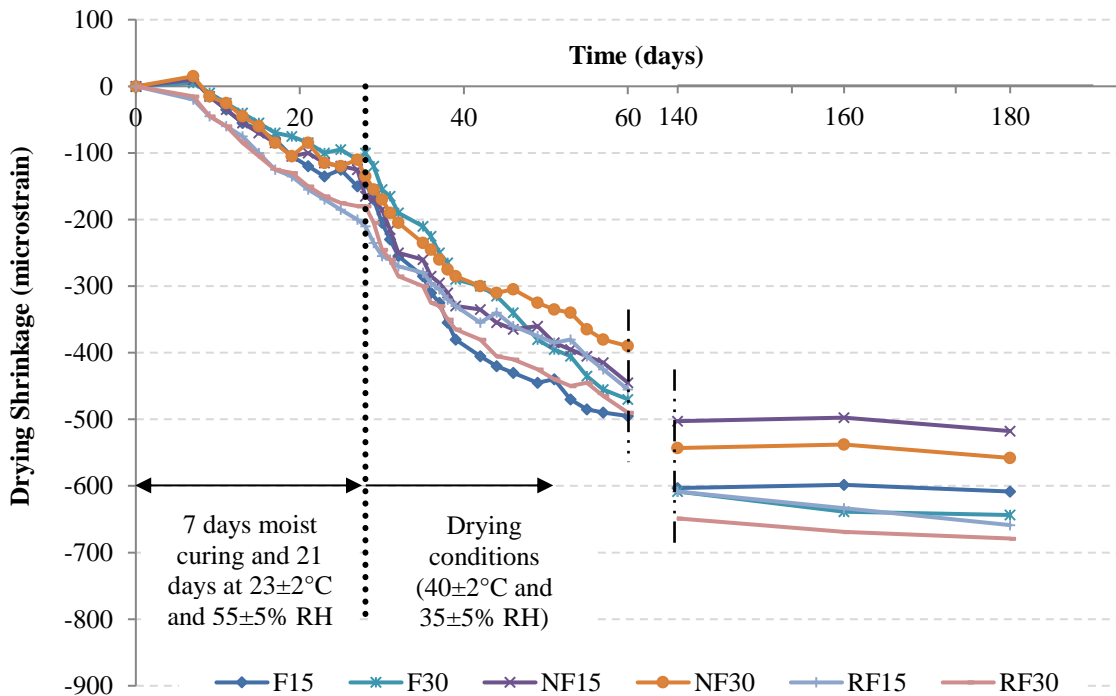
Figure 9.4: Free shrinkage of the concrete prims (7 days moist curing).

Increasing the dosage of fly ash in the mixtures led to insignificantly different (Table 9.2) levels of drying shrinkage for the specimens cured for 3 and 7 days during the hot-dry period, as depicted in Figs. 9.3 and 9.4. For example, the N and R specimens containing the higher dosage of fly ash (30%) exhibited slightly higher (8 to 11% and 4 to 7%, respectively) total drying shrinkage, compared to the corresponding specimens containing 15% fly ash. Previous studies showed that dosages of 20 to 60% Class F fly ash inadequately cured concrete have a profound effect on reducing its drying shrinkage due to the matrix densification, which may reduce internal moisture evaporation (Maslehuddin et al. 2013; Holt 2005). It appears that this trend was not replicated herein due to insufficient curing time for concrete incorporating 30% fly ash concrete without or with nanosilica, which affected the evolution of microstructure and mechanical properties of specimens (Table 9.3).

9.4.2.2 Moist curing for 28 days

The longer period of moist curing (28 days) caused notable swelling (25 to 140 microstrain) for all specimens (Fig. 9.5), which significantly discounted (by 22 to 62%) the net shrinkage of specimens at 180 days, compared to the corresponding specimens cured for 3 and 7 days. This swelling can be linked to the continuous supply of moisture, allowing the cement gel to absorb water and expand (Mehta et al. 2014; Nevile 2011). Moreover, water imbibed by the cementitious matrix over a longer duration of curing can effectively mitigate self-desiccation during early-age due to diffusion of moisture from the high relative humidity environment into the core of specimens (Maslehuddin et al. 2013). In comparison to the reference specimens, the N specimens (NF15 and NF30) exhibited

significantly (Table 9.2) lower rates (average of 45%) of shrinkage up to 140 days with almost negligible/small change afterwards; these specimens yielded the lowest shrinkage at the end of the exposure, which ranged from 280 to 355 microstrain. This behaviour may be correlated to the matrix densification (highest proportion of mesopore, Table 9.3) due to the synergistic effects of nanosilica and fly ash when longer moist curing duration was applied, which may reduce internal moisture movement and evaporation.

It has been reported that the stiffness of C-S-H, comprising low density (LD; 18 to 24 GPa) and high density (HD; 29 to 34 GPa), has a critical influence on the drying shrinkage of hardened cement paste in concrete (Kim et al. 2013; Mondal et al. 2010; Juengera et al. 2002). High-stiffness (HD) C-S-H, which makes up around 33% of the volume of C-S-H present in the paste of normal concrete (Kim et al. 2013), is highly resistant to shrinkage and can be considered as a restraining phase similar to aggregates (Juengera et al. 2002). Kong et al. (2015) and Mondal et al. (2010) reported that the presence of nanosilica in concrete may increase the volume fraction of HD C-S-H up to two times the LD C-S-H, especially after long (at least 28 days) period of moist curing. This trend might be reflected herein by the very high proportion (75 to 82%) of mesopores, which implicates additional C-S-H gel from the enhanced degree of hydration of this ternary binder, as shown in Chapter 8, and the simultaneous low shrinkage of the N specimens. Correspondingly, there was a significant increase of the mechanical properties (tensile capacity by 46% to 63% and stiffness by 38% to 49%, Table 9.3) of the N specimens, and thus the matrix effectively controlled shrinkage deformations over time (high dimensional stability).

The R specimens showed lower swelling deformations within the first 28 days, which corresponds to high autogenous shrinkage (Fig. 9.2) and reactivity of their binder

system comprising the accelerator. Afterwards, the drying shrinkage rates were quickly developed and diverged from the corresponding N specimens (increased by an average of 3.0 microstrain/day from 28 to 140 days), and RF15 yielded the highest (540 microstrain) total shrinkage (Fig. 9.5). The increase of the drying shrinkage for the R specimens may be correlated to the relatively less dense microstructure in these specimens compared to the corresponding N specimens (Table 9.3), which facilitated internal moisture movement and evaporation to the external environment. Moreover, the lower stiffness (reduction of 10 to 20%) of the R specimens compared to the N specimens from 28 to 180 days (Table 9.3) made these specimens less resistant to shrinkage deformations. In Chapter 8, it was shown that the nano-modified concrete comprising the accelerator increased early-age mechanical properties up to 7 days; however, the nano-modified concrete without the accelerator showed higher mechanical properties at 28 days and later-ages. This was attributed to the slower diffusion of water through thicker hydration products in the binder system comprising the accelerator (Mehta et al. 2014; Nevile 2011).
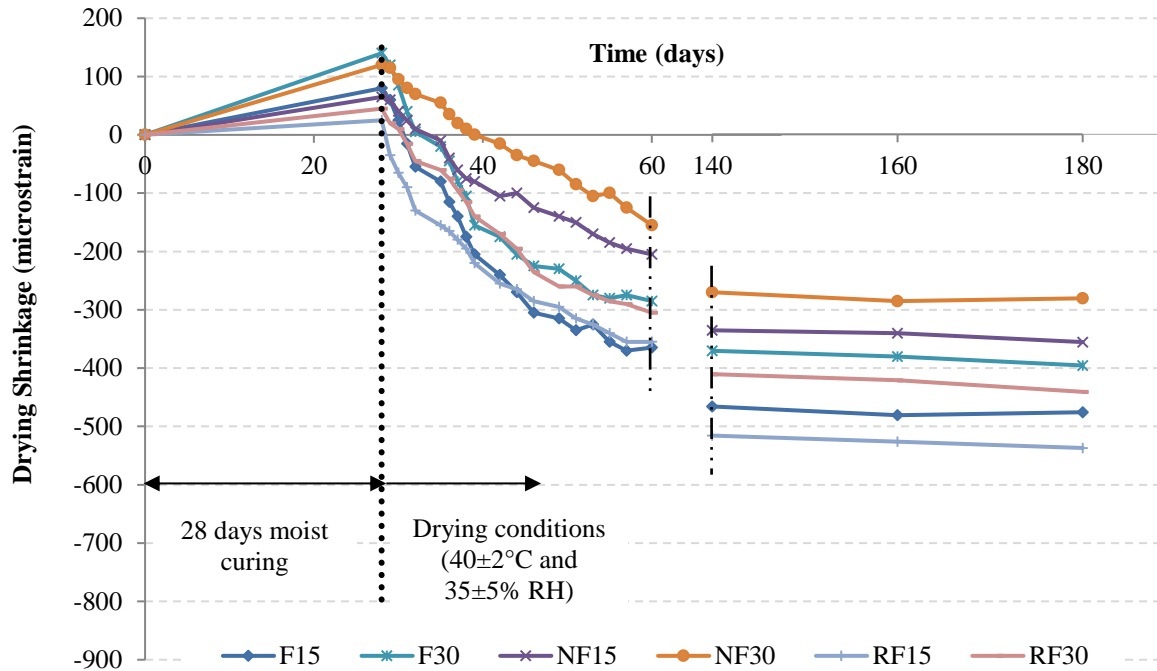
Figure 9.5: Free shrinkage of the concrete prims (28 days moist curing).

After 28 days moist curing, increasing the dosage of fly ash led to notable reduction (Fig. 9.5) in the total shrinkage of the reference specimens, which conforms to previous studies (Maslehuddin et al. 2013; Holt 2005). Similarly, there was a significant effect of increasing the dosage of fly ash on reducing the drying shrinkage of the N and R specimens (Table 9.2). For example, increasing the fly ash content from 15% to 30% in the N mixtures (NF15 and NF30) led to 23% reduction in the shrinkage rates up to 140 days, and specimens from NF30 yielded the lowest drying shrinkage at the end of the exposure (280 microstrain). This reduction of shrinkage may be ascribed to cement dilution, thereby decreasing autogenous shrinkage in the mixtures containing 30% fly ash at early-age (Fig.

9.2); consequently, the total free shrinkage decreased. Also, with sufficient curing time, the presence of nanosilica catalyzed the reactivity of fly ash in the mixtures containing a higher dosage of fly ash (30%), resulting in an improved level of hydration and evolution of microstructure, as reflected by the refinement of the pores and high mechanical properties (Table 9.3); therefore, these matrices can better control internal stresses, which improves dimensional stability.

9.4.2.3 Curing compound (CC)

Figure 9.6 shows the results of the free shrinkage test for all specimens cured by the CC. Generally, before the hot-dry exposure (28 days), the shrinkage for all specimens cured by the CC was notably lower than the corresponding specimens cured for 3 days and close to that of specimens cured for 7 days, which ranged from 100 to 250 microstrain. This indicates that the CC provided better resistance to water evaporation by blocking water transmission due to the relatively impermeable film formed; thus, improving the dimensional stability of specimens. Also, at 180 days, all specimens exhibited lower (up to 29%) total drying shrinkage than that of the corresponding specimens cured for 7 days with a clear distinction among the specimens similar to specimens cured for 28 days. In addition to the reduction of the water loss due to the film effect (primary effect described earlier), the increase of the mechanical properties (tensile capacity by 3 to 20% and stiffness by 8 to 31%, Table 9.3) of the specimens cured by the CC might have contributed to reducing the shrinkage deformations of the matrix.

In comparison to the reference specimens (F15 and F30), the NF15 and NF30 specimens exhibited higher rates (11% to 30%) of shrinkage up to 28 days with a significant (Table 9.2) reduction in the rate of shrinkage afterwards up to a total shrinkage of 435 and 390 microstrain, respectively. This increase of the rates of shrinkage before the

hot-dry exposure corresponds to the higher rates of autogenous shrinkage (Fig. 9.2) and chemical reactivity in these binders. Subsequently, the reduction of the total shrinkage of these specimens may be ascribed to notable enhancement of the mechanical properties (66% to 86%, Table 9.3). Again, the presence of the accelerator in the R mixtures significantly (Table 9.2) increased the rates of shrinkage (48% to 65%) up to 28 days and RF15 yielded the highest (640 microstrain) total shrinkage (Fig. 9.6).

Complying with the trends of specimens cured for 28 days, increasing the fly ash content in the mixtures treated with the CC led to significant (Table 9.2) reduction of shrinkage deformations as depicted in Fig. 9.6. The reference mixture containing 30% fly ash (F30) exhibited the lowest shrinkage rate (3.4 microstrain/day) before the hot-dry conditions and ended up with a total value of 505 microstrain at 180 days. Also, increasing the fly ash content from 15% to 30% in the N and R mixtures (NF30 and RF30) led to reduction in the rates (18% and 28%, respectively) of shrinkage up to 28 days, and NF30 specimens yielded the lowest drying shrinkage at 180 days (390 microstrain). As mentioned earlier, the effect of cement dilution and slow pozzolanic reaction for fly ash at early-age decreased the chemical shrinkage in the mixtures containing 30% fly ash; consequently, the total free shrinkage decreased. In addition to the impermeable film effect discussed earlier, the higher level of internal humidity due to the application of the CC likely promoted the hydraulic/pozzolanic reactions in the 30% fly ash mixtures, resulting in more homogenous and dense matrix that further reduced water loss. This was also reflected by the higher mechanical properties before and after the hot-dry conditions (Table 9.3).
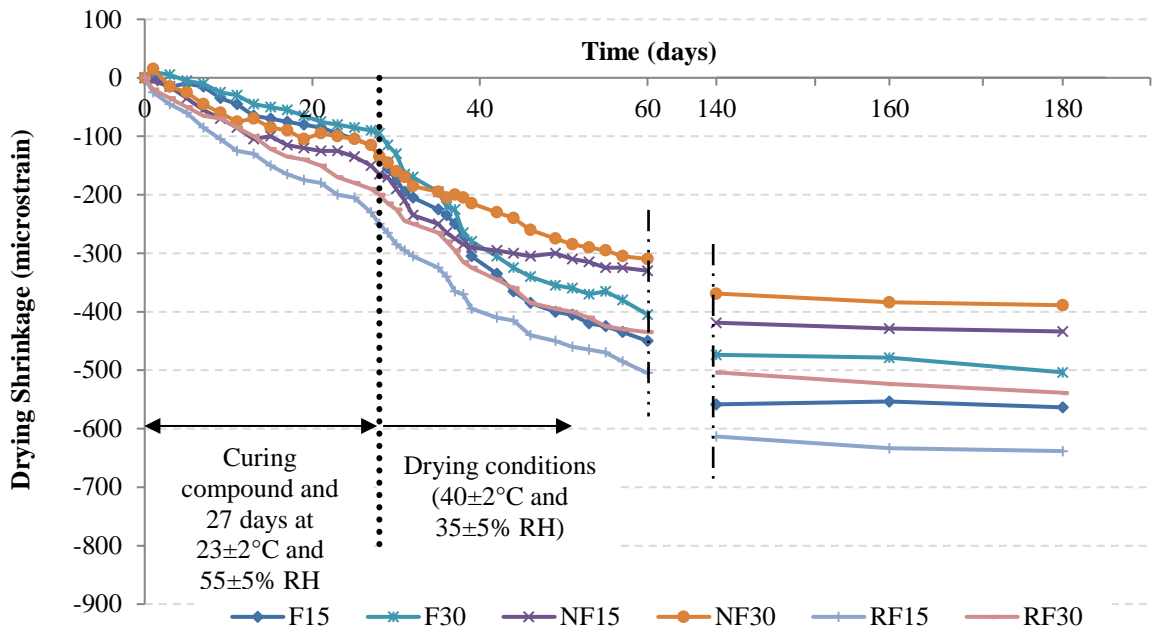
Figure 9.6: Free shrinkage of the concrete prims (CC).

9.4.3 Restrained Shrinkage

Although the free shrinkage test can provide useful trends on how the drying shrinkage deformations affect dimensional stability of concrete, this test alone cannot provide complete information on the shrinkage behaviour of concrete as a repair material since virtually all repair materials are restrained in some way. Figure 9.7 shows the results of the restrained shrinkage test for all mixtures with the application of CC after casting. In addition, the crack patterns after 180 days are presented in Fig. 9.8. It is conceivable that the intensity of cracking herein is exaggerated due to the continual hot-dry exposure for 152 days. In the field, frequent rise of relative humidity and precipitation may reduce shrinkage and cracking. Generally, similar trends to that of the free shrinkage test for the specimens treated with the CC were obtained with reduction of shrinkage strains due to restrainment by the substrate concrete.
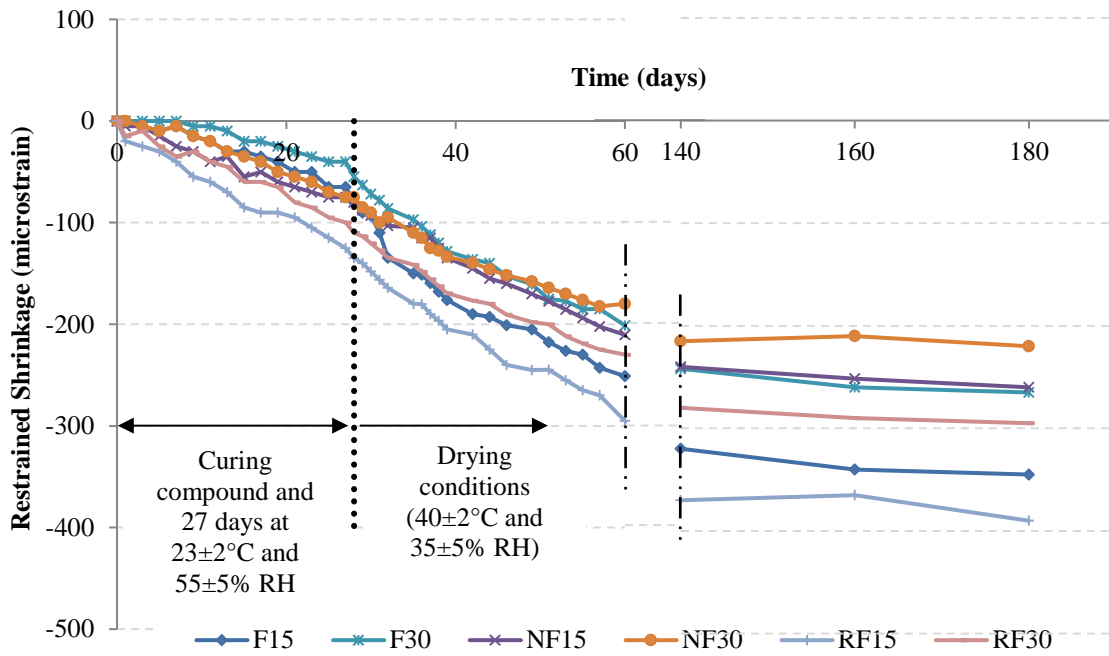
Figure 9.7: Restrained shrinkage of the repair layer in the concrete slabs.
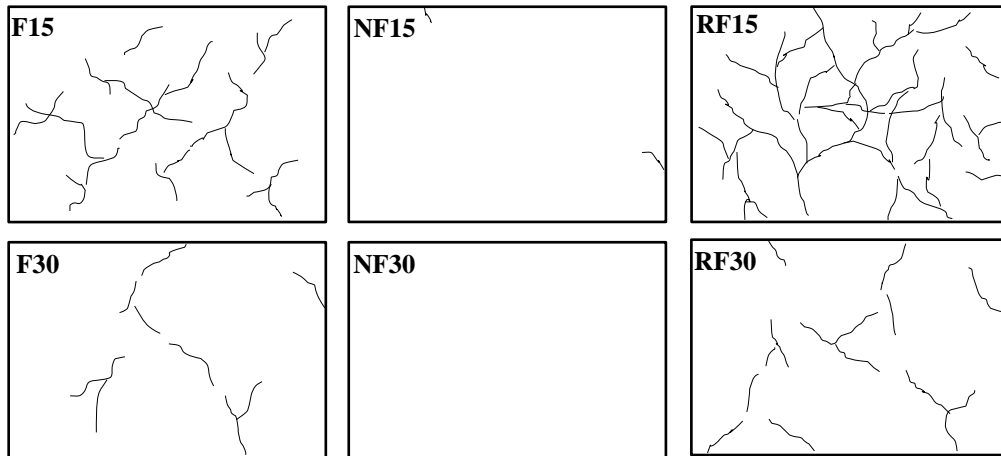
Figure 9.8: Crack patterns of the repair layer in the concrete slabs at 180 days.

In comparison to the reference specimens (F15 and F30), the N specimens (NF15 and NF30) exhibited slightly higher rates (average of 20%) of shrinkage up to 28 days (before drying) with almost steady rates (approximately 2 microstrain/day) of shrinkage afterwards (up to 180 days). These specimens yielded the lowest shrinkage at the end of

the exposure, which ranged from 220 to 260 microstrain, with no or negligible cracking (Fig. 9.8). As explained earlier, the increase of the shrinkage rates for these specimens at early stage corresponds to the acceleration in the hydration process (Table 9.1) and consequently autogenous shrinkage (Fig. 9.2). In addition, it has been shown that nanosilica catalyzes the reactivity of fly ash in concrete even during the first 28 days (Chapter 8). The significant (Table 9.2) reduction of the total shrinkage of these specimens afterwards (from 28 to 180 days) may be ascribed to their higher mechanical properties as well as reduction of moisture loss (during the drying period) due to densification of their microstructure (Table 9.3).

Complying with the trends of the free shrinkage test, the presence of the accelerator in the R mixtures significantly (Table 9.2) amplified the shrinkage rates up to 28 days (increased by 47% to 59%) and their total shrinkage at 180 days (increased by 34% to 50%) in comparison to the corresponding N mixtures. This was particularly notable for specimen RF15, which showed intensive crack propagation (less than 0.05 mm in width) on the surface as depicted in Fig. 9.8. Again, the increase of the shrinkage rate for the R specimens may be ascribed to the vigorous reaction activities and consequently autogenous shrinkage (Fig. 9.2) during early-age. In addition, the lower mechanical properties of the R mixtures (Table 9.3), which conforms to effect of accelerators on the strength and stiffness development of concrete at later ages due to the slower diffusion of water through thicker hydration products (Mehta et al. 2014; Nevile 2011), made the matrix less resistant to shrinkage deformations under the aggravated drying conditions.

The significant effect (Table 9.2) of increasing the dosage of fly ash on reducing restrained shrinkage and subsequent cracking of concrete is depicted in Figs. 9.7 and 9.8. The reference specimen containing 30% fly ash (F30) exhibited the lowest shrinkage rate

(1.9 microstrain/day) before the drying conditions and ended up with a total value of 265 microstrain at 180 days. Increasing the fly ash content from 15% to 30% in the N specimens comprising 6% nanosilica (NF15 and NF30) led to reduction in the rate of shrinkage (14%) up to 28 days, and the total shrinkage of specimen NF30 was the lowest (220 microstrain). This trend was replicated for the R mixtures as specimen RF30 had less total shrinkage and cracking than that of specimen RF15 (Figs. 9.7 and 9.8). As mentioned earlier, the action of the higher dosage of fly ash can be linked to its dilution effect and slower reactivity at early-age, resulting in decreasing the rate of the shrinkage (up to 28 days). Moreover, the densification and higher tensile capacity and elastic modulus of these mixtures (Table 9.3) alleviated the effect of restrained shrinkage (Fig. 9.8) up to 180 days.

CHAPTER 10 – PHASE III: FIELD TRIAL OF NMFC AS A REPAIR MATERIAL

10.1 Introduction

Partial depth repair (PDR) of concrete pavements is a rehabilitation technique used to restore pavements with localized surface distress such as spalls and wide cracks. PDR is normally limited to a maximum of *1/3* the slab thickness. Often, the selection of the repair material is based on the allowable lane closure time, which is linked to the strength development of the material over time, so PDR materials typically include accelerators and Type III cement or proprietary rapid-setting binders. However, this approach may not necessarily lead to selecting the most compatible and durable repair product. Some high-early strength cementitious repair materials have sufficient strength at early-age; however, many of these materials are vulnerable to cracking, poor bonding, and premature deterioration due to incompatibility with the existing (parent) concrete pavement or their susceptibility to thermal gradients and autogenous shrinkage, as shown in Chapters 8 and 9.

The University of Manitoba, in collaboration with the City of Winnipeg (COW), MB, Canada, recently developed an owner's guide for PDR applications. The guide includes a list of approved PDR concretes that provide adequate early-age and long-term performance, with optimized cost and appropriate service life.

In Chapters 8 and 9, nanosilica was used to produce nano-modified fly ash concrete (NMFC) as a repair material. Nanosilica has been proven to accelerate hydration, setting time, and strength development; improve mechanical properties; and reduce total shrinkage as well as permeability. The latter benefits can contribute to

improving the durability and longevity of concrete. The repair mixtures comprised fly ash (Class F) to be compatible with concrete pavement mixtures used in Manitoba, in which 15% fly ash is typically used. NMFC mixtures produced in the laboratory achieved a reasonable balance of early-age and long-term behaviour, as demonstrated by setting time, strength development, compatibility/bonding, and resistance to infiltration of fluids and salt-frost scaling, as shown in Chapter 8 and 9. Hence, they have been included in the guide for PDR of concrete pavements for Winnipeg. This Chapter reports on the first field trial of NMFC for partial-depth repair of transverse joints located on a major urban arterial road in Winnipeg.

10.2 Application

10.2.1 Materials

The materials and procedures used to develop the nano-modified fly ash concrete in the field trial were similar to that used in Chapter 8 (refer to Sections 8.3.1 and 8.3.2). The NMFCs with 15% fly ash were discontinued from the field trial due to the intensive crack propagation observed in these mixtures in the restrained shrinkage test (Chapter 9).

10.2.2 Construction Procedures

Each test joint was surveyed and prepared in accordance with the protocol descried in the Guide for Partial Depth Repair of Concrete Pavements - City of Winnipeg (Fig. 10.1) (Guide for Partial Depth Repair of Concrete Pavements 2015). A schematic cross-section of a repair is shown in Fig. 10.2. The repaired areas in this field trial (transverse joints; symmetrically cut to the left and right to reestablish new joints) represent a critical scenario for repair applications since they are likely vulnerable to drying/restrained shrinkage (high surface-to-volume ratio) and premature deterioration (entrapment of salt-solutions and freezing-thawing cycles) (Panchmatia et al. 2014; Arribas-Colón et al. 2012). Therefore, it

240

is desirable for candidate repair materials to exhibit a balance between early-age properties and long-term performance. The NMFC mixtures were designed to satisfy these requirements while providing a cost-effective and sustainable repair alternative.

Figure 10.1: Preparation of the transverse joints before repair.
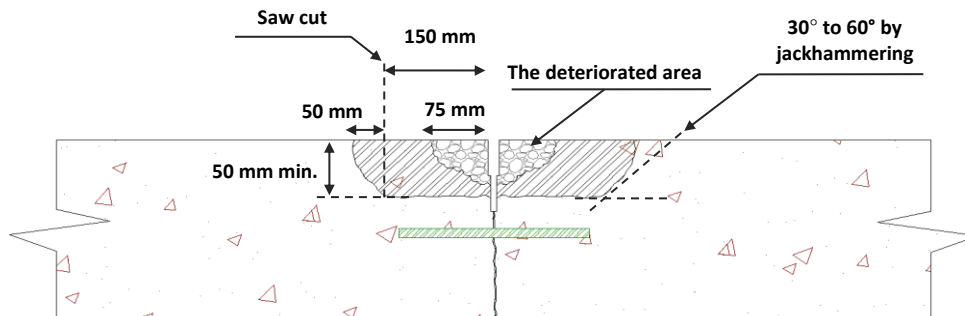
Figure 10.2: Configuration of the repair cross-section.

Two concrete mixtures with normal setting times (designated as N) were prepared with two dosages of fly ash (22.5% and 30% replacement by mass of the total binder comprising GU cement and fly ash (385 kg/m^3). Nanosilica was added to the mixtures at a dosage of 6% by mass of the base binder (a solid content of 23 kg/m^3). In addition, two corresponding rapid-setting concrete mixtures (designated as R) were prepared with an accelerating admixture. The proportions of all mixtures are shown previously in Table 8.2.

To improve quality, efficiency, and productivity of the repair process, the constituents were prepackaged in the laboratory and delivered to the site (Fig. 10.3). The binders were packaged in heavy-duty polyethylene lined bags, each yielding 15 L with the aggregate. The water, nanosilica, and admixtures were packaged together in sealed containers. Materials were mixed in a portable concrete mixer at 60 revolutions per minute with a 90 L lift/rotating drum. The mixing sequence is shown in Fig. 10.4. Roughly two, 60 L batches were needed for each area.

Figure 10.3: Prepackaged constituents for NMFC mixture (NF30).

Figure 10.4: Sequence of mixing for the NMFC repairs. : (a) liquid components (water, nanosilica, and admixtures) were stirred vigorously at 1800 to 2600 rpm for 45 seconds; (b) about 15% of the liquid was added to the aggregates while mixing for 30 seconds; (c) cement and fly ash were blended with the aggregates and mixed in the mixer for 60 seconds; (d) the remaining liquid was added and mixing continued for 2 minutes; and (e) the mixture was ready for placement.

Before placing the NMFC mixtures, the repair areas (joints) were moistened (Fig. 10.5a) and compression relief strips (polyethylene) were installed to re-establish the joints at their original locations (Fig. 10.5b). The placement was planned to limit the number of batches, as mentioned earlier, for each repair area (each mixture) to avoid cold joints. Slight over-filling of the repair areas was done to allow for volume reduction during consolidation. Immediately after casting, a pencil vibrator was used to ensure good compaction. Finally, the surface of the NMFC mixtures was finished with a hand trowel and flushed with the existing pavement (Fig. 10.5c). After finishing, two coats of white-pigmented curing compound were sprayed over the patched areas as soon as bleed water evaporated from the surface of the mixtures (Fig. 10.5d).
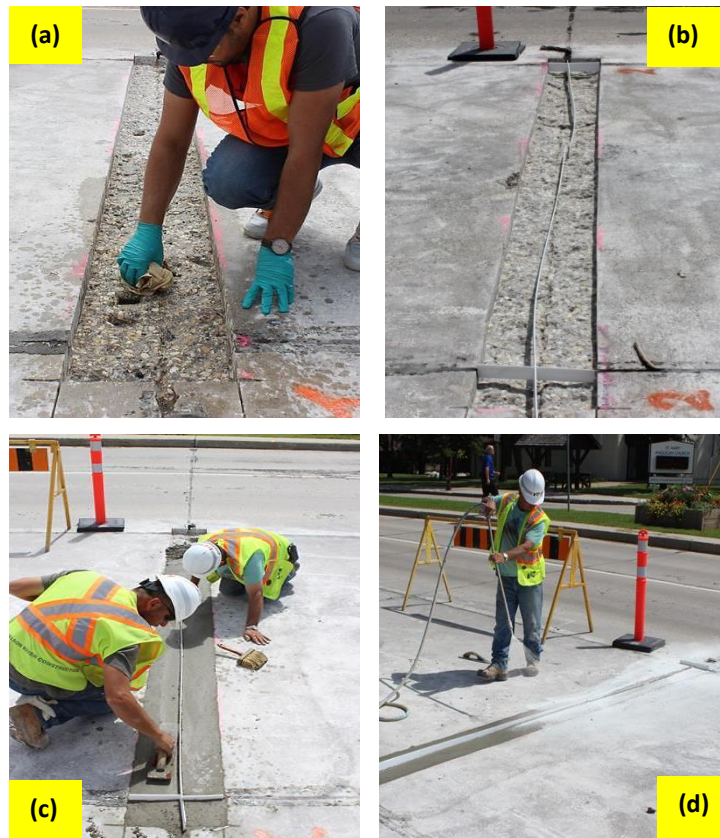
Figure 10.5: Placement, finishing, and curing of the NMFC repair mixtures in the field.

10.2.3 Mixture Tests

The following tests were performed to assess the quality of the NMFC repair mixtures:

- Slump and slump loss per ASTM C143, "Standard test method for slump of hydraulic cement concrete";

- Air content per ASTM C231, "Standard test method for air content of freshly mixed concrete by the pressure method";

- Temperature per ASTM C1064, "Standard test method for temperature of freshly mixed hydraulic cement concrete";

- Strength per ASTM C39, "Standard test method for compressive strength of cylindrical concrete specimens". Test cylinders were prepared during field placement

and kept outside the laboratory under similar climatic conditions to that of the repair patches. Tests were made at 16 hours, and 1, 3, and 28 days;

- Penetrability (at 28 days) per ASTM C1202, "Standard test method for electrical indication of concrete's ability to resist chloride ion penetration." Cylinders were prepared and cured similar to those used for compressive strength tests. After completing the RCPT, the specimens were axially split and sprayed with 0.1 M silver nitrate solution, which forms a white precipitate of silver chloride in approximately 15 minutes, to measure the physical penetration depth of chloride ions; and

- Ultrasonic pulse velocity was measured in the repair areas before opening to traffic (1 day for the R mixtures and 3 days for the N mixtures) and after 28 days.

10.3 Findings and Discussion

10.3.1 Fresh Properties

The properties of fresh NMFC mixtures are listed in Table 10.1. All NMFC mixtures were below 30°C at the time of placement, which met the COW specifications. Also, 30% fly ash addition was effective at reducing the temperature rise during hydration. Incorporation of 22.5 to 30% Class F fly ash helped control the shrinkage of NMFC as indicated by the absence of surface cracks after 28 days (Fig. 10.6). This can be attributed to its dilution effect (by replacement of the cement component) and balancing the reactivity of nano-silica, especially at early-age, as shown in Chapter 8. The average daily temperatures and RH over 28 days after casting were 22°C and 82%, respectively, with intermittent rainfall (four days during the first week), which contributed to improving the curing efficiency of the NMFC. Moreover, the NMFC mixtures retained adequate consistency and cohesiveness up to 30 minutes after initial mixing allowing added flexibility in casting, compaction, and finishing of the repair patches.

The incorporation of the accelerator made the initial slump of the R mixtures higher than that of the N mixtures, whereas the residual slump was higher for the N mixtures after 15 and 30 minutes of mixing. This is ascribed to the effect of Type E accelerator, which initially improved the consistency (plasticizing effect), and subsequently shortened the rate of hardening (accelerating effect) as shown in Table 10.1. Incorporation of a higher dosage of fly ash (30%) had a pronounced effect on improving the consistency up to 30 minutes after mixing due to increasing the volume fraction of paste comprising spherical fly ash particles with slower reactivity. Generally, all the fresh properties of NMFC produced in the field conformed to that of laboratory concrete (Chapter 8), indicating the success of the prepacking and mixing procedures adopted in this field trial.

Table 10.1: Properties of fresh NMFC

Mixture ID	Temperature, °C (°F)	Density, kg/m^3	Slump, mm			Air content, %
			Test time, minutes			
			0	15	30	
NF22.5	25.5	2225 (139)	105 (4.13)	75 (2.95)	30 (1.18)	7.7
NF30	21.5	2224 (139)	125 (4.92)	90 (3.54)	40 (1.57)	6.8
RF22.5	28.5	2231 (139)	135 (5.31)	55 (2.17)	10 (0.39)	7.3
RF30	27.0	2230 (139)	155 (6.10)	70 (2.76)	25 (0.98)	7.1

Figure 10.6: Repair patches at 28 days.

10.3.2 Hardened Properties

Compressive strength values for the NMFC cylinders prepared in the field and cured under the same conditions of patched joints at different ages (16 hours, and 1, 3, and 28 days) are listed in Table 10.2. As previously mentioned, the selection of the repair material is typically based on the opening times required for a specific site. Therefore, the R mixtures were designed for an opening time of 1 day, at which the mixtures would reach a compressive strength of at least 15 MPa. Comparatively, the N mixtures are recommended for sites where opening to traffic is not required during the first 72 hours. The R mixtures gained the target compressive strength after 16 to 24 hours, as shown in Table 10.2. The average early-age (up to 3 days) strength for the R mixtures increased approximately by 31% in comparison to the N mixtures. This is ascribed to the presence of the accelerating admixture, which sped up the rate of hydration reactions and increased the early-age strength.

On the other hand, the compressive strength of the N mixtures markedly improved at and after 3 days, as these mixtures gained 25 MPa or more. Hence, the slow rate of strength development for concrete incorporating Class F fly ash was controlled by the addition of a small dosage of nanosilica. After 28 days, the compressive strength for all the NMFC mixtures ranged between 41 to 48 MPa, which is overlapping with the target range for the parent concrete (40 to 43 MPa), suggesting that the assembly will behave as an integral system owing to compatibility. The compatibility and strength development of the NMFC mixtures in terms of hydration evolution, bonding, and microstructural features were presented in Chapters 8 and 9.

Table 10.2: Compressive strength of NMFC at different ages

Mixture ID	Compressive strength, MPa				
	Test time				
	16 hours	1 day	3 days	28 days	180 days
NF22.5	--	18 (2.55)	27 (1.97)	47 (2.18)	51 (1.11)
NF30	--	16 (3.15)	25 (3.86)	48 (1.57)	53 (2.53)
RF22.5	19 (2.76)	22 (4.54)	32 (2.87)	43 (3.39)	45 (2.47)
RF30	16 (4.93)	20 (3.84)	29 (4.31)	41 (3.98)	46 (2.71)

*The values between brackets are the standard deviation.

Before opening the repaired areas for traffic (after 1 day for R mixtures and 3 days for N mixtures), a total of 40 UPV measurements (indirect mode) were made on each joint to inspect the quality of the repair patches in terms of homogeneity and integrity. In addition, the same procedure was repeated for all patches at 28 days. Indirect measurements were conducted using a coordinate system drawn on the repair surface, as shown in Fig. 10.7. Repairs for all NMFC mixtures had an average pulse velocity greater than 3500 m/s at the time of opening to traffic (Fig. 10.8), indicating that they had adequate uniformity and minimal internal flaws, shrinkage cracks, or debonding (del Rio et al. 2004). Moreover, the UPV results at 28 days indicated that all repairs continued to densify over time, as the lowest pulse velocity at 28 days was more than 5100 m/s.

Figure 10.7: A grid was applied to the surface of a repaired joint to allow locations to be correlated with UPV measurements.
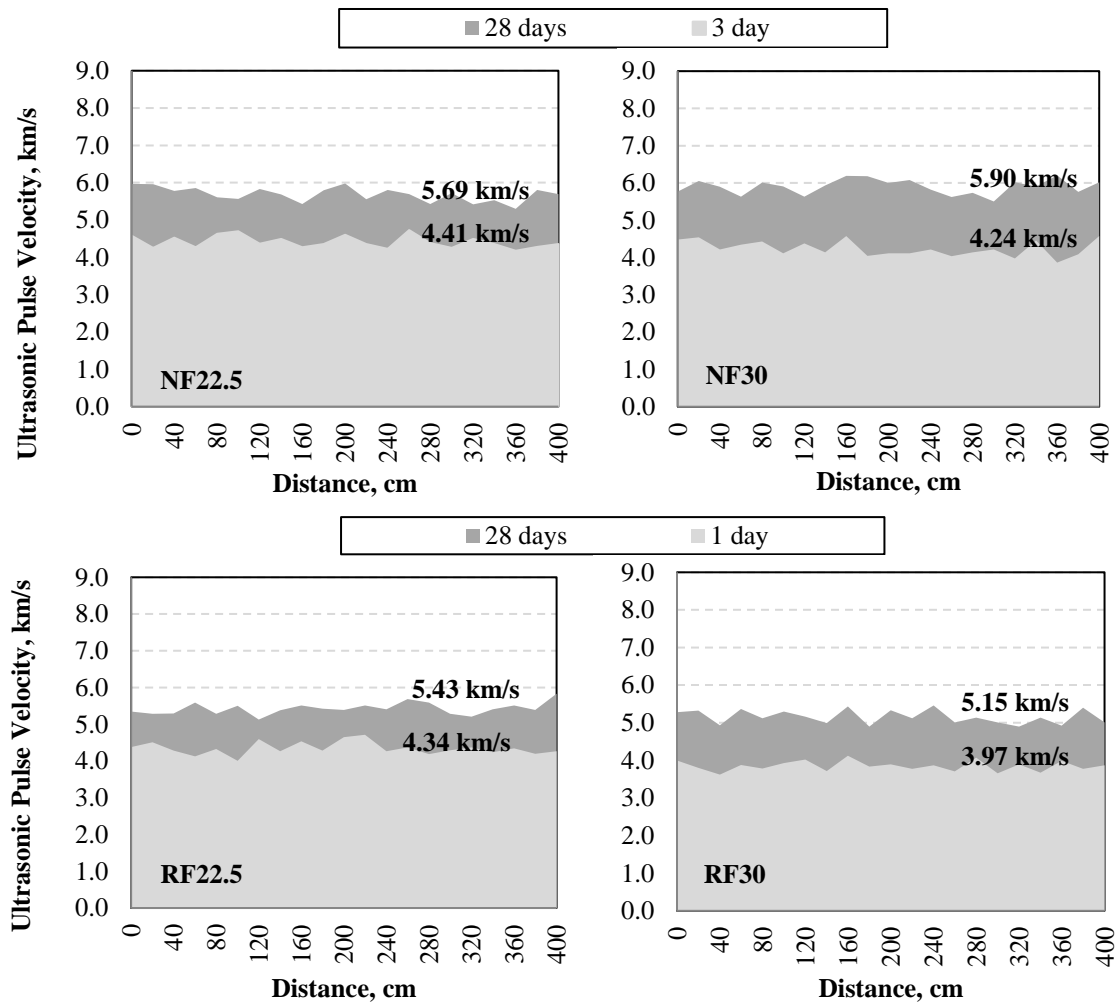
Figure 10.8: The UPV measurements along the repaired joints.

RCPT data for cylinders exposed to the same environmental conditions as the repair patches are listed in Table 10.3. The chloride penetration depths are shown in Fig. 10.9. Using the classification recommended in ASTM C1202, all NMFC mixtures had "very low" penetrability, as the charge passed was less than 1000 coulombs. All mixtures also had markedly low chloride penetration depths (less than 10 mm), indicating densification of the mixture and discontinuity of the pore structure. The same trends were observed in the laboratory work (Chapter 8).

Table 10.3: Rapid chloride penetrability test (RCPT) results at 28 days

Mixture ID	Charge passed, coulombs	Average penetration depth, mm (Standard Error)
NF22.5	541	6 (0.46)
NF30	423	5 (0.24)
RF22.5	581	7 (0.32)
RF30	622	9 (0.29)
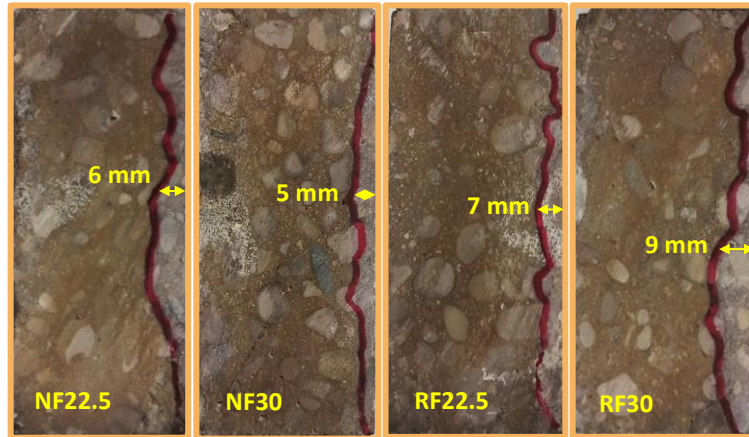
Figure 10.9: Whitish precipitate showing the average penetration depth of chloride ions.

10.4 Potential for NMFC

The NMFC mixtures produced and applied in this field trial had reasonable consistency and slump retention suitable for placement and finishability operations. In addition, they achieved the target rate of strength development, homogeneity of elastic behaviour, and resistance to ingress of fluids. Whether mixed in the field or the laboratory, the uniformity and quality of the NMFC mixtures were comparable. NMFC shows the potential for allowing transportation agencies to control fresh and/or hardened properties by adjusting the proportions of ingredients. Costs will also be reduced due to the greater use of fly ash as a cement replacement. We estimate that the direct cost of NMFC materials with normal or accelerated setting times will be comparable or about 12% higher, respectively than the cost of normal concrete. Thus, NMFC presents a sustainable and cost-effective option for repair of concrete pavements, with an anticipated measurable impact

on reducing life-cycle cost of partial depth repairs due to its projected durability and longevity. This field trial demonstrated the mixing, placement, and testing procedures of NMFC as a novel repair material for pavements with promising long-term performance.

CHAPTER 11: SUMMARY, CONCLUSIONS, AND RECOMMENDATIONS

11.1 Summary

In this thesis, field, experimental and modeling studies were conducted in order to comprehend the synergistic effects of environmental conditions with different types/concentrations of de-icing salts on concrete degradation to minimize the risk of premature deterioration in concrete pavements.

In Phase I, a forensic evaluation was performed to classify the source of this damage and identify aspects contributing to joint deterioration of regional (chloride-based salts are directly applied) and residential roads (salts are borne by vehicles tires) in Winnipeg, Canada. Subsequently, laboratory conditions (Phase II) were carried out to elucidate the damage mechanisms of concrete under the most widely used chloride-based de-icing salts (individual and combined) when combined with different environmental conditions to different climatic conditions experienced by concrete pavements. Conditioned mode (adjusted temperature and relative humidity) environmental scanning electron microscopy (ESEM) was specifically used to avoid changes in the crystal structures of reaction products, and thus capture their unaltered morphology and existence/effects on concrete specimens. The physico-mechanical performance and microstructural features of novel concrete mixture designs, incorporating general use and portland limestone cement, Class F fly ash and nanosilica exposed to these aggressive conditions were studies. Also, in Phase II, an adaptive neuro-fuzzy inference system (ANFIS) was developed to model and predict the starting time of failure of concrete exposed to the harsh exposure scenarios implemented in the experimental part. In Phase III

of this thesis, nano-modified fly ash concretes (NMFC) were developed in the laboratory, and then applied in a field trial as a partial-depth repair of concrete pavements in Winnipeg to document its performance.

11.2 Conclusions

11.2.1 Phase I: assessment of joints in concrete pavements

- Cores extracted from the regional roads exhibited higher rates of absorption and penetrability. Microstructural analysis disclosed that these cores had high intensity of micro-cracking and the majority of air voids were filled with secondary depositions. Also, direct application of de-icing salts in regional roads further enhanced the degree of saturation at joints.

- Forensic evaluation of cores suggested that the principal reason for the deterioration of concrete pavement in regional roads appears to be related freezing/thawing (F/T) damage, as a result of an inadequate air-void system due to gradual in-filling of voids with secondary depositions (mostly ettringite).

- Residential streets, which were indirectly exposed to de-icing salts, had reduced absorption and penetrability, due to homogenous microstructure that was free of micro-cracks. Cores from residential streets showed incidental occurrences of secondary depositions partially in-filling air voids; however, this had an insignificant effect on the quality of air-void parameters, and thus these pavements maintained high resistance to F/T cycles.

- Irrespective of the application of de-icing salts, the pavement cross slope and drainage system played a significant role in improving the performance of joints in the residential streets by preventing them from critical saturation compared to that in

regional roads which continued to entrap solutions long after wetting events. The proper design and frequent maintenance of the drainage system in residential streets would extend the service life of concrete pavement in such areas and mitigate serviceability issues. Therefore, frequent inspection of the drainage system needs to be a key component of the maintenance plan for concrete pavements.

11.2.2 Phase II: laboratory exposures and modeling

11.2.2.1 Laboratory exposures

- The damage manifestations of de-icing salts on concrete can be characterized by decomposition/softening, expansion, cracking and scaling. The extent and occurrence of these features depend on the type and the concentration of the de-icers, and the type of binder. Therefore, a combination of physico-mechanical parameters (e.g. mass loss, expansion, dynamic modulus of elasticity) is needed to evaluate the relative performance of various concrete mixtures exposed to de-icing salts.

- The frequently used exposure (continuous immersion at low temperature) for evaluating chemical degradation of concrete under de-icing chemicals is not suitable for binders comprising slow reactivity supplementary cementitious materials (SCMs) (e.g. fly ash) as this exposure hindered the long-term activity of these materials.

- The reversible formation of hydrous and anhydrous calcium oxychloride (COX) during wetting/drying (W/D) cycles had a significant effect on aggravating the kinetics of damage of concrete due to alternating formation of high and low-density reaction products.

- The combined exposure to cyclic environments and de-icing salt solutions had additive and perhaps synergistic effects on specimens, causing the coexistence of multiple degradation mechanisms (surface scaling, salt crystallization, chemical attack) and

254

complex assemblages depositing in the matrix. This is fundamentally different from studying a single damage mechanism acting on concrete in an individual exposure.

- The results indicate that NaCl is not aggressive with respect to chemical degradation of concrete, as no formation of complex salts was detected in all exposures. However, the subsequent evaporation of NaCl solution and nucleation and growth of salt due to W/D cycles may result in enough crystallization pressure to cause surface scaling of concrete.

- Chloride (Cl^-) ions and cations (Mg^{2+}, and Ca^{2+}) in $MgCl_2$, $CaCl_2$ and combined ($MgCl_2+CaCl_2$) salts enter into chemical reactions with hydrated cement paste forming complex salts (COX, Friedel's salt, ettringite, magnesium oxychloride (MOX), and gypsum, depending on the type of solution). The combined salt, which simulates using a synergistic maintenance and protective strategy for concrete pavements in winter, was the most aggressive solution; thus, this practice should be reconsidered by transportation agencies.

- Acicular flattened blades crystals, which predominantly grew as interlocked bundles, were a prevailing feature in deteriorated concrete specimens as observed by ESEM for the 3- and 5-form MOX. These crystals seemed to be stable at both 5 and 40°C. On the other hand, subhedral pseudo-hexagonal plates and tiny fibrous crystals were the dominant morphology for 3:1:12 and 3:1:15 COX in concrete, respectively. However, the hot-dry conditions (40°C and 30% RH) led to its conversion to anhydrous COX shaped as elongated bladed prismatic crystals. This conversion was reversible upon wetting at 5°C.

- The overall results indicate that the resistance of concrete exposed to moderate and high concentrations de-icing salts is a function of physical penetrability, amount of

C_3A in cement and content of portlandite available for chemical reactions in the hydrated paste. Depending on the type of binder and dosage and nature of SCMs, the interaction of these parameters dictated different modes of deterioration, and in turn physico-mechanical trends.

- The control binders made from 100% GU cement had the highest physical penetrability, amount of aluminate and initial portlandite contents, facilitating migration of chloride ions towards the inner core and formation of reaction products (COX, Friedel's salt, ettringite, MOX, and gypsum), which amplified the damage of specimens. In contrast, PLC mixtures had better resistance to degradation by different concentrations of de-icing salts due to synergistic physical and chemical actions of the limestone component in the binder.

- Compared to the control (GU) binder, the incorporation of 30% fly ash in concrete improved its resistance to chemical/physical degradation by de-icing salt solutions due to reduced solution uptake and amount of portlandite. This trend was magnified by using an ultrafine pozzolan 'nanosilica' as no single mixture made with binary or ternary binders comprising nanosilica showed any features of damage. Generally, concrete comprising nanosilica had enhanced physical resistance to all high concentration deicing-salts in all exposures.

- The overall results from the laboratory investigations implicate that the restrictive limits on fly ash in concrete serving in chloride-rich environments, for example stipulated in North American guides and codes for concrete may produce less durable concrete than alternative noncompliant mixtures with higher fly ash dosages. Indeed, the performance of concrete exposed to such conditions was much enhanced by an innovative SCM such as nanosilica or a new type of cement (portland limestone

cement: PLC). Thus, concerted efforts are needed to improve and update current codes and guides for durability of concrete, especially with the intensive winter maintenance practices adopted by transportation agencies to cope with climatic changes.

11.2.2.2 Modeling

- The present thesis showed that adaptive neuro-fuzzy inference systems (ANFIS) can be successfully used to predict the complex behavior of cement-based materials under combined damage mechanisms. This model combines the advantages of artificial neural networks (e.g. self-learning and pattern recognition) and fuzzy inference systems (e.g. accommodating uncertainty, linguistic use, and approximation).

- The ANFIS model developed predicted the time of failure (TF) of a wide range of concrete mixture designs under various exposure regimes combined with the most widely used chloride-based de-icing salts (individual and combined). The model had a good generalization capacity beyond the training stage as verified by results obtained on new testing data within the range of training database.

- Sensitivity analyses showed that the developed model captured the effect of individual input parameters on the results. Thus, this model could be used to forecast the deterioration of tailor-made concrete mixtures exposed to such conditions. In the design and prequalification stage of a construction project, this model can reduce the need for exhaustive trial batches and long-term experiments, thus facilitating decision-making on optimum mixtures.

- The developed ANFIS model is versatile and can be re-trained to encompass wider ranges of input variables, different concentrations of de-icing salt solutions, other types of de-icing salts, other environmental conditions, etc. Once, this data becomes available in the future, the re-training process of this model would be readily

257

achievable.

11.2.3 Phase III: nano-modified fly ash concrete as a repair material

- This study indicates that the high early-strength of rapid setting materials is an insufficient criterion to consider a product acceptable as a repair material for concrete pavements, as the commercial products may have adverse performance in many aspects such as placement/finishability, incompatibility, and salt-frost scaling.

- The normal and rapid NMFC mixtures developed herein had ample hardening times, without excessive delay, which improves the flexibility and quality of the repair process with suitability for different repair applications (e.g. multiple/large patch areas with less critical opening time to traffic).

- The incorporation of 6% nano-silica in concrete with up to 30% fly ash significantly shortened the dormant period and accelerated the rate of hydration reactions, which discounted the retarding effect of Class F fly ash on the rate of hardening of concrete.

- The rapid change from the plastic to pseudo-rigid state, due to accelerated kinetics of reactions, for the nano-modified fly ash binders, especially those containing the accelerator increased autogenous shrinkage up to 5 h; however, as the paste solidified (6-13 h), the autogenous shrinkage became small/nil.

- The synergistic effects of nano-silica and fly ash in both the N and R mixtures improved the early-age and long-term compressive, tensile and bond (even after the combined exposure) strengths of concrete, which indicate that the inherently slower rate of strength and microstructural development of concrete containing Class F fly ash can be controlled by the addition of small dosages of nano-silica.

- When adequate curing (28 days moist curing) was applied, addition of 30% fly ash could effectively control the effect of 6% nanosilica on increasing the autogenous, free

and restrained shrinkage of concrete, even with the addition of the accelerator.

- Application of the curing compound (CC) led to reducing moisture loss from specimens to surrounding environment and increasing the mechanical properties, thus improving their dimensional stability. This alludes to the suitability of using curing compounds for field applications of NMFC.

- The combination of fly ash with nano-silica led to a dense pore structure and improved tensile capacity, which suggests that the addition of nano-silica with fly ash enhanced its binding in the matrix. In addition to the effects of nano-silica on improving the hydration and pore structure characteristics by multiple mechanisms, TG results showed that addition of 6% nano-silica to concrete incorporating up to 30% fly ash catalyzed the reactivity of Class F fly ash, resulting in improved level of hydration and evolution of microstructure with age.

- The overall results indicate that the NMFC mixtures (except RF15) can achieve balanced early-age and long-term performance as well as controlling shrinkage deformations and behaving similar to substrate concrete. Hence, they present a viable option for a suite of repair applications in concrete pavements, with an anticipated measurable impact on reducing life-cycle costs.

- Similar to laboratory results, the NMFC mixtures produced and applied in the field trial had reasonable consistency and slump retention suitable for placement and finishability operations. In addition, they achieved the target rate of strength development, homogeneity of elastic behavior, and resistance to ingress of fluids. This field trial demonstrated the mixing, placement, and testing procedures of NMFC as a novel repair material for pavements with promising long-term performance.

- NMFC may enable transportation agencies to control fresh and/or hardened properties

by adjusting the proportions of ingredients. Costs were also reduced due to the greater use of fly ash as a cement replacement. It is estimated that the direct cost of NMFC materials with normal or accelerated setting times will be comparable or about 12% higher, respectively than the cost of normal concrete.

11.3 Recommendations for Future Work

- Based on the results obtained from this research, effects of exposure to combined salts should be further explored for concrete serving in cold environments. For example, the use of combined salts of either sodium chloride/magnesium chloride or sodium chloride/calcium chloride should be studied.

- To develop performance-based standards and specifications for concrete, there is need to standardize a multi-damage performance regime that is capable of capturing synergistic damage mechanisms which cannot be identified by individual exposures that subject concrete to a single aging mechanism at a time. Thus, it is recommended that standardization agencies such as CSA and ASTM motivate research programs in this direction.

- With an increase in data available from different case studies related to durability of cement-based materials serving in cold climates, new concepts such as materials genome can be applied as a powerful engineering tool. Materials genome is a set of information (databases) encoded in the language of thermodynamics in order to allow for the prediction of a material's structure, as well as its response to processing and usage conditions.

- The NMFC mixtures developed in the current thesis present a viable option for a suite of repair applications in concrete pavements, with an anticipated measurable impact

on reducing life-cycle costs. The potential for placing NMFC at low temperatures should be also explored as it would extend repair and maintenance seasons, if successful.

REFERENCES

Abbasnia, R., Godossi, P. and Ahmadi, J., 2005. Prediction of restrained shrinkage based on restraint factors in patching repair mortar. *Cement and concrete research*, *35*(10), pp.1909-1913.

Álava, H.E., De Belie, N. and De Schutter, G., 2016. Proposed mechanism for the formation of oxychloride crystals during sodium chloride application as a deicer salt in carbonated concrete. *Construction and Building Materials*, *109*, pp.188-197.

Al-Ostaz, A., Irshidat, M., Tenkhoff, B. and Ponnapalli, P.S., 2010. Deterioration of bond integrity between repair material and concrete due to thermal and mechanical incompatibilities. *Journal of Materials in Civil Engineering*, *22*(2), pp.136-144.

Aly, T. and Sanjayan, J.G., 2009. Mechanism of early age shrinkage of concretes. *Materials and structures*, *42*(4), p.461-468.

American Concrete Institute (ACI). 2006. *Guide for the Selection of Materials for the Repair of Concrete*. ACI 546.3R-06. ACI, Farmington Hills, MI.

American Concrete Institute, 2013. ACI 228.2R-13 Report on nondestructive test methods for evaluation of concrete in structures. Farminton Hills, Michigan.

American Concrete Institute, 2016. ACI 201.2R-16 Guide to durable concrete. Farminton Hills, Michigan.

American Concrete Pavement Association (ACPA), 2002. Life cycle cost analysis: a guide for comparing alternate pavement designs. Skokie, Illinois, 57p.

American Society of Civil Engineers (ASCE), 2013. Report Card for America's Infrastructure. Available at: http://www.infrastructurereportcard.org/wp-content/uploads/2013ReportCardforAmericasInfrastructure.pdf.

Amsler, D. E., 2006. Snow and Ice Control. *Cornell Local Roads Program*. New York, 94p.

Anderson, J., Daczko, J. and Luciano, J., 2003. Producing and evaluating portland cement-based rapid strength concrete. *Concrete International*, *25*(8), pp.77-82.

Anoop, M.B., Rao, K.B. and Rao, T.V.S.R.A., 2002. Application of fuzzy sets for estimating service life of reinforced concrete structural members in corrosive environments. *Engineering Structures*, *24*(9), pp.1229-1242.

Arribas-Colón, M., Radliński, M., Olek, J., and Whiting, N. 2012. Investigation of premature distress around joints in PCC pavements: Parts I & II. *FHWA/IN/JTRP-2012/25 & FHWA/IN/ JTRP-2012/26*, Joint Transportation Research Program, West Lafayette, Indiana, 75 p.

ASTM C 157, 2014. Standard test method for length change of hardened hydraulic-cement mortar and concrete. *ASTM International*, *04.02*, West Conshohocken, Pennsylvania.

ASTM C 215, 2014. Standard test method for fundamental transverse, longitudinal, and torsional resonant frequencies of concrete specimens. *ASTM International*, *04.02*, West Conshohocken, Pennsylvania.

ASTM C1064, 2011. Standard test method for temperature of freshly mixed hydraulic cement concrete. *ASTM International*, *04.02*, West Conshohocken, Pennsylvania.

ASTM C1202, 2012. Standard test method for electrical indication of concrete's ability to resist chloride ion penetration. *ASTM International*, *04.02*, West Conshohocken, Pennsylvania.

ASTM C143, 2015. Standard test method for slump of hydraulic cement concrete. *ASTM International*, *04.02*, West Conshohocken, Pennsylvania.

ASTM C192, 2016. Standard practice for making and curing concrete test specimens in the laboratory. *ASTM International*, *04.02*, West Conshohocken, Pennsylvania.

ASTM C231, 2014. Standard test method for air content of freshly mixed concrete by the pressure method. *ASTM International*, *04.02*, West Conshohocken, Pennsylvania.

ASTM C309, 2011 Standard specification for liquid membrane-forming compounds for curing concrete. *ASTM International*, *04.02*, West Conshohocken, Pennsylvania.

ASTM C39, 2016. Standard test method for compressive strength of cylindrical concrete specimens. *ASTM International*, *04.02*, West Conshohocken, Pennsylvania.

ASTM C494, 2016. Standard specification for chemical admixtures for concrete. *ASTM International*, *04.02*, West Conshohocken, Pennsylvania.

ASTM C496, 2011. Standard test method for splitting tensile strength of cylindrical concrete specimens. *ASTM International*, *04.02*, West Conshohocken, Pennsylvania.

ASTM C672/C672M, 2014. Standard test method for scaling resistance of concrete surfaces exposed to de-icing chemicals. *ASTM International*, *04.02*, West Conshohocken, Pennsylvania.

ASTM D4327, 2011. Standard test method for anions in water by suppressed ion chromatography. *ASTM International*, *04.02*, West Conshohocken, Pennsylvania.

Balasubramaniam, V., Raghunath, P.N. and Suguna, K., 2012. An adaptive neuro-fuzzy inference system based modeling for corrosion-damaged reinforced HSC beams strengthened with external glass fibre reinforced polymer laminates. *Journal of Computer Science*, *8*(6), pp.879-890.

Balonis, M., Lothenbach, B., Le Saout, G. and Glasser, F.P., 2010. Impact of chloride on the mineralogy of hydrated Portland cement systems. *Cement and Concrete Research*, *40*(7), pp.1009-1022.

Bassuoni, M.T. and Nehdi, M.L., 2008. Neuro-fuzzy based prediction of the durability of self-consolidating concrete to various sodium sulfate exposure regimes. *Computers and Concrete*, *5*(6), pp.573-597.

Bassuoni, M.T., Nehdi, M.L. and Greenough, T.R., 2006. Enhancing the reliability of evaluating chloride ingress in concrete using the ASTM C 1202 rapid chloride penetrability test. *Journal of ASTM International*, *3*(3), pp.1-13.

Belkowitz, J.S., Belkowitz, W.B., Nawrocki, K. and Fisher, F.T., 2015. Impact of Nanosilica Size and Surface Area on Concrete Properties. *ACI Materials Journal*, *112*(3), pp. 419-427.

Bentz, D.P. and Peltz, M.A., 2008. Reducing thermal and autogenous shrinkage contributions to early-age cracking. *ACI Materials Journal*, *105*(4), pp.414-420.

Beushausen, H., 2016. A parameter study on the age at cracking of bonded concrete overlays subjected to restrained shrinkage. *Materials and Structures*, *49*(5), pp.1905-1916.

Bianchini, A. and Bandini, P., 2010. Prediction of Pavement Performance through Neuro-Fuzzy Reasoning. *Computer-Aided Civil and Infrastructure Engineering*, *25*(1), pp.39-54.

Bilodeau, A. and MalhotraI, V.M., 1992. Concretes Incorporating High Volumes of ASTM Class F Fly Ashes: Mechanical Properties and Resistance to De-icing Salt Scaling and to Chloride-Ion Penetration. *ACI Special Publication*, *132*, pp.319-350.

Birnin-Yauri, U.A. and Glasser, F.P., 1998. Friedel's salt, $Ca_2Al(OH)_6$ (Cl,OH)· $2H_2O$: its solid solutions and their role in chloride binding. *Cement and Concrete Research*, *28*(12), pp.1713-1723.

BNQ NQ 2621-900, 2002. Determination of the scaling resistance of concrete surfaces exposed to freezing-and-thawing cycles in the presence of de-icing chemicals, Bureau de Normalisation du Québec, Annexe A.

Boğa, A.R., Öztürk, M. and Topçu, İ.B., 2013. Using ANN and ANFIS to predict the mechanical and chloride permeability properties of concrete containing GGBFS and CNI. *Composites Part B: Engineering*, *45*(1), pp.688-696.

Bouzoubaâ, N., Bilodeau, A., Fournier, B., Hooton, R.D., Gagné, R. and Jolin, M., 2011. Deicing salt scaling resistance of concrete incorporating fly ash and (or) silica fume: laboratory and field sidewalk test data. *Canadian Journal of Civil Engineering*, *38*(4), pp.373-382.

Brew, D.R.M. and Glasser, F.P., 2005. Synthesis and characterisation of magnesium silicate hydrate gels. *Cement and Concrete Research*, *35*(1), pp.85-98.

Brown, M. and Harris, C.J., 1994. Neurofuzzy adaptive modelling and control. Prentice Hall, USA.

Brown, M.E. and Gallagher, P.K., 2011. Handbook of thermal analysis and calorimetry: recent advances, techniques and applications.

Brown, P. and Bothe, J., 2004. The system CaO-Al_2O_3-$CaCl2$-H_2O at $23\pm2°C$ and the mechanisms of chloride binding in concrete. *Cement and Concrete Research*, *34*(9), pp.1549-1553.

Brown, S. and Needham, D., 2000. A study of cement modified bitumen emulsion mixtures. *Asphalt Paving Technology*, *69*, pp.92-121.

California State Department of Transportation (2001), Available at: http://www.dot.ca.gov/. (Oct. 1, 2017).

Caltrans, 2008. *Isolated partial depth concrete repair*, Sacramento, CA, 20 p.

Canadian Standards Association, 2013. CAN/CSA-A3001 Cementitious materials for use in concrete. Mississauga, Ontario, Canada.

Canadian Standards Association, 2014. CSA A23.2-6B Determination of bond strength of bonded toppings and overlays and of direct tensile strength of concrete, mortar, and grout. Mississauga, Ontario, Canada.

Canadian Standards Association, 2014. CSA-A23.1/A23.2 Concrete materials and methods of concrete construction/test methods and standard practices for concrete. Mississauga, Ontario, Canada.

Chatterji, S. and Gudmundsson, H., 1977. Characterization of entrained air bubble systems in concretes by means of an image analysing microscope. *Cement and Concrete Research*, *7*(4), pp.423-428.

Chen, D.H., Lin, H.H. and Sun, R., 2011. Field performance evaluations of partial-depth repairs. *Construction and Building Materials*, *25*(3), pp.1369-1378.

Cho, H.C., Ju, H., Oh, J.Y., Lee, K.J., Hahm, K.W. and Kim, K.S., 2016. Estimation of Concrete Carbonation Depth Considering Multiple Influencing Factors on the Deterioration of Durability for Reinforced Concrete Structures. *Advances in Materials Science and Engineering*, *2016*, 18p.

Choi, P. and Yun, K.K., 2014. Experimental analysis of latex-solid content effect on early-age and autogenous shrinkage of very-early strength latex-modified concrete. *Construction and Building Materials*, *65*, pp.396-404.

City of Toronto, 2016. Salt management plan. Available at: http://www1.toronto.ca/City%20Of%20Toronto/Transportation%20Services/Snow%20management/Files/pdf/SMP_2016_Summary.pdf.

City of Winnipeg, 2011. Policy on snow clearing and ice control. Available at: http://winnipeg.ca/publicworks/snow/snowClearing/snowClearingPolicy.stm#StreetPriorities.

Cody, R.D., Cody, A.M., Spry, P.G. and Gan, G.L., 1996. Experimental deterioration of highway concrete by chloride deicing salts. *Environmental & Engineering Geoscience*, *2*(4), pp.575-588.

Cody, R.D., Spry, P.G., Cody, A.M. and Gan, G.L., 1994. The role of magnesium in concrete deterioration. *Final report* (Iowa DOT HR-355).

Collepardi, M., Coppola, L. and Pistolesi, C., 1994. Durability of concrete structures exposed to CaCl 2 based deicing salts. *ACI Special Publication*, *145*, pp.107-120.

Czarnecki, L., Garbacz, A., Lukowski, P. and Clifton, J.R., 1999. Polymer composites for repairing of portland cement concrete: compatibility project. *NIST Interagency/Internal Report (NISTIR)-6394*.

Damidot, D. and Glasser, F.P., 1994. Thermodynamic investigation of the CaO-Al_2O_3-$CaCl_2$-H_2O system at 25°C and the influence of Na_2O. *Cement and Concrete Research*, *23*(1), pp.221-238.

Darwin, D., Browning, J., Gong, L. and Hughes, S.R., 2008. Effects of deicers on concrete deterioration. *ACI Materials Journal*, *105*(6), pp. 622-627.

Dehua, D. and Chuanmei, Z., 1999. The formation mechanism of the hydrate phases in magnesium oxychloride cement. *Cement and concrete research*, *29*(9), pp.1365-1371.

Del Río, L.M., Jiménez, A., López, F., Rosa, F.J., Rufo, M.M. and Paniagua, J.M., 2004. Characterization and hardening of concrete with ultrasonic testing. *Ultrasonics*, *42*(1), pp.527-530.

Delagrave, A., Pigeon, M. and Revertégat, É., 1994. Influence of chloride ions and pH level on the durability of high performance cement pastes. *Cement and concrete research*, *24*(8), pp.1433-1443.

Delagrave, A., Pigeon, M., Marchand, J. and Revertégat, É., 1996. Influence of chloride ions and pH level on the durability of high performance cement pastes (part II). *Cement and Concrete Research*, *26*(5), pp.749-760.

Delatte, N.J., 2014. Concrete pavement design, construction, and performance. New York: CRC Press, 392 pp.

Depasse, J., 1999. Simple experiments to emphasize the main characteristics of the coagulation of silica hydrosols by alkaline cations: Application to the analysis of the model of Colic et al. *Journal of colloid and interface science*, *220*(1), pp.174-176.

Detwiler, R.J. and Powers-Couche, L.J., 1999. Effect of sulfates in concrete on their resistance to freezing and thawing. *ACI Special Publication*, *177*, pp.219-248.

Detwiler, R.J., Bhatty, J.I. and Battacharja, S., 1996. Supplementary cementing materials for use in blended cements (No. R&D Bulletin RD112T), Portland Cement Association, Skokie, Illinois.

Do, J., Song, H., So, S. and Soh, Y., 2005. Fuzzy methodology application for modeling uncertainties in chloride ingress models of RC building structure. *Computers and Concrete*, *2*(4), pp.325-343.

Do, J.Y., 2006. Fuzzy inference based cover thickness estimation of reinforced concrete structure quantitatively considering salty environment impact. *Computers and Concrete*, *3*(2_3), pp.145-161.

Dubberke, W. and Marks, V.J., 1985. The effect of deicing salt on aggregate durability, *Iowa Department of Transportation*, Storm Lake, Iowa.

Emmons, P.H. and Sordyl, D.J., 2006. The state of the concrete repair industry, and a vision for its future. *Concrete Repair Bulletin*, pp.7-14.

Famy, C. and Taylor, H.F., 2001. Ettringite in hydration of Portland cement concrete and its occurrence in mature concretes. *Materials Journal*, *98*(4), pp.350-356.

Fang, Y.F., 2001. Environmental Influences on Warping and Curling of PCC Pavement. In *Seventh International Conference on Concrete Pavements. The Use of Concrete in Developing Long-Lasting Pavement Solutions for the 21st Century* (Vol. 1).

Farnam, Y., Dick, S., Wiese, A., Davis, J., Bentz, D. and Weiss, J., 2015a. The influence of calcium chloride deicing salt on phase changes and damage development in cementitious materials. *Cement and Concrete Composites*, *64*, pp.1-15.

Farnam, Y., Washington, T. and Weiss, J., 2015c. The influence of calcium chloride salt solution on the transport properties of cementitious materials. *Advances in Civil Engineering*, *2015*, 13p.

Farnam, Y., Wiese, A., Bentz, D., Davis, J. and Weiss, J., 2015b. Damage development in cementitious materials exposed to magnesium chloride deicing salt. *Construction and Building Materials*, *93*, pp.384-392.

FHWA, 2005. *Partial-depth repair of portland cement concrete pavements, pavement preservation checklist series*. Federal Highway Administration. Washington, DC.

Frentress, D.P. and Harrington, D.S., 2012. Guide for partial-depth repair of concrete pavements. Iowa State University Institute for Transportation, Storm Lake, Iowa.

Galan, I., Perron, L. and Glasser, F.P., 2015. Impact of chloride-rich environments on cement paste mineralogy. *Cement and Concrete Research*, *68*, pp.174-183.

Ghazy, A. and Bassuoni, M.T., 2017a. Resistance of concrete to different exposures with chloride-based salts. *Cement and Concrete Research*, *101*, pp. 144-158.

Ghazy, A., Bassuoni, M.T. and Shalaby, A., 2016. Nano-modified fly ash concrete: A Repair Option for Concrete Pavements. *ACI Materials Journal*, *113*(2), pp. 231-242.

Glasser, F.P., Pedersen, J., Goldthorpe, K. and Atkins, M., 2005. Solubility reactions of cement components with NaCl solutions: I. Ca (OH)$_2$ and CSH. *Advances in Cement Research*, *17*(2), pp.57-64.

Goktepe, A.B., Inan, G., Ramyar, K. and Sezer, A., 2006. Estimation of sulfate expansion level of PC mortar using statistical and neural approaches. *Construction and Building Materials*, *20*(7), pp.441-449.

Goni, S. and Guerrero, A., 2003. Accelerated carbonation of Friedel's salt in calcium aluminate cement paste. *Cement and Concrete Research*, *33*(1), pp.21-26.

Guide for Partial Depth Repair of Concrete Pavements, City of Winnipeg, MB, Canada, 2015, 21 pp.

Hall, C., 1989. Water sorptivity of mortars and concretes: a review. *Magazine of Concrete Research*, *41*(147), pp.51-61.

Hall, K., Dawood, D., Vanikar, S., Tally Jr, R., Cackler, T., Correa, A., Deem, P., Duit, J., Geary, G., Gisi, A. and Hanna, A., 2007. *Long-life concrete pavements in Europe and Canada* (No. FHWA-PL-07-027). Available at: http://international.fhwa.dot.gov/ (Oct. 1, 2017).

Harnik, A.B., Meier, U. and Roesli, A., 1980. Combined influence of freezing and deicing salt on concrete—Physical aspects. In *Durability of building materials and components*. ASTM International. West Conshohocken, Pennsylvania.

Harrington, D. and Fick, G., 2014. Guide to concrete overlays: sustainable solutions for resurfacing and rehabilitating existing pavements. American Concrete Pavement Association (ACPA publication TB021. 03P), Washington, DC.

Haykin, S., 1994. Neural networks: a comprehensive foundation. Prentice Hall, USA, 842p.

Heisig, A., Urbonas, L., Beddoe, R.E. and Heinz, D., 2016. Ingress of NaCl in concrete with alkali reactive aggregate: effect on silicon solubility. *Materials and Structures*, *49*(10), pp.4291-4303.

Hertz, J., Krogh, A. and Palmer, R.G., 1991. Introduction to the theory of neural computation. Westview Press.

Holt, A., Sullivan, S. and Hein, D., 2011, September. Life cycle cost analysis of municipal pavements in southern and eastern Ontario. In *2011 Conference and exhibition of the transportation association of Canada.*

Holt, E., 2005. Contribution of mixture design to chemical and autogenous shrinkage of concrete at early ages. *Cement and Concrete Research*, *35*(3), pp.464-472.

Hou, P., Kawashima, S., Kong, D., Corr, D.J., Qian, J. and Shah, S.P., 2013. Modification effects of colloidal nanoSiO$_2$ on cement hydration and its gel property. *Composites Part B: Engineering*, *45*(1), pp.440-448.

HU, M.Y. and TANG, M.S., 2006. Use of fuzzy neural network to evaluate effect of composition of fly ash in suppressing AAR. *ACI Materials Journal*, *103*(3), pp.161-168.

Huang, C.H., Lin, S.K., Chang, C.S. and Chen, H.J., 2013. Mix proportions and mechanical properties of concrete containing very high-volume of Class F fly ash. *Construction and Building Materials*, *46*, pp.71-78.

Ipavec, A., Vuk, T., Gabrovšek, R. and Kaučič, V., 2013. Chloride binding into hydrated blended cements: The influence of limestone and alkalinity. *Cement and Concrete Research*, *48*, pp.74-85.

Jacobsen, S., Sœther, D.H. and Sellevold, E.J., 1997. Frost testing of high strength concrete: frost/salt scaling at different cooling rates. *Materials and Structures*, *30*(1), pp.33-42.

Jain, J., Olek, J., Janusz, A. and Jozwiak-Niedzwiedzka, D., 2012. Effects of deicing salt solutions on physical properties of pavement concretes. *Transportation Research Record: Journal of the Transportation Research Board*, *2290*, pp.69-75.

Jang, J.S., 1993. ANFIS: adaptive-network-based fuzzy inference system. *IEEE transactions on systems, man, and cybernetics*, *23*(3), pp.665-685.

Johannesson, B.F., 2003. A theoretical model describing diffusion of a mixture of different types of ions in pore solution of concrete coupled to moisture transport. *Cement and Concrete Research*, *33*(4), pp.481-488.

Juenger, M.C.G. and Jennings, H.M., 2002. Examining the relationship between the microstructure of calcium silicate hydrate and drying shrinkage of cement pastes. *Cement and Concrete Research*, *32*(2), pp.289-296.

Julio-Betancourt, G.A. and Hooton, R.D., 2009. Calcium and magnesium chloride attack on cement-based materials: formation, stability, and effects of oxychlorides. In *Concrete Durability and Service Life Planning – ConcreteLife'09*, RILEM Publications, pp.432-439.

Jung, K.C., Roh, I.T. and Chang, S.H., 2014. Evaluation of mechanical properties of polymer concretes for the rapid repair of runways. *Composites Part B: Engineering*, *58*, pp.352-360.

Justnes, H., Reyniers, B. and Sellevold, E.J., 1994. An evaluation of methods for measuring chemical shrinkage of cementitious pastes. *Nordic Concrete Research*, *14*(1), pp.45-61.

Kang, Y., Hansen, W. and Borgnakke, C., 2012. Effect of air-void system on frost expansion of highway concrete exposed to deicer salt. *International Journal of Pavement Engineering*, *13*(3), pp.259-266.

Katayama, T., Tagami, M., Sarai, Y., Izumi, S. and Hira, T., 2004. Alkali-aggregate reaction under the influence of deicing salts in the Hokuriku district, Japan. *Materials Characterization*, *53*(2), pp.105-122.

Kawamura, K. and Miyamoto, A., 2003. Condition state evaluation of existing reinforced concrete bridges using neuro-fuzzy hybrid system. *Computers & Structures*, *81*(18), pp.1931-1940.

Kelting, D.L. and Laxon, C.L., 2010. Review of effects and costs of road de-icing with recommendations for winter road management in the Adirondack Park. Adirondack Watershed Institute.

Kim, J.J., Foley, E.M. and Taha, M.M.R., 2013. Nano-mechanical characterization of synthetic calcium–silicate–hydrate (C–S–H) with varying CaO/SiO_2 mixture ratios. *Cement and Concrete Composites*, *36*, pp.65-70.

Kim, Y.M., Kim, C.K. and Hong, S.G., 2006. Fuzzy based state assessment for reinforced concrete building structures. *Engineering Structures*, *28*(9), pp.1286-1297.

Kong, D., Corr, D.J., Hou, P., Yang, Y. and Shah, S.P., 2015. Influence of colloidal silica sol on fresh properties of cement paste as compared to nano-silica powder with agglomerates in micron-scale. *Cement and Concrete Composites*, *63*, pp.30-41.

Kong, D., Du, X., Wei, S., Zhang, H., Yang, Y. and Shah, S.P., 2012. Influence of nano-silica agglomeration on microstructure and properties of the hardened cement-based materials. *Construction and Building Materials*, *37*, pp.707-715.

Korpa, A., Kowald, T. and Trettin, R., 2008. Hydration behaviour, structure and morphology of hydration phases in advanced cement-based systems containing micro and nanoscale pozzolanic additives. *Cement and Concrete Research*, *38*(7), pp.955-962.

Kozikowski, R.L., Taylor, P.C. and Pyć, W.A., 2007. *Evaluation of Potential Concrete Deterioration Related to Magnesium Chloride (MgCl₂) Deicing Salts*. Portland Cement Association, Skokie, Illinois, 30 p.

Lee, H., Cody, R.D., Cody, A.M. and Spry, P.G., 2000. Effects of various deicing chemicals on pavement concrete deterioration. In *Mid-Continente Transportation Symposium Proceedings,* pp. 151-155.

Li, J., Zhang, W. and Cao, Y., 2014. Laboratory evaluation of magnesium phosphate cement paste and mortar for rapid repair of cement concrete pavement. *Construction and Building Materials*, *58*, pp.122-128.

Li, L.G., Chen, J.J. and Kwan, A.K., 2017. Roles of packing density and water film thickness in strength and durability of limestone fines concrete. *Magazine of Concrete Research*, *69*(12), pp.595-605.

Li, M. and Li, V.C., 2011. High-Early-Strength Engineered Cementitious Composites for Fast, Durable Concrete Repair-Material Properties. *ACI Materials Journal*, *108*(1), pp. 3-12.

Li, S.E., Frantz, G.C. and Stephens, J.E., 1999. Bond performance of rapid-setting repair materials subjected to deicing salt and freezing-thawing cycles. *Materials Journal*, *96*(6), pp.692-697.

Litvan, G.G., 1976. Frost action in cement in the presence of de-icers. *Cement and Concrete Research*, *6*(3), pp.351-356.

Liu, Z. and Hansen, W., 2015. Freezing characteristics of air-entrained concrete in the presence of deicing salt. *Cement and Concrete Research*, *74*, pp.10-18.

Loser, R., Münch, B. and Lura, P., 2010. A volumetric technique for measuring the coefficient of thermal expansion of hardening cement paste and mortar. *Cement and Concrete Research*, *40*(7), pp.1138-1147.

Lothenbach, B., Le Saout, G., Gallucci, E. and Scrivener, K., 2008. Influence of limestone on the hydration of Portland cements. *Cement and Concrete Research*, *38*(6), pp.848-860.

Madani, H., Bagheri, A. and Parhizkar, T., 2012. The pozzolanic reactivity of monodispersed nanosilica hydrosols and their influence on the hydration characteristics of Portland cement. *Cement and concrete research*, *42*(12), pp.1563-1570.

Malhotra, V.M., Zhang, M.H., Read, P.H. and Ryell, J., 2000. Long-term mechanical properties and durability characteristics of high-strength/high-performance concrete incorporating supplementary cementing materials under outdoor exposure conditions. *Materials Journal*, *97*(5), pp.518-525.

Marchand, J. and Samson, E., 2009. Predicting the service-life of concrete structures–Limitations of simplified models. *Cement and Concrete Composites*, *31*(8), pp.515-521.

Marchand, J., Jolin, M. and Machabée, Y., 2005. Deicer salt scaling resistance of supplementary cementing material concrete: Laboratory results against field performance. In *Cement Combinations for Durable Concrete: Proceedings of the International Conference held at the University of Dundee, Scotland, UK,* pp. 579-590

Marchand, J., Pigeon, M., Bager, D. and Talbot, C., 1999. Influence of chloride solution concentration on deicer salt scaling deterioration of concrete. *Materials Journal*, *96*(4), pp.429-435.

Marchand, J., Sellevold, E.J. and Pigeon, M., 1994. The deicer salt scaling deterioration of concrete. *ACI Special Publication*, *145*, pp.1-1.

Markey, S.M., Lee, S.I., Mukhopadhyay, A.K., Zollinger, D.G., Whitney, D.P. and Fowler, D.W., 2006. Investigation of spall repair materials for concrete pavement (No. FHWA/TX-06/0-5110-1), Texas Transportation Institute, Texas.

Marzouki, A., Lecomte, A., Beddey, A., Diliberto, C. and Ouezdou, M.B., 2013. The effects of grinding on the properties of Portland-limestone cement. *Construction and Building Materials*, *48*, pp.1145-1155.

Maslehuddin, M., Ibrahim, M., Shameem, M., Ali, M.R. and Al-Mehthel, M.H., 2013. Effect of curing methods on shrinkage and corrosion resistance of concrete. *Construction and Building Materials*, *41*, pp.634-641.

Mather, B., 2001. Crystal Growth in Entrained-Air Voids. *Concrete International*, *23*(5), pp.35-36.

MATLAB Documentation. 2016. *Fuzzy toolbox user's guide of MATLAB*. The MathWorks, Inc., Natick, Massachusetts.

Mehta, P. K., and Monteiro, P., 2014. Concrete: Microstructure, properties, and materials. San Francisco: McGraw-Hill.

Mindess, S., Young, J.F. and Darwin, D., 2003. Concrete. Prentice Hall, USA.

Minnesota Snow and Ice Control. 2012. Field Handbook for Snowplow Operators. Available at: http://www.mnltap.umn.edu/.

Mondal, P., Shah, S., Marks, L. and Gaitero, J., 2010. Comparative study of the effects of microsilica and nanosilica in concrete. *Transportation Research Record: Journal of the Transportation Research Board*, *2141*, pp.6-9.

Monical, J., Unal, E., Barrett, T., Farnam, Y. and Weiss, W.J., 2016. Reducing Joint Damage in Concrete Pavements: Quantifying Calcium Oxychloride Formation. *Transportation Research Record: Journal of the Transportation Research Board*, *2577*, pp.17-24.

Monosi, S. and Collepardi, M., 1990. Research on $3CaO \cdot CaCl_2 \cdot 15H_2O$ identified in concretes damaged by $CaCl_2$ attack. *Il Cimento*, *87*, pp.3-8.

Monosi, S. and Collepardi, M., 1993. Chemical attack of calcium chloride on the Portland cement paste. *Cemento*, *90*, pp.169-169.

Montgomery, D.C., 2014. Design and Analysis of Experiments. New York: John Wiley & Sons, 225p.

Mori, H., Kuga, R., Ogawa, S. and Kubo, Y., 2013. Chemical Deterioration of Hardened Cement Pastes Immersed in Calcium Chloride Solution. In *3rd International Conference on Sustainable Construction Materials and Technologies*.

MTO LS-412, 1997. Method of test for scaling resistance of concrete surfaces exposed to deicing chemicals, Ontario Lab Testing Manual, Ministry of Transportation.

Neville, A. M., 2011. Properties of concrete. London: Prentice Hall, 983 pp.

Nilsson, L.O., 2006. Present limitations of models for predicting chloride ingress into reinforced concrete structures. In *Journal de Physique IV (Proceedings)* (Vol. 136) EDP sciences, pp. 123-130.

Nixon, P.J. and Page, C.L., 1987. Pore solution chemistry and alkali aggregate reaction. *ACI Special Publication*, *100*, pp.1833-1862.

Nixon, P.J., Page, C.L., Canham, I. and Bollinghaus, R., 1988. Influence of sodium chloride on alkali-silica reaction. *Advances in Cement Research*, *1*(2), pp.99-106.

NT BUILD 492. 2011 Chloride migration coefficient from non-steady-state migration experiments. Nordtest. Finland.

Oertel, T., Hutter, F., Tänzer, R., Helbig, U. and Sextl, G., 2013. Primary particle size and agglomerate size effects of amorphous silica in ultra-high performance concrete. *Cement and Concrete Composites*, *37*, pp.61-67.

Ondova, M., Stevulova, N. and Meciarova, L., 2013. The potential of higher share of fly ash as cement replacement in the concrete pavement. *Procedia Engineering*, *65*, pp.45-50.

Ontario Ministry of Transportation, 2016. Snow and Ice Control. Available at: https://www.ontario.ca/.

Ontario provincial standard specification, 2014. Materials and Production. Ontario Provincial Standards for Roads and Public Works, 77p.

Ouyang, C., 1999. Effect of infilling of air voids by ettringite on resistance of concretes to freezing and thawing. *ACI Special Publication*, *177*, pp.249-262.

Panchmatia, P., Olek, J. and Whiting, N. 2014. Joint Deterioration in Concrete Pavements. In *4th International Conference on the Durability of Concrete Structures*, Purdue University, West Lafayette, IN, USA, pp. 12-21.

Pannach, M., Bette, S. and Freyer, D., 2017. Solubility Equilibria in the System $Mg(OH)_2$–$MgCl_2$–H_2O from 298 to 393 K. *Journal of Chemical & Engineering Data*, *62*(4), pp.1384-1396.

Parker Jr, F. and Lee Shoemaker, W., 1991. PCC pavement patching materials and procedures. *Journal of Materials in Civil Engineering*, *3*(1), pp.29-47.

Penttala, V., 2006. Surface and internal deterioration of concrete due to saline and non-saline freeze–thaw loads. *Cement and Concrete Research*, *36*(5), pp.921-928.

Peterson, K., Julio-Betancourt, G., Sutter, L., Hooton, R.D. and Johnston, D., 2013. Observations of chloride ingress and calcium oxychloride formation in laboratory concrete and mortar at 5 $^{\circ}$C. *Cement and Concrete Research*, *45*, pp.79-90.

Pigeon, M., Marchand, J. and Pleau, R., 1996. Frost resistant concrete. *Construction and Building Materials*, *10*(5), pp.339-348.

Powers, T.C. and Helmuth, R.A., 1953. Theory of volume changes in hardened portland-cement paste during freezing. *In Highway research board proceedings, 32*, pp. 285-297.

Powers, T.C., 1945. A working hypothesis for further studies of frost resistance of concrete. In *Journal Proceedings, 41(1)* pp. 245-272.

Powers, T.C., 1975. Freezing effects in concrete. *ACI Special Publication*, *47*, pp.1-12.

Qiao, C., Suraneni, P. and Weiss, J., 2017. Measuring volume change caused by calcium oxychloride phase transformation in a $Ca(OH)_2$-$CaCl_2$-H_2O system. *Advances in Civil Engineering Materials*, *6*(1), pp.157-169.

Ramakrishna, D.M. and Viraraghavan, T., 2005. Environmental impact of chemical deicers–a review. *Water, Air, and Soil Pollution*, *166*(1-4), pp.49-63.

Ramezanianpour, A.M. and Hooton, R.D., 2013. Sulfate resistance of Portland-limestone cements in combination with supplementary cementitious materials. *Materials and Structures*, *46*(7), pp.1061-1073.

Rangaraju, P., 2002. Investigating premature deterioration of a concrete highway. *Transportation Research Record: Journal of the Transportation Research Board*, *1798*, pp.1-7.

Rechenberg, W. and Sylla, H.M., 1996. The effect of magnesium on concrete. *ZKG International*, *49*(1), pp.44-56.

Roh, I.T., Jung, K.C., Chang, S.H. and Cho, Y.H., 2015. Characterization of compliant polymer concretes for rapid repair of runways. *Construction and Building Materials*, *78*, pp.77-84.

Rösli, A. and Harnik, A.B., 1980. Improving the durability of concrete to freezing and deicing salts. In *Durability of Building Materials and Components*. ASTM International, West Conshohocken, Pennsylvania.

Said, A.M., Zeidan, M.S., Bassuoni, M.T. and Tian, Y. 2012. Properties of concrete incorporating nano-silica. *Construction and Building Materials*, *36*, pp.838-844.

Samson, E. and Marchand, J., 2007. Modeling the transport of ions in unsaturated cement-based materials. *Computers & Structures*, *85*(23), pp.1740-1756.

Santagata, M.C. and Collepardi, M., 2000. The effect of CMA deicers on concrete properties. *Cement and Concrete Research*, *30*(9), pp.1389-1394.

Scherer, G.W., 1999. Crystallization in pores. *Cement and Concrete Research*, *29*(8), pp.1347-1358.

Scherer, G.W., 2004. Stress from crystallization of salt. *Cement and Concrete Research*, *34*(9), pp.1613-1624.

Schlorholtz, S., Dawson, B. and Scott, M., 2003. Development of in-situ detection methods for materials-related distress (MRD). In *concrete pavements: phase 1 report* (No.1), 48p.

Sears, G.W., 1956. Determination of specific surface area of colloidal silica by titration with sodium hydroxide. *Analytical Chemistry*, *28*(12), pp.1981-1983.

Seehra, S.S., Gupta, S. and Kumar, S., 1993. Rapid setting magnesium phosphate cement for quick repair of concrete pavements—characterisation and durability aspects. *Cement and Concrete Research*, *23*(2), pp.254-266.

Sglavo, V.M., De Genua, F., Conci, A., Ceccato, R. and Cavallini, R., 2011. Influence of curing temperature on the evolution of magnesium oxychloride cement. *Journal of Materials Science*, *46*(20), pp.6726-6733.

Shahin, M. Y. 2005. Pavement maintenance management for airports, roads, and parking lots, New York: Chapman & Hall.

Shi, C., 2001. Formation and stability of $3CaO \cdot CaCl_2 \cdot 12H_2O$. *Cement and Concrete Research*, *31*(9), pp.1373-1375.

Shi, X., Fay, L., Peterson, M.M. and Yang, Z., 2010. Freeze–thaw damage and chemical change of a portland cement concrete in the presence of diluted deicers. *Materials and Structures*, *43*(7), pp.933-946.

Shi, X., Fay, L., Peterson, M.M., Berry, M. and Mooney, M., 2011. A FESEM/EDX investigation into how continuous deicer exposure affects the chemistry of Portland cement concrete. *Construction and Building Materials*, *25*(2), pp.957-966.

Shi, X., Veneziano, D., Xie, N. and Gong, J., 2013. Use of chloride-based ice control products for sustainable winter maintenance: A balanced perspective. *Cold Regions Science and Technology*, *86*, pp.104-112.

Sibbick, R.G. and Page, C.L., 1998. Mechanisms affecting the development of alkali-silica reaction in hardened concretes exposed to saline environments. *Magazine of Concrete Research*, *50*(2), pp.147-159.

Silva, H.M., 2005. Study on the Use of Bituminous Mixtures Modified with Acrylic Fibres in Road Pavement Overlays. In *First International Conference on Transport Infrastructure, Beijing, China*.

Skalny, J., Marchand, J., and Odler, I., 2002. Sulfate attack on concrete. London: Spon Press.

Slatnick, S., Riding, K.A., Folliard, K.J., Juenger, M.C. and Schindler, A.K., 2011. Evaluation of autogenous deformation of concrete at early ages. *ACI Materials Journal*, *108*(1), pp.21-28.

Soliman, H. and Shalaby, A. 2012. *Partial-depth repair of rigid pavements: materials and processes.* Materials Engineering Branch, Manitoba Infrastructure and Transportation and Public Works Department, City of Winnipeg, 49 p.

Soliman, H. and Shalaby, A., 2014. Characterizing the performance of cementitious partial-depth repair materials in cold climates. *Construction and Building Materials*, *70*, pp.148-157.

Sonebi, M., García-Taengua, E., Hossain, K.M.A., Khatib, J. and Lachemi, M., 2015. Effect of nanosilica addition on the fresh properties and shrinkage of mortars with fly ash and superplasticizer. *Construction and Building Materials*, *84*, pp.269-276.

Song, Z., Jiang, L. and Zhang, Z., 2016. Chloride diffusion in concrete associated with single, dual and multi cation types. *Computers and Concrete*, *17*(1), pp.53-66.

Soraru, G.D. and Tassone, P., 2004. Mechanical durability of a polymer concrete: a Vickers indentation study of the strength degradation process. *Construction and Building Materials*, *18*(8), pp.561-566.

Spragg, R.P., Castro, J., Li, W., Pour-Ghaz, M., Huang, P.T. and Weiss, J., 2011. Wetting and drying of concrete using aqueous solutions containing deicing salts. *Cement and Concrete Composites*, *33*(5), pp.535-542.

Sprinkel, M., 1999. Very-early-strength latex-modified concrete overlay. *Transportation Research Record: Journal of the Transportation Research Board*, (1668), pp.18-23.

Stark, J. and Bollmann, K., 1999. Laboratory and field examinations of ettringite formation in pavement concrete. *ACI Special Publication*, *177*, pp.183-198.

Stein, H.N. and Stevels, J.M., 1964. Influence of silica on the hydration of $3CaO \cdot SiO_2$. *Journal of Chemical Technology and Biotechnology*, *14*(8), pp.338-346.

Štemberk, P., da Silva, W.R., Sýkorová, J. and Bartová, J., 2013. Fuzzy modeling of combined effect of winter road maintenance and cyclic loading on concrete slab bridge. *Advances in Engineering Software*, *62*, pp.97-108.

Sun, Z. and Scherer, G.W., 2010. Effect of air voids on salt scaling and internal freezing. *Cement and Concrete Research*, *40*(2), pp.260-270.

Suraneni, P., Azad, V.J., Isgor, O.B. and Weiss, W.J., 2016. Deicing Salts and Durability of Concrete Pavements and Joints. *Concrete International*, *38*(4), pp.48-54.

Suraneni, P., Azad, V.J., Isgor, O.B. and Weiss, W.J., 2017. Use of Fly Ash to Minimize Deicing Salt Damage in Concrete Pavements. *Transportation Research Record: Journal of the Transportation Research Board*, *2629*, pp.24-32.

Suryavanshi, A.K. and Swamy, R.N., 1996a. Stability of Friedel's salt in carbonated concrete structural elements. *Cement and Concrete Research*, *26*(5), pp.729-741.

Suryavanshi, A.K., Scantlebury, J.D. and Lyon, S.B., 1996b. Mechanism of Friedel's salt formation in cements rich in tri-calcium aluminate. *Cement and Concrete Research*, *26*(5), pp.717-727.

Sutter, L., Peterson, K., Julio-Betancourt, G., Hooton, D., Vam Dam, T., and Smith, K., 2008. *The Deleterious Chemical Effects of Concentrated Deicing Solutions on Portland Cement Concrete - Final Report*. South Dakota Department of Transportation, Final Report Federal Highway Administration, 56 p.

Sutter, L., Peterson, K., Touton, S., Van Dam, T. and Johnston, D., 2006. Petrographic evidence of calcium oxychloride formation in mortars exposed to magnesium chloride solution. *Cement and Concrete Research*, *36*(8), pp.1533-1541.

Tamimi, A.K., Abdalla, J.A. and Sakka, Z.I., 2008. Prediction of long term chloride diffusion of concrete in harsh environment. *Construction and Building Materials*, *22*(5), pp.829-836.

Taylor, P. C., Kosmatka, S. H., Voigt, G. F., Ayers, M. E., Davis, A., Fick, G. J., Gajda, J., Grove, J., Harrington, D., Kerkhoff, B., Ozyildirim, C., Shilstone, J. M., Smith, K., Tarr, S. M., Tennis, P. D., Van Dam, T. J., and Waalkes, S., 2006. *Integrated Materials and Construction Practices for Concrete Pavement: A State of the Practice Manual*. FHWA HIF-07-004, Washington, DC, 189 p.

Thomas, M.D.A., Cail, K., Blair, B., Delagrave, A., Masson, P. and Kazanis, K., 2010. Use of low-CO_2 Portland limestone cement for pavement construction in Canada. *International Journal of Pavement Research and Technology*, *3*(5), pp.228-233.

Tiznobaik, M., and Bassuoni, M.T., 2017. A test protocol for evaluating absorption of joints in concrete pavements. *ASTM Journal of Testing and Evaluation*. (In press).

Transportation in Canada. 2016. Available at: https://www.tc.gc.ca/. (Oct. 1, 2017).

Tsivilis, S., Tsantilas, J., Kakali, G., Chaniotakis, E. and Sakellariou, A., 2003. The permeability of Portland limestone cement concrete. *Cement and Concrete Research*, *33*(9), pp.1465-1471.

Valenza, I.I., JJ and Scherer, G.W., 2007. A review of salt scaling: II. Mechanisms. *Cement and Concrete Research*, *37*(7), pp.1022-1034.

Valenza, J.J. and Scherer, G.W., 2006. Mechanism for salt scaling. *Journal of the American Ceramic Society*, *89*(4), pp.1161-1179.

Vaysburd, A.M., Brown, C.D., Bissonette, B. and Emmons, P.H., 2004. Realcrete" versus "Labcrete. *Concrete international*, *26*(2), pp.90-94.

Vol'nov, I. I., and Latysheva, E. I., 1957. Separation of calcium chloride from solvay spent liquor through calcium hydroxichloride. *Journal of Applied Chemistry of the USSR, 30*, pp. 1039-1046.

Wang, K., Nelsen, D.E. and Nixon, W.A., 2006a. Damaging effects of deicing chemicals on concrete materials. *Cement and Concrete Composites*, *28*(2), pp.173-188.

Wang, S. and Li, V.C., 2006b. High-early-strength engineered cementitious composites. *ACI Materials Journal*, *103*(2), pp.97-105.

Weiss, W.J., Yang, W. and Shah, S.P., 1998. Shrinkage cracking of restrained concrete slabs. *Journal of Engineering Mechanics*, *124*(7), pp.765-774.

Whiting, D. and Nagi, M., 1994. Strength and durability of rapid highway repair concretes. *Concrete International*, *16*(9), pp.36-41.

Wilson, T. P., Smith, K. L., and Romine, A. R. 1999. *Materials and procedures for rapid repair of partial depth spalls in concrete pavements - manual of practice.* McLean, VA: Federal Highway Administration. Report No. FHWA-RD, pp 99-152.

Winkler, E.M. and Singer, P.C., 1972. Crystallization pressure of salts in stone and concrete. *Geological Society of America Bulletin*, *83*(11), pp.3509-3514.

Wu, Z., Shi, C., Gao, P., Wang, D. and Cao, Z., 2015. Effects of deicing salts on the scaling resistance of concrete. *Journal of Materials in Civil Engineering*, *27*(5), 04014160.

Xia, S., Xing, P. and Gao, S., 1991. Studies on the basic compounds of magnesia cement: the thermal behaviour of magnesium oxychlorides. *Thermochimica acta*, *183*, pp.349-363.

Yehia, S.A. and Tuan, C.Y., 1998. Bridge deck deicing. Iowa State University.

Yener, E., 2015. A new frost salt scaling mechanism for concrete pavements based on brine rejection from ice layer adhered to concrete surface. *Road Materials and Pavement Design*, *16*(1), pp.89-100.

Yodsudjai, W. and Wang, K., 2013. Chemical shrinkage behavior of pastes made with different types of cements. *Construction and Building Materials*, *40*, pp.854-862.

Yun, K.K. and Choi, P., 2014. Causes and controls of cracking at bridge deck overlay with very-early strength latex-modified concrete. *Construction and Building Materials*, *56*, pp.53-62.

Zadeh, V.Z. and Bobko, C.P., 2013. Nanoscale mechanical properties of concrete containing blast furnace slag and fly ash before and after thermal damage. *Cement and Concrete Composites*, *37*, pp.215-221.

Zalocha, D. and Kasperkiewicz, J., 2005. Estimation of the structure of air entrained concrete using a flatbed scanner. *Cement and Concrete research*, *35*(10), pp.2041-2046.

Zerrouk, R., Foissy, A., Mercier, R., Chevallier, Y. and Morawski, J.C., 1990. Study of Ca2+-induced silica coagulation by small angle scattering. *Journal of Colloid and Interface Science*, *139*(1), pp.20-29.

Zhang, J. and Lounis, Z., 2009. Nonlinear relationships between parameters of simplified diffusion-based model for service life design of concrete structures exposed to chlorides. *Cement and Concrete Composites*, *31*(8), pp.591-600.

Ïnan, G., Göktepe, A.B., Ramyar, K. and Sezer, A., 2007. Prediction of sulfate expansion of PC mortar using adaptive neuro-fuzzy methodology. *Building and Environment*, *42*(3), pp.1264-1269.

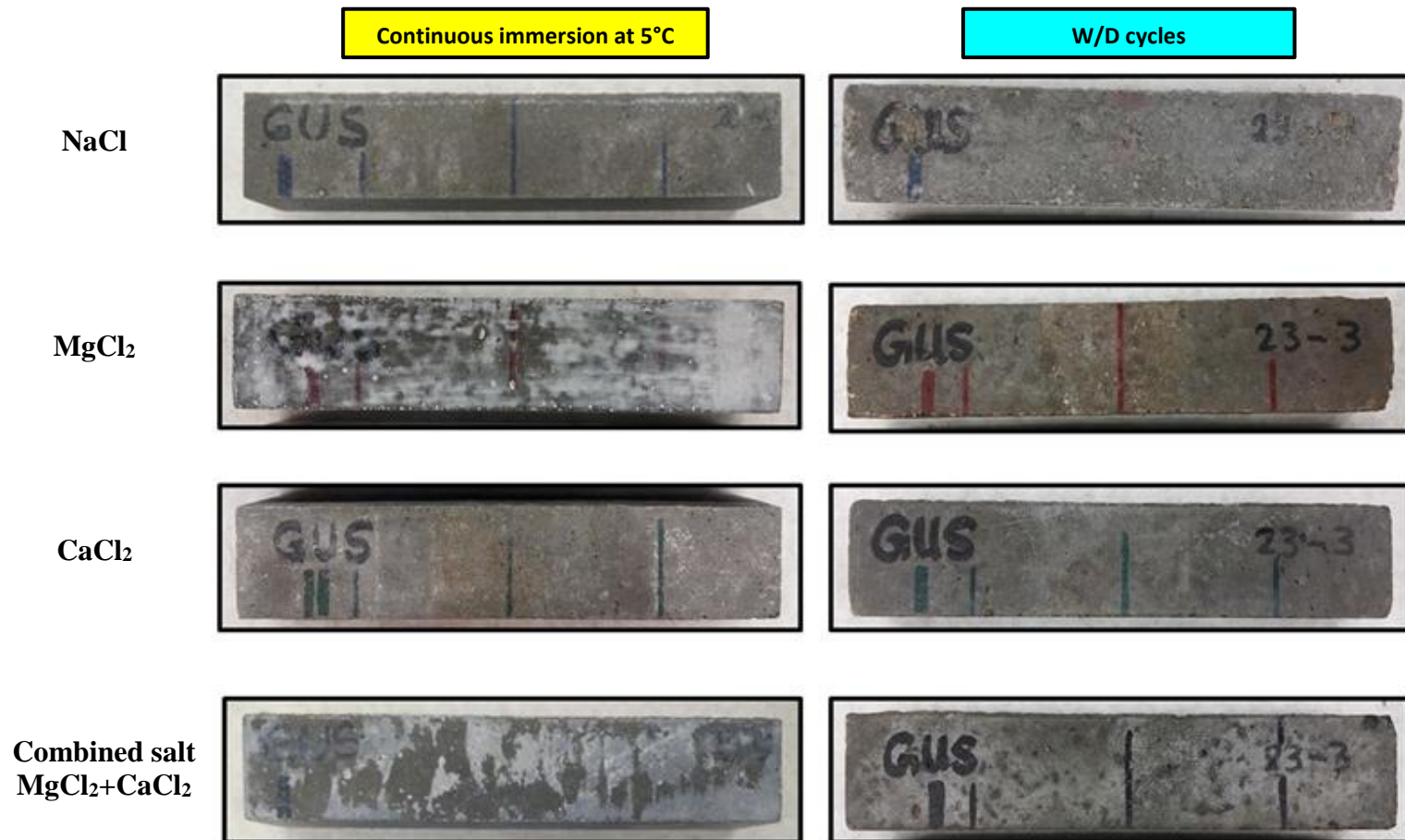# APPENDIX A: EXEMPLAR SPECIMENS COMPRESSING NANOSILICA EXPOSED TO DIFFERENT EXPOSURES

Figure A.1: Exemplar specimens (GUS) made with binary binders compressing 6% nanosilica exposed to different de-icing salts at 540 days: continuous immersion at 5°C (left), and W/D cycles (right).
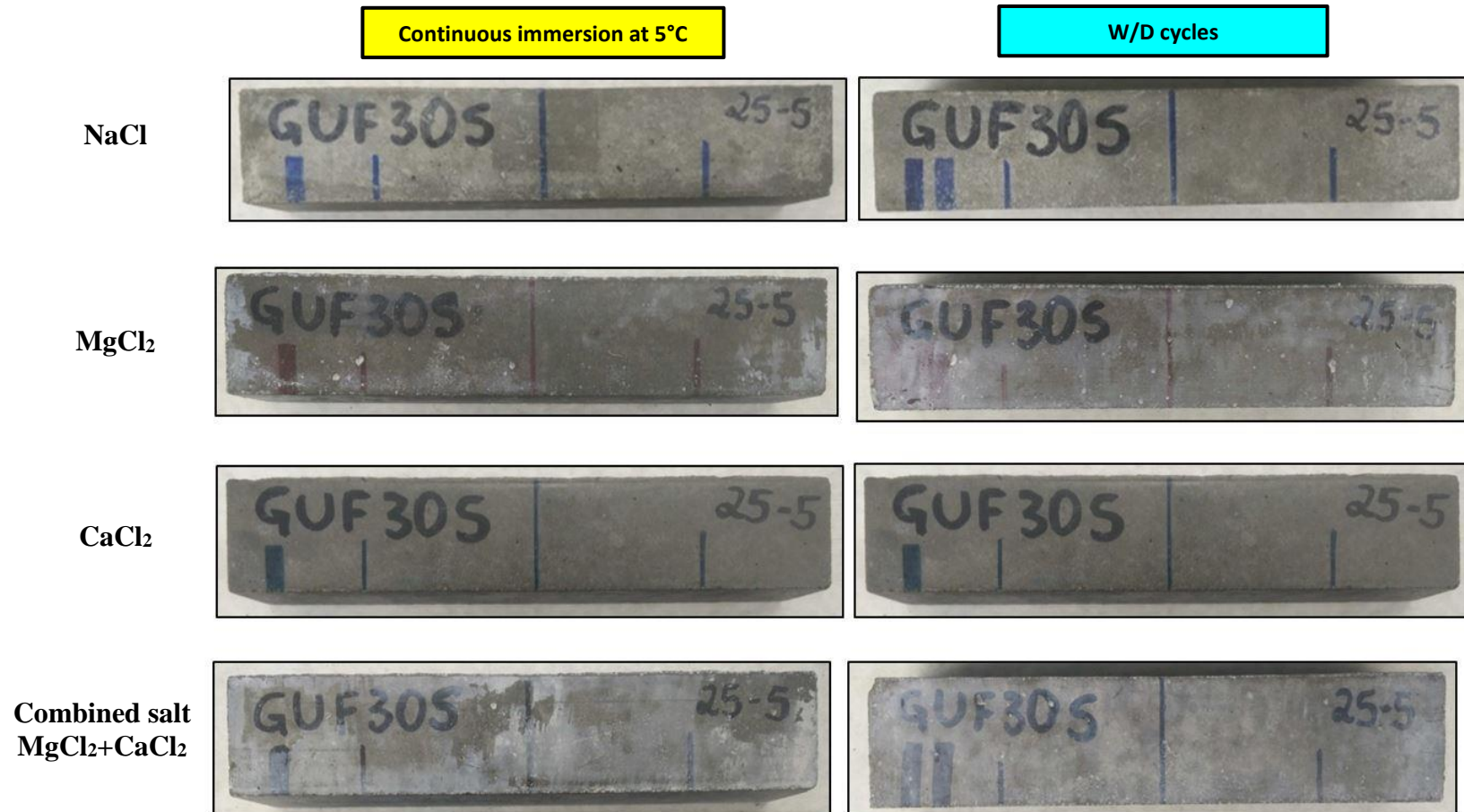
Figure A.2: Exemplar specimens (GUF30S) made with ternary binders compressing 30% fly ash and 6% nanosilica exposed to different de-icing salts at 540 days: continuous immersion at 5°C (left), and W/D cycles (right).
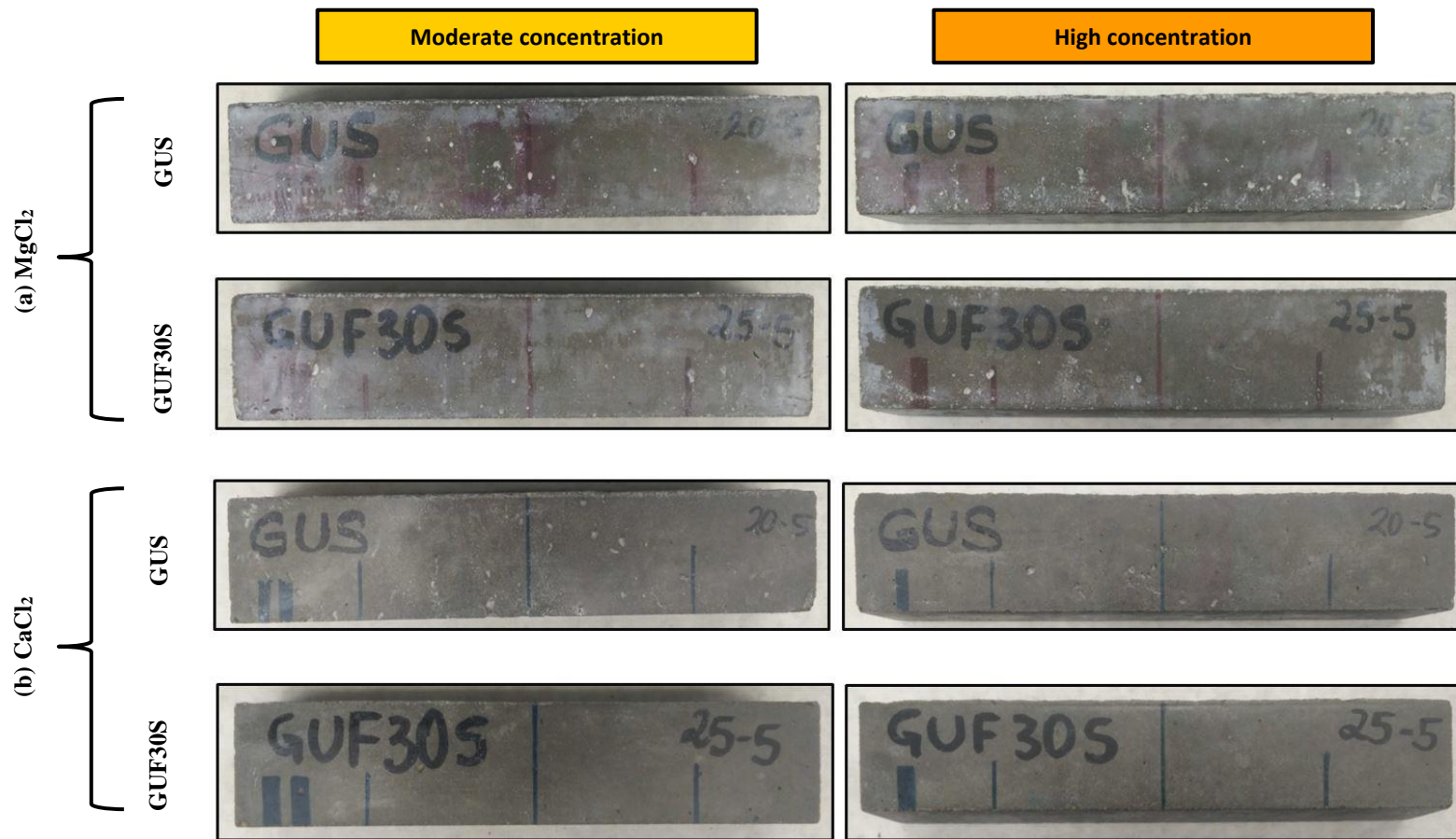
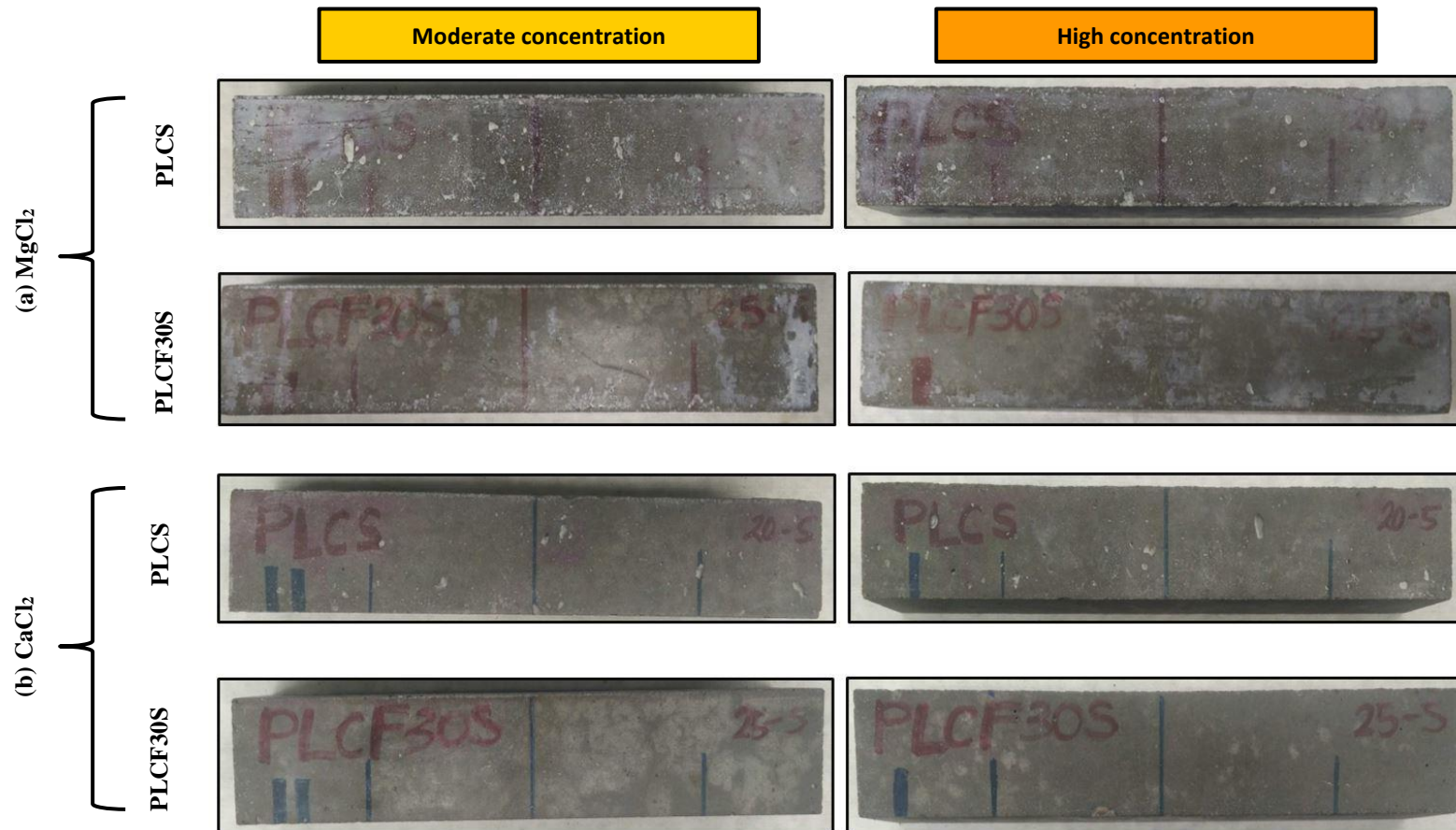Figure A.3: Exemplar GUS and GUF30S specimens exposed to 600 F/T cycles: (a) $MgCl_2$ and (b) $CaCl_2$ salts.

Figure A.4: Exemplar PLCS and PLCF30S specimens exposed to 600 F/T cycles: (a) $MgCl_2$ and (b) $CaCl_2$ salts.
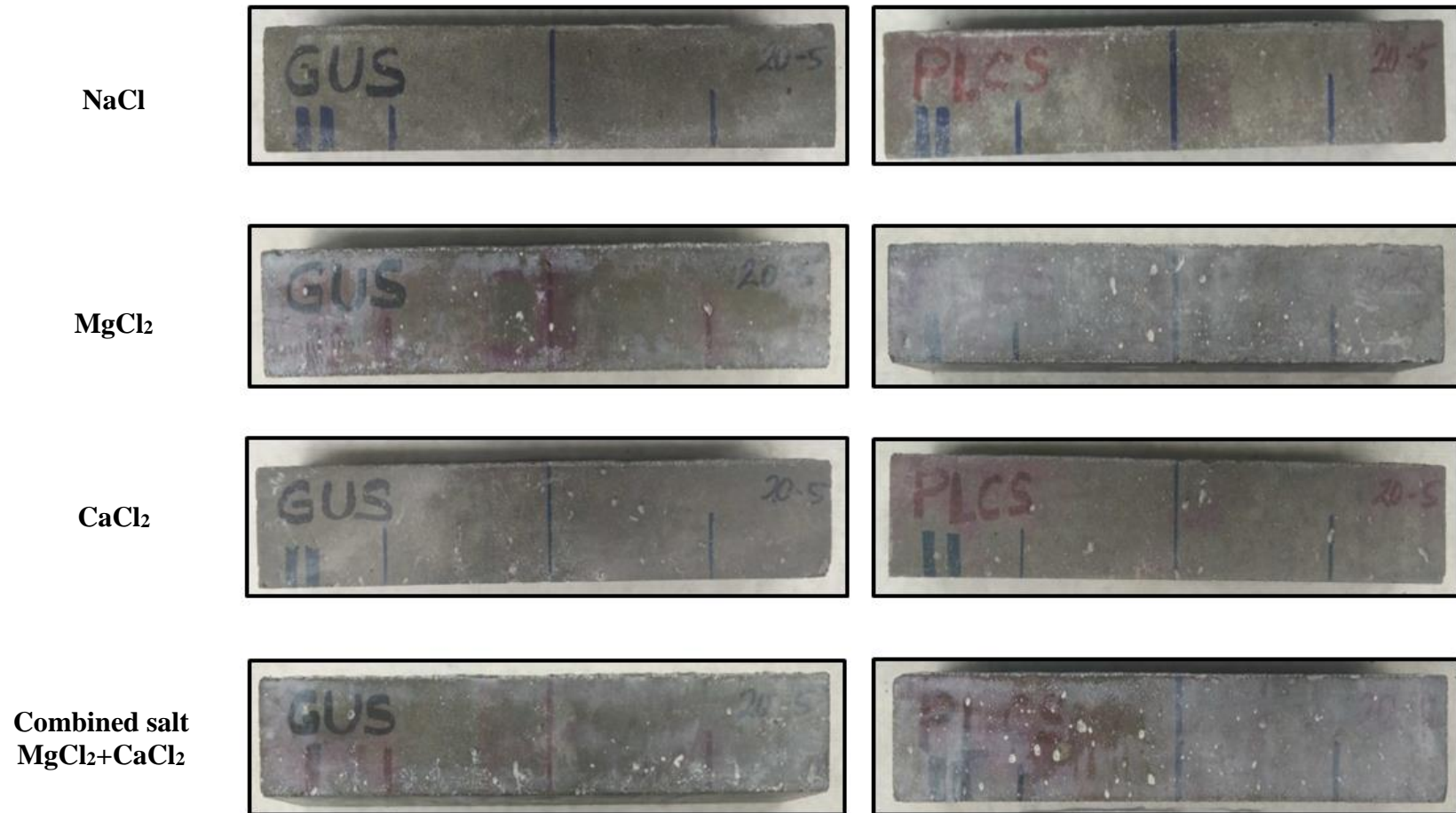
Figure A.5: Exemplar specimens made with binary binders compressing 6% nanosilica exposed to different de-icing salts at 540 days for combined exposure: GUS mixtures (left), and PLCS mixtures (right).
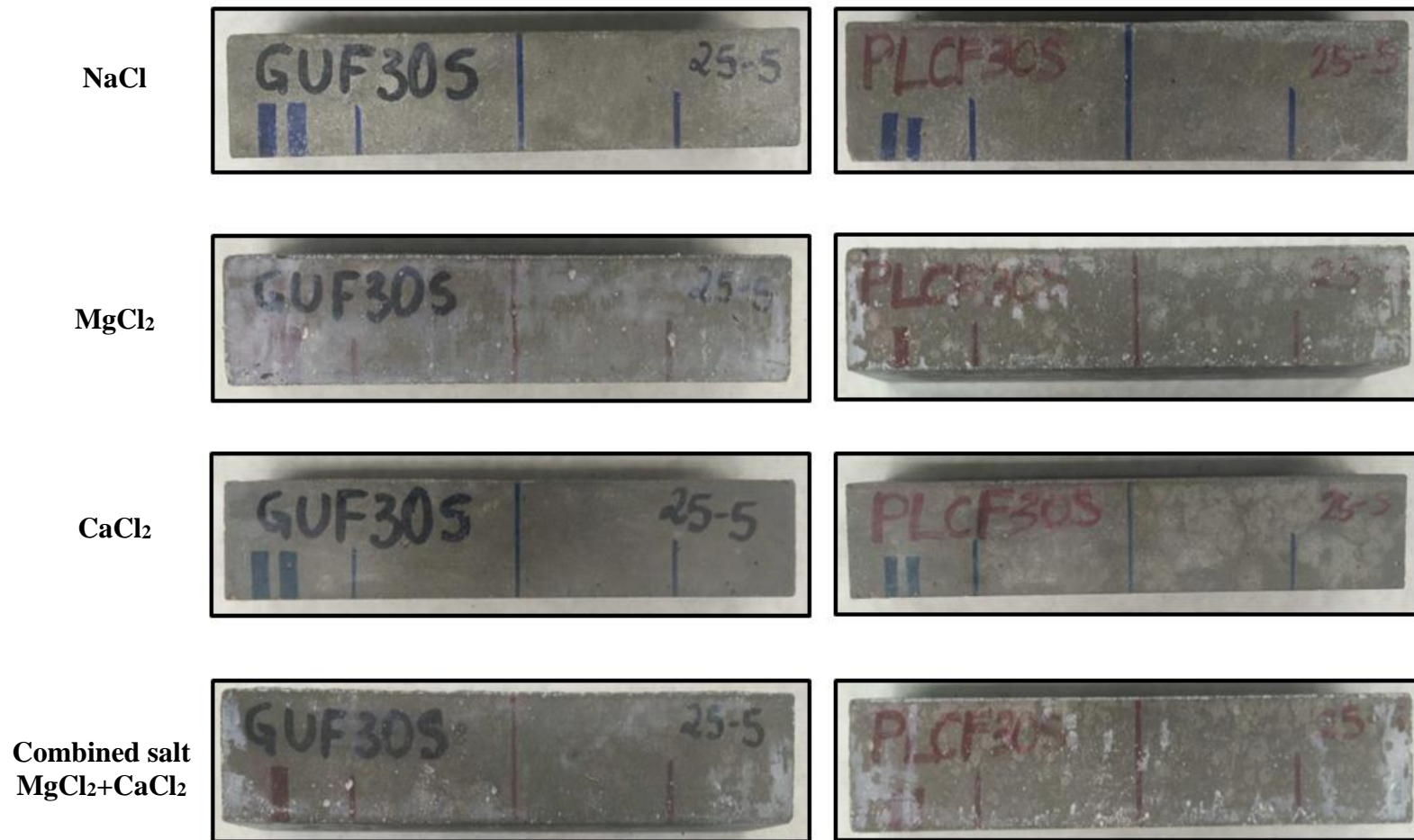
Figure A.6: Exemplar specimens made with ternary binders compressing 30% fly ash and 6% nanosilica exposed to different de-icing salts at 540 days for combined exposure: GUF30S mixtures (left), and PLCF30S mixtures (right).